GEMS & GEMOLOGY

SUMMER 2023
VOLUME LIX

THE QUARTERLY JOURNAL OF THE GEMOLOGICAL INSTITUTE OF AMERICA

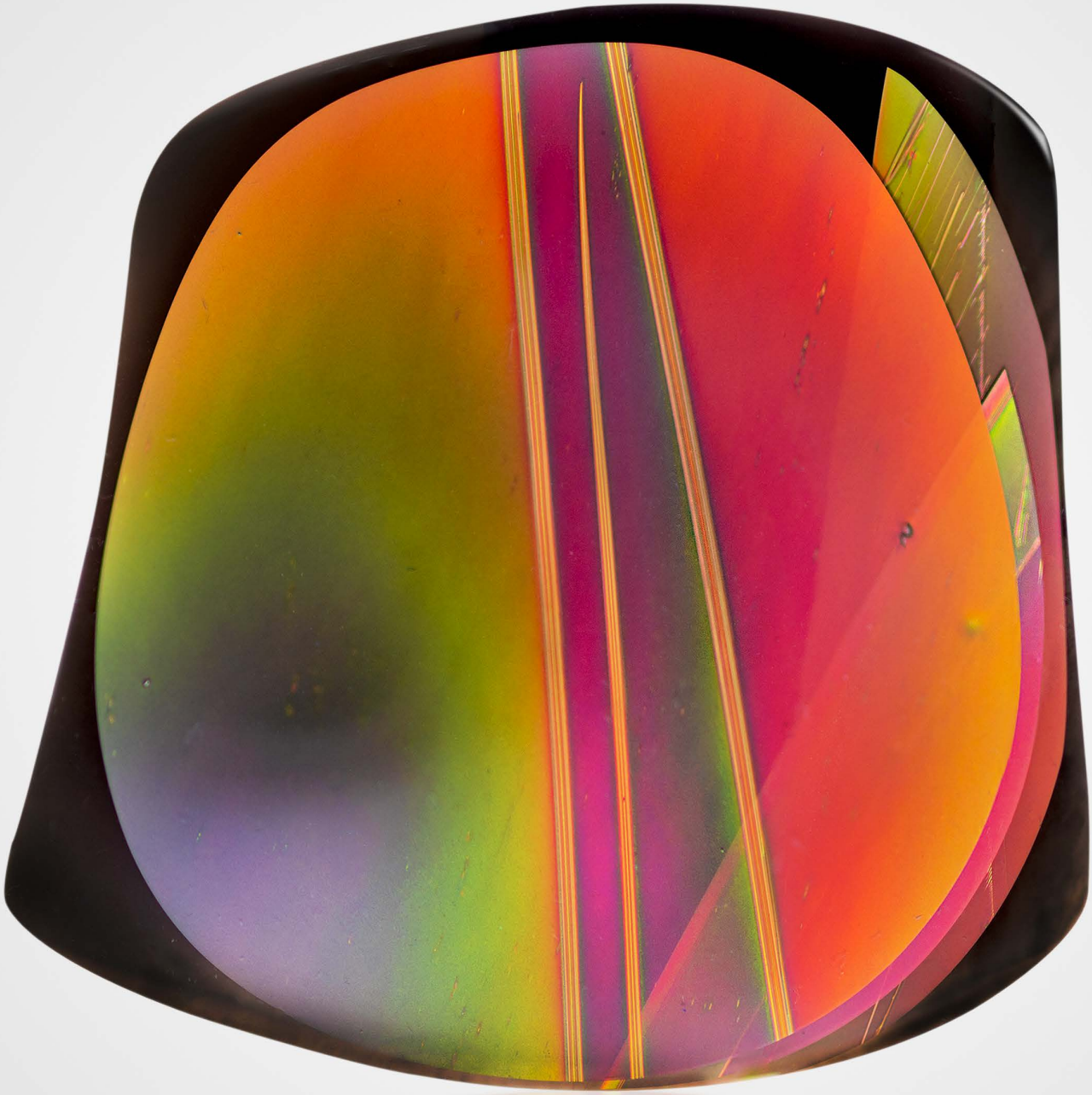

Nickel Diffusion Treatment of Spinel

Gem-Quality Augite from Vietnam

Color Origin of Brown Mammoth Ivory

Vibrant Colors of Fire Obsidian from Oregon

GEMS & GEMOLOGY®
Summer 2023
VOLUME 59, No. 2


p. 180


p. 186


p. 217

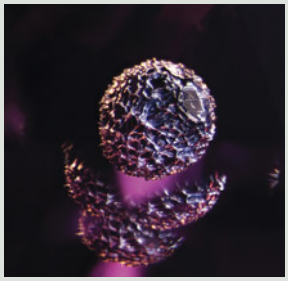
p. 226


p. 257

Editorial

Feature Articles

Regular Features

GEMS & GEMOLOGY

gia.edu/gems-gemology

Customer Service
(760) 603-4200
gandg@gia.edu

Subscriptions
Copies of the current issue may be purchased for $29.95 plus shipping. Subscriptions are $79.99 for one year (4 issues) in the U.S. and $99.99 elsewhere. Canadian subscribers should add GST. Discounts are available for renewals, group subscriptions, GIA alumni, and current GIA students. To purchase print subscriptions, visit store.gia.edu or contact Customer Service. For institutional rates, contact Customer Service.

Database Coverage
Gems & Gemology's impact factor is 2.045, according to the 2021 Journal Citation Reports by Clarivate Analytics (issued June 2022). *G&G* is abstracted in Thomson Reuters products (Current Contents: Physical, Chemical & Earth Sciences and Science Citation Index—Expanded, including the Web of Knowledge) and other databases. For a complete list of sources abstracting *G&G*, go to gia.edu/gems-gemology, and click on "Publication Information."

Manuscript Submissions
Gems & Gemology, a peer-reviewed journal, welcomes the submission of articles on all aspects of the field. Please see the Author Guidelines at gia.edu/gems-gemology or contact the Managing Editor. Letters on articles published in *G&G* are also welcome. Please note that Field Reports, Lab Notes, Gem News International, Micro-World, Colored Stones Unearthed, Diamond Reflections, Charts, and In the Spotlight are not peer-reviewed sections but do undergo technical and editorial review.

Gems & Gemology is published quarterly by the Gemological Institute of America, a nonprofit educational organization for the gem and jewelry industry.

Postmaster: Return undeliverable copies of *Gems & Gemology* to GIA, The Robert Mouawad Campus, 5345 Armada Drive, Carlsbad, CA 92008.

Our Canadian goods and service registration number is 126142892RT.

About the Cover

This issue spotlights a rare volcanic glass known as "fire obsidian," found only in central Oregon. The front cover features a 110.78 ct (41.9 × 40.9 mm) specimen cut by Tom Dodge, whose work reveals a vibrant spectrum of iridescent colors. A photomicrograph of the same piece (field of view 3.68 mm) is shown on the back cover, showing a distinctive pattern in the obsidian. Photo by Robert Weldon; photomicrograph by Nathan Renfro. Courtesy of Tom Dodge.

Printing is by L+L Printers, Carlsbad, CA.

GIA World Headquarters The Robert Mouawad Campus 5345 Armada Drive Carlsbad, CA 92008 USA

ISSN 0016-626X

FSC www.fsc.org MIX Paper from responsible sources FSC® C006300

Nickel-Diffused Spinel, Vietnamese Augite, Brown Mammoth Ivory, and More…

Welcome to the Summer 2023 issue of *Gems & Gemology*! Loaded with noteworthy content, the articles in this volume cover timely topics, such as a new treatment process identified in natural spinel, a recent source of augite in Vietnam, and research identifying the origin of the surface color of brown mammoth ivory.

In our lead article, Dr. Michael Jollands and fellow GIA researchers report on an undisclosed diffusion treatment process for spinel that is being used to convert lightly colored gems to hues ranging from green to blue. Testing a set of spinel samples represented as "cobalt diffused" revealed that the stones were actually diffused with nickel. With this treatment now present in the gem market, the authors suggest identification criteria for spinel samples within the green to blue color range.

"…an undisclosed diffusion treatment process for spinel that is being used to convert lightly colored gems to hues ranging from green to blue."

Next, a team led by Le Ngoc Nang investigates a variety of gem-quality augite from Dong Nai, Vietnam. The magnesium-rich augite, characterized by its intense dark orangy brown or dark green color under transmitted light, has potential use in jewelry and as a carving material.

Another carving material, mammoth ivory, is typically found with a brown surface color. Our third article, from Zhaoying Huang and coauthors, examines the origin of this color. They determine that iron oxides and sulfides and manganese oxides and hydroxides crystallized on the mammoth ivory's surface while underground, causing it to turn brown.

Our regular columns offer a host of interesting finds from all over the globe, including an aquamarine displaying asterism, a CVD-grown diamond over 34 carats, and an exceptionally large South Sea cultured pearl in the *Lab Notes* section. Explore the inner wonders of gemstones in *Micro-World*, with a feather inclusion resembling a mountain range in natural diamond, metallic platelets in Brazilian Paraíba tourmaline, an intriguing metal sulfide crystal in garnet, and more. *Colored Stones Unearthed* returns in this issue, covering gemstones that formed through metamorphic processes. Highlights from the *Gem News International* section include the characteristics of treated rubies from Greenland as they become more common in the market, the 2023 Sinkankas Symposium, and the latest auction season. Also in this issue, we put fire obsidian *In the Spotlight*. Tom Dodge's impressive lapidary work reveals the vivid spectrum of iridescent colors in this rare volcanic glass found only in the Glass Buttes region of Oregon.

Lastly, we invite you to join the *G&G* Facebook group (facebook.com/groups/giagemsgemology). Since its launch in February 2020, our growing community has surpassed 35,000 members. Thank you for your continued support and interest in *Gems & Gemology*!

Duncan Pay | Editor-in-Chief | dpay@gia.edu

Color Modification of Spinel by Nickel Diffusion: A New Treatment

Michael Jollands, Abadie Ludlam, Aaron C. Palke, Wim Vertriest, Shiyun Jin, Pamela Cevallos, Sarah Arden, Elina Myagkaya, Ulrika D'Haenens-Johannson, Vararut Weeramongkhonlert, and Ziyin Sun

A set of faceted spinel with blue to green hues, marked as "cobalt diffused," were obtained by researchers from GIA in Bangkok. Analyses of the absorption, luminescence, and chemistry of the stones have revealed that they were not diffused with cobalt, but instead with nickel. Laser ablation–inductively coupled plasma–mass spectrometry indicated high nickel concentrations (tens of thousands of ppma) at the edge of the stones, and a compositional traverse across one spinel showed a decrease of nickel toward the core, consistent with diffusion treatment. The trace element concentrations in the cores were consistent with natural spinel, as were the refractive indices. A similar decrease in lithium concentration was also seen, suggesting that treatment was done in the presence of a flux melt. Absorption spectra recorded in the ultraviolet/visible/near-infrared region contained characteristic bands at 369, 381, 475, 597, and 639 nm. Annealing experiments conducted on one spinel demonstrated that the 475 nm band is sensitive to the oxygen partial pressure (pO_2) in the experiment. The band increases in intensity following a high-pO_2 anneal, then decreases following an anneal at low pO_2. Photoluminescence spectra were consistent with heated natural spinel. This treatment now exists in the gem market and should be considered a possibility in spinel with blue or green hues.

In November 2022, a parcel of 24 spinels weighing approximately 0.51–1.19 ct and described as "cobalt diffused" was obtained by the research team at GIA in Bangkok. Of these, eight possessed the deep blue color characteristic of cobalt diffusion, while the others had lighter blue, greenish blue, bluish green, or blue-green color (figure 1). Wafers were cut from the core of several stones, and all showed diffuse color zonation, from more blue/green at the rim to near-colorless at the core (figure 2).

The concentrations of various elements were recorded along culet-to-table transects in the wafers using laser ablation–inductively coupled plasma–mass spectrometry (LA-ICP-MS). The expectation was that all stones would show simple cobalt diffusion profiles, meaning high cobalt concentrations at the edge, changing gradually to lower concentrations in the core. This has been well described by Saeseaw et al. (2015), Peretti et al. (2015), and Krzemnicki et al. (2017). For the deep blue stones, the result was as expected: high cobalt, thousands of atomic parts per million (ppma) at the rim, changing gradually to low cobalt in the core. This is clear evidence of cobalt diffusion treatment. However, all other stones (i.e., those that were not deep blue) showed something quite different. The cobalt concentration in these crystals was negligible, generally below a few atomic ppm. The nickel concentration, conversely, was extremely elevated, generally around 10000 to 20000 ppma at the rim and dropping to a few ppma in the core. An initial conclusion was that these "cobalt-diffused" spinels were actually nickel diffused. Sub-

In Brief

- Nickel-diffused spinel was discovered in a parcel of spinel marked as "cobalt diffused."
- The diffusion treatment was likely conducted in the presence of a nickel-bearing flux melt, in an oxidizing atmosphere such as air or oxygen gas, potentially at temperatures exceeding 1500°C.
- This treatment can be readily identified by high nickel content and the presence of bands at 597 and 639 nm in absorption spectroscopy.

See end of article for About the Authors.

Gems & Gemology, Vol. 59, No. 2, pp. 164–181,
http://dx.doi.org/10.5741/GEMS.59.2.164

Figure 1. Suite of faceted nickel-diffused spinel (0.67–1.01 ct) showing a range of color from blue to bluish green. Photo by Aaron Palke and Diego Sanchez.

sequent investigations using various absorption, luminescence, and fluorescence techniques along with gemological observations confirmed that the samples were indeed nickel diffused and that natural near-colorless spinel was likely used as the starting material. Additionally, nickel was confirmed to be the main chromophore responsible for the modified color. These observations are described in detail below, along with the results of some preliminary experiments on the diffused stones, discussion of heat treatment methods, and some potential identification criteria.

Figure 2. Wafers cut from the center of a nickel-diffused spinel (top) and a cobalt-diffused spinel (bottom). The cobalt-diffused stone was in the same parcel as the nickel-diffused stones, showing a clearly different hue and color intensity. Photos were taken using a Nikon SMZ1500 microscope with the wafers placed on a white diffuser plate.

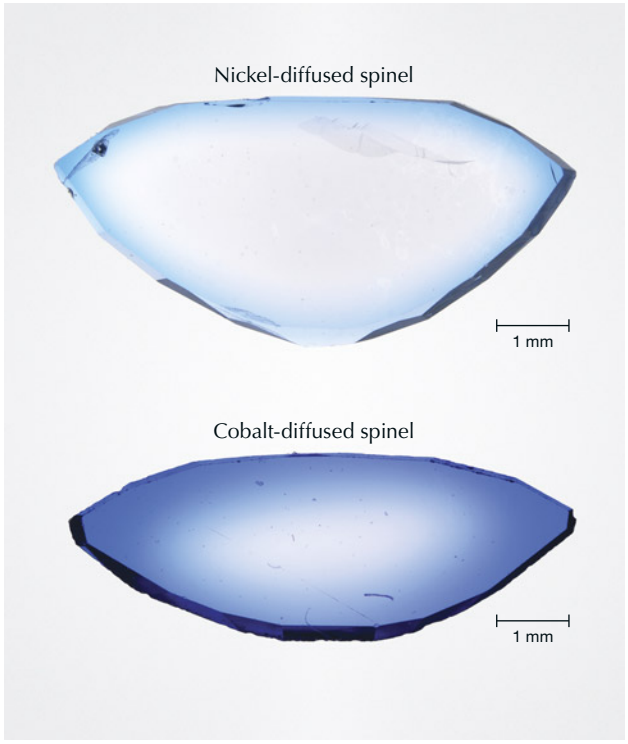

MATERIALS AND METHODS

Materials. Twenty-four faceted spinel samples were purchased by GIA Bangkok for scientific examination. These were all oval cut and weighed between 0.51 and 1.19 ct. Eighteen of them (thirteen nickel-diffused and five cobalt-diffused) were left in their original faceted state, but three nickel-diffused and three cobalt-diffused stones were fabricated into doubly polished wafers perpendicular to the table. The wafers were polished on both faces using a tin alloy lap impregnated with 6 µm diamond paste. Colors, weights, and forms (faceted or wafer) of the nickel-diffused stones are presented in table 1.

Analytical Methods. *Gemological Testing*. A total of 16 stones were studied using standard gemological methods at GIA in New York, Carlsbad, and Bangkok. The eight stones in the original parcel that were clearly cobalt diffused were not studied beyond identification of cobalt diffusion treatment. Refractive indices were measured on faceted stones and on doubly polished wafers using a GIA-built refractometer. The fluorescence reactions to both long-wave (365 nm) and short-wave (254 nm) UV light were de-

TABLE 1. The 16 nickel-diffused spinel samples analyzed for this study.

Sample no.	Color[a]	Original (faceted) weight (ct)	Form
17407059	Greenish blue	0.861	Faceted oval
17407060	Greenish blue	0.764	Faceted oval
17407068	Blue	0.674	Faceted oval
17407066	Greenish blue	0.940	Faceted oval
17407062	Greenish blue	0.895	Faceted oval
17407061	Blue	0.906	Faceted oval
17407070	Blue	1.009	Faceted oval
17407067	Bluish green	0.812	Faceted oval
17407058	Bluish green	1.045	Faceted oval
17407064	Green	0.884	Faceted oval
17407065	Green	0.940	Faceted oval
17407071	Greenish blue	0.850	Faceted oval
17407072	Greenish blue	0.553	Faceted oval
17407057[b]	Greenish blue	0.513	Wafer
17407126	Greenish blue	0.513	Wafer
17407123	Bluish green	1.192	Wafer
17407124[c]	Blue	0.827	Wafer
17407069	Blue	0.827	Wafer

[a]*Color was assessed visually on faceted stones.*
[b]*17407057 and 17407126 were both cut from one stone.*
[c]*17407124 and 17407069 were both cut from one stone.*

termined using mercury lamps. Additionally, faceted stones were viewed through a Chelsea color filter and also immersed in methylene iodide in order to observe internal color variations.

Energy-Dispersive X-ray Fluorescence (EDXRF). EDXRF spectra were recorded at GIA in Carlsbad by placing faceted stones in a Thermo Quant'X EDXRF spectrometer, operating at 12 kV and 1.92 mA, with an aluminum filter. Fluorescence was recorded between 0 and 40 keV. These data are not quantified, so no detection limits are provided.

LA-ICP-MS. LA-ICP-MS data were recorded using a Thermo iCAP Q ICP-MS coupled to an Elemental Scientific 213 nm (Nd:YAG) laser ablation system via helium carrier gas. This was done using three identical LA-ICP-MS systems, at GIA in New York, Carlsbad, and Bangkok. Most stones were analyzed by ablating 35 µm circular spots on the girdles, at 20 Hz, with a ~11 J/cm^2 fluence. The doubly polished wafers were ablated using the same conditions, but on one of the two main polished faces rather than on the girdle, and using a 50 µm circular spot with a centroid located at approximately 50 µm from the edge on the table side.

The analyzed elements (isotopes in parentheses) were lithium (^{7}Li), beryllium (^{9}Be), magnesium (^{25}Mg), aluminum (^{27}Al), titanium (^{47}Ti), vanadium (^{51}V), chromium (^{53}Cr), manganese (^{55}Mn), iron (^{57}Fe), cobalt (^{59}Co), nickel (^{60}Ni and/or ^{62}Ni), zinc (^{66}Zn), and gallium (^{69}Ga). Dwell times were between 0.01 and 0.05 s per isotope. To record a compositional transect across one doubly polished stone, the sample was moved below a stationary, continuously ablating 40 µm circular spot, with 20 Hz repetition rate and fluence around 7 J/cm^2, while the ICP-MS counted continuously. Dwell times for the transect were 0.05–0.10 s per isotope, analyzing the same isotopes as listed above. Magnesium was not quantified in any analysis, but the compositional transect shows resolvable magnesium variation when calculated as magnesium/aluminum (counts per second), which can still be used to understand relative magnesium concentrations along the transect.

In all cases, background analyses were recorded for around 1 minute. The primary standard was NIST SRM 610 glass, using the reference values from Jochum et al. (2011). Data were processed using Iolite software (Paton et al., 2011), with ^{27}Al as the internal standard, initially assuming a constant value of 39.7 wt.%. This implicitly assumes that nickel incorporation into spinel is accomplished by removal of magnesium rather than aluminum.

Detection limits were determined for each analysis using the Longerich et al. (1996) method, generally using at least 30 s of manually selected background. Minimum and maximum detection limits for all analyses, for each element, were: lithium: 0.1–0.6 ppma; beryllium: 0.1–0.5 ppma; titanium: 0.04–0.2 ppma; vanadium: 3–84 ppba; chromium: 0.06–0.36 ppma; manganese: 9–140 ppba; iron: 0.4–1.9 ppma; cobalt: 2–30 ppba; nickel: 0.05–0.4 ppma; zinc: 13–68 ppba; and gallium: 2–12 ppba. No correction was made for the decreasing aluminum content by weight associated with an increased nickel content. This is necessary for accurately determining concentrations by weight, given the difference in atomic mass between nickel and magnesium (58.69 u and 26.98 u, respectively), again assuming that nickel incorporation is associated with magnesium removal. The justification is that even at around 5 wt.% nickel, the highest measured in this study, the discrepancy between actual concentrations and calculated concentrations is <3% (figure 3). Additionally, making this correction would require *a priori* assumptions about valence state and coordination environment of nickel, which cannot be confidently made.

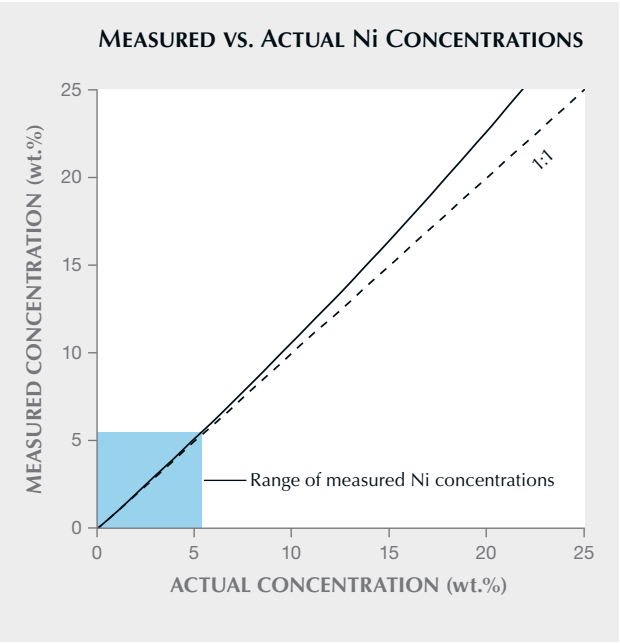

Figure 3. Calculated discrepancies arising from the assumption that spinel is pure $MgAl_2O_4$, then using the appropriate value for the aluminum concentration (39.7 wt.%) as an internal standard when reducing LA-ICP-MS data recorded from stones with high nickel (in wt.%). The x-axis shows the actual nickel concentration, and the y-axis shows the concentration that would be calculated using this internal standard value. At high concentrations, the nickel becomes systematically overestimated. The same degree of overestimation would be seen for all analyzed elements. In these stones, the nickel concentrations are still low enough (blue box) that the maximum inaccuracy from this calculation is around 3% in the most extreme case.

In addition to collecting LA-ICP-MS data from the nickel-diffused stones in this study, we extracted data from a larger GIA database, from analyses of blue, green, green-blue, bluish green, and greenish blue spinel determined to be natural. This yielded 1,495 individual analyses. These data were compiled for comparison with data from the diffused stones.

Energy-Dispersive Spectroscopy (EDS) Mapping. EDS spectra were recorded from sample 17407069 following gold-coating, using an Oxford X-Max^N 20 EDS detector on a Zeiss EVO Ma 10 scanning electron microscope at GIA in New York, operating at 15 keV accelerating voltage, 30 nA current, and 71× magnification. The pixel dwell time was 60 µs. Counts

were extracted from spectra as the maxima on the Kα bands of oxygen, aluminum, magnesium, and nickel. Post-processing was done on the extracted X-Y-counts matrices using MATLAB. Due to the large size of the area being mapped and analytical limitations, the total count rate was not constant; therefore, all counts on aluminum, magnesium, and nickel were normalized to counts on oxygen. Additionally, a swath of data (400 × 1291 point rectangle) was extracted from the larger data matrix along a table-to-culet transect and averaged parallel to the table, to give one-dimensional transects of oxygen-normalized counts.

Ultraviolet/Visible/Near-Infrared (UV-Vis-NIR) Spectroscopy. UV-Vis-NIR spectra were recorded in absorbance mode between 200 and 1500 nm from five doubly polished wafers using a Perkin Elmer Lambda 950 UV-Vis spectrometer at GIA in New York. Four of the wafers were nickel diffused (samples 17407057, 17407124, 17407123, and 17407126), and one was cobalt diffused (17407125), with the latter analyzed for comparison only. The wafers were mounted onto an aluminum plate containing a 0.5 mm circular aperture located as close as possible to the stone's edge. For the sample that was annealed experimentally (17407067), spectra were recorded from the whole stone using a using a custom-built UV-Vis system at GIA in Carlsbad, operating in transmission mode from 250 to 980 nm, with an integrating time of 3000 ms and 3 accumulations.

Photoluminescence (PL) Spectroscopy. PL spectra were recorded from 630 to 750 nm on the core and rim of one doubly polished wafer (sample 17407124) using a Renishaw inVia Raman microscope with a 514 nm laser, 1800 l/mm grating, and a 5× objective at GIA in New York. The power and counting times were adjusted to obtain maximum signal while avoiding saturation. The high concentration of nickel appeared to be associated with quenched fluorescence, which meant that higher power and longer accumulation times were required for spectra recorded near the high-nickel rim.

Diffusion Modeling. Diffusion is described using Fick's first and second laws, two partial differential equations that can be thought of as defining the way in which particles spread out over space and time. In order to apply these laws to a real situation, the equations must be solved for a given set of conditions, which require approximations to be made regarding the geometry of the system (e.g., a stone) and the nature of the source of diffusing species (e.g., a high-nickel powder or melt placed into contact with the stone). The aim here is to determine Dt, which is the diffusion coefficient (D, in units of square meters per second, m^2/s) multiplied by the time (t, in units of seconds, s). In this case, the diffusion coefficient is a number that describes how rapidly a given element, such as nickel, moves through spinel.

In order to determine diffusion coefficients from the LA-ICP-MS transect, concentration vs. distance data were fitted to the solution of Fick's second law describing diffusion in a one-dimensional semi-infinite medium, using a constant boundary condition (Crank, 1975):

$$C(x,t) = C_{core} + (C_{rim} - C_{core})\,erfc\frac{x}{2\sqrt{Dt}} \quad (1)$$

In this equation, x is the distance (in meters, m) from the edge, C is the concentration (in ppma) at the core (C_{core}) and rim (C_{rim}) at a given distance at a given time ($C(x,t)$), and *erfc* is the complementary error function.

This fitting was only done for half profiles, meaning the data were recorded from the core to the table, instead of table-to-culet or core-to-culet. This is because the shape of the culet renders this solution to Fick's second law inappropriate—the solution is strictly valid only for a plane sheet with infinite extent. The flat table of a faceted stone is a reasonable approximation of this geometry, but the culet is not. The data was fitted to the model using nonlinear least squares regression implemented in MATLAB, with the output being Dt (units of m^2). These Dt values are presented as their base-10 logarithm.

Experimental Methods. To complement analyses on the as-received stones, one faceted spinel (sample 17407067, bluish green) was annealed at various temperature (T) and oxygen partial pressure (pO_2) conditions, and then UV-Vis spectra were recorded on the whole spinel after each step. The aim was to determine whether temperature and oxygen partial pressure could modify the defects present in the stone, and therefore potentially the color. Pure O_2 at atmospheric pressure has pO_2 = 1 atm. The O_2 content in air is 21%, and therefore pO_2 = 0.21 atm. The pO_2 can also be controlled by mixing gases. In one experiment, the furnace was filled with a mixture of CO_2 and H_2

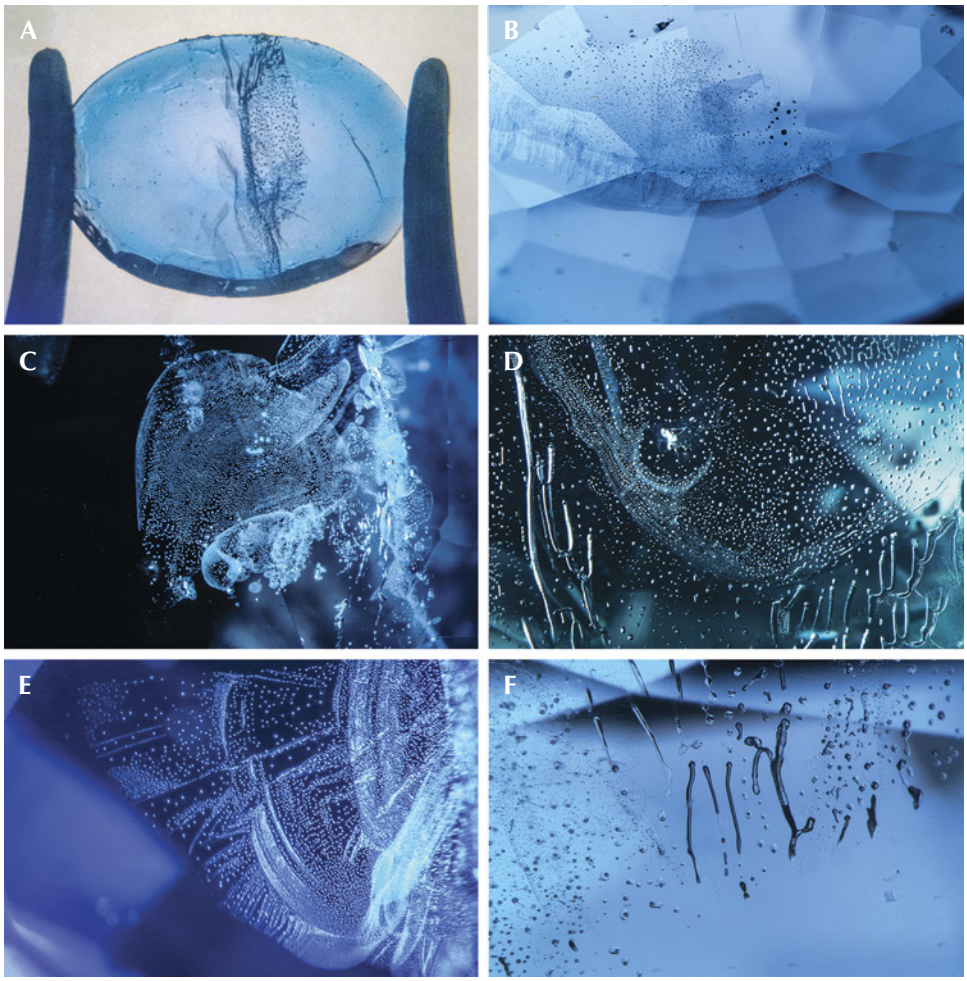

Figure 4. Nickel-diffused spinel shows subtle color concentration along facet junctions (A and B) and features suggesting flux-assisted healing of the fractures during the heating process (C–F). Photos by Aaron Palke; fields of view 10.24 mm (A), 2.90 mm (B), 2.34 mm (C and D), 1.76 mm (E), and 1.99 mm (F).

gases, which react to form CO, H_2O, CH_4, and O_2, yielding a very low partial pressure of O_2. A 2:1 mix of CO_2:H_2 was used, giving $pO_2 = 4 \times 10^{-6}$ atm at 1750°C (Prunier and Hewitt, 1981). Experiments were conducted in a 1000-3560-FP24 Thermal Technology gas mixing furnace. The temperature/time/pO_2 annealing conditions, for sequentially heating the same stone, were: (1) 1100°C for 10 hours at 1 atm, (2) 1700°C for 18 hours at 1 atm, and (3) 1750°C for 40 hours at 4×10^{-6} atm.

RESULTS

Gemological Observations. Gemological observations were consistent with spinel. Refractive indices for the nickel-diffused samples were generally 1.718, but some samples had values as high as 1.725, possibly due to the increased concentration of nickel at the surface. All samples were inert to long-wave UV light. Most were also inert to short-wave UV, but a few showed faint chalky yellow fluorescence near the edges when prepared as doubly polished wafers. All faceted stones had a weak to strong red reaction when viewed through the Chelsea color filter. The doubly polished wafers viewed in this way showed color zonation: red at the rim and colorless in the center.

When immersed in methylene iodide, the faceted stones displayed a strong concentration of color around the rim of the stone (figure 4A), sometimes with additional subtle color concentration along the facet junctions (figure 4B). Microscopic observations sometimes revealed this same color concentration along facet junctions, particularly at the keel of the stones, although the effect was more subtle here than in other treated material, such as titanium-diffused sapphire. The most striking microscopic feature was the abundance of artificially healed fractures, likely associated with the presence of a flux material during heating (figure 4, C–F). This is also supported by the trace element data, described below, which show

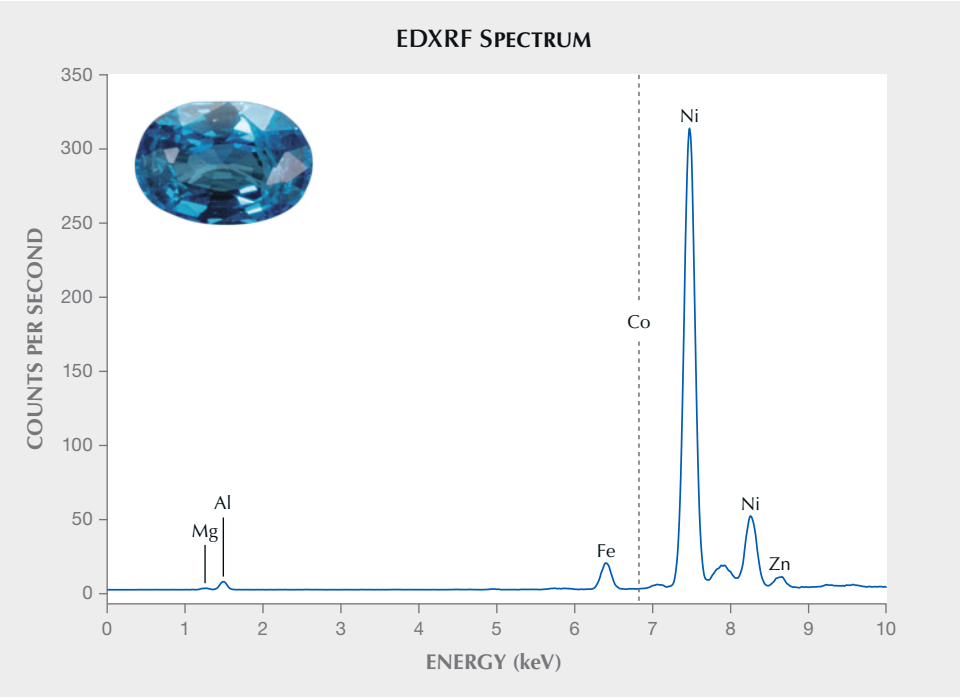

Figure 5. An EDXRF spectrum of a nickel-diffused spinel (sample 17407067) acquired at 12 kV with an aluminum filter. Distinct nickel fluorescence peaks are visible. The position of the main cobalt peak, absent in this spectrum, is shown by the dashed line.

high amounts of lithium at the stones' edge—lithium is a common component of flux material.

Compositional Analysis. *X-ray Fluorescence.* EDXRF spectra of nickel-diffused stones (e.g., figure 5) consistently showed the strongest bands at 7.47 keV, interpreted as the sum of the nickel Kα lines ($K\alpha_1$ and $K\alpha_2$ at 7.48 and 7.46 keV, respectively), with an associated Kβ band at 8.26 keV. No nickel L lines are visible in figure 5. Also clearly visible are Mg Kα (1.25), Al Kα (1.48), Fe Kα (6.40), Fe Kβ (7.06), and Zn Kα (8.64). No Co Kα line is visible at 6.93 keV.

LA-ICP-MS. *Single Point Analyses*. Table 2 shows the concentrations of measured trace elements, measured either on the girdle of as-received faceted stones or at around 50 µm from the table in doubly polished wafers. The concentration of nickel at the edge of the spinel was high, around 10000–20000 ppma. These nickel concentrations are very high compared to natural gem-quality spinel submitted for analyses at GIA (figure 6A). It should be noted, however, that the nickel end member of the spinel group (chihmingite, $NiAl_2O_4$) does exist in nature (Miyawaki et al., 2022).

Along with elevated nickel, some but not all stones also contained high lithium concentrations, up to around 3000 ppma at the surface (see table 1). Such high lithium is rare in natural, untreated gem spinel (figure 6B). Concentrations of other elements, even if added or removed during the diffusion treatment, were generally within normal ranges for gem spinel. Notably, this also includes beryllium (figure 6C), despite the increasing concentration of beryllium toward the edge in the LA-ICP-MS transect, described below (figure 7).

Additionally, the concentrations of all other measured elements (titanium, vanadium, chromium, manganese, iron, cobalt, zinc, and gallium) were highly variable between stones. Preliminary analyses from the cores of other doubly polished wafers (samples 17407047, 17407126, 17407123, and 17407069) showed different concentrations of elements other than nickel (see table 2) in areas apparently unaffected by diffusion, suggesting that these concentration variations relate at

Figure 7 (opposite page). Concentrations of magnesium, nickel, lithium, iron, zinc, vanadium, titanium, beryllium, manganese, gallium, chromium, and cobalt recorded along a ~3.3 mm culet-to-table transect across a wafer cut from the core of a nickel-diffused spinel (sample 17407124). Magnesium is not quantified, so the y-axis in the top right plot is arbitrary. Notably, nickel shows an extreme concentration decrease from rim to core, whereas cobalt shows a very small decrease with sub-ppm concentration along the whole transect. The transects for elements showing clear concentration changes are replotted in figure 12 for the purpose of diffusion modeling.

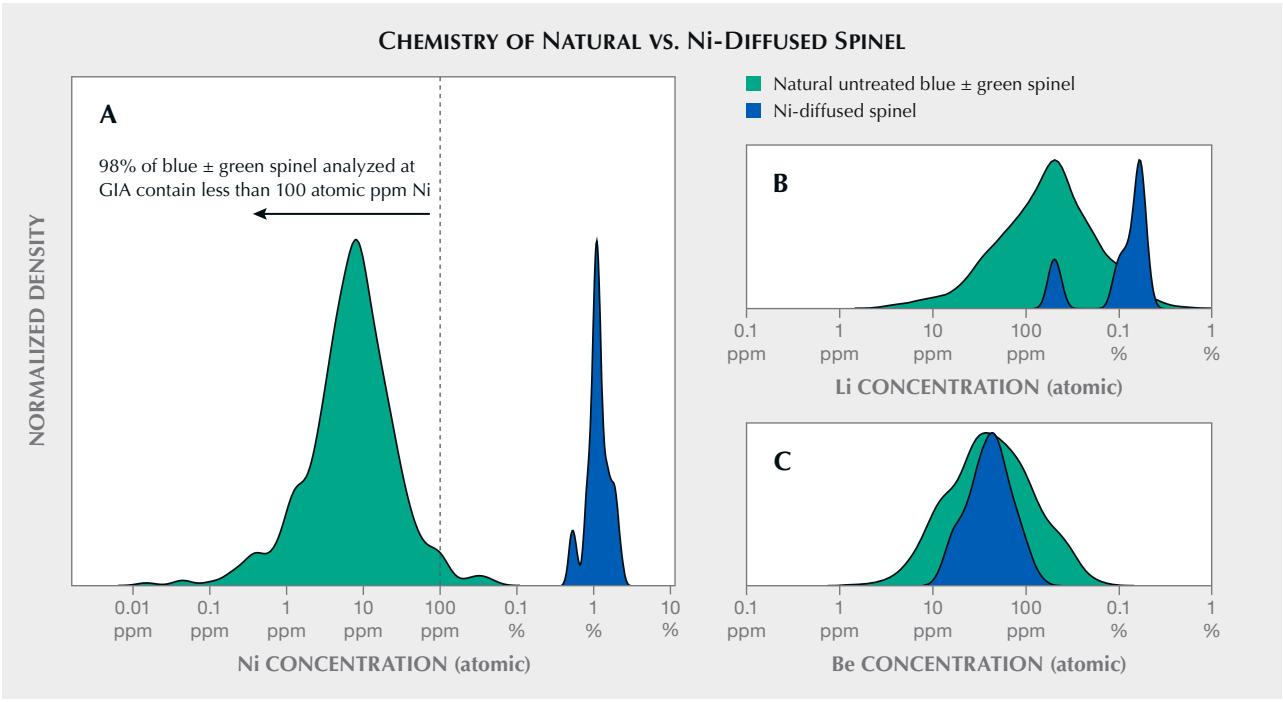

Figure 6. A: Kernel density plots of nickel concentrations measured on the girdles of nickel-diffused stones, along with the range of nickel concentrations seen in a subset of spinel (1,495 analyses) submitted to GIA. This subset includes natural, untreated spinel with the following hues: blue, greenish blue, green-blue, blue-green, and bluish green. The nickel concentrations are considerably higher (100–10,000×) in the nickel-diffused stones. Also shown are the concentrations of lithium (B) and beryllium (C), both of which are also elevated at the rims, as shown in the LA-ICP-MS transect (figure 7). Lithium concentrations in diffused stones are generally higher than the natural range, but beryllium concentrations are indistinguishable between natural untreated spinel and nickel-diffused spinel.

least partially to different starting materials (i.e., different natural spinel) rather than different treatment conditions. At this point, however, we cannot confidently describe the nature of the starting materials.

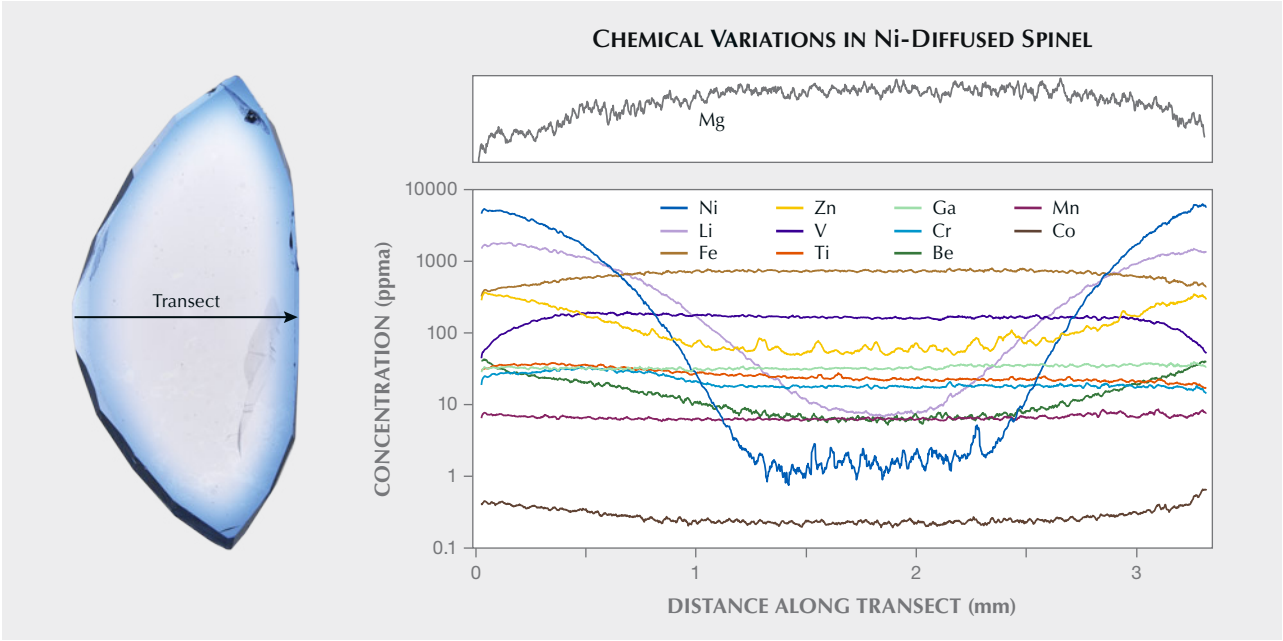

TABLE 2. Concentrations of trace and minor elements in nickel-diffused spinel (in ppma), measured using LA-ICP-MS on the girdle or near the edge of the spinel.[a]

Sample no.	Li	Be	Ti	V	Cr	Mn	Fe	Co	Ni	Zn	Ga
17407059	924	79.0	5.9	19.1	5.9	16.9	183	1.4	13929	250	50
17407060	1084	44.7	13.3	16.7	17.8	14.6	174	1.1	17840	360	40
17407068	1980	90.4	9.7	22.9	147.4	24.1	396	12.9	18995	925	66
17407066	1208	28.2	13.8	29.1	3.8	6.7	182	0.6	8194	276	33
17407062	185	31.0	3.2	19.0	0.9	14.2	180	1.2	19030	474	45
17407061	1617	58.8	19.6	7.1	36.5	27.0	473	1.3	10746	150	36
17407070	192	32.5	7.7	13.3	15.3	13.1	349	0.8	12021	288	43
17407067	1343	69.9	8.0	29.6	5.3	38.5	420	1.1	14857	286	50
17407058	222	16.6	5.0	13.8	18.5	6.0	169	0.7	10339	410	42
17407064	1631	51.0	9.0	7.0	10.4	12.1	433	0.9	11399	458	56
17407065	1773	26.5	6.6	7.4	12.0	8.9	333	0.6	10123	512	64
17407071	1649	49.0	9.4	5.0	45.1	33.6	578	0.8	9961	204	34
17407072	1640	41.5	29.4	6.9	54.3	28.8	500	0.8	11601	249	41
17407057	899	16.3	7.7	98.8	30.6	6.4	6	0.5	5794	451	64
17407126	1024	18.2	8.5	98.3	29.4	5.9	7	0.5	5177	478	59
17407023	1338	116.9	15.7	7.8	15.8	62.1	13	0.4	4977	292	79
17407024	1722	36.8	18.2	69.8	19.2	10.9	14	0.8	7854	334	45
17407069	1573	40.2	18.7	53.6	15.1	10.2	16	1.3	8298	330	42

[a]*Concentration values are means of 2–3 analyses. Concentrations in the last five samples were measured on doubly polished wafers using 50 µm diameter circular LA-ICP-MS spots with centroids 50 µm from the edge of the spinel closest to the table. All others were measured using a 35 µm spot on the girdle on faceted stones.*

These data show that nickel appears to be a weak chromophore, as thousands to tens of thousands of ppma led to relatively weak colors. In contrast, cobalt diffusion treatment requires only a few hundred to thousands of ppma cobalt to create deep blue colors (e.g., Saeseaw et al., 2015; Krzemnicki et al., 2017). This may relate to the incorporation mechanism of nickel, described below (in the "Nickel Incorporation Mechanism and Valence State" section).

Concentrations Recorded Along a Transect. In one stone where trace element concentrations were recorded along a central transect (sample 17407124), nickel, lithium, beryllium, zinc, manganese, and cobalt show decreasing concentrations from the rim to the core (figure 7), with U-shaped profiles. The largest concentration change is associated with nickel, from ~1 ppma in the core to ~5000 ppma at the rim. Cobalt shows the smallest change, from ~0.4 ppma at the core to ~0.8 ppma at the rim. Conversely, vana-

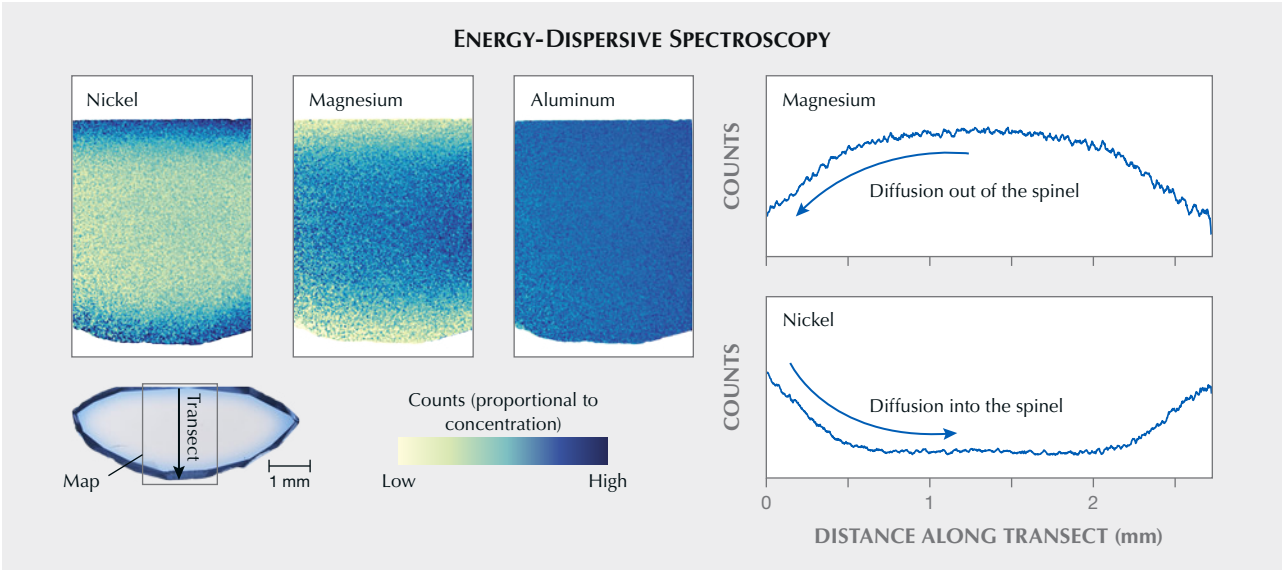

Figure 8. Maps of nickel, magnesium, and aluminum recorded by EDS from sample 17407069. Colors represent counts on nickel, magnesium, and aluminum normalized to total signal intensity by dividing by counts on oxygen (all Kα lines). The normalization was necessary given nonconstant total signal across the mapped area. Color scales are set to maximize contrast; the ranges (normalized to oxygen) are 0–0.04 for nickel, 0.85–1.2 for magnesium, and 1–2.6 for aluminum. Also shown are profiles of magnesium and nickel, extracted from the maps in table-culet transects.

dium, iron, and magnesium display inverted U-shaped profiles—i.e., lower concentrations at the rim than at the core. The magnesium profile is displayed separately, as this cannot be accurately quantified when using NIST SRM 610 as a primary standard and aluminum as the internal standard. The likely reason is that the magnesium concentration in the NIST SRM 610 standard glass is around three orders of magnitude lower than in the spinel. As a result, using the analytical and data reduction routine described above, the quantified magnesium content is about 30% lower than expected. This is not problematic for estimating diffusion coefficients, though. Chromium and titanium show variable concentrations, but neither has a clear U-shaped or inverted U-shaped profile. Gallium shows no apparent concentration change.

EDS. EDS has considerably higher spatial resolution than LA-ICP-MS but suffers from much poorer detection limits, so the only elements that could be measured were nickel, magnesium, aluminum, and oxygen (figure 8). Nickel shows a clear concentration decrease from rim to core. Magnesium shows the opposite, which is discussed later, and aluminum shows no apparent zonation. The zonation pattern of nickel conforms to the faceted stone's shape.

UV-Vis-NIR Spectroscopy. UV-Vis-NIR spectra recorded from the rims of double-polished wafers recovered from as-received stones show main peaks at 369, 381, 475, 597, and 639 nm (figure 9). These positions are consistent with those present in spectra recorded from nickel aluminate powders synthesized for use as cyan dyes (Serment et al., 2020), nickel-doped single-crystal spinel (Jouini et al., 2007), and nickel-doped gahnite ($ZnAl_2O_4$; Lorenzi et al., 2006). Figure 9 also shows a spectrum recorded from a cobalt-diffused spinel, obtained in the same parcel as these nickel-diffused crystals, showing clearly different absorption band positions.

Following the experimental anneal at 1100°C in pure O_2 (10 hours), the 475 nm band increased in intensity relative to the as-received stone (figure 10). There was no clear change in the intensity of the 369, 381, 597, and 639 nm bands. There was no apparent change in the spectra following a subsequent higher-temperature anneal in pure O_2 at 1700°C (18 hours). Following the 1750°C anneal in a low-pO_2 2:1 CO_2-H_2 mix (40 hours), however, the 475 nm band was completely eliminated and the intensity of the 369, 381, 597, and 639 nm bands decreased considerably, as did the overall absorbance. This is consistent with the final color, which was a much lighter blue than the original stone.

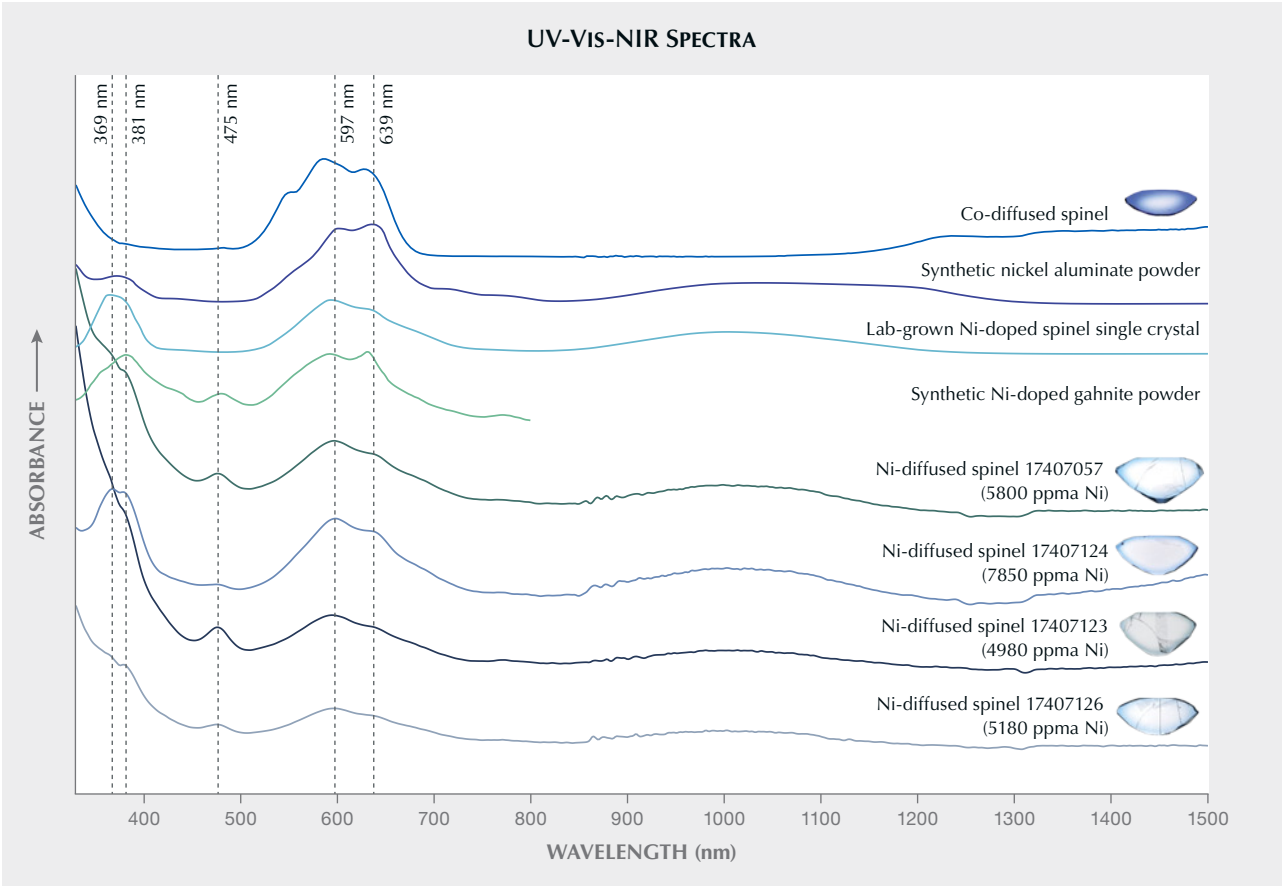

Figure 9. UV-Vis-NIR spectra recorded from the near-rim regions of doubly polished wafers fabricated from nickel-diffused spinel (bottom four curves). These were recorded by placing the stone over a 0.5 mm circular aperture, located as close as possible to the stone's edge at the table. Images of the stones are shown. Also presented are concentrations of nickel recorded using a 50 µm LA-ICP-MS spot, centered at 50 µm from the stone's edge at the table. This gives an approximation of the relative nickel concentration between stones, but is likely an overestimation of the mean nickel concentration in the area from which the UV-Vis-NIR spectrum was recorded given the nature of the nickel concentration gradients. Also shown are spectra recorded from a synthetic nickel aluminate ($NiAl_2O_4$; Serment et al., 2020), a single crystal of nickel-doped spinel (Jouini et al., 2007), a synthetic nickel-doped gahnite ($ZnAl_2O_4$) powder (Lorenzi et al., 2006), and a cobalt-diffused spinel. The positions of the main bands in the nickel-diffused material are denoted by dashed lines. Spectra are offset for clarity.

PL Spectroscopy. PL spectra recorded with 514 nm excitation are shown in figure 11. Spectra of the nickel-diffused stones are similar to those of heat-treated natural spinel (Widmer et al., 2015), which is in line with visual observations of inclusions and refractive indices. As with most natural spinel, the spectra are dominated by bands attributed to chromium. The spectra show broadening of the band(s) at around 686 nm.

PL spectra recorded near the spinel rims are different from those recorded in the cores, with the rim spectra showing a dominant band at 687.5 nm and core spectra showing a strong doublet with maxima at 685.6 and 687.3 nm. This difference in PL spectra may be associated with nickel, but it is notable that a spectrum recorded from a natural, unheated spinel with relatively high nickel (around 350 ppma) from GIA's production database did not clearly display this feature. Spectra recorded from faceted stones using nonconfocal PL spectroscopy will likely show some combination of these spectra.

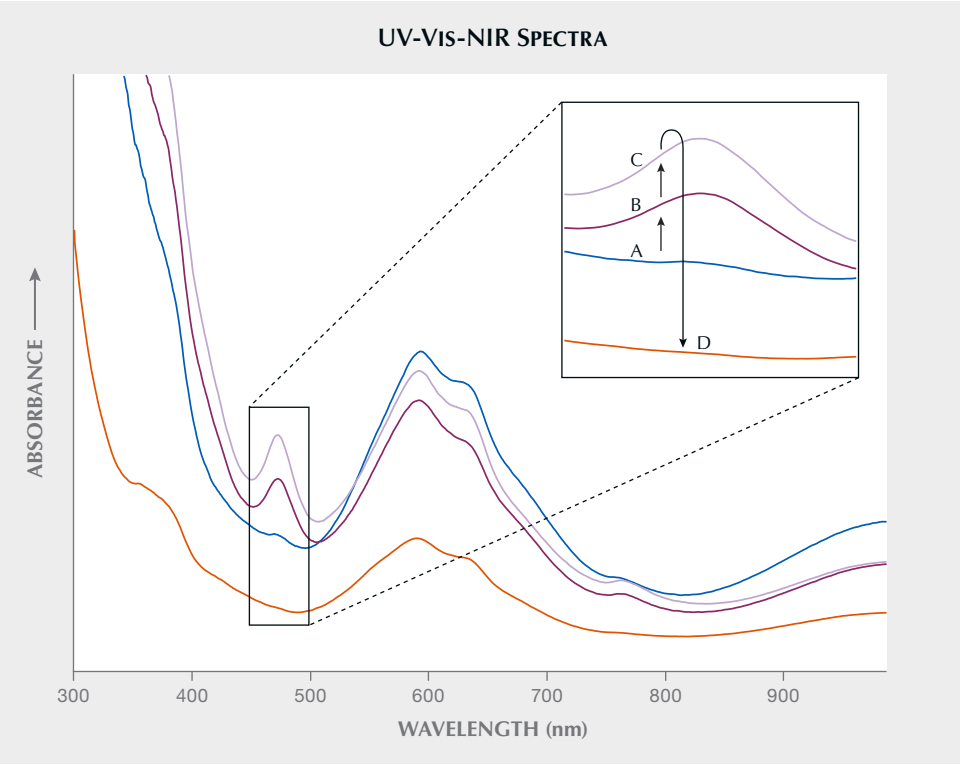

Figure 10. UV-Vis spectra of faceted sample 17407067 before and after heating experiments. The inset shows detail of the 475 nm band. The arrows in the inset show the order of experiments. Spectrum A was recorded from the as-received, nickel-diffused stone. Spectrum B was recorded after a 10-hour anneal at 1100°C in pure O_2. Spectrum C was recorded after an 18-hour anneal in pure O_2 at 1700°C. Spectrum D was recorded after a 40-hour anneal at 1750°C in a 2:1 H_2:CO_2 mix. Spectra were recorded in nearly the same position on the stone, so absorbance intensities are closely (but not exactly) comparable, as the stone's position was not perfectly reproduced in each case.

DISCUSSION

Nickel Incorporation Mechanism and Valence State. First, there are two likely valence states of nickel ions in spinel: Ni^{2+} and Ni^{3+}. The superscripts refer to the charges of the cation where Ni^{2+} has lost two electrons, and Ni^{3+} has lost three, relative to nickel in its

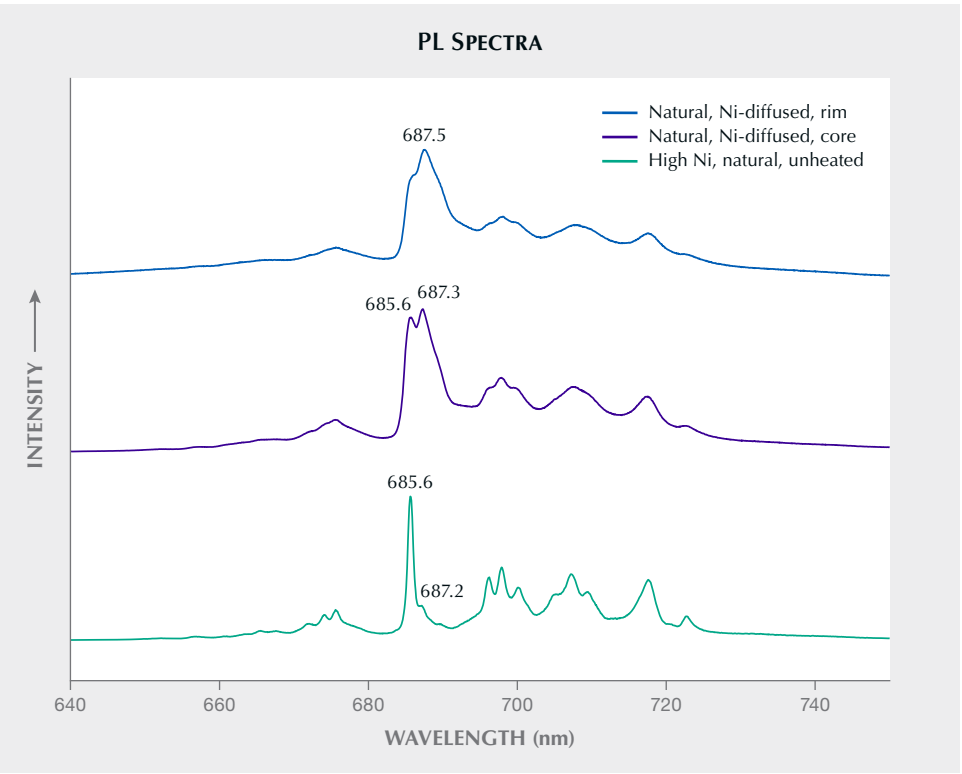

Figure 11. PL spectra recorded from the rim and core of a nickel-diffused natural spinel (sample 17407124), revealing features characteristic of heating. Also shown is a spectrum from a natural, unheated high-nickel spinel (>300 ppma nickel). Spectra are offset for clarity.

normal metallic state with zero charge. Because the loss of electrons is oxidation, the expected result is that, all other things being equal, a spinel treated with nickel in an oxidizing environment (generally an atmosphere having a high oxygen concentration, such as air), will have a relatively high ratio of Ni^{3+} to total nickel. Conversely, a spinel treated in a reducing (generally low-oxygen) atmosphere will have a relatively high ratio of Ni^{2+} to total nickel.

With two valence states, there are also two locations for nickel incorporation in spinel, either on the tetrahedral or octahedral site. The terms "tetrahedral" and "octahedral" refer to the location of these cations in the crystal structure with respect to the O^{2-} anions (ions with a negative charge). A cation in a tetrahedral site in spinel is bonded to four O^{2-} anions, forming the shape of a tetrahedron with the cation in the center. In octahedral coordination, the cation is bonded to six O^{2-} anions, which form an octahedron. These octahedra and tetrahedra stack together to form the atomic structure of spinel. Overall, then, there are four main possibilities for nickel incorporation, with two valence states (Ni^{2+} and Ni^{3+}) and two sites (octahedral and tetrahedral).

In natural spinel ($MgAl_2O_4$), which is likely to be the starting material for the diffusion treatment, Mg^{2+} mainly occupies the tetrahedral site, and Al^{3+} mostly occupies the octahedral site (O'Neill and Navrotsky, 1983; Widmer et al., 2015). This can be described as a low "degree of inversion." Chihmingite, $NiAl_2O_4$, is more complex because it tends toward an "inverse" spinel structure (having a high degree of inversion), meaning the octahedral sites are considerably occupied by Ni^{2+}, and Al^{3+} tends towards tetrahedral sites (Datta and Roy, 1967; Porta et al., 1974; O'Neill et al., 1991). This potentially means that a nickel-diffused spinel will show a degree of inversion that is intermediate between $MgAl_2O_4$ and $NiAl_2O_4$.

While we do not have sufficient information to fully assign valence states and sites to the nickel in these diffused spinel, we can make some speculations based on the data collected. First, from the LA-ICP-MS traverse and EDS maps, the decrease in nickel concentration from the rim to the core of the stones, coupled with magnesium showing the opposite trend, suggests nickel primarily replacing magnesium—i.e., Ni^{2+} and/or Ni^{3+} replacing Mg^{2+}.

Second, the main visible absorption bands in the spectra of the nickel-diffused spinel, at 597 and 639 nm, were assigned by, for example, Porta et al. (1974) and Serment et al. (2020), to nickel in tetrahedral coordination. The generally smaller bands at 369 and 381 nm were associated with nickel in octahedral coordination. The similarity between the absorption spectra of the nickel-diffused spinel and a spectrum of single-crystal nickel-doped spinel grown in a relatively low (but undefined) pO_2 argon atmosphere (figure 9; see also Jouini et al., 2007) suggests that the nickel is predominantly in its reduced form Ni^{2+}.

Third, the experimental results are useful for interpreting the 475 nm band, assigned by Sakurai et al. (1969) to nickel in tetrahedral coordination. This grew during a low-temperature (1100°C) anneal in pure O_2, suggesting that it relates to Ni^{3+}. During longer and higher-temperature anneals in pure O_2, the band did not increase further. When annealed at very low pO_2, the 475 nm band was completely eliminated, which would be consistent with Ni^{3+} being reduced to Ni^{2+}. Therefore, we can assign this band to Ni^{3+} with some confidence. As the 475 nm band absorbs in the visible range, this suggests that the color of a nickel-diffused spinel can be fine-tuned after treatment by a second oxidation or reduction treatment. Oxidation leads to more greenish hues, while reduction removes the green and shifts the color into a more exclusively blue hue.

Overall, the data suggest that the main nickel incorporation mechanism responsible for the spinel's color is Ni^{2+} replacing Mg^{2+} in tetrahedral coordination, shown by the 597 and 639 nm bands. The 475 nm band may be related to Ni^{3+} in tetrahedral coordination. However, this does not mean that all nickel is in tetrahedral coordination; in fact, it might only be a small fraction of the Ni^{2+} (e.g., Porta et al., 1974), although we cannot directly address this with our data.

This could explain the observation that nickel is apparently a weak chromophore in spinel. It is possible, however, that the main chromophore is Ni^{2+} in tetrahedral coordination, with a minor contribution of Ni^{3+}, but the majority of the nickel is Ni^{2+} in octahedral coordination.

Diffusivities. Fits of the compositional profiles for nickel, lithium, iron, zinc, vanadium, beryllium, cobalt, and magnesium to equation 1 (from the "Diffusion Modeling" section) are presented in figure 12, along with values of Dt (with units of m^2). These Dt values are also presented in figure 13. They increase in the following order: V<Ni<Mg<Fe≈Co<Zn≈Be<Li.

Because the durations (t) of the heat treatment of the stones studied are not known, it is not possible

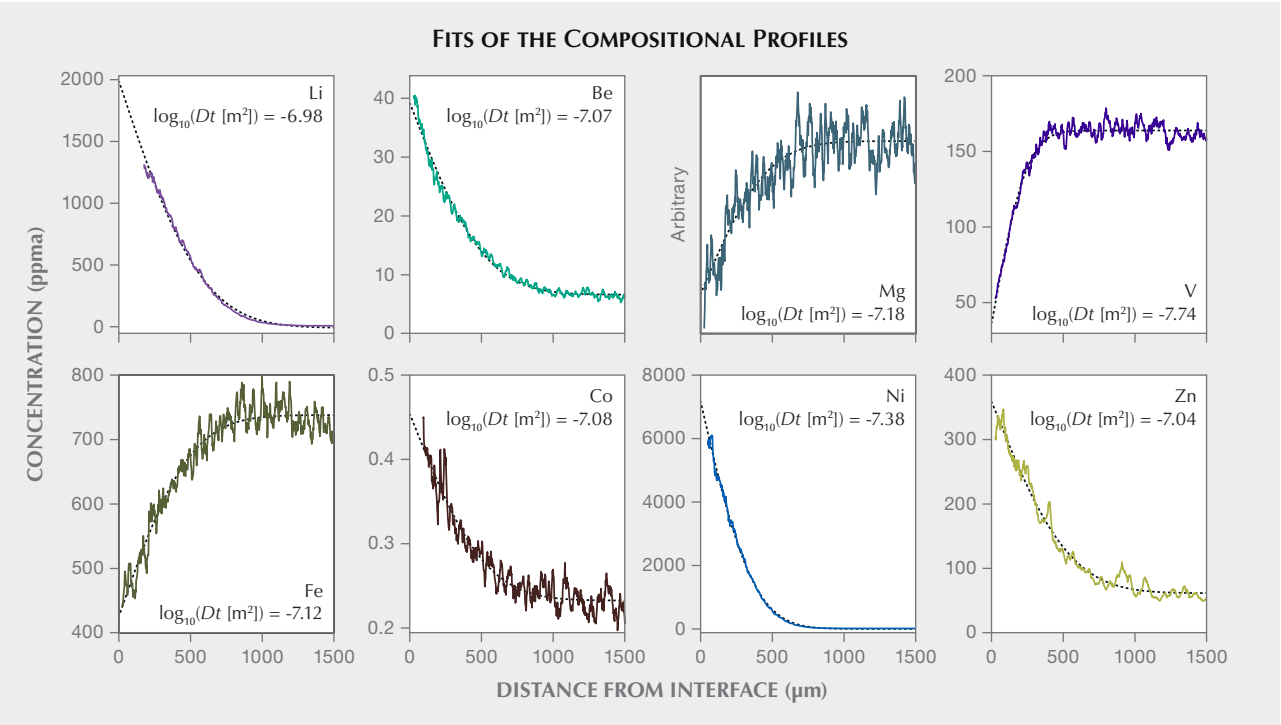

Figure 12. Profiles of lithium, beryllium, magnesium, vanadium, iron, cobalt, nickel, and zinc, as shown in figure 7, fitted to equation 1. Solid lines represent LA-ICP-MS data, while dashed lines represent the model fits. The "interface" is at the table of the stone. Also shown are the fitted values of Dt *(presented as their base-10 logarithm)—i.e., the diffusion coefficient multiplied by the time. Note that magnesium is not quantified, but this has no effect on the* Dt *value, which is independent of concentration according to equation 1.*

to precisely or accurately obtain D from Dt. Likewise, because the temperatures of the treatment are also not known to us, and because experimental datasets describing diffusion coefficients are extremely limited in any case, neither can t be determined using a known D. It is tempting to use the zonation in iron and magnesium to extract duration using iron and magnesium diffusion coefficients that have been determined experimentally (Sheng et al., 1992; Liermann and Ganguly, 2002), but the different measured D values for iron and magnesium lead to a 3–4 orders of magnitude discrepancy at temperatures over 1500°C, notwithstanding the usual potential inaccuracies associated with data extrapolation.

However, we can reasonably make two broad assumptions about the nature of the heat treatment. The first is that it is likely conducted at 1500–1700°C, the upper limit being both a safe temperature to avoid partial melting in a spinel with considerable concentrations of impurities (i.e., nickel) and the normal upper limit for continuous operation of standard high-temperature muffle furnaces with molybdenum disilicide elements. The lower limit is conservative—based on previously published data (e.g., Sheng et al., 1992), it is unlikely that diffusion can lead to hundreds of micrometers of diffusive penetration into the stone. Given the economics of treatment, we assume a short duration (again, extremely conservative) of one hour to one week.

With these very broad constraints, a range of D values for nickel can be estimated from Dt using t = 3600 s (1 hour) and 6×10^5 s (1 week). These can then be placed onto an Arrhenius diagram, which describes D (as its base-10 logarithm $\log_{10}$D, in m^2/s) as a function of temperature (as inverse temperature in Kelvins, $1/T$). This is shown in figure 13, along with some other experimentally determined diffusion coefficients for divalent cations in spinel as well as hydrogen for comparison. Also shown is the diffusion coefficient estimated for beryllium in corundum by

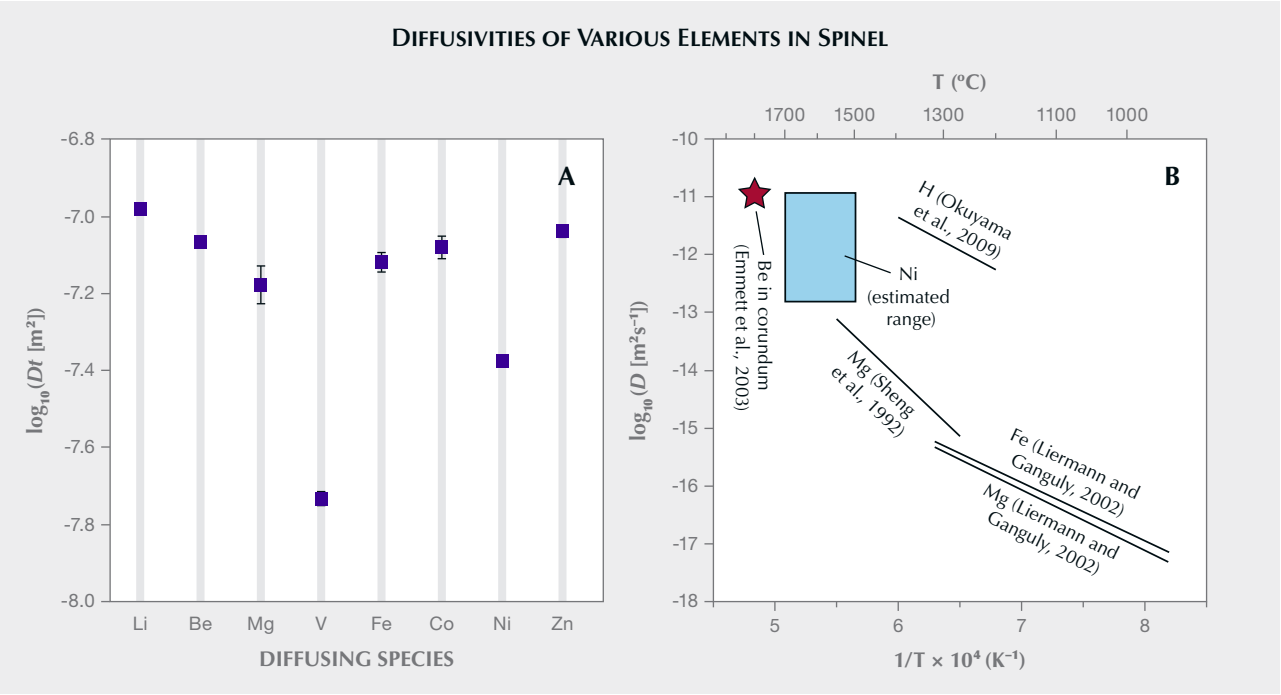

Figure 13. Results of fitting data to equation 1. Plot A shows the Dt *values from figure 12. Error bars represent 95% confidence intervals. Where not visible, the 95% confidence interval is smaller than the marker size. Vanadium has the lowest diffusivity and lithium the highest. Plot B shows some estimations of nickel diffusion coefficients extracted from the* Dt *values in plot A, making broad assumptions about treatment duration and temperature. These are presented on an Arrhenius diagram, with the base-10 logarithm of the diffusion coefficient plotted against the inverse temperature in K (temperatures in °C are presented at the top of the plot). Also shown are some experimentally determined diffusion coefficients for magnesium and iron (Sheng et al., 1992; Liermann and Ganguly, 2002), which can be expected to behave similarly to nickel in this system, and hydrogen (Okuyama et al., 2012), which is the fastest-diffusing element in many minerals. A diffusion coefficient of beryllium in corundum estimated by Emmett et al. (2003) is also included—this is important for a general understanding of diffusion treatment of gemstones.*

Emmett et al. (2003), which is pertinent for general considerations of heat treatment of gemstones. While these values are imprecise, they should provide a useful starting point for future experimental efforts.

The shapes of nickel diffusion profiles—i.e., the forms of concentration vs. distance data in figure 7—correspond almost perfectly to equation 1. This means that there is a smooth decrease in nickel concentration, and associated color, from the edge of a spinel to the core. This implies that diffusion in this system is relatively simple, with little or no trapping behavior—such non-simple behavior could be expressed as sharp color changes, as is often observed in titanium-diffused sapphires, for example. The likely diffusion mechanism would then involve a simple exchange of vacancies with Ni^{2+}, which has been proposed as one mechanism of Cr^{3+} diffusion in spinel (Posner et al., 2016).

Zonation Patterns. The zonation patterns extracted from the EDS map, shown in figure 8, can be used to provide some information regarding the heat treatment method. In the maps, we can see that the zonation patterns are broadly parallel to the edges of the stone, excluding the noise in the data. In other words, if contours were drawn defining regions of equal nickel concentration, they would generally have the same shape as the stone.

In a mineral with cubic symmetry (such as spinel), diffusion treatment will lead to concentration contours that are smooth but generally parallel to the edges of the stone, regardless of the stone's geometry. An example is shown in figure 14, where diffusion has been modeled in a simplified two-dimensional system for both a faceted shape and an example "rough" shape. If faceting is done before the diffusion treatment, then the contours of equal concentration will essentially match the shape of the faceted stone. This is what is

seen in the nickel-diffused spinel, as in figure 8. However, if the diffusion treatment is done on a rough stone that is subsequently faceted, the contours will likely be intersected by the newly cut surface. In the example in figure 14, this would lead to a patchy appearance, with the degree of patchiness dependent on the relative geometries of the rough and faceted stones.

What cannot be accurately determined using our data, though, is whether the faceting done before the diffusion treatment was complete or partial. The diffusion treatment could have been done on a partially faceted, unpolished stone, with final faceting and polishing after the treatment.

To demonstrate this process, two flame-fusion synthetic spinels were diffused with nickel at 1800°C in a furnace at GIA in Carlsbad, California. The two stones were completely colorless beforehand and facet patterns were roughly ground in. Diffusing these stones with nickel at 1800°C created a rich blue color as seen in the polished gems in figure 15.

It is also notable that local color concentrations were visible at facet junctions, which is consistent with diffusion treatment conducted after faceting.

Speculations Regarding the Heat Treatment Method. The most salient lines of evidence in determining the heat treatment method are:

- The presence of high nickel and lithium concentrations at the stone's edge.
- The lower trace and minor element contents in the core (e.g., beryllium and zinc), relative to the edge, measured using an LA-ICP-MS transect.
- The PL spectra, which are consistent with heated natural spinel.
- The presence of healed fractures.
- The presence of a band in the UV-Vis-NIR spectra of all measured stones at 475 nm, which can be removed by annealing at low pO_2.

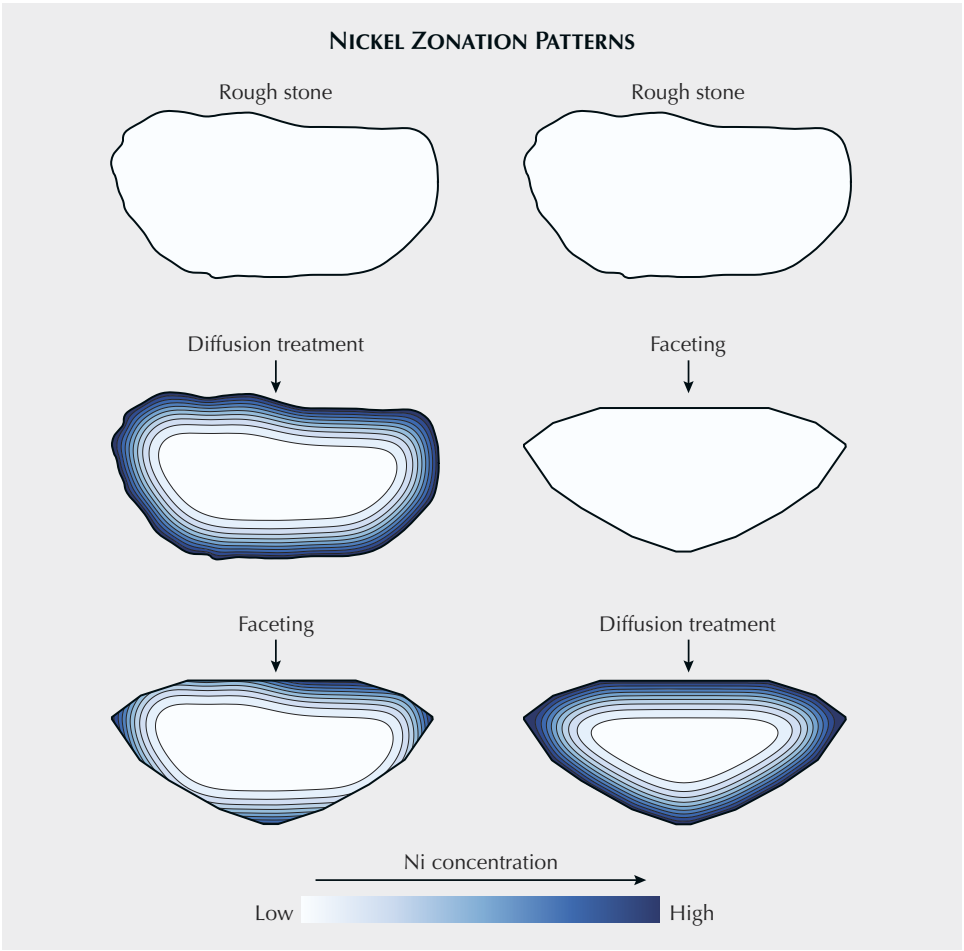

Figure 14. Models showing the nickel zonation patterns that would be observed with diffusion treatment done before (left column) or after (right column) faceting, using a generic "rough" shape. The zonation pattern broadly follows the shape of the stone, which would then be retained if the stone were faceted after diffusion treatment. These models were created using an explicit finite difference approximation of Fick's second law in two dimensions, using an arbitrary initial concentration of 0 and a constant boundary concentration of 1. Contours are at intervals of 0.1, from 0.0 to 1.0. The girdle-to-girdle length in the model is 4 mm, the grid spacing is 10 µm, the modeled D *is* 10^{-13} m^2/s*, and the total modeled time is* 2×10^6 *s.*

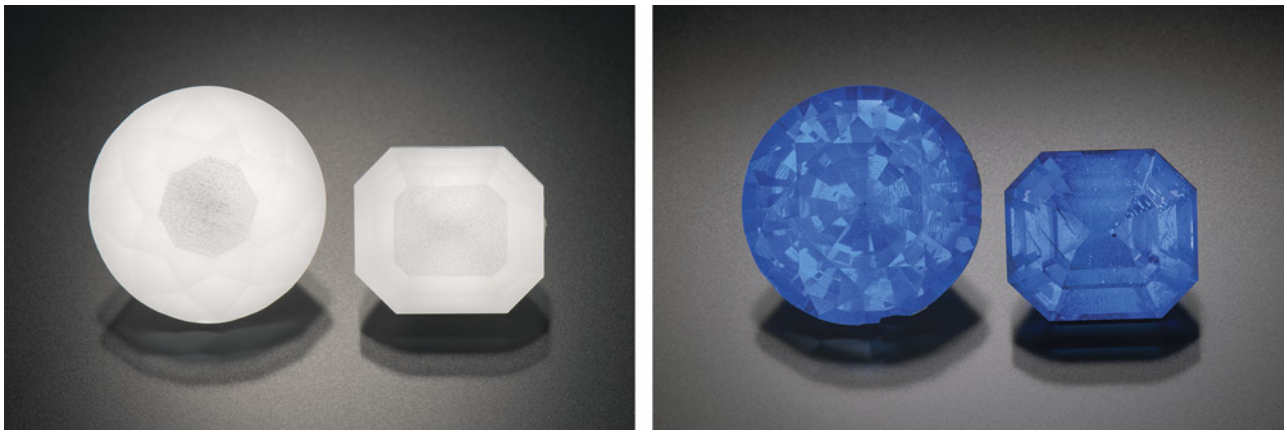

Figure 15. Two synthetic spinels before and after a diffusion experiment carried out at GIA in Carlsbad, California. The stones were faceted by Jessa Rizzo (GIA) and weigh 9.25 and 14.72 ct. Photos by Kevin Schumacher.

- The long diffusive penetration distances (over 1 mm).
- The nickel concentration variations in the EDS map, where zonation is approximately parallel to the edges of the stone.
- The fact that the stones were mixed into a parcel of cobalt-diffused spinel and sold as such.

Overall, the evidence suggests the treatment of natural faceted or partially faceted spinel in the presence of a high-nickel melt, where some lithium compound is used to enable flux melting. This is often advantageous because any adhered melt can be readily dissolved off the stone after treatment. As described above, the treatment is likely at high temperature (>1500°C), given the depth of the diffusion profiles as well as considerations of the economics of heat treatment. The presence of the 475 nm band suggests that the treatment was done in an oxidizing atmosphere, which could simply be air, because this band is eliminated if annealed in a reducing gas mix.

Finally, there is a possibility that the use of nickel rather than cobalt as a diffusant was accidental, or alternatively that the term "cobalt-diffused" is now used by some treaters as a generic term for diffusion treatment in spinel.

CONCLUSIONS

Blue or green hues can be added to spinel by nickel diffusion. Spinel modified using this treatment method now exists in the gem trade. The possibility for color modification by nickel diffusion should be considered for any spinel with such colors. The following criteria are proposed for identifying nickel diffusion treatment in spinel:

- High concentrations of nickel at the stone's surface, potentially thousands of atomic parts per million or more. This may be associated with high lithium concentrations.
- PL spectra characteristic of heated natural spinel, although we cannot rule out the possibility of treatment of lab-grown spinel.
- Characteristic UV-Vis absorption spectra, with bands at around 370, 470, and 600 nm.
- Subtle color concentrations at the facet junctions, although this may be limited if the stones are repolished after treatment.
- Textures associated with flux-assisted healing of fractures.

Overall, the treatment should be readily identifiable using standard gemological techniques and equipment.

ABOUT THE AUTHORS

Dr. Michael Jollands, Abadie Ludlam, Pamela Cevallos, Sarah Arden, Elina Myagkaya, and Dr. Ulrika D'Haenens-Johannson are researchers with GIA in New York. Dr. Aaron Palke, Dr. Shiyun Jin, and Ziyin Sun are with GIA in Carlsbad. Wim Vertriest and Vararut Weeramongkhonlert are with GIA in Bangkok.

REFERENCES

Crank J. (1975) *The Mathematics of Diffusion*. Oxford University Press, Oxford, UK.

Datta R.K., Roy R. (1967) Equilibrium order-disorder in spinels. *Journal of the American Ceramic Society*, Vol. 50, No. 11, pp. 578–583, http://dx.doi.org/10.1111/j.1151-2916.1967.tb15002.x

Emmett J.L., Scarratt K., McClure S.F., Moses T., Douthit T.R., Hughes R., Novak S., Shigley J.E., Wang W., Bordelon O., Kane R.E. (2003) Beryllium diffusion of ruby and sapphire. *G&G*, Vol. 39, No. 2, pp. 84–135, http://dx.doi.org/10.5741/GEMS.39.2.84

Jochum K.P., Weis U., Stoll B., Kuzmin D., Yang Q., Raczek I., Jacob D.E., Stracke A., Birbaum K., Frick D.A., Günther D., Enzweiler J. (2011) Determination of reference values for NIST SRM 610–617 glasses following ISO guidelines. *Geostandards and Geoanalytical Research*, Vol. 35, No. 4, pp. 397–429, http://dx.doi.org/10.1111/j.1751-908X.2011.00120.x

Jouini A., Yoshikawa A., Guyot Y., Brenier A., Fukuda T., Boulon G. (2007) Potential candidate for new tunable solid-state laser between 1 and 2µm: Ni^{2+}-doped $MgAl_2O_4$ spinel grown by the micro-pulling-down method. *Optical Materials*, Vol. 30, No. 1, pp. 47–49, http://dx.doi.org/10.1016/j.optmat.2006.11.027

Krzemnicki M., Wang H., Stephan T., Henn U. (2017) Cobalt diffusion treated spinel. *Proceedings of the 35th International Gemmological Conference*, Windhoek, Namibia.

Liermann H.-P., Ganguly J. (2002) Diffusion kinetics of Fe^{2+} and Mg in aluminous spinel: Experimental determination and applications. *Geochimica et Cosmochimica Acta*, Vol. 66, No. 16, pp. 2903–2913, http://dx.doi.org/10.1016/S0016-7037(02)00875-X

Longerich H., Jackson S., Gunther D. (1996) Inter-laboratory note: Laser ablation inductively coupled plasma mass spectrometric transient signal data acquisition and analyte concentration calculation. *Journal of Analytical Atomic Spectrometry*, Vol. 11, No. 9, pp. 899–904, http://dx.doi.org/10.1039/JA9961100899

Lorenzi G., Baldi G., Di Benedetto F., Faso V., Lattanzi P., Romanelli M. (2006) Spectroscopic study of a Ni-bearing gahnite pigment. *Journal of the European Ceramic Society*, Vol. 26, No. 3, pp. 317–321, http://dx.doi.org/10.1016/j.jeurceramsoc.2004.10.027

Miyawaki R., Hatert F., Pasero M., Mills S.J. (2022) IMA Commission on New Minerals, Nomenclature and Classification (CNMNC) – Newsletter 69. *European Journal of Mineralogy*, Vol. 34, No. 5, pp. 463–468, http://dx.doi.org/10.5194/ejm-34-463-2022

O'Neill H.S.C., Dollase W.A., Ross C.R. (1991) Temperature dependence of the cation distribution in nickel aluminate ($NiAl_2O_4$) spinel: A powder XRD study. *Physics and Chemistry of Minerals*, Vol. 18, No. 5, pp. 302–319, http://dx.doi.org/10.1007/BF00200188

O'Neill H.S.C., Navrotsky A. (1983) Simple spinels: crystallographic parameters, cation radii, lattice energies, and cation distribution. *American Mineralogist*, Vol. 68, No. 1-2, pp. 181–194.

Okuyama Y., Kurita N., Sato D., Douhara H., Fukatsu N. (2012) Determination of the maximum solubility of hydrogen in α-alumina by DC polarization method. *Solid State Ionics*, Vol. 213, pp. 92–97, http://dx.doi.org/10.1016/j.ssi.2011.05.023

Paton C., Hellstrom J., Paul B., Woodhead J., Hergt J. (2011) Iolite: Freeware for the visualisation and processing of mass spectrometric data. *Journal of Analytical Atomic Spectrometry*, Vol. 26, No. 12, pp. 2508–2518, http://dx.doi.org/10.1039/c1ja10172b

Peretti A., Kanpraphai-Peretti A., Günther D. (2015) New type of treatment of spinel involving heat-treatment and cobalt diffusion. In World of Magnificent Spinels: Provenance and Identification. *Contributions to Gemology*, No. 11, pp. 279–282.

Porta P., Stone F.S., Turner R.G. (1974) The distribution of nickel ions among octahedral and tetrahedral sites in $NiAl_2O_4$-$MgAl_2O_4$ solid solutions. *Journal of Solid State Chemistry*, Vol. 11, No. 2, pp. 135–147, http://dx.doi.org/10.1016/0022-4596(74)90108-X

Posner E.S., Ganguly J., Hervig R. (2016) Diffusion kinetics of Cr in spinel: Experimental studies and implications for ^{53}Mn–^{53}Cr cosmochronology. *Geochimica et Cosmochimica Acta*, Vol. 175, pp. 20–35, http://dx.doi.org/10.1016/j.gca.2015.11.018

Prunier A.R., Hewitt D.A. (1981) Calculation of temperature-oxygen fugacity tables for H_2-CO_2 gas mixtures at one atmosphere total pressure. *Geological Society of America Bulletin*, Vol. 92, No. 7 Part II, pp. 1039–1068, http://dx.doi.org/10.1130/GSAB-P2-92-1039

Saeseaw S., Weeramonkhonlert V., Khowpong C., Ng-Pooresatien N., Sangsawong S., Raynaud V., Ito C. (2015) Cobalt diffusion of natural spinel: A report describing a new treatment on the gem market. *GIA News from Research*, June 3, https://www.gia.edu/doc/Cobalt-Diffusion-in-Spinel-v2.pdf

Sakurai T., Ishigame M., Arashi H. (1969) Absorption spectrum of Ni^{2+} ions in spinel. *Journal of Chemical Physics*, Vol. 50, No. 8, pp. 3241–3245, http://dx.doi.org/10.1063/1.1671546.

Serment B., Gaudon M., Demourgues A., Noël A., Fleury G., Cloutet E., Hadziioannou G., Brochon C. (2020) Cyan $Ni_{1-x}Al_{2+2x/3}\square_{x/3}O_4$ single-phase pigment synthesis and modification for electrophoretic ink formulation. *ACS Omega*, Vol. 5, No. 30, pp. 18651–18661, http://dx.doi.org/10.1021/acsomega.0c01289

Shannon R. (1976) Revised effective ionic radii and systematic studies of interatomic distances in halides and chalcogenides. *Acta Crystallographica Section A: Crystal Physics, Diffraction, Theoretical and General Crystallography*, Vol. 32, No. 5, pp. 751–767, http://dx.doi.org/10.1107/S0567739476001551

Sheng Y.J., Wasserburg G.J., Hutcheon I.D. (1992) Self-diffusion of magnesium in spinel and in equilibrium melts: Constraints on flash heating of silicates. *Geochimica et Cosmochimica Acta*, Vol. 56, No. 6, pp. 2535–2546, http://dx.doi.org/10.1016/0016-7037(92)90207-Y

Widmer R., Malsy A.-K., Armbruster T. (2015) Effects of heat treatment on red gemstone spinel: single-crystal X-ray, Raman, and photoluminescence study. *Physics and Chemistry of Minerals*, Vol. 42, No. 4, pp. 251–260, http://dx.doi.org/10.1007/s00269-014-0716-7

GEM-QUALITY AUGITE FROM DONG NAI, VIETNAM

Le Ngoc Nang, Lam Vinh Phat, Pham Minh Tien, Pham Trung Hieu, Kenta Kawaguchi, and Pham Minh

Augite from Dong Nai Province in Vietnam occurs as xenocrysts hosted by Cenozoic basalt and its regolith. Found as irregularly shaped crystals a few millimeters to centimeters in size, these augites exhibit two dominant colors: brown and green. They are very dark in tone, making them appear almost black in reflected light and are translucent to transparent, with vitreous luster. Most of the samples' gemological properties are similar except for refractive index and birefringence values, which are both higher in green augite. The brown and green augite samples show differences in Raman peak positions. The chemical composition as determined by electron probe microanalysis suggests that Dong Nai augite should be classified as magnesium-rich augite. This material is promising for jewelry use, as gem-quality material is readily found over a large area.

Augite is a monoclinic member of the pyroxene group [(M2)(M1)$(T)_2O_6$] with the general formula $(Ca,Na)(Mg,Fe,Al,Ti)(Si,Al)_2O_6$ (Morimoto, 1989), where M1 and M2 are octahedrally coordinated cation sites and T is a tetrahedrally coordinated cation site. Augite is most commonly found in mafic igneous rocks such as basalts and gabbros, as well as in ultramafic rocks (Anthony et al., 2001). The pyroxene group includes a wide range of well-known and highly valuable gem varieties used in jewelry, including jadeite ($NaAlSi_2O_6$), spodumene ($LiAlSi_2O_6$), diopside ($CaMgSi_2O_6$), and omphacite ($(Ca,Na)(Mg, Fe^{2+},Al)Si_2O_6$) (Mei et al., 2003; O'Donoghue et al., 2006). However, augite is generally not considered a gem material because most examples are opaque, with unattractive colors (Hurwit, 1988; Johnson et al., 1996).

In 2018, two types of gem-quality augite appeared in the Ho Chi Minh City marketplace: dark green and dark orangy brown (figure 1). All of these were loose stones (faceted, cabochon cut, or carved). The gems appeared black in reflected light, but color could be seen in transmitted light. One dealer noted that they were mined in Dong Nai Province and initially mistaken for diopside and tourmaline. The samples were later submitted to Liu Gemological Research and Application Center (LIULAB) and identified as augite.

After learning of this potential source of gem-quality augite, the authors decided to visit the deposit. We began our study in the center of Dong Nai Province (figure 2), where we collected a large quantity of gem-quality samples during two field trips in May 2020 and October 2021. The augite occurred as xenocrysts hosted by basalt bedrock, which was covered by a regolith layer of basaltic laterite. This paper aims to identify the variety of augite from Dong Nai and describe its formation and gemological characteristics.

In Brief

- An abundant source of xenocrystic gem-quality augite was discovered in an alkali basalt formation in Dong Nai, Vietnam.
- Dark green and dark brown are the two color varieties of this augite; except for RI, their gemological properties are similar.
- Raman spectroscopy helps differentiate the two varieties of augite and distinguish between green augite and diopside.
- Augite from Dong Nai is suitable for fashioning in faceted, cabochon, and especially carved form.

GEOLOGICAL SETTING

The augite deposit is located in the center of Gia Kiem commune in the Thong Nhat district of Dong Nai Province (figure 3) in the southeast region of

See end of article for About the Authors and Acknowledgments.
GEMS & GEMOLOGY, Vol. 59, No. 2, pp. 182–194,
http://dx.doi.org/10.5741/GEMS.59.2.182

Figure 1. The deep colors of green and brown augite from Dong Nai, observed in transmitted light. Top: The 9.78 g rough on the left yielded a 24.20 ct carving (24.99 cm in height). Bottom: The 11.22 g rough on the left yielded a 56.10 ct carving (36.50 cm in height). Photos by Le Ngoc Nang.

Vietnam, about 90 km north of Ho Chi Minh City. In May 2020 and October 2021, we conducted field trips to this area to collect samples and investigate the site. The sampling site is in the midland, a tran-

Figure 2. View of a valley in Dong Nai, Vietnam, where vegetation grows on the topsoil of the augite-bearing basaltic regolith. Photo by Lam Vinh Phat.

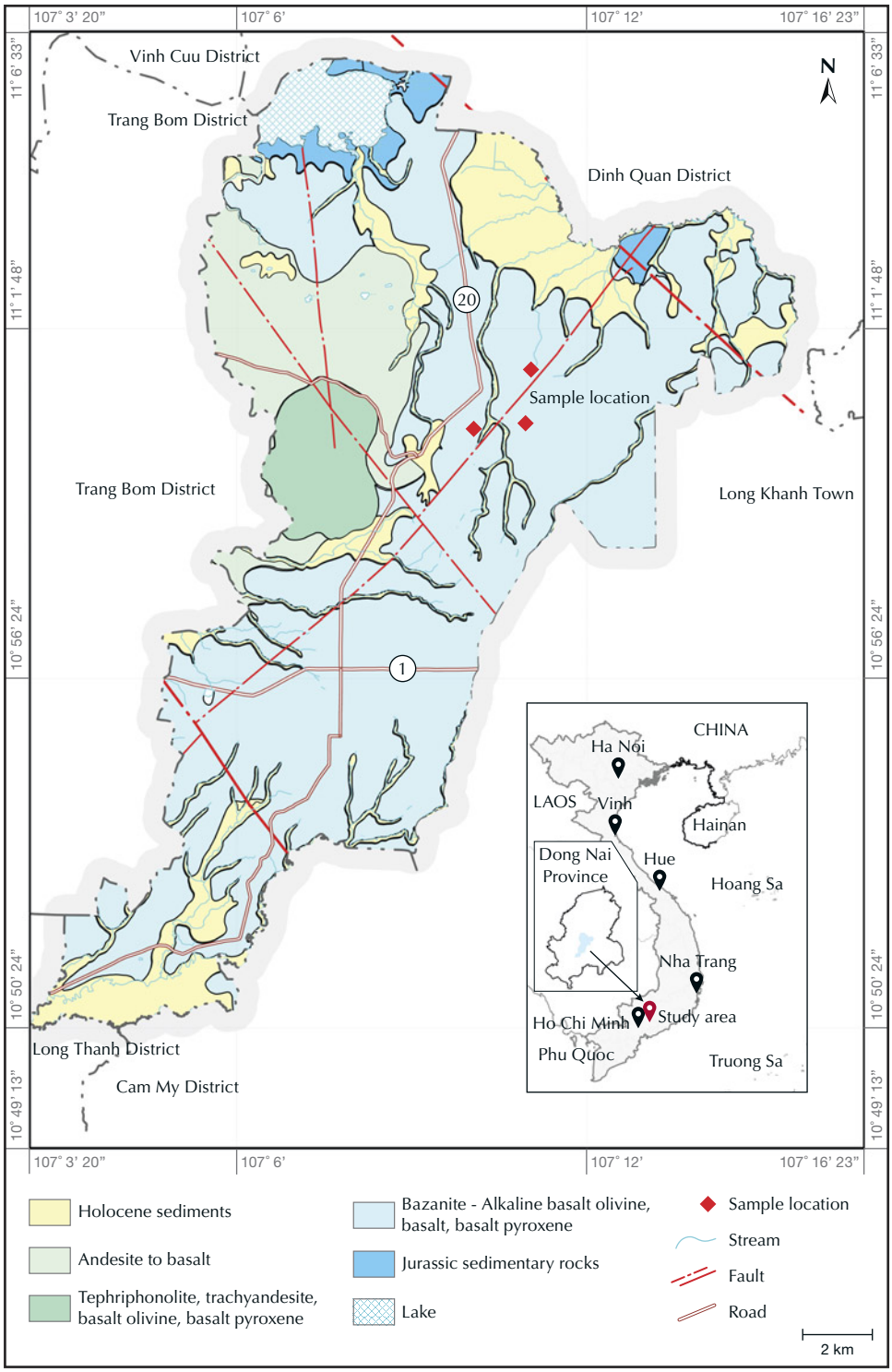

Figure 3. The augite occurrence is hosted by a Cenozoic basaltic formation and Quaternary sediments along the stream in the valley. Modified from Son et al. (2005).

sition zone between the plains and the highlands. From the north, the terrain descends gradually toward the south, and temporary streams and springs carve through rolling hills. The average elevation is about 139 m above mean sea level, with the slope steepness varying from 30° to 80°. Landforms include a plain of denudation and cinder cones (Son et al., 2005; Bac and Bao, 2020). The plain of denudation occurs on Jurassic sedimentary rock, with the erosion surface dating to the Late Pliocene to Early Pleistocene, before the eruption of the basaltic lava that covers almost the entire erosion surface (Bac and Bao,

Figure 4. Augite is abundant in Dong Nai Province and easy to collect. A: Augite hosted by basalt. B: Augite buried in laterite soil. C: Samples obtained during the field trips, which appear black under reflected light before revealing an orangy brown or a green color when observed in transmitted light. Photos by Lam Vinh Phat.

2020). The study location in Dong Nai is centered on a dormant volcano zone that was active during the period from the Neogene to the Quaternary (Bac and Bao, 2020) (again, see figure 3). The regolith is quite thick, containing mostly red and gray soils and sometimes basaltic boulders. Due to the area's tropical climate, mechanical weathering also causes exfoliation on most of the bedrock.

Dong Nai augite xenocrysts are found in basalt and its laterite (figure 4). In the mid-Pleistocene, the xenocryst-bearing basalt formed by volcanic eruption, resulting in a 70–200 m high terrain covering a large area. The augite-bearing basalt is dark bluish gray and light to dark gray and consists mainly of alkaline olivine (Co and Hai, 1994; Son et al., 2005; Bac and Bao, 2020). The xenocryst-bearing basalt is of vesicular structure with a void ratio varying from 3% to 15% with round, oval, and sometimes irregular shapes. The average void size ranges from 0.5 × 1.0 mm to 4.0 × 8.0 mm. In addition to pyroxene, other rock-forming minerals such as feldspar and clusters of olivine are contained sparsely in the basalt, with xenocrysts ranging in size from 0.5 to 10.0 cm and clusters of olivine from 2 to 15 cm (1–2 mm per crystal) (Son et al., 2005; Bac and Bao, 2020).

At a height of approximately 120 m above mean sea level, the augite-bearing basalt is weathered to varying degrees into brown to yellowish brown regolith. The regolith is moderately thick, about 2–3 m. The weathering profile contains the saprolite and the saprock of weathered basalt overlain by topsoil (Son et al., 2005).

During land reclamation since 2019, farmers in Dong Nai have been collecting the augite by hand and shovel. No mining activity takes place in this area. The authors connected with three merchants who gather and cut these augites for sale as tourmaline or diopside. These merchants gather 120 kg of gem-quality augite annually from the farmers and own 20,000 carats of faceted material, none of which is exported. Their current consumer market is limited to Ho Chi Minh City and some Vietnamese provinces.

Figure 5. Augite samples from this study were fashioned as faceted gems, cabochons, and carvings. These are shown in reflected light (first and third rows) and transmitted light (second and fourth rows). Photos by Le Ngoc Nang.

MATERIALS AND METHODS

Samples. During the two field trips, we collected more than 100 samples ranging from 2.4 to 100 g (figure 4C). We selected a total of 16 clear transparent to translucent samples (eight green and eight brown) for standard gemological testing as well as powder X-ray diffraction (XRD) and electron probe microanalysis (EPMA). We had 12 samples cut from the rough (figure 5). These samples included six faceted pieces (brown samples A1, A2, and A3; green samples A7, A8, and A9); four flat-bottom cabochons (brown samples A4 and A5; green samples A10 and A11); and two carved pieces (brown sample A6; green sample A12). All the faceted and cabochon samples were cut at a lapidary facility in Ho Chi Minh City, and the rest were carved by a freelance gem cutter in Ho Chi Minh City. We used the six faceted gems to analyze the Raman and Fourier-transform infrared spectra. Two other samples, a 15.56 ct transparent brown sample (A13) and a 12.08 ct transparent green sample (A14), had their surface impurities removed by a lapidary machine before being ground for powder XRD analysis (figure 6). Lastly, a 34.36 ct brown sample (A15) and a 41.20 ct green sample (A16) were ground into thin sections for EPMA measurement (figure 6).

Standard Gemological Methods. Standard gemological testing was performed on the fashioned augite samples (A1–A12) at LIULAB to determine their refractive index (RI), hydrostatic specific gravity (SG), and fluorescence reaction to long-wave (365 nm) and short-wave (254 nm) UV light. Optical properties and pleochroism were observed with a polariscope and dichroscope, respectively. The physical appearance was documented using fiber-optic lighting, both ambient and transmitted using a 60W GLS LED daylight bulb with a temperature of approximately 5000–6000K. For ambient lighting the settings were 8 volts and 10 watts, and for transmitted lighting the settings were 8 volts and 20 watts. Microscopic features were viewed using a Carton 7×–50× gemological microscope.

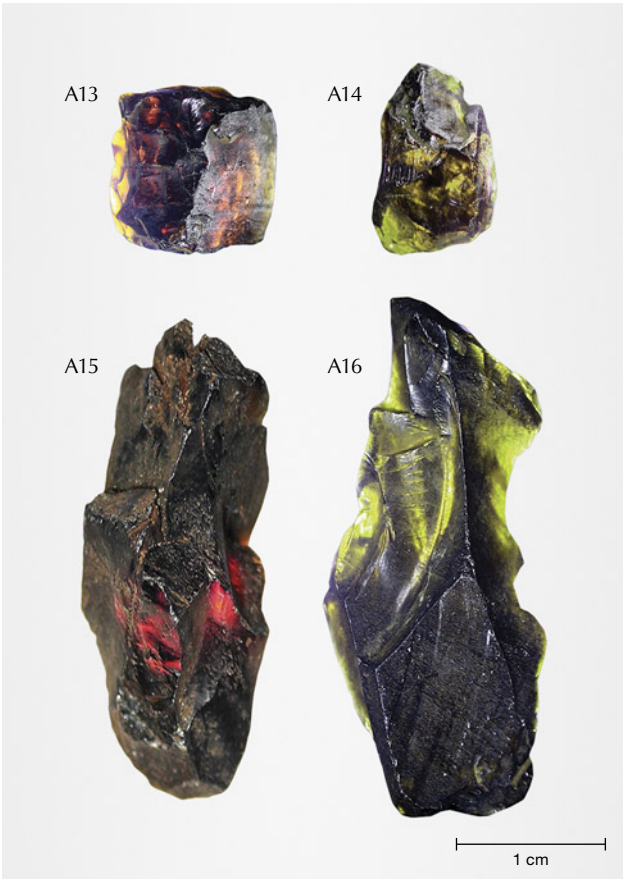

Figure 6. Rough augite samples before grinding and polishing for XRD (A13 and A14) and EPMA (A15 and A16), shown in transmitted light. Photos by Pham Minh Tien.

Analytical Methods. EPMA was performed on samples A15 (brown) and A16 (green) using a JEOL JXA-8200 instrument. Analyses were obtained with an electron probe diameter of 3 µm, an accelerating voltage of 15 kV, and a beam current of 20 nA, following the methods of Kawaguchi et al. (2022). Measurements of the oxides SiO_2, TiO_2, Al_2O_3, FeO, Cr_2O_3, MnO, CaO, Na_2O, K_2O, MgO, and P_2O_5 were obtained to determine the variety of pyroxene (Lindsley, 1983; Morimoto, 1989). The calibration standards included quartz for silicon, corundum for aluminum, manganosite for manganese, periclase for magnesium, nickel oxide for nickel, fayalite for iron, wollastonite for calcium, jadeite for sodium, and potassium titanium phosphate for potassium.

XRD is a common technique used to identify a mineral based on the scattering of X-rays by the atoms in a crystal structure. The diffraction patterns were collected by a Bruker D2 Phaser powder XRD, using CuKα (1.5406 Å) radiation in the range of 5–75° 2θ with a scan speed of 0.02°/s, at 40 kV and 30 mA. Brown sample A13 and green sample A14 were ground to a particle size of 5 µm. We used X'Pert HighScore software to analyze the results and compare them to the standard data in the Inorganic Crystal Structure Database (ICSD).

Raman spectroscopy was performed using a Horiba Xplora One Raman confocal microscope in the range of 0 to 3750 cm^{-1} with three brown samples (A1, A2, and A3) and three green samples (A7, A8, and A9). Measurements were performed at a laser excitation wavelength of 532 nm, laser mode power at 50%, and a 900 lines/mm diffraction grating, with a spectral resolution of 5 cm^{-1}. The objective selected was of 50× magnification. Raman spectra were collected over 15 s with two signal accumulations.

X-ray diffraction and Raman spectroscopy were conducted at the Institute of Chemical Technology, Vietnam Academy of Science and Technology. EPMA was performed at Hiroshima University in Japan.

RESULTS AND DISCUSSION

Appearance. The fabricated augite samples from Dong Nai were transparent to translucent, with vitreous luster. All of them appeared black under daylight-equivalent lighting. When observed in transmitted light, they displayed one of two colors: dark green or dark orangy brown.

Augite generally receives little attention in the jewelry industry because of its very dark appearance (see video at https://www.gia.edu/gems-gemology/summer-2023-augite-from-vietnam). Dong Nai augite appears homogenously black and opaque in reflected light but transparent and dark green, or orangy brown, when viewed in transmitted light. Moreover, a low degree of fracturing with massive form allows Dong Nai augite to be well polished and fashioned, particularly as carvings and cabochons (figures 1 and 5). After evaluating these features on the specimens processed from our samples, we concluded that augite from Dong Nai has potential application in the jewelry industry.

Gemological Properties and Identification. The gemological properties of the Dong Nai augite samples are described and summarized in table 1. Specific gravity values ranged from 3.36 to 3.38. The RI values measured for the five brown samples were n_p 1.674–1.676 and n_g 1.685–1.686, for a birefringence Δn of 0.009–0.012. RI values for the five green specimens were n_p 1.683–1.688 and n_g 1.703–1.706, for a

TABLE 1. Gemological properties of 16 augite samples from Dong Nai, Vietnam.

Sample no.	Weight (ct)	Color[a]	Form	SG	RI		Birefringence	Pleochroism
					n_p	n_g		
A1	4.60	Dark orangy brown	Faceted square	3.36	1.674	1.686	0.012	Brown to black
A2	4.97	Dark orangy brown	Faceted oval	3.34	1.672	1.682	0.010	Brown to black
A3	10.08	Dark orangy brown	Faceted oval	3.37	1.675	1.685	0.010	Greenish brown to black
A4	12.70	Dark orangy brown	Oval cabochon	3.34	1.673	1.685	0.012	Brown to black
A5	8.51	Dark orangy brown	Oval cabochon	3.36	1.672	1.682	0.010	Brown to black
A6	31.55	Dark orangy brown	Carving	3.35	1.67[b]		na[c]	Deep green to black
A7	12.65	Dark green	Faceted oval	3.37	1.685	1.705	0.020	Deep green to black
A8	7.28	Dark green	Faceted round	3.37	1.686	1.702	0.016	Deep green to black
A9	3.89	Dark green	Faceted rectangle	3.35	1.685	1.702	0.017	Deep green to black
A10	12.53	Dark green	Oval cabochon	3.36	1.688	1.703	0.015	Deep green to black
A11	9.59	Dark green	Oval cabochon	3.34	1.688	1.705	0.017	Deep green to black
A12	14.18	Dark green	Carving	3.35	1.70[b]		na	Deep green to black
A13	15.56	Dark orangy brown	Rough	3.33	—	—	na	Brown to black
A14	12.08	Dark green	Rough	3.35	—	—	na	Deep green to black
A15	34.36	Dark orangy brown	Rough	3.35	—	—	na	Brown to black
A16	41.20	Dark green	Rough	3.36	—	—	na	Deep green to black

[a]*Observed in transmitted light*
[b]*Spot RI*
[c]*na = not analyzed*

birefringence of 0.016–0.020. The RI values measured by spot reading method of two carved samples (A6 and A12) were 1.67 and 1.70. All samples were biaxial when viewed with a polariscope. None of them reacted to either long-wave or short-wave UV light. When viewed with a dichroscope, the green samples showed strong pleochroism from deep green to black (table 1), while the brown stones showed brown to black. The Mohs hardness of the rough samples was about 5–6. All of these gemological properties were consistent with augite (Manutchehr-Danai, 2005).

The gemological properties of the green and brown gems were similar except for RI and birefringence, which were higher for the green group (table 1).

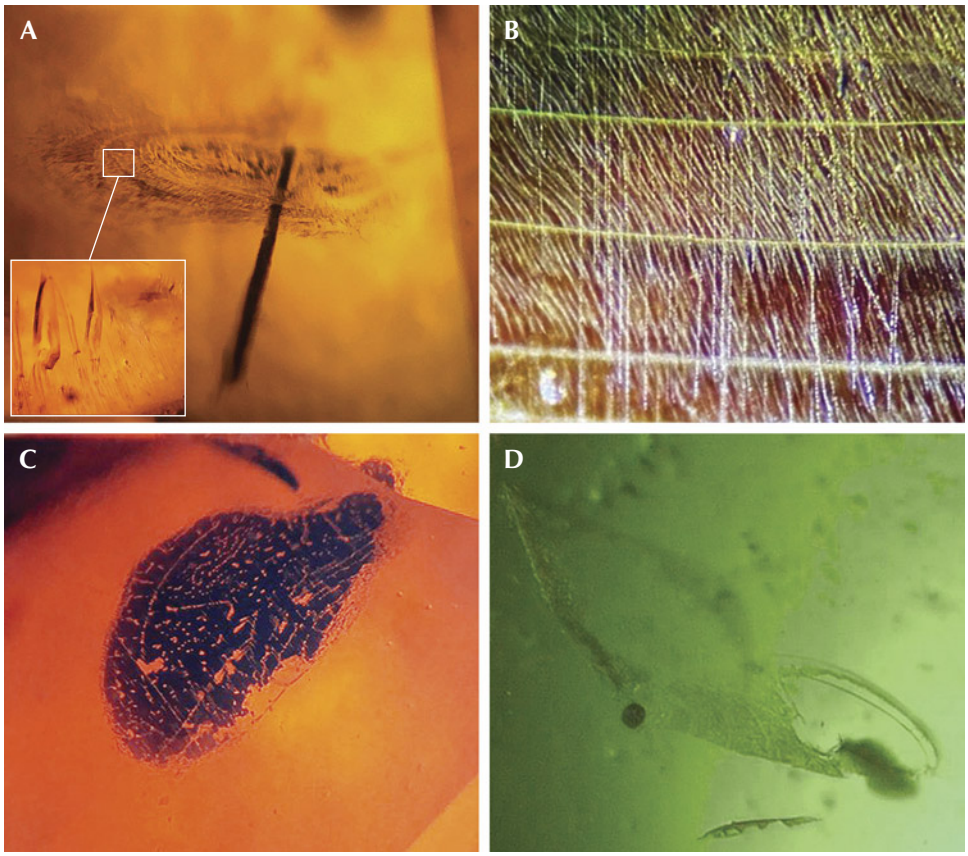

Figure 7. The internal microscopic features of Dong Nai augite. A: In sample A1, a long solid black amphibole inclusion pierces through the center of a fingerprint inclusion resembling a lily pad. B: Sample A4 shows white broken silk-like inclusions of magnetite that cross the twin planes. C and D: Thin films of fingerprint inclusions were commonly found in both green and brown augites (A2 and A11, respectively). Photomicrographs by Le Ngoc Nang; fields of view 4.5 mm (A, C, and D) and 5.5 mm (B).

The hardness of Dong Nai augite was lower than that of other pyroxene gem varieties such as jadeite (7.0–7.5), spodumene (6.5–7.0), and diopside (5.5–6.5). Yet the gemological properties of the green augite were nearly identical to those of chrome diopside, making it difficult to distinguish the two (Anthony et al., 2001).

Internal Features. When examined with a gemological microscope, the 12 cut samples (A1–A12) revealed three types of features: fingerprint inclusions, solid inclusions, and twin planes. The fingerprint inclusions were the most common features, observed as flat roundish or oval shapes and associated with elongate fluid inclusions with pointed tips (figure 7). In one instance, a long solid black acicular inclusion pierced through the center of a fingerprint inclusion resembling a lily pad (figure 7A). This black inclusion was identified as amphibole by Raman analysis. The solid inclusions in figure 7B were broken silk-like crystals that only appeared "white" in reflected light (Bown and Gay, 1959) and were observed only in the brown group. These crystals were aligned in parallel clusters. Raman spectroscopy identified these silk-like crystals as magnetite. Lastly, the twin planes intersected the magnetite crystals (figure 7B).

Chemical Composition and Species. EPMA was used to determine the chemical composition of two of the study samples (A15 and A16). Table 2 reveals some variability for all six oxides: SiO_2 50.64–51.05 wt.%, Al_2O_3 7.88–8.08 wt.%, FeO 5.97–6.33 wt.%, Cr_2O_3 0.010–0.014 wt.%, CaO 15.12–15.74 wt.%, and an unusually high MgO content from 16.69 to 17.22 wt.%. The total alkali ($Na_2O + K_2O$) fell between 1.25 and 1.39 wt.%. There was a much higher amount of sodium than potassium. These oxide concentrations were comparable to the compositions of augite from the state of Montana and Stoffel, Germany (Anthony et al., 2001). In addition, the TiO_2 content of augite from Dong Nai (0.25–0.95 wt.%) was much lower than that of augite from Stoffel (4.33 wt.%) and within range of material from Montana (0.49 wt.%), while the MnO content of Dong Nai augite (0.16–0.19 wt.%) was slightly lower than augite from these other two locations. We noted that the Al_2O_3, MgO, and Na_2O concentrations of Dong Nai augite were much higher than those of augite from Montana and Stoffel, while the opposite was true for CaO concentrations. Based on the measured data in table 2, the percentages of wollastonite (Wo = $Ca_2Si_2O_6$), enstatite (En = $Mg_2Si_2O_6$), and ferrosilite (Fs = $Fe_2Si_2O_6$) in the ternary

TABLE 2. Chemical composition (in wt.%) of six measured points from Dong Nai augite samples A15 and A16.

Chemical composition	A15			A16			Detection limit (wt.%)
	1	2	3	4	5	6	
SiO_2	50.90	50.64	50.95	51.05	50.75	50.87	0.016
TiO_2	0.56	0.59	0.54	0.55	0.52	0.55	0.021
Al_2O_3	8.08	7.88	8.08	7.92	7.92	8.02	0.012
FeO	6.24	5.97	6.16	6.23	6.24	6.33	0.019
MnO	0.10	0.14	0.12	0.16	0.13	0.14	0.017
MgO	16.92	17.2	16.86	17.17	16.69	17.22	0.011
Cr_2O_3	0.010	0.013	0.013	0.011	0.012	0.014	0.010
CaO	15.74	15.59	15.26	15.26	15.12	15.47	0.013
P_2O_5	bdl[a]	0.02	bdl	0.01	0.01	0.03	0.012
Na_2O	1.39	1.28	1.28	1.29	1.25	1.27	0.014
K_2O	bdl	0.01	bdl	bdl	bdl	0.02	0.009
Total	99.93	99.32	99.25	99.64	98.63	99.92	
Atoms per formula unit, 6 O (charge balance)							
Si	1.835	1.835	1.850	1.845	1.856	1.834	—
Ti	0.015	0.016	0.015	0.015	0.014	0.015	—
Al	0.343	0.336	0.346	0.337	0.341	0.341	—
Fe^{3+}	0.052	0.049	0.013	0.030	0.003	0.048	—
Fe^{2+}	0.136	0.132	0.174	0.158	0.187	0.142	—
Mn	0.003	0.004	0.004	0.005	0.004	0.004	—
Mg	0.910	0.929	0.912	0.925	0.910	0.925	—
Cr	0.002	0.003	0.003	0.003	0.003	0.003	—
Ca	0.608	0.605	0.594	0.591	0.592	0.597	—
Na	0.097	0.090	0.090	0.091	0.088	0.089	—
Ternary system (mol. %)							
Wollastonite ($Ca_2Si_2O_6$)	36.8	36.3	35.3	35.3	35.1	35.9	
Enstatite ($Mg_2Si_2O_6$)	55.0	55.8	54.3	55.3	53.9	55.6	
Ferrosilite ($Fe_2Si_2O_6$)	8.2	7.9	10.3	9.4	11.1	8.6	

[a]*bdl = below detection limit*

system were calculated to be 35.1–36.8%, 53.0–55.0%, and 7.9–11.1%, respectively.

Chemical Formula. The elemental concentration data in table 2 show that the cations in the Dong Nai augite can be partitioned among tetrahedral T and octahedral M1 and M2 sites. Morimoto (1989) provides a flow chart for these assignments. Using it, we derive a formula of $(Ca_{0.608}Na_{0.097}Fe^{2+}_{0.038}Mg_{0.254})(Mg_{0.656}Fe^{3+}_{0.053}Fe^{2+}_{0.098}Ti_{0.015}Al_{0.178})(Si_{1.835}Al_{0.165})O_6$ (sample A15, spot 1), similar to the chemical formula of augite from Stoffel, Germany: $(Ca_{0.91}Na_{0.07}Fe^{2+}_{0.04})(Mg_{0.66}Fe^{3+}_{0.13}Fe^{2+}_{0.09}Ti_{0.08}Al_{0.04})(Si_{1.69}Al_{0.31})O_6$ (Anthony et al., 2001). However, the ratio of cations in each site is distributed somewhat differently. At the M2 position, the high amount of Mg^{2+} and low amount of Ca^{2+} in Dong Nai augite are the opposite of the Mg^{2+} and Ca^{2+} content in augite from Stoffel. Secondly, the Al^{3+} content of Dong Nai augite is distributed relatively equally at positions M1 and T, while most of the Al^{3+} in augite from Stoffel is concentrated at position T. The substantial difference in cation distribution at the T, M1, and M2 positions between Dong Nai and Stoffel augites suggests a complicated isomorphic replacement in pyroxene in general and augite in particular, which depends mainly on temperature (Chen et al., 2021).

The concentrations of aluminum and chromium allow augite to be distinguished from chrome diopside. For chrome diopside from the Kola Peninsula in northwestern Russia, the chromium content is higher (0.52–1.45 wt.% Cr_2O_3) and the aluminum content is lower (1.34–3.80 wt.% Al_2O_3) (Zozulya et al., 2009). Similarly, chrome diopside from Schwartzenstein, Austria, shows high chromium content (1.06–1.47 wt.% Cr_2O_3) and low aluminum content (0.07 wt.% Al_2O_3) (Yamaguchi, 1961; Anthony et al., 2001). While chromium is the chromophore for chrome diopside, the chromium content in Dong Nai augite was negligible and could not be the cause of the dark green color. We infer that iron content controls the color in this augite. However, no direct evidence has yet been found, and this will require further study.

X-Ray Diffraction. According to the X-ray diffraction results of brown sample A13 and green sample A14, the main peaks of Dong Nai augite matched those of augite sample 01-080-1864 from the ICSD (Levin, 2018) (figure 8). This confirmed that the studied samples belong to the augite species, a species of monoclinic pyroxene.

Species. Based on chemical composition, the Dong Nai pyroxenes were plotted and classified using the

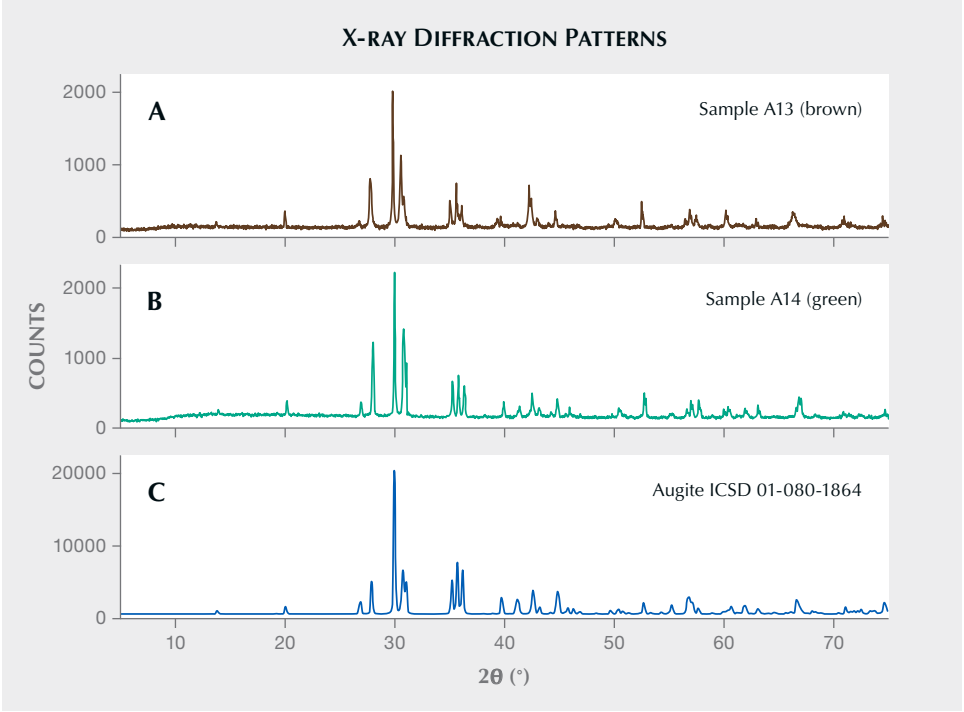

Figure 8. The XRD patterns of augite from Dong Nai (A and B) contain peaks consistent with the pattern of an augite sample from Levin (2018).

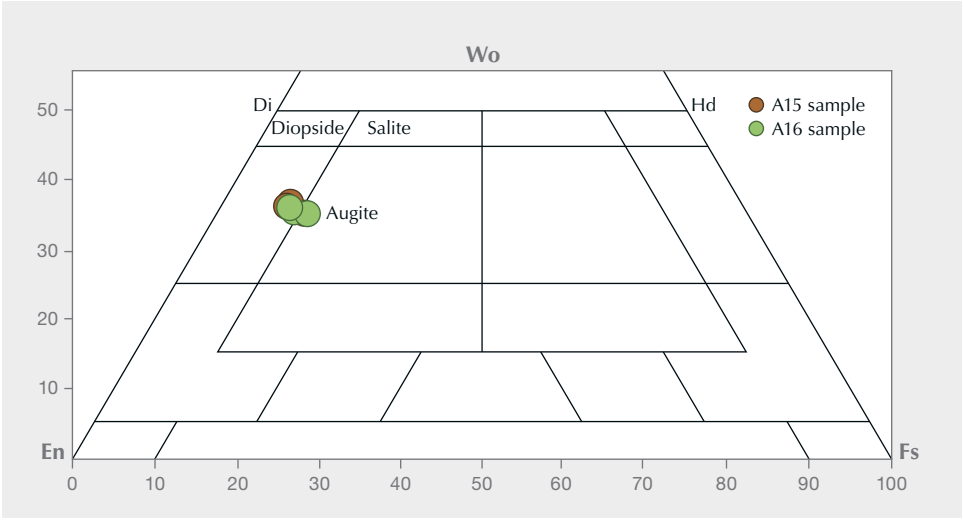

Figure 9. In this classification diagram for quadrilateral pyroxenes, six measured points from samples A15 and A16 (table 2) indicate the zone of magnesium-rich augite (Poldervaart and Hess, 1951).

pyroxene quadrilateral with end members diopside ($CaMgSi_2O_6$ or Di), hedenbergite ($CaFeSi_2O_6$ or Hd), enstatite ($Mg_2Si_2O_6$ or En), and ferrosilite ($Fe_2Si_2O_6$ or Fs) (Poldervaart and Hess, 1951). Wollastonite does not belong to the pyroxenes but to the pyroxenoids, with the formula $Ca_2Si_2O_6$. From table 2, the wollastonite, enstatite, and ferrosilite values were plotted in the pyroxene classification diagram, and the data fell within the augite field (figure 9). Based on Morimoto (1989) and the approval of the Commission on New Minerals and Mineral Names, the Dong Nai pyroxene should be described as magnesium-rich augite.

Raman Spectroscopy. The Raman spectra of the Dong Nai augite samples (brown A1, A2, and A3; green A7, A8, and A9) displayed peaks in the range of 100–1200 cm^{-1} (figure 10), including four vibrational bands assigned to metal-oxygen bond (M-O) stretching and bending (100–400 cm^{-1}), Si-O-Si bending (400–600 cm^{-1}), Si-O_{br} stretching (600–700 cm^{-1}, where O_{br} represents bridging oxygen), and Si-O_{nbr} stretching (700–1200 cm^{-1}, where O_{nbr} represents nonbridging oxygen). The Raman spectra revealed some differences between brown and green augite.

The region from 100 to 400 cm^{-1} exhibited both stretching and bending vibrations of the M-O

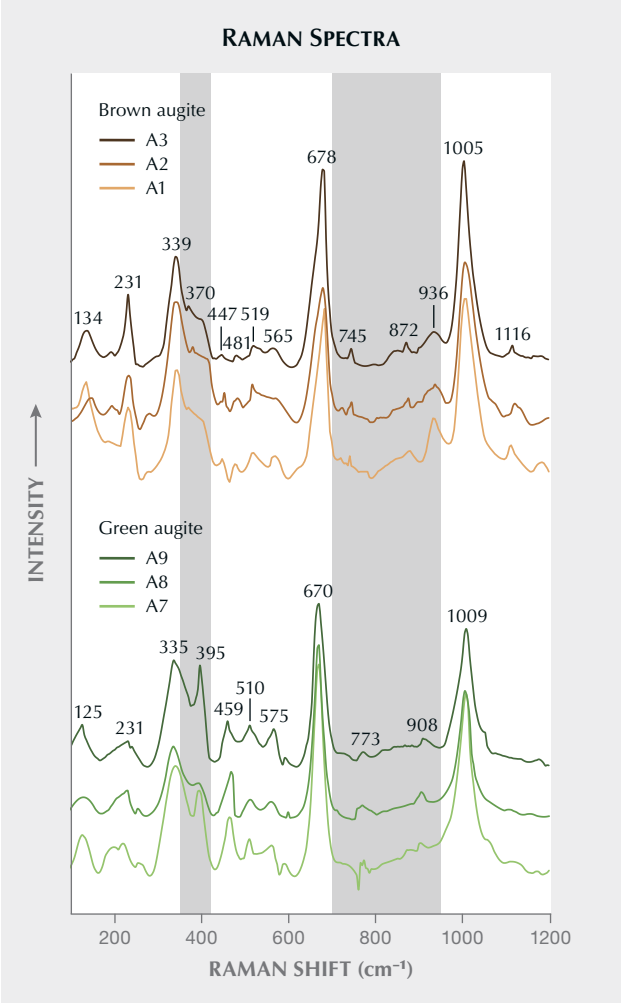

Figure 10. Raman spectra of the two Dong Nai sample groups indicate several differences between green augite (top) and brown augite (bottom) in the ranges of 350–420 cm^{-1} and 700–950 cm^{-1}. Note that a sharp peak at 395 cm^{-1} in the green samples is not observed in the brown samples. In contrast, the peaks at 1116 cm^{-1} and around 872 cm^{-1} are present only in the brown samples. Spectra are offset for clarity.

(Buzatu and Buzgar, 2010; Buzgar et al., 2013). The brown augite group showed peaks around 134, 231, 339, and 370 cm^{-1}, while the green group yielded peaks at 125, 231, 335, and 395 cm^{-1}. We noticed that a strong peak at 395 cm^{-1} was found only in the green augites. Second, the 400–600 cm^{-1} region displayed weak bands at 447, 481, 519, and 565 cm^{-1} for the brown augite, and 459, 510, and 575 cm^{-1} for the green, all related to the bending vibrations of the Si-O group. A peak at 447 cm^{-1} in the brown group was missing in the green samples, whereas other vibrations were similar. Third, a sharp band in the range of 600–700 cm^{-1} is attributed to Si-O_{br} stretching, located at 678 and 670 cm^{-1} for the brown and green samples, respectively. Lastly, the 700–1200 cm^{-1} region is related to Si-O_{nbr} stretching and presented a sharp line around 1005–1009 cm^{-1} for both groups, while the other bands were quite different. In particular, we recorded peaks around 745, 872, 936, and 1116 cm^{-1} for the brown augites and around 773 and 908 cm^{-1} for the green samples. In particular, a peak at 1116 cm^{-1} was well defined in the brown samples but not observed in the green samples. Differences in the 700–1200 cm^{-1} region are typically attributed to the substitution of silicon for aluminum (Buzatu and Buzgar, 2010). In summary, the Raman spectral features of Dong Nai augite displayed the two strongest bands in the 600–700 cm^{-1} range and around 700–1200 cm^{-1}.

The peaks of augite are much stronger in the 700–1000 cm^{-1} region than those of diopside, which only has a peak at 865 cm^{-1} (Buzatu and Buzgar, 2010). Hence, this feature is useful to distinguish augite from diopside when the gemological properties are similar.

CONCLUSIONS

This study has clarified our understanding of the variety and characteristics of augite from Dong Nai Province in Vietnam. The pyroxene xenocrysts from Dong Nai are classified as magnesium-rich augite with the chemical formula $(Ca_{0.608}Na_{0.097}Fe^{2+}_{0.038}Mg_{0.254})(Mg_{0.656}Fe^{3+}_{0.053}Fe^{2+}_{0.098}Ti_{0.015}Al_{0.178})(Si_{1.835}Al_{0.165})O_6$. This material is characterized by its intense dark brown or dark green color, its vitreous luster, and its transparency or translucence. The gemological properties of the green and brown color varieties are identical except for the higher RI and birefringence values for the green samples. The Raman spectra indicate two sharp lines around 1005–1009 cm^{-1}, assigned to Si-O_{nbr} stretching, and 670–678 cm^{-1}, related to Si-O_{br} stretching, along with weaker bands distributed in the 100–1200 cm^{-1} region. Compared with brown augite, the green samples show considerable differences in the 350–400 cm^{-1} range and the 700–950 cm^{-1} range. Augite from Dong Nai has the potential for use in jewelry, particularly as a carving material, and is worthy of further scientific study.

ABOUT THE AUTHORS

Le Ngoc Nang is a postgraduate in the Faculty of Geology at the University of Science, Vietnam National University in Ho Chi Minh City, and CEO of Liu Gemological Research and Application Center (LIULAB). Lam Vinh Phat is manager of gemstone identification, and Pham Minh Tien is a technical specialist, at LIULAB. Dr. Pham Trung Hieu is associate professor and Pham Minh is a lecturer in the Faculty of Geology at the University of Science, Vietnam National University Ho Chi Minh City. Dr. Kenta Kawaguchi is a research fellow in the Faculty of Social and Cultural Studies, Kyushu University in Fukuoka, Japan.

ACKNOWLEDGMENTS

This research was funded by Vietnam National University, Ho Chi Minh City (VNU-HCM) under grant number B2023-18-11. We would also like to express our deep gratitude to Tran Ngoc Vien, who guided us to the study location during our research in the field. We are sincerely thankful to Yasuhiro Shibata of Hiroshima University for technical assistance with EPMA measurements.

REFERENCES

Anthony J.W., Bideaux R.A., Bladh K.W., Nichols M.C., Eds. (2001) *Handbook of Mineralogy*. Mineral Data Publishing, Tucson, Arizona, 813 pp.

Bac D.K., Bao D.V. (2020) Analyzing bio-geo-chemical factors in relation to land use trends on basalt terrain in Dong Nai and nearby areas. *VNU Journal of Science: Earth and Environmental Sciences*, Vol. 36, No. 2, pp. 79–89, http://dx.doi.org/10.25073/2588-1094/vnuees.4542

Bown M.G., Gay P. (1959) The identification of oriented inclusions in pyroxene crystals. *American Mineralogist*, Vol. 44, No 5-6, pp. 592–602.

Buzatu A., Buzgar N. (2010) The Raman study of single-chain silicates. *Analele Ştiintifice de Universitatii "Al. I. Cuza" din Iasi, Seria Geologie*, Vol. 56, No. 1, pp. 107–125.

Buzgar N., Apopei A.I., Diaconu V., Buzatu A. (2013) The composition and source of the raw material of two stone axes of Late

Bronze Age from Neamt County (Romania) - A Raman study. *Analele Ştiintifice de Universitatii "Al. I. Cuza" din Iasi, Seria Geologie*, Vol. 59, No. 1, pp. 5–22.
Chen W., Li Y., La P., Xue Y., Li Z., Xu S., Sheng J. (2021) Influences of thermal treatment temperature on microstructures and properties of glass-ceramics from gold tailings. *Ferroelectrics*, Vol. 579, No. 1, pp. 23–32, http://dx.doi.org/10.1080/00150193.2021.1903264
Co M.C., Hai H.Q. (1994) Report on the result of geological mapping and mineral exploration, Ho Chi Minh City East map series, scale 1:50.000. South Vietnam Geological Mapping Division, General Department of Geology and Minerals of Vietnam [in Vietnamese].
Hurwit K.N. (1988) Gem Trade Lab Notes: Augite, Chinese "onyx." *G&G*, Vol. 24, No. 3, p. 170.
Johnson M.L., McClure S.F., DeGhionno D.G. (1996) Some gemological challenges in identifying black opaque gem materials. *G&G*, Vol. 32, No. 4, pp. 252–261, http://dx.doi.org/10.5741/GEMS.32.4.252
Kawaguchi K., Hayasaka Y., Minh P., Das K., Kimura K. (2022) Origin and tectonic relationship of metagabbro of the Sambagawa Belt, and associated Karasaki mylonites of western Shikoku, Southwest Japan. *Geosciences Journal*, Vol. 26, No. 1, pp. 37–54, http://dx.doi.org/10.1007/s12303-021-0022-6
Levin I. (2018) NIST Inorganic Crystal Structure Database (ICSD), National Institute of Standards and Technology, http://dx.doi.org/10.18434/M32147
Lindsley D.H. (1983) Pyroxene thermometry. *American Mineralogist*, Vol. 68, No. 5-6, pp. 477–493.
Manutchehr-Danai M. (2005) *Dictionary of Gems and Gemology*, 2nd ed. Springer, Berlin, Heidelberg, 1030 pp.
Mei O., Qi L.-J., Hansheng L., Kwok B. (2003) Recent studies on inky black omphacite jade, a new variety of pyroxene jade. *Journal of Gemmology*, Vol. 28, pp. 337–344.
Morimoto N. (1989) Nomenclature of pyroxenes. *Canadian Mineralogist*, Vol. 27, No. 1, pp. 143–156.
O'Donoghue M., Ed. (2006) *Gems: Their Sources, Descriptions, and Identification*, 6th ed. Butterworth-Heinemann, Oxford, UK, 937 pp.
Poldervaart A., Hess H.H. (1951) Pyroxenes in the crystallization of basaltic magma. *Journal of Geology*, Vol. 59, No. 5, pp. 472–489, http://dx.doi.org/10.1086/625891
Son N.D., Du D.C., Hanh D.V., Nam L.D., Phuong H., Phuong D.T., Tue T., Van V.V. (2005) Geological mapping of mineral resource and prospective zoning of Dong Nai Province, scale 1:50.000, Dong Nai Department of Science and Technology [in Vietnamese].
Yamaguchi M. (1961) Chrome-diopsides in the Horoman and Higashi-Akaishi peridotites, Japan. *Memoirs of the Faculty of Science, Kyūsyū University. Series D, Geology*, Vol. 10, No. 2, pp. 233–245, http://dx.doi.org/10.5109/1526111
Zozulya D.R., O'Brien H., Peltonen P., Lehtonen M. (2009) Thermobarometry of mantle-derived garnets and pyroxenes of Kola region (NW Russia): Lithosphere composition, thermal regime and diamond prospectivity. *Bulletin of the Geological Society of Finland*, Vol. 81, No. 2, pp. 143–158, http://dx.doi.org/10.17741/bgsf/81.2.003

The Science of Diamond Reporting.

GIA®

Continuing to lead the world of gemology forward with the GIA App.

Secure
An encrypted database protects your information.

Efficient
Worldwide access to diamond grading reports.

Trusted
The global standard for diamond grading, now at your fingertips.

Origins of Color in Brown Mammoth Ivory

Zhaoying Huang, Tao Chen, Jinyu Zheng, Duo Wang, and Xing Xu

Mammoth ivory is a notable organic gem material, most commonly found with a brown surface color. To investigate the origins of this color, Fourier-transform infrared spectroscopy, X-ray diffraction, and scanning electron microscopy with energy-dispersive X-ray spectroscopy were used to study the samples' spectroscopic and mineralogical characteristics, surface morphology, and chemical composition. Brown mammoth ivory is composed mainly of hydroxyapatite, carbonate hydroxyapatite, and collagen. With the dissolution and loss of organic matter and phosphate anions, fissures and cracks formed. Subsequently, hematite, pyrite, pyrolusite, and manganite crystallized on the mammoth ivory's surface and concentrated in the cracks of the cementum layer. The phase transformation processes during the burial time promoted the formation of iron oxides, manganese oxides, manganese hydroxides, and iron sulfides, which resulted in the brown surface color.

The mammoth species were once the largest terrestrial mammals in the world during the Late Pleistocene (approximately 350,000 to 10,000 years ago), inhabiting the northern hemisphere, starting in Europe and extending as far east as North America (Zhou, 1978; Lister and Sher, 2001; Nogués-Bravo et al., 2008). Mammoths disappeared toward the end of the Late Glacial period (approximately 15,000 or 14,000 to 10,000 years ago). Their ivory has typically been extracted from natural permafrost deposits near rivers, lakes, or basins (Saunders et al., 1990; Cieszkowski et al., 2010).

Mammoth ivory can provide biological information for the Pleistocene period, and paleontologists usually study mammoth tusks as fossils. These fossils yield insights into the genus classification, distribution, migration, and evolution of mammoth, mainly on the Eurasian and North American continents, providing more information about the paleoenvironment and climate change during the Pleistocene (Saunders et al., 1990; Cieszkowski et al., 2010; Han et al., 2013; Wooller et al., 2021).

Mammoth ivory has a long history of use in jewelry (e.g., figure 1) and artworks because of its beauty and pleasing texture (Saunders et al., 1990; Lázničková-Galetová, 2015; Pitulko et al., 2015). The Schreger lines in mammoth ivory increase its elasticity; this can be reflected by a corrugated texture in the cementum and a reduction in mechanical dam-

Figure 1. Mammoth ivory carving with part of the brown surface retained to depict the characters. Courtesy of Duo Wang.

See end of article for About the Authors and Acknowledgments.
Gems & Gemology, Vol. 59, No. 2, pp. 196–209,
http://dx.doi.org/10.5741/GEMS.59.2.196

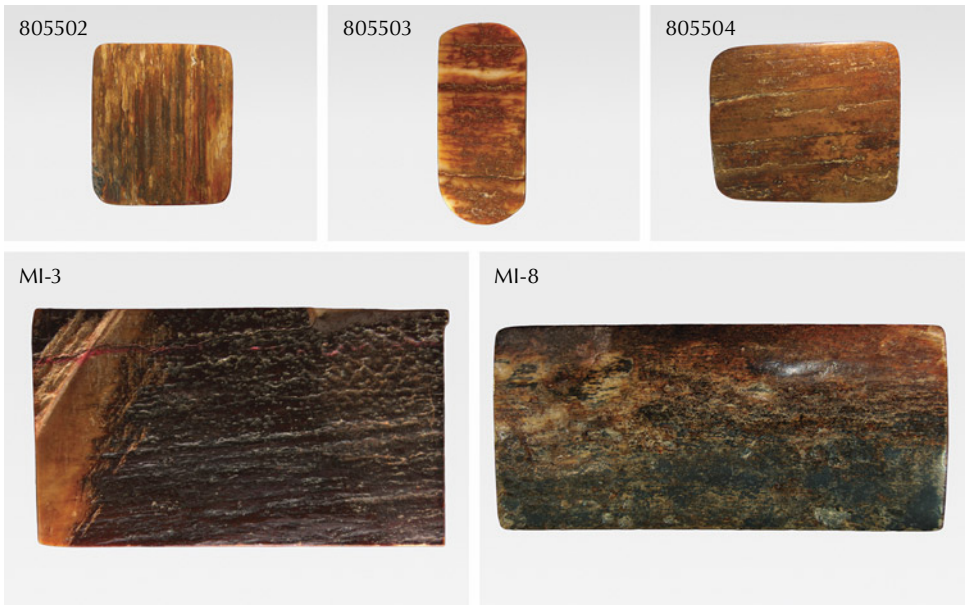

Figure 2. The five mammoth ivory samples in this study weighed 4.16–37.48 g and ranged from 2.8 × 2.5 × 0.6 cm to 6.5 × 3.0 × 1.0 cm. Photos by Zhaoying Huang.

age. High-quality mammoth ivory has a fine, smooth texture and high tensile strength, and it has a unique luster and feel when carved into ornamental objects or jewelry (Pitulko et al., 2015). Similar to elephant ivory, it exhibits fascinating colors and patterns and can take on a smoother polish than other organic raw materials (Pfeifer et al., 2019). Due to various international bans on the sale of elephant ivory, mammoth ivory has gradually replaced it as an organic gem (Martin, 2006; Qi et al., 2010; Yin et al., 2013).

In Brief

- Mammoth ivory that can be used for jewelry and ornamental objects usually has a brown or blue-black surface, but the origin of the brown color on the surface had not been previously explained.
- Fossilization of the mammoth ivory during burial time caused the loss of collagen and promoted the formation of iron oxides, iron sulfides, manganese oxides, and manganese hydroxides.
- The iron oxides and sulfides and the manganese oxides and hydroxides crystallized on the mammoth ivory surface, causing it to turn brown.

To date, gemological studies of mammoth ivory have focused mainly on the material's composition, the crystallographic characteristics of inorganic minerals within, and the means of separating it from elephant ivory (Qi et al., 2010; Wu et al., 2013; Ngatia et al., 2019; Sun et al., 2022). Hydroxyapatite, $Ca_{10}(PO_4)_6(OH)_2$, is considered the main mineral component in mammoth ivory (Sakae et al., 2005; Shen et al., 2021; Sun et al., 2022). Newberyite ($Mg(PO_3OH)\cdot 3H_2O$), organic matter, quartz (SiO_2), and vivianite ($Fe^{2+}{}_3(PO_4)_2\cdot 8H_2O$) along with its oxidation products—e.g., metavivianite ($Fe^{2+}Fe^{3+}{}_2(PO_4)_2(OH)_2\cdot 4H_2O$) and santabarbaraite ($Fe^{3+}{}_3(PO_4)_2(OH)_3\cdot 5H_2O$)—have been found to exist in all structures of mammoth ivory (Shen et al., 2021). Research suggests that elephant ivory and mammoth ivory can be distinguished by the angles formed by their characteristic Schreger lines (Espinoza and Mann, 1993; Singh et al., 2006; Palombo et al., 2012). In mammoth ivory, this angle is generally less than the angle in elephant ivory (Qi et al., 2010).

The surface of mammoth ivory usually has a brown color but is occasionally blue to dark blue or even black. Research on the origins of this surface color is scarce, however. A blue encrustation on some previously studied samples was identified as vivianite (McClure, 2001).

In this paper, Fourier-transform infrared spectroscopy (FTIR), X-ray diffraction (XRD), and scanning electron microscopy (SEM) with energy-dispersive X-ray spectroscopy (EDS) were used to study the mineral and chemical compositions and the surface morphology characteristics of brown mammoth ivory to illustrate the origins of this color.

MATERIALS AND METHODS

Five mammoth ivory samples were chosen for this research (figure 2). Samples 805502, 805503, and

TABLE 1. Gemological characteristics of mammoth ivory samples for this study.

Sample no.	Weight (g)	Dimensions (cm)	Specific gravity	Schreger line angles	UV fluorescence response	Surface color
805502	6.77	2.8 × 2.5 × 0.6	1.835	100°	Long-wave: Blue Short-wave: Light blue	Dark brown and brown
805503	4.16	3.2 × 1.2 × 0.5	1.893	—	Long-wave: Blue Short-wave: Light blue	Reddish brown and milky white
805504	11.35	3.4 × 2.8 × 0.8	1.876	90°	Long-wave: Blue Short-wave: Light blue	Brown and randomly distributed reddish brown dots
MI-3	31.29	5.2 × 2.9 × 1.1	1.882	105°	Long-wave: Blue Short-wave: Light blue	Dark brown and reddish brown
MI-8	37.48	6.5 × 3.0 × 1.0	1.837	95°	Long-wave: Blue Short-wave: Light blue	Mainly brown with local blue-black discoloration

805504 (top row) were provided by the Gemmological Institute, China University of Geosciences in Wuhan. Samples MI-3 and MI-8 (bottom row) were collected from the Liwan Plaza jewelry market in Guangzhou. None of the samples included information about their original source. The five samples ranged from 2.8 × 2.5 × 0.6 cm to 6.5 × 3.0 × 1.0 cm and weighed 4.16–37.48 g. Each had a brown to dark brown surface, with sample MI-8 also displaying a blue-black area on the surface.

All samples were tested at the Gemmological Institute and the State Key Laboratory of Geological Process and Mineral Resources, both at the China University of Geosciences in Wuhan. The color distribution, surface fissures, and cementum layers were observed and photographed using a Leica M205A microscope camera. Ultraviolet fluorescence was observed using a Baoguang Instruments UV5000XL long-wave (365 nm) and short-wave (254 nm) UV light.

FTIR spectra were obtained with a Bruker Vertex 80 Fourier-transform infrared spectrometer. The surface, cementum, and dentine layers were each tested. The following conditions were used: 220 V scanning voltage, 6 mm raster, 10 kHz scanning rate, 32 scans in the range of 4000–400 cm^{-1}, and a resolution of 4 cm^{-1}, with reflection modes from the Kramers-Kronig transform method applied.

XRD patterns were collected by an X'Pert Pro X-ray diffractometer. The brown surface and cementum layer of the samples were pulverized to 200 mesh powder for testing. The system was equipped with a conventional copper source (λ=1.5406 Å) at 40 kV and 40 mA, with a scanning speed of 3.35°/min in the 2θ range 3°–70° and a step size of 0.0167°/s.

Surface morphology characteristics were acquired using a Quanta 450 FEG scanning electron microscope and a Thermo Fisher Helios G4 double-beam electron microscope at an accelerating voltage of 20 kV. Both SEM instruments were equipped with an energy-dispersive X-ray spectroscope, operating at a voltage of 20 kV to collect chemical composition information. Chemical compositions were analyzed using OxfordAztec 5.0 and calibrated using wollastonite (Ca), gallium phosphide (P), iron (Fe), manganese (Mn), ferrous disulfide (S), aluminum oxide (Al), silicon dioxide (Si), magnesium oxide (Mg), and potassium bromide (K). Because mammoth ivory has abundant cracks, fissures, and pores, the samples needed to be pretreated with resin to ensure that the SEM experiments could be performed under a vacuum environment. A carbon film (approximately 10–20 nm) was deposited on the surface by sputtering to make the samples conductive. Backscattered electron (BSE) mode was used to collect images.

RESULTS

Microscopic Observation. The gemological characteristics of the five samples are presented in table 1. Each sample showed the characteristic structure of

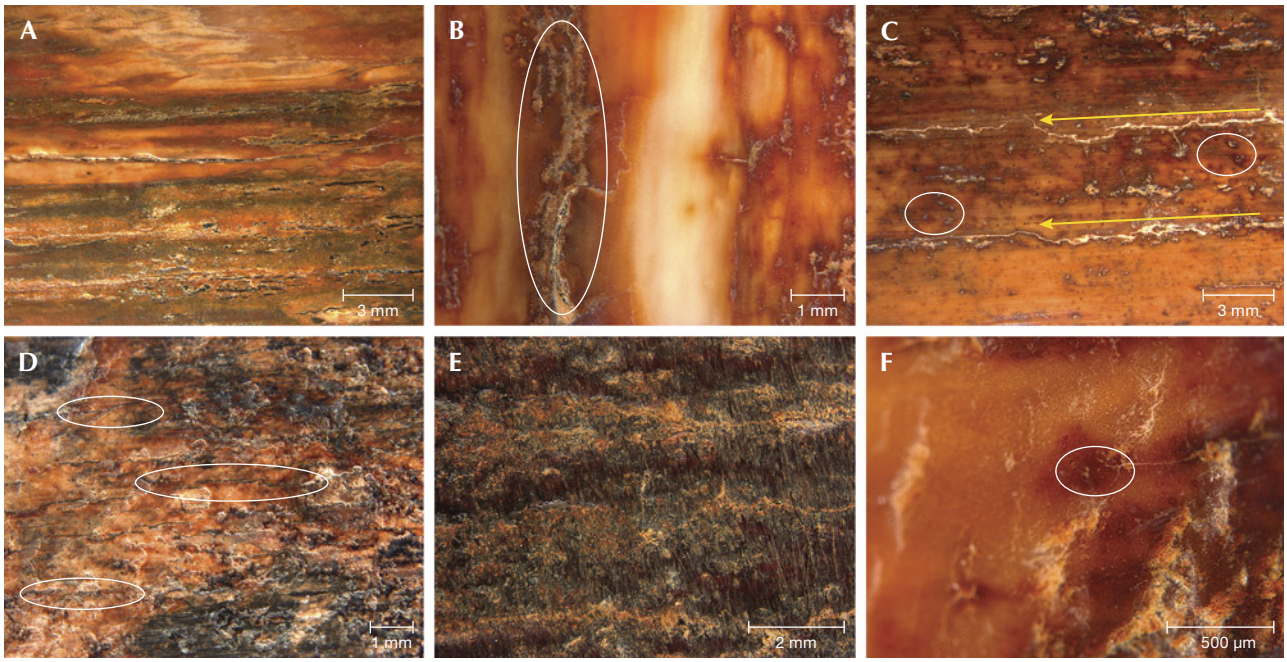

Figure 3. Photomicrographs of the surface of mammoth ivory. A: Uneven color distribution (sample 805502). B: Large crack (white oval, sample 805503). C: Two parallel cracks (yellow arrows) and tan dots (white ovals, sample 805504). D: Irregular color distribution and darker brown cracks (white ovals, sample MI-8). E: Brown and darker brown areas of color interspersed (sample MI-3). F: Tan dots (white oval, sample MI-3). Photomicrographs by Zhaoying Huang.

mammoth ivory on the surface and in cross section. The color distribution on the surface was not uniform, displaying tan and dark brown colors with irregular tan dots and cracks distributed randomly (figure 3). Some large cracks were parallel to each other (figure 3, A and C). The cracks showed a darker brown color than the other areas (figure 3D), and the surface exhibited a waxy luster in reflected light.

Cross-section images of the cementum are shown in figure 4. The cementum is a thick layer (approximately 4–7 mm) on the outside of the tusk. Its structure differs from the interior, which contains no Schreger lines but does have a layered structure running parallel to the length of the tusk (figure 4A). The cementum in mammoth ivory samples is much thicker than that of modern, unfossilized

Figure 4. Photomicrographs of mammoth ivory cross sections, with Schreger line angles indicated by the blue lines. A: Sample MI-8 has a thick concentric top layer (4–7 mm thickness) and downward-penetrating brown crevices (yellow arrow). The angle of the Schreger lines is about 95°. B: Sample MI-3 has downward-penetrating brown crevices (yellow arrows) and transitional color. The angle of the Schreger lines is about 105°. C: Sample 805502 shows obvious Schreger lines with an angle of about 100°. Photomicrographs by Zhaoying Huang.

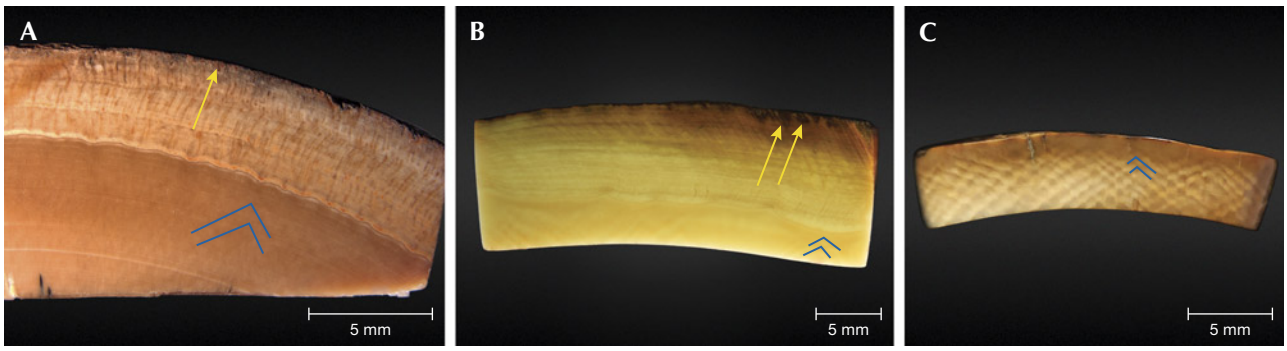

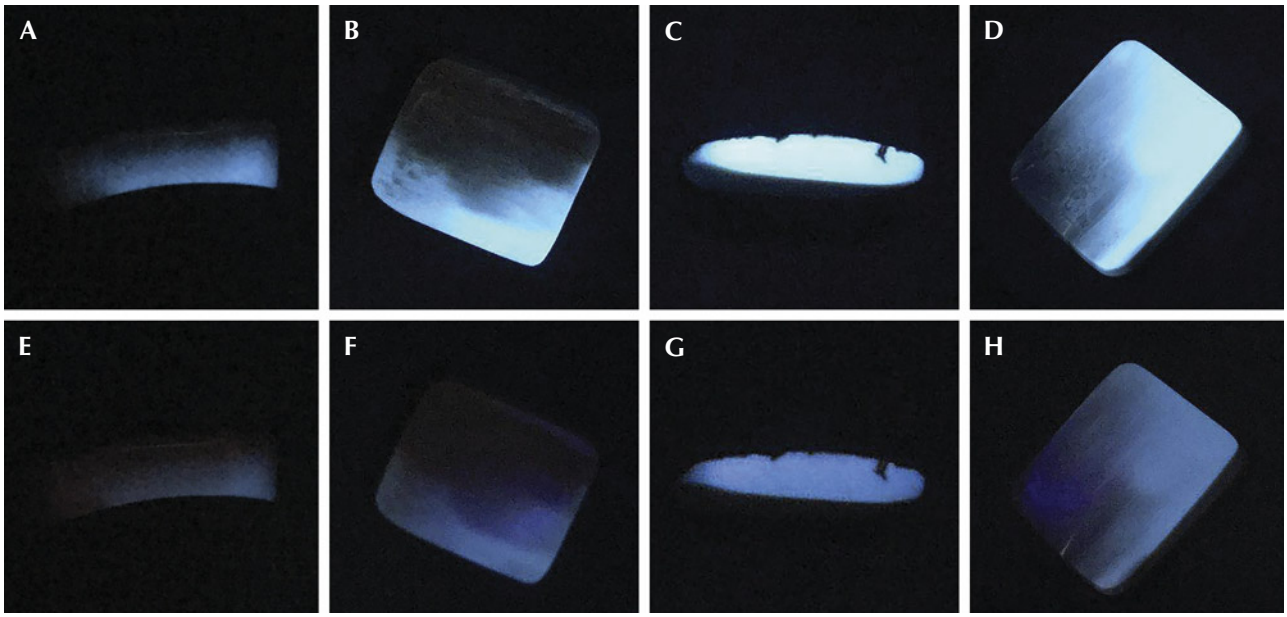

Figure 5. UV fluorescence images of mammoth ivory under long-wave UV (A–D) and short-wave UV (E–H). A and E: UV fluorescence of sample 805502 cross section. B and F: UV fluorescence of the dentine in sample 805502. C and G: UV fluorescence of sample 805503 cross section. D and H: UV fluorescence of the dentine in sample 805504. Photos by Zhaoying Huang.

Asian and African ivory (Yin et al., 2013). Compared to the surface, the cementum layer has fewer cracks. The brown color entered the samples' cementum along the cracks from the surface (figure 4, A–C). From the surface to the cementum, the color becomes gradually lighter (figure 4B). In the dentine layer, the angle of the Schreger lines ranged from 95° to 105° (except for sample 805503, which showed no obvious Schreger lines). This angle was lower than the mean value for Asian and African ivory, which is above 105° (Espinoza and Mann, 1993; Singh et al., 2006).

UV Fluorescence Characteristics. The mammoth ivory samples exhibited blue fluorescence under UV light (figure 5). The fluorescence intensity under long-wave UV (figure 5, A–D) was stronger than under short-wave UV (figure 5, E–H). The blue fluorescence is caused mainly by organic matter, so it is stronger in the dentine. The surface and some dentine areas that underwent fossilization showed no fluorescence reaction (figure 5, B–D and F–H), indicating that the composition of the mammoth ivory had changed and some organic matter might have been lost.

Infrared Spectra Characteristics. The infrared spectra of the surface, cementum, and dentine layers are shown in figure 6. The spectral peaks at 2926 and 2856 cm^{-1} were related to collagen (Yin et al., 2013; Xu and He, 2015). In the three peaks known collectively as the collagen amide bond, these vibrations include a peak at 1653 cm^{-1} associated with C=O bond stretching, a peak at 1557 cm^{-1} associated with both an N-H bending vibration and a C-H stretching vibration, and the peak at 1241 cm^{-1} was associated with an N-H bending vibration and a C-N stretching vibration. An additional peak at 1457 cm^{-1} was due to a C-H bending vibration. These four peaks in the range of 1600–1200 cm^{-1} were also related to the presence of collagen (Huang et al., 2004; Qi et al., 2010; Wu et al., 2013; Shen et al., 2021). The peaks at 1418 and 874 cm^{-1} were caused by a carbonate anion (CO_3^{2-}) group vibration, indicating that CO_3^{2-} replaced the phosphate anion (PO_4^{3-}) group in mammoth ivory. The peaks at 1054, 608, and 575 cm^{-1} were associated with PO_4^{3-} group vibration (Zhou et al., 1999; Shen et al., 2021; Sun et al., 2022). Therefore, the mammoth ivory samples were found to be composed of inorganic matrix and organic protein.

Comparing the infrared spectra of the surface and the dentine of our mammoth ivory samples, the absorption peak positions were similar but the relative intensities were different for four of the samples. The exception was sample 805503, which is not severely fossilized and whose surface is not completely discolored, so the differences in the infrared spectra of

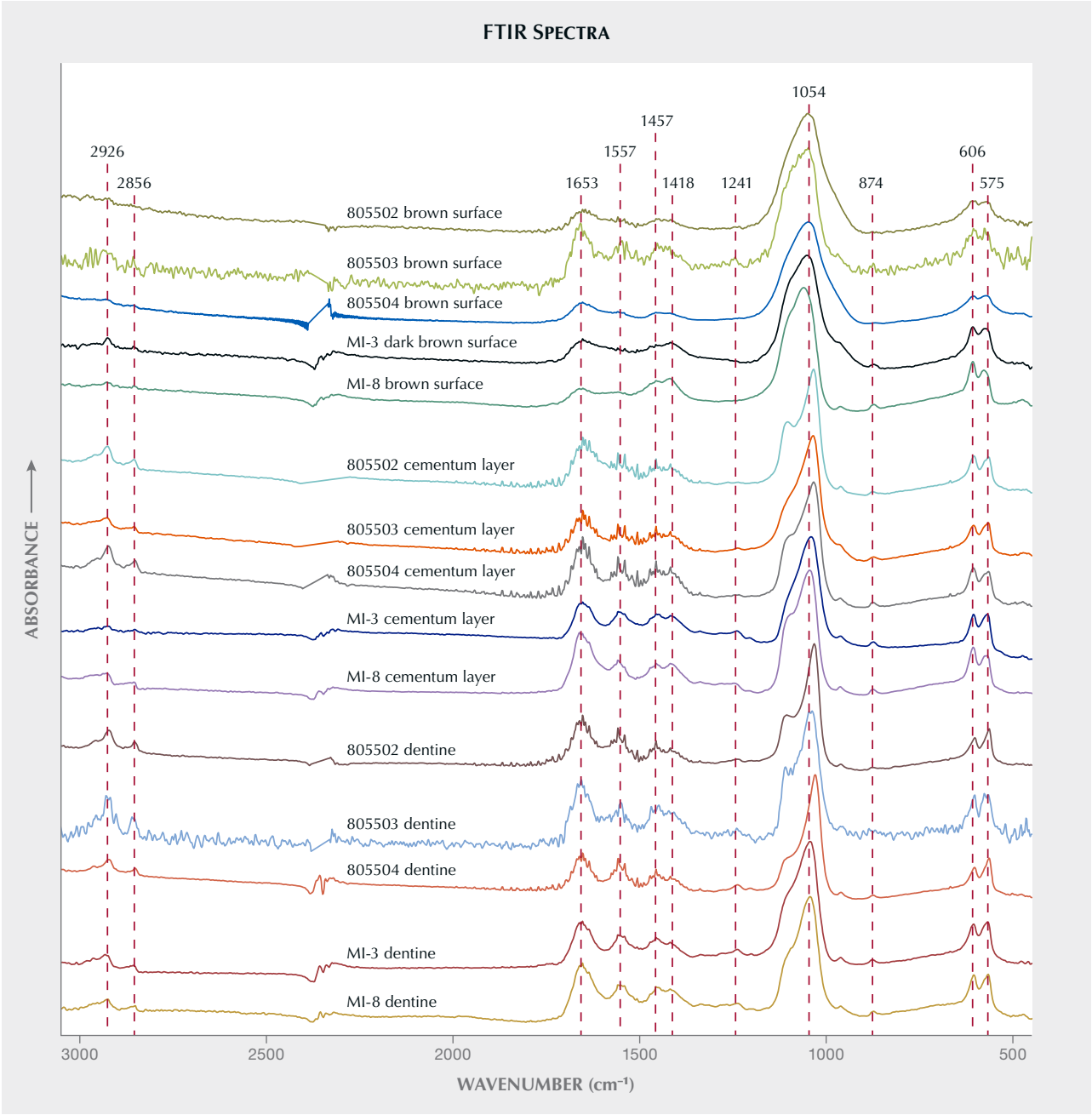

Figure 6. The infrared spectra of mammoth ivory samples (by Kramers-Kronig transform). From the dentine to the surface, the intensity of absorption peaks related to collagen (in the range of 2900–2800 cm^{-1} and 1600–1200 cm^{-1}) decreases. Spectra are offset for clarity.

the surface, cementum, and dentine are not obvious. For samples 805502, 805504, MI-3, and MI-8, the relative intensities of the collagen bands decreased, while the intensity of the PO_4^{3-} group vibration was unchanged. For example, the intensity ratio of the absorption peak at 1653 cm^{-1} and the absorption peak at 1054 cm^{-1} decayed from nearly one-half to less than one-third from dentine to surface. Also, the peaks at 1557 and 1241 cm^{-1} are almost too weak to be observed in the surface's infrared spectra. This indicates that organic protein components of mammoth ivory decreased from the inner dentine layer toward the surface. Elephant ivory, on the other hand, shows almost no change in organic protein content between the two layers (Qi et al., 2010; Yin et al., 2013).

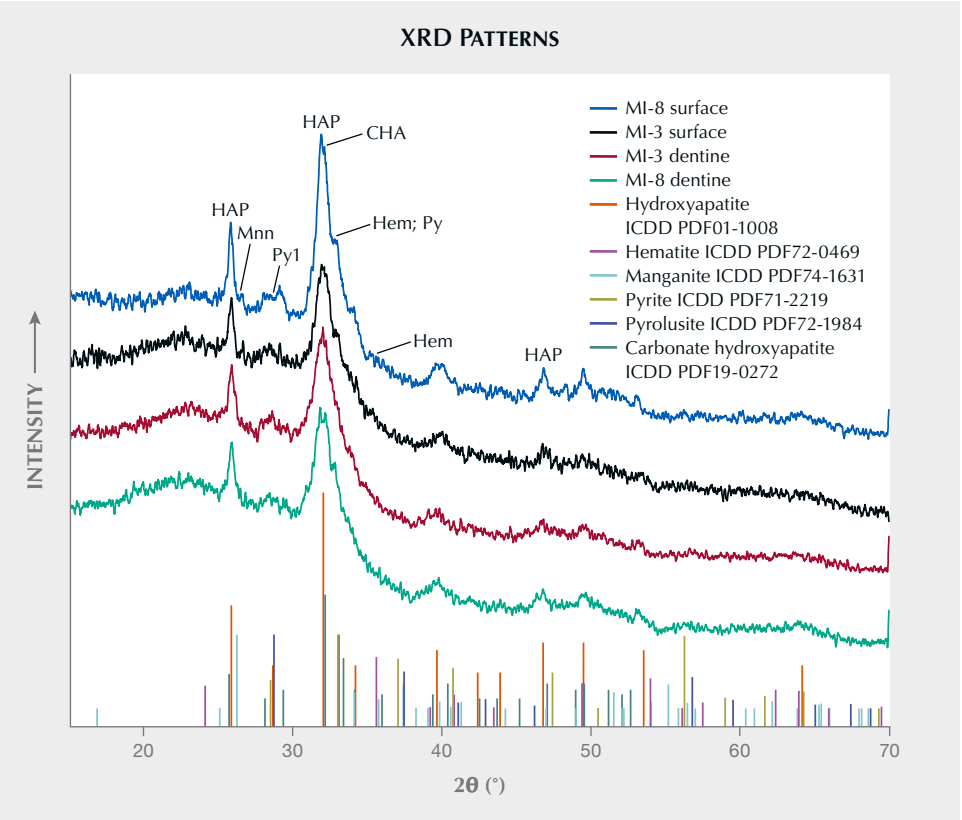

Figure 7. Powder XRD patterns of mammoth ivory samples. Characteristic peaks of hydroxyapatite (HAP), hematite (Hem), manganite (Mnn), pyrite (Py), pyrolusite (Pyl), and carbonate hydroxyapatite (CHA) can be distinguished in the XRD pattern. Spectra are offset for clarity.

X-Ray Diffraction. The powder XRD patterns for the different layers of samples MI-3 and MI-8 are shown in figure 7. Most of the peaks—including the three strongest peaks at d_{002} = 3.44 Å (2θ = 25.82°), d_{211} = 2.81 Å (2θ = 32.00°), and d_{222} = 1.94 Å (2θ = 46.84°)—belonged to hydroxyapatite, $Ca_{10}(PO_4)_6(OH)_2$; see International Centre for Diffraction Data Powder Diffraction File (ICDD PDF01-1008; Wang et al., 2012). This indicates that hydroxyapatite is the dominant phase in mammoth ivory. Hydroxyapatite is generally amorphous in elephant ivory and was considered to be amorphous in mammoth ivory as well (Sakae et al., 2005; Shen et al., 2021; Sun et al., 2022). But after it has undergone burial and weathering, hydroxyapatite in mammoth ivory is considered to be petrified, and its crystallinity can increase (Yin et al., 2013; Xu and He, 2015). The crystallinity of hydroxyapatite can be calculated by the full width at half maximum (FWHM) of the (002) peak using XrayRun software with Gaussian peak profile fitting, where a larger FWHM value indicates a lower crystallinity (Sun et al., 2022). The mean FWHM value of the (002) peak on the surface was 0.397° (standard deviation 0.034°), compared to 0.596° (standard deviation 0.017°) for the dentine. Therefore, the crystallinity of hydroxyapatite was higher on the surface.

Some weak peaks in the XRD patterns, especially from the surface, did not belong to hydroxyapatite

TABLE 2. Powder XRD results of minor minerals in the mammoth ivory samples.

Mineral	2θ (°)	d-spacing (Å)	(hkl)
Hematite	24.04	3.70	(012)
Hematite	32.99	2.71	(104)
Hematite	35.60	2.52	(110)
Pyrolusite	28.48	3.13	(110)
Manganite	26.58	3.35	(210)
Pyrite	32.81	2.71	(200)
Carbonate hydroxyapatite	32.14	2.78	(112)

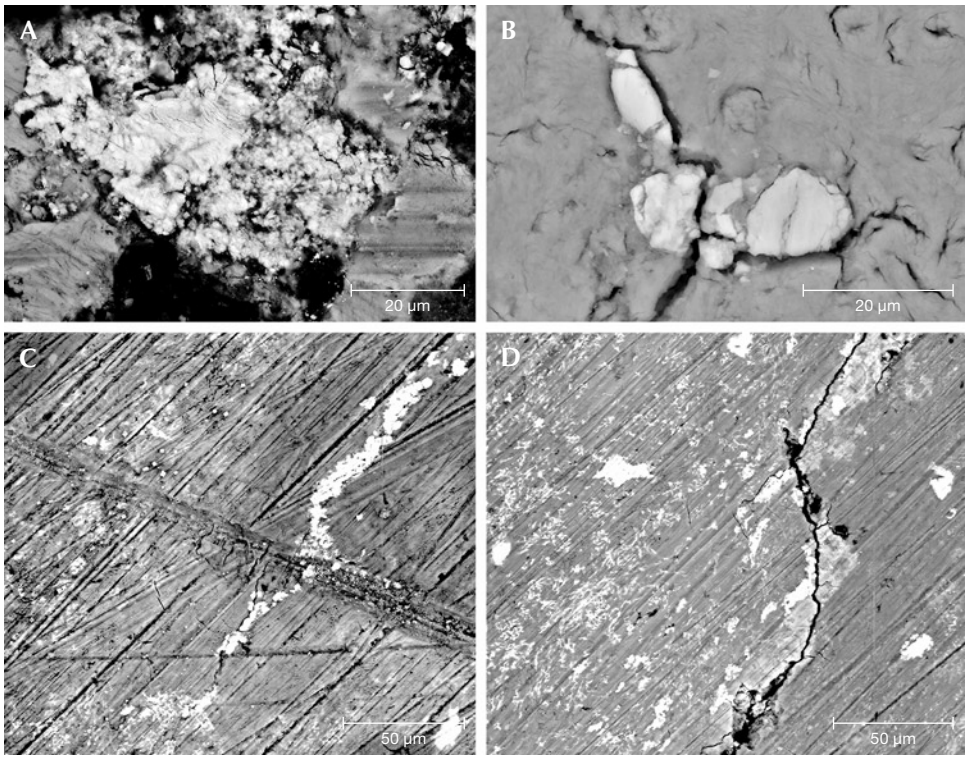

Figure 8. BSE images of samples MI-3 (A and B) and MI-8 (C and D) showing newly formed particles (particles with brighter color) filling cracks and irregularly distributed on the non-crack area on the mammoth ivory's surface. The long dark lines in images C and D are polish lines.

(table 2), indicating other phases existed in the samples. The peaks at d_{012} = 3.70 Å (2θ = 24.04°), d_{104} = 2.71 Å (2θ = 32.99°), and d_{110} = 2.52 Å (2θ = 35.60°) were attributed to hematite (Fe_2O_3, ICDD PDF72-0469; Malik et al., 2014). The peak at d_{210} = 3.35 Å (2θ = 26.58°) was attributed to the strongest peak of manganite (MnO(OH), ICDD PDF74-1631; López et al., 2002), the peak at d_{110} = 3.13 Å (2θ = 28.48°) was attributed to the strongest peak of pyrolusite (MnO_2, ICDD PDF72-1984; Costa et al., 2019), and the peak at d_{112} = 2.78 Å (2θ = 32.14°) was attributed to the strongest peak of carbonate hydroxyapatite (ICDD PDF19-0272; Wei et al., 2003). This indicates that minor hematite, manganite, pyrolusite, and carbonate hydroxyapatite existed in mammoth ivory. Furthermore, the peak at 2θ = 32.8°–33.0° in the surface was broad and asymmetrical, demonstrating that more than one diffraction peak merged in this area. The peak at 32.81° may be attributed to pyrite (FeS_2), whose strongest peak is at d_{200} = 2.71 Å (ICDD PDF71-2219; Horng and Roberts, 2018). Further evidence such as SEM-EDS is needed to prove the existence of hematite, pyrite, manganite, and pyrolusite on the surface.

Morphology Characteristics. Figures 8 and 9 show the BSE images of the surface and a cross section of

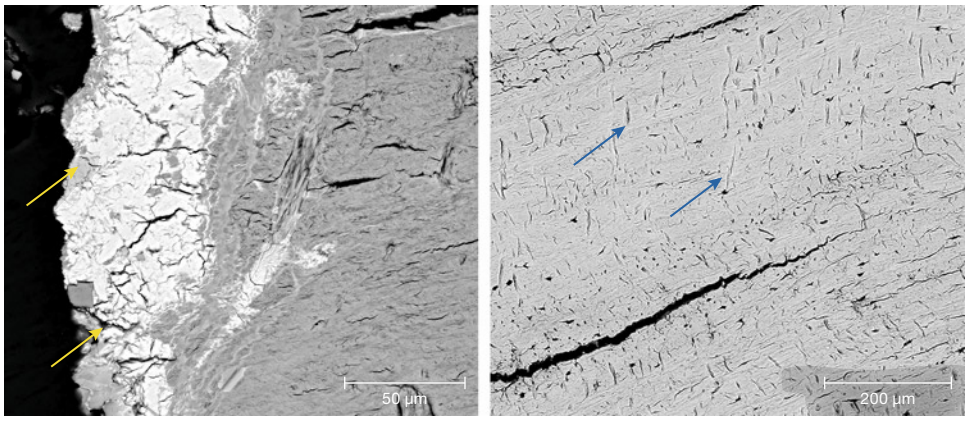

Figure 9. BSE images of the cementum layer in sample MI-8. Left: Cracks (indicated by yellow arrows) extend from the surface into the cementum. Right: Tiny fissures (indicated by blue arrows) are randomly distributed in the cementum.

TABLE 3. Chemical composition (in wt.%) of mammoth ivory samples, obtained by EDS.

Element	MI-3 surface	MI-3 cementum		MI-8 surface			MI-8 cementum		Detection limit
	1	1	2	1	2	3	1	2	
Ca	1.16	6.17	5.78	2.88	37.19	30.22	0.78	39.45	0.17
P	2.72	17.91	17.34	0.47	15.92	11.93	16.63	17.19	0.18
O	26.21	36.74	36.65	42.73	37.96	34.74	35.81	39.51	—
Fe	65.53	37.66	37.25	32.02	8.92	2.74	44.69	2.05	0.26
Mn	1.11	0.52	bdl[a]	bdl	bdl	17.56	bdl	bdl	0.15
S	bdl	bdl	bdl	21.14	bdl	0.36	bdl	bdl	0.12
Si	2.04	bdl	bdl	bdl	bdl	bdl	bdl	bdl	0.09
K	0.39	1.00	0.84	0.76	bdl	0.47	0.33	bdl	0.07
Mg	bdl	bdl	0.61	bdl	bdl	0.48	1.76	1.13	0.11
Al	0.83	bdl	0.32	bdl	bdl	0.20	bdl	bdl	0.07
Na	bdl	bdl	1.20	bdl	bdl	0.34	bdl	0.68	0.13
Ba	bdl	bdl	bdl	bdl	bdl	0.88	bdl	bdl	0.17
Ir	bdl	bdl	bdl	bdl	bdl	0.08	bdl	bdl	0.45
Total[b]	100.00	100.00	100.00	100.00	100.00	100.00	100.00	100.00	—

[a]*bdl = below detection limit*
[b]*Results were normalized. Oxygen was calculated by cation pairing based on 26 per formula unit.*

the cementum layer of samples MI-3 and MI-8. The contrast of the BSE image is related to chemical composition. The elements with the higher atomic number appear brighter. In figure 8, irregular particles with different size and contrast are distributed on the surface, indicating that elements with a higher atomic number than that of calcium coexisted with matrix hydroxyapatite (figure 8, A and B). In addition, some of the cracks observed on the surface were filled with brighter microparticles (figure 8C). The dark parallel lines are residual polish marks (figure 8, C and D).

In figure 9, an abundance of cracks can be seen in the cementum layer. The larger cracks were stretching into the piece from the surface, and the direction of stretching is perpendicular to the surface (figure 9, left). The tiny fissures were distributed randomly, some of them parallel to the surface (figure 9, right). Brighter microparticles were also observed in the cementum in the mammoth ivory samples (figure 9, left). The quantity of these particles decreased from the surface to the interior.

Chemical Composition. The surface chemical composition of samples MI-3 and MI-8 was tested by EDS. The EDS data revealed that the matrix hydroxyapatite contained calcium, phosphorus, and oxygen, while the brighter microparticles were composed of iron, manganese, oxygen, and sulfur (table 3). Element mapping was used to explore the element distribution. As

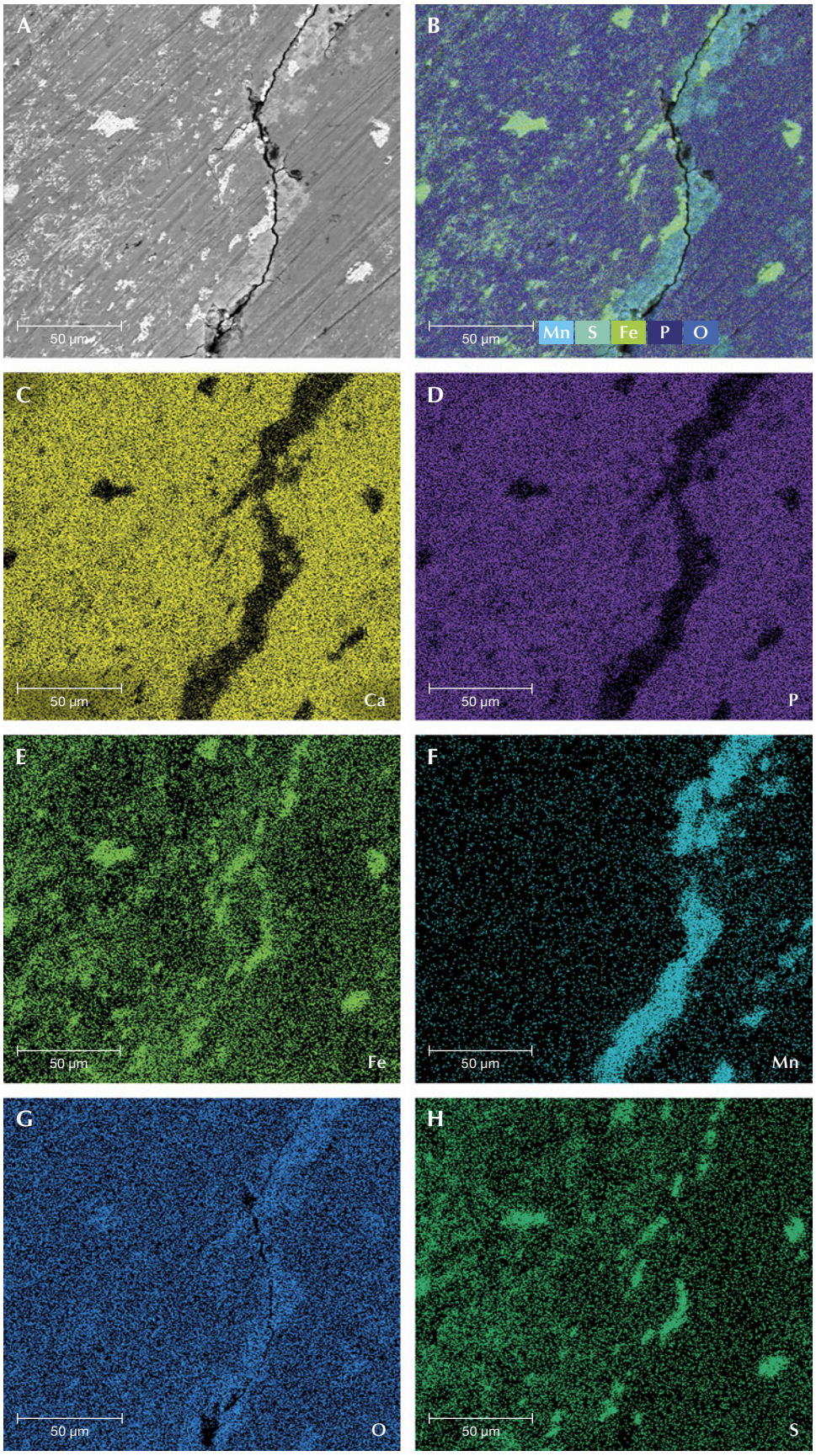

Figure 10. Element maps from EDS data showing iron sulfide, manganese oxide, and manganese hydroxide mainly crystallized on the surface of sample MI-8. The BSE image (A) and an integrated element distribution map (B). EDS mapping of calcium (C), phosphorus (D), iron (E), manganese (F), oxygen (G), and sulfur (H).

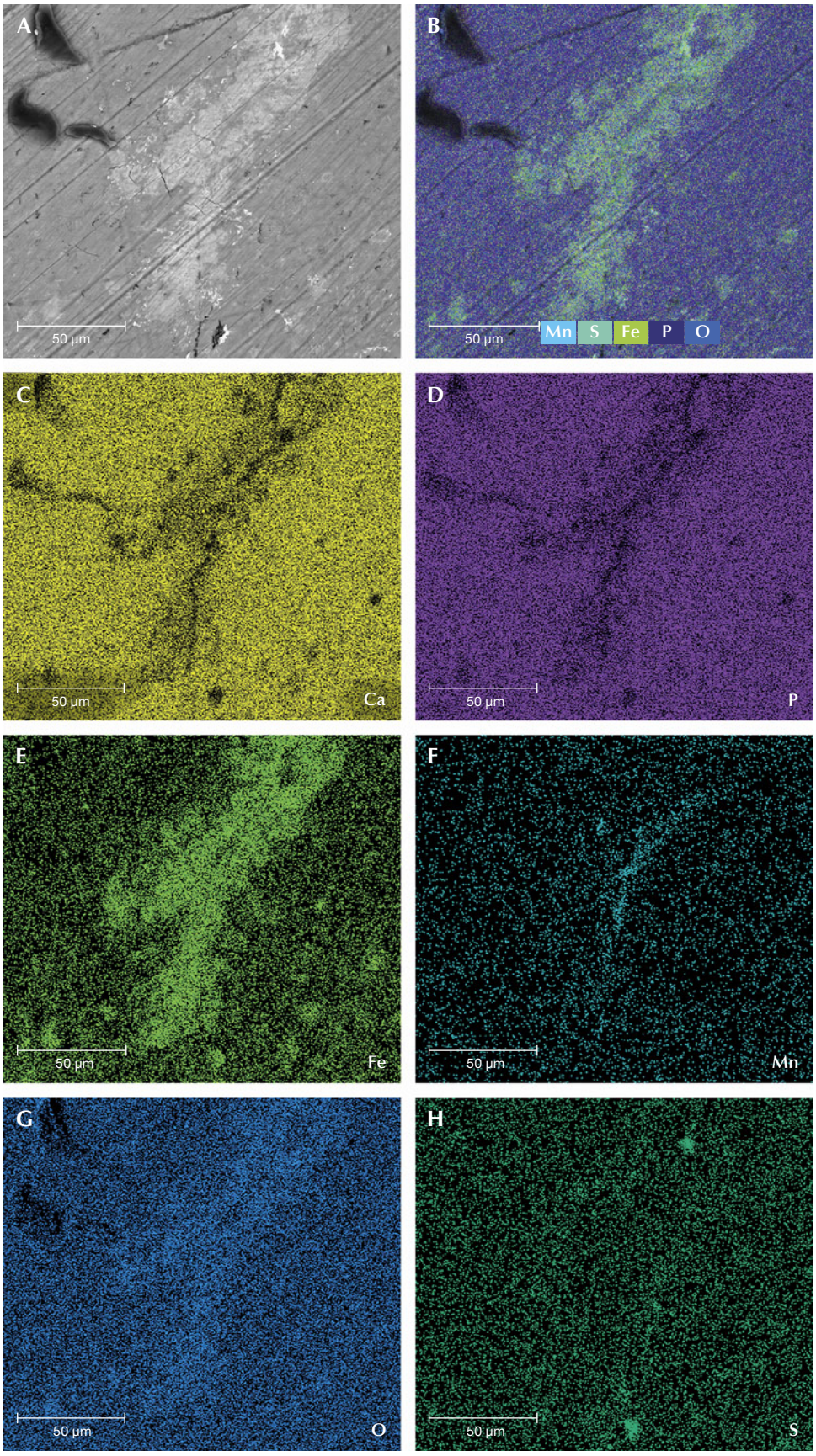

Figure 11. Element maps from EDS data showing iron oxide mainly crystallized on the surface of sample MI-8. The BSE image (A) and an integrated element distribution map (B). EDS mapping of calcium (C), phosphorus (D), iron (E), manganese (F), oxygen (G), and sulfur (H).

shown in figure 10 (C and D) and figure 11 (C and D), calcium and phosphorus were the main elements on the surface and correspond to hydroxyapatite. The brighter-contrast areas (particles) were the same areas that had no calcium and phosphorus but instead contained iron, manganese, oxygen, and sulfur (E–H in figures 10 and 11). As shown in the element maps, particles of manganese oxide and manganese hydroxide were concentrated in the cracks while iron oxide and iron sulfide particles were distributed evenly on the mammoth ivory's surface, some of them concentrated on the fissures. The iron sulfide particles (or their aggregations) were larger than the iron oxide particles. Combining these findings with XRD results, it can be determined that these iron- and/or manganese-rich minerals are hematite (Fe_2O_3), pyrite (FeS_2), pyrolusite (MnO_2), and manganite (MnO(OH)).

DISCUSSION

Testing showed that our mammoth ivory samples were composed mainly of hydroxyapatite, carbonate hydroxyapatite, and collagen. Hydroxyapatite was characterized by carbonate anions replacing phosphate anions during recrystallization. After burial, the mammoth ivory began to lose its organic matter and phosphate anions due to fossilization. At the same time, the mammoth ivory gradually formed fissures and cracks, which increased the dissolution and the loss of organic matter and phosphate anions. An abundance of irregular iron or manganese oxide particles (hematite and pyrolusite), manganese hydroxide particles (manganite), and iron sulfide (pyrite) were found distributed on the surface, even penetrating the cementum layer.

The fossilization processes led to changes in the mammoth ivory composition. The loss of collagen caused the inorganic components to become more susceptible to erosion by other substances in the external aquatic environment (Edwards et al., 2005; Heckel et al., 2014). Manganese oxides, which are very common in the geochemical environment, were able to form on the substrate of mammoth ivory during fossilization (Reiche and Chalmin, 2008). Some reddish brown deposits in fossil ivories have already been proved to be iron oxides (hematite) or a mixture of iron and manganese oxides (Reiche and Chalmin, 2008; Reiche et al., 2013).

On the other hand, phosphate anions (PO_4^{3-}) interact strongly with iron oxides. Phosphate anions can act as a template for hematite formation at all temperatures for most of the pH and phosphorus/iron ratio ranges (Gálvez et al., 1997; Kim et al., 2022). The newly formed microminerals on the mammoth ivory's surface are composed of iron and phosphate minerals, such as vivianite, that are usually unstable and easily transit to more stable phases (McConnell, 1979; Shen et al., 2021). The phase transformation resulted in tiny spherical hematite nanoparticles approximately 5 nm in size (Gálvez et al., 1997; Kim et al., 2022). The iron phosphate mineral (vivianite) detected on one blue-black encrustation was thought to be the result of a chemical reaction of phosphate in mammoth ivory over a long period of time (McClure, 2001).

The fossilization of tusks may involve organic reactions. Bacteria have been detected previously in mammoth ivory (Edwards et al., 2005). Both iron and manganese have chemical properties that tend to form complexes with various inorganic or organic compounds and undergo reactions such as adsorption or ion exchange on solid surfaces (Nealson, 1983). The life activities of microorganisms and changes in the environment, such as changes in temperature, humidity, and pH value, could affect the process of biomineralization (McConnell, 1979). These conditions can lead to changes in the ion valence of iron and manganese and the formation of oxides, hydroxides, or sulfides on the surface of mammoth ivory.

As a result, the dissolution and loss of organic matter and phosphate anion from buried mammoth ivory provide more opportunities for the crystallization of iron oxides, manganese oxides, manganese hydroxides, and iron sulfides on the surface of the material. A combination of microscopic observation and comprehensive phase studies (FTIR, XRD, and SEM with EDS) revealed that on the surface of mammoth ivory, pyrite is usually yellowish brown, hematite is mostly red or dark gray, and pyrolusite and manganite are generally black. These microminerals cause the brown surface color.

CONCLUSIONS

The main components of the mammoth ivory samples from this study were hydroxyapatite, carbonate hydroxyapatite, and collagen, identified by FTIR, XRD, and EDS. From the inner dentine out toward the cementum layer, organic protein components decreased and the crystallinity of hydroxyapatite increased. During burial time, fissures and cracks formed on the surface and cementum layer, and iron oxides (hematite), manganese oxides and hydroxides (pyrolusite and manganite), and iron sulfide (pyrite)

crystallized on the surface. These compounds were identified by XRD, SEM, and EDS. Through complex processes, fossilized mammoth ivory was covered with iron oxides, manganese oxides, manganese hydroxides, and iron sulfide, which produced its brown surface color.

ABOUT THE AUTHORS

Zhaoying Huang (HZYgemology@cug.edu.cn) is a postgraduate student, and Dr. Tao Chen (chentao@cug.edu.cn, corresponding author) is a professor and the dean of the gemology department, at the Gemmological Institute, China University of Geosciences (CUG) in Wuhan. Jinyu Zheng (gemfisher@cug.edu.cn) is a PhD student at the School of Earth Sciences, CUG in Wuhan. Dr. Duo Wang (gt@gtc-china.cn) is the director of the Guangdong Gemstones & Precious Metals Testing Centre in Guangzhou, and Xing Xu (xmzgic@sina.com) is a laboratory technician at the Gemmological Institute, CUG in Wuhan.

ACKNOWLEDGMENTS

This research was funded by the National Natural Science Foundation of China (42072252 and 41572033) and the Fundamental Research Funds of the Gemmological Institute, China University of Geosciences in Wuhan (CIGTWZ-2022001). The authors thank Feng Shi for help in pretreating the mammoth ivory samples for SEM analysis.

REFERENCES

Cieszkowski M., Zuchiewicz W., Alexandrowicz W.P., Wojtal P. (2010) A new find of mammoth tusk in loess-like sediments of the Zakliczyn Basin (Outer Western Carpathians, Poland). *Annales Societatis Geologorum Poloniae*, Vol. 80, No. 1, pp. 89–99.

Costa E., Ronchetti S., Pistarino A., Delmastro A., Gallo L.M., Tomalino M.U. (2019) Erroneous attribution of Mn-oxides minerals in primary mineralogy collections. *Scientific Museology*, Vol. 13, pp. 96–102.

Edwards H.G.M, Jorge Villar S.E., Nik Hassan N.F., Arya N., O'Connor S., Charlton D.M. (2005) Ancient biodeterioration: An FT–Raman spectroscopic study of mammoth and elephant ivory. *Analytical and Bioanalytical Chemistry*, Vol. 383, No. 4, pp. 713–720, http://dx.doi.org/10.1007/s00216-005-0011-z

Espinoza E.O., Mann M.-J. (1993) The history and significance of the Schreger pattern in proboscidean ivory characterization. *Journal of the American Institute for Conservation*, Vol. 32, No. 3, pp. 241–248, http://dx.doi.org/10.1179/019713693806124866

Gálvez N., Barrón V., Torrent J. (1999) Effect of phosphate on the crystallization of hematite, goethite, and lepidocrocite from ferrihydrite. *Clays and Clay Minerals*, Vol. 47, No. 3, pp. 304–311, http://dx.doi.org/10.1346/CCMN.1999.0470306

Han J.-E., Shao Z.-G., Meng X.-G., Zhu D.-G., Yu J., Wang J., Chen Q.-G., Quan K. (2013) Discovery and significance of Manmuthus fossil in Gonghe basin, Qinghai Province. *Geological Bulletin of China,* Vol. 32, No. 5, pp. 730–733.

Heckel C., Müller K., White R., Floss H., Conard N.J., Reiche I. (2014) Micro-PIXE/PIGE analysis of Palaeolithic mammoth ivory: Potential chemical markers of provenance and relative dating. *Palaeogeography, Palaeoclimatology, Palaeoecology*, Vol. 416, pp. 133–141, http://dx.doi.org/10.1016/j.palaeo.2014.09.010

Horng C.-S., Roberts A.P. (2018) The low-temperature Besnus magnetic transition: Signals due to monoclinic and hexagonal pyrrhotite. *Geochemistry, Geophysics, Geosystems*, Vol. 19, No. 9, pp. 3364–3375, http://dx.doi.org/10.1029/2017GC007394

Huang Z.-L., Zhang W., Cui F.-Z. (2004) Study of the nucleation sites in collagen mineralization. *Spectroscopy and Spectral Analysis*, Vol. 24, No. 5, pp. 539–542.

Kim H.J., Hong J.S., Choi J.H., Han G.S., Jung H.S. (2022) Effect of phosphate ions on the formation of iron oxide/hydroxide as a stabilizer. *Journal of Solid State Chemistry*, Vol. 305, article no. 122688, http://dx.doi.org/10.1016/j.jssc.2021.122688

Lázničková-Galetová M. (2015) The phenomenon of Gravettian necklaces – Mammoth ivory necklaces from Dolní Věstonice I (Moravia, Czech Republic). *Quaternary International*, Vol. 359-360, pp. 229–239, http://dx.doi.org/10.1016/j.quaint.2014.08.040

Lister A.M., Sher A.V. (2001) The origin and evolution of the woolly mammoth. *Science*, Vol. 294, No. 5544, pp. 1094–1097, http://dx.doi.org/10.1126/science.1056370

López E.F., Escribano V.S., Gallardo-Amores J.M., Resini C., Busca G. (2002) Structural and morphological characterization of Mn–Zr mixed oxides prepared by a sol–gel method. *Solid State Sciences*, Vol. 4, No. 7, pp. 951–961, https://doi.org/10.1016/S1293-2558(02)01350-X

Malik V., Sen S., Gelting D.R., Gajdardziska-Josifovska M., Schmidt M., Guptasarma P. (2014) Field-enhanced magnetic moment in ellipsoidal nano-hematite. *Materials Research Express*, Vol. 1, No. 2, article no. 026114, http://dx.doi.org/10.1088/2053-1591/1/2/026114

Martin E. (2006) Are we winning the case for ivory substitutes in China? *Pachyderm*, Vol. 40, pp. 89–101.

McClure S.F. (2001) Lab Notes: Fossil ivory. *G&G*, Vol. 37, No. 4, pp. 322–323.

McConnell D. (1979) Biogeochemistry of phosphate minerals. In P.A. Trudinger and D.J. Swaine, Eds., *Biogeochemical Cycling of Mineral-Forming Elements*. Elsevier Scientific Publishing Company, Amsterdam, pp. 163–199.

Nealson K.H. (1983) Microbial oxidation and reduction of manganese and iron. In Westbroek P. and de Jong E.W., Eds, *Biomineralization and Biological Metal Accumulation*. D. Reidel Publishing Company, Dordrecht, Holland, pp. 459–479.

Ngatia J.N., Lan T.M., Ma Y., Dinh T.D., Wang Z., Dahmer T.D., Xu Y.C. (2019) Distinguishing extant elephants ivory from mammoth ivory using a short sequence of cytochrome b gene. *Scientific Reports*, Vol. 9, article no. 18863, http://dx.doi.org/10.1038/s41598-019-55094-x

Nogués-Bravo D., Rodríguez J., Hortal J., Batra P., Araújo M.B. (2008) Climate change, humans, and the extinction of the woolly mammoth. *PLoS Biology*, Vol. 6, No. 4, pp. 685–692, http://dx.doi.org/10.1371/journal.pbio.0060079

Palombo M.R., Ferretti M.P., Pillola G.L., Chiappini L. (2012) A reappraisal of the dwarfed mammoth *Mammuthus lamarmorai* (Major, 1883) from Gonnesa (south-western Sardinia, Italy). *Quaternary International*, Vol. 255, pp. 158–170, http://dx.doi.org/10.1016/j.quaint.2011.05.037

Pfeifer S.J., Hartramph W.L., Kahlke R.-D., Müller F.A. (2019)

Mammoth ivory was the most suitable osseous raw material for the production of Late Pleistocene big game projectile points. *Scientific Reports*, Vol. 9, No. 1, article no. 2303, http://dx.doi.org/10.1038/s41598-019-38779-1
Pitulko V.V., Pavlova E.Y., Nikolskiy P.A. (2015) Mammoth ivory technologies in the Upper Palaeolithic: A case study based on the materials from Yana RHS, Northern Yana-Indighirka lowland, Arctic Siberia. *World Archaeology*, Vol. 47, No. 3, pp. 333–389, http://dx.doi.org/10.1080/00438243.2015.1030508
Qi L.J., Zhou Z.Y., Liao G.L., Lin S.S. (2010) Differences on growth microstructure and FTIR absorption spectra between mammoth teeth and ivory. *Journal of Gems and Gemmology*, Vol. 12, No. 3, pp. 1–4.
Reiche I., Chalmin E. (2008) Synchrotron radiation and cultural heritage: Combined XANES/XRF study at Mn K-edge of blue, grey or black coloured palaeontological and archaeological bone material. *Journal of Analytical Atomic Spectrometry*, Vol. 23, No. 6, pp. 799–806, http://dx.doi.org/10.1039/b717442j
Reiche I., Müller K., Albéric M., Scharf O., Wähning A., Bjeoumikhov A., Radtke M., Simon R. (2013) Discovering vanished paints and naturally formed gold nanoparticles on 2800 years old Phoenician ivories using SR-FF-MicroXRF with the color X-ray camera. *Analytical Chemistry*, Vol. 85, No. 12, pp. 5857–5866, http://dx.doi.org/10.1021/ac4006167
Sakae T., Oinuma H., Higa M., Kozawa Y. (2005) X-ray diffraction and FTIR study on heating effects of dentin from mammoth tusk. *Journal of Oral Biosciences*, Vol. 47, No. 1, pp. 83–88, http://dx.doi.org/10.1016/S1349-0079(05)80013-1
Saunders J.J., Haynes Jr. C.V., Stanford D., Agogino G.A. (1990) A mammoth-ivory semifabricate from Blackwater Locality No. 1, New Mexico. *American Antiquity*, Vol. 55, No. 1, pp. 112–119, http://dx.doi.org/10.2307/281497
Shen M., Lu Z., Xu Y., He X. (2021) Vivianite and its oxidation products in mammoth ivory and their implications to the burial process. *ACS Omega*, Vol. 6, No. 34, pp. 22284–22291, http://dx.doi.org/10.1021/acsomega.1c02964
Singh R.R., Goyal S.P., Khanna P.P., Mukherjee P.K., Sukumar R. (2006) Using morphometric and analytical techniques to characterize elephant ivory. *Forensic Science International*, Vol. 162, No. 1-3, pp. 144–151, http://dx.doi.org/10.1016/j.forsciint.2006.06.028
Sun X., He M., Wu J. (2022) Crystallographic characteristics of inorganic mineral in mammoth ivory and ivory. *Minerals*, Vol. 12, No. 2, article no. 117, http://dx.doi.org/10.3390/min12020117
Wang Z.L., Yan Y.H., Wan T. (2012) Fabrication and characterization of hydroxyapatite/collagen bone-like nanocomposite through a self-assembly method. *Science and Engineering of Composite Materials*, Vol. 19, No. 2, pp. 177–182.
Wei M., Evans J.H., Bostrom T., Grøndahl L. (2003) Synthesis and characterization of hydroxyapatite, fluoride-substituted hydroxyapatite and fluorapatite. *Journal of Materials Science: Materials in Medicine*, Vol. 14, No. 4, pp. 311–320, http://dx.doi.org/10.1023/A:1022975730730
Wooller M.J., Bataille C., Druckenmiller P., Erickson G.M., Groves P., Haubenstock N., Howe T., Irrgeher J., Mann D., Moon K., et al. (2021) Lifetime mobility of an Arctic woolly mammoth. *Science*, Vol. 373, No. 6556, pp. 806–808, http://dx.doi.org/10.1126/science.abg1134
Wu X., Zhang J., Lu X.H. (2013) Study on ivory and mammoth teeth. *2013 China Gems & Jewelry Academic Conference*, pp. 143–146.
Xu Y., He X.M. (2015) Analysis of composition and microstructure of mammoth ivory. *2015 China Gems & Jewelry Academic Conference*, pp. 168–172.
Yin Z.W., Zhang P.F., Chen Q.L., Luo, Q.F., Zheng C., Li Y.L. (2013) A comparison of modern and fossil ivories using multiple techniques. *G&G*, Vol. 49, No. 1, pp. 16–27, http://dx.doi.org/10.5741/GEMS.49.1.16
Zhou B.X. (1978) The distribution of the woolly rhinoceros and woolly mammoth. *Vertebrata Palasiatica*, Vol. 16, No. 1, pp. 47–59.
Zhou L.D., Liu Y.K., Zhou G.F. (1999) A study on modern biological apatite and fossil apatite. *Acta Mineralogica Sinica*, Vol. 19, No. 1, pp. 41–47.

Lab Notes

Editors
Thomas M. Moses | Shane F. McClure
Sally Eaton-Magaña

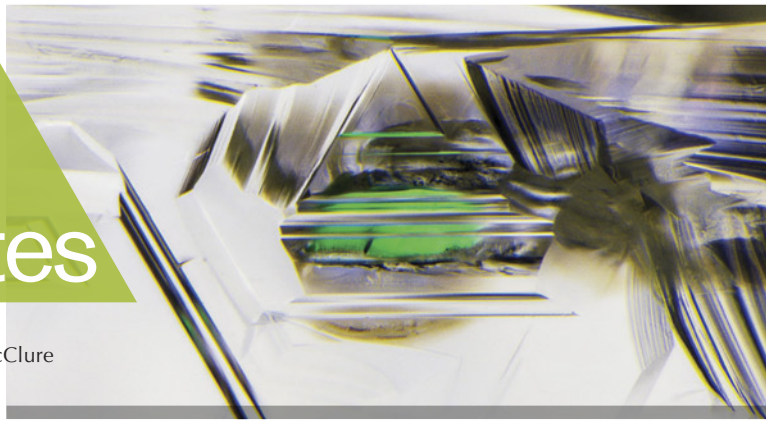

Star AQUAMARINE

The Carlsbad laboratory recently received a grayish blue aquamarine for an identification report. The unique 13.37 ct oval double cabochon displayed a six-rayed star (figure 1). Standard gemological testing revealed a spot refractive index of 1.570 and a hydrostatic specific gravity of 2.68. Raman analysis confirmed that the stone was beryl.

Under magnification (figure 2), the stone displayed planes of negative crystals, film-like inclusions, ilmenite, and reflective particles that resulted in a six-rayed star. Asterism in aquamarine is due to three sets of elongated channel-like or thin-film inclusions oriented in three different directions perpendicular to the *c*-axis (e.g., Spring 2004 Gem News International, p. 104; K. Schmetzer et al., "Asterism in beryl, aquamarine, and emerald—an update," *Journal of Gemmology*, Vol. 29, No. 2, 2004, pp. 66–71). Of all the aquamarines examined at GIA laboratories, this was one of the first to display asterism.

Jessa Rizzo

Figure 1. A 13.37 ct grayish blue aquamarine displaying asterism.

Rare Faceted BRUCITE

Gem-quality transparent blue brucite is a very rare, very soft and heat-sensitive magnesium hydroxide ($Mg(OH)_2$) with a Mohs hardness of approximately 2.5–3.0 and perfect cleavage. Brucite was named in 1824 in honor of the first person to describe the species: Archibald Bruce, an American mineralogist, physician, and editor of the *American Mineralogical Journal.*

Recently the Carlsbad laboratory received for identification services a transparent greenish blue stone weighing 3.09 ct and measuring 9.74 × 9.71 × 5.98 mm (figure 3). Microscopic observation revealed numerous scratches and abrasions on the surface, as well as strong doubling, some needles, and a large fracture. Standard gemological testing yielded a specific gravity of 2.37. Refractive index was not measured for fear of damaging this soft and fragile stone. A uniaxial optic character was observed with a polari-

Figure 2. Negative crystals, film-like inclusions, and ilmenite were observed under magnification in the star aquamarine. Field of view 3.57 mm.

Editors' note: All items were written by staff members of GIA laboratories.

Gems & Gemology, Vol. 59, No. 2, pp. 210–221.

Figure 3. A rare and very fragile 3.09 ct brucite.

scope and optic figure sphere. Raman spectroscopy confirmed the gem's identity as brucite. Worldwide, this was the second brucite examined by GIA.

Michaela Damba

DIAMOND

Natural Diamond with CVD-Like Fluorescence Pattern

Fluorescence images collected using the DiamondView are very useful in identifying whether a diamond is natural or laboratory grown (S. Eaton-Magaña and J.E. Shigley, "Observations on CVD-grown synthetic diamonds: A review," Fall 2016 *G&G*, pp. 222–245). In many cases, type II natural diamonds show varying dislocation networks in these images. Meanwhile, high-pressure, high-temperature (HPHT) synthetic diamonds show cuboctahedral growth patterns, and chemical vapor deposition (CVD) laboratory-grown diamonds show growth striations.

The Mumbai laboratory recently received a 0.40 ct colorless round brilliant for diamond grading service. Spectroscopy identified it as a type IIa diamond, and it was examined further for color origin determination. DiamondView imaging showed uncommon and interesting patterns. In figure 4, the lower right is dominated by green fluorescence while the upper left shows mainly blue fluorescence, with a clear and straight boundary. Detailed examination revealed numerous sharp and clear dislocation lines in multiple orientations in both parts of this diamond. These dislocation lines were introduced by plastic deformation and provide strong evidence that the diamond crystallized in nature. It should be pointed out that the interface layer seen in the fluorescence image is uncommon for natural diamonds but similar to that of CVD laboratory-grown diamonds. Further photoluminescence spectroscopy analysis confirmed this natural diamond was treated by annealing under high pressure and high temperature to improve its color, reinforcing our assertion that advanced analytical study is often crucial in identifying a diamond.

Natural grown diamonds with fluorescence patterns similar to those of HPHT synthetic diamonds have also been reported previously (Spring 2013 Lab Notes, pp. 45–46). With recent advances in technology, manufactured diamonds with unique features have become more widely available on the market. Therefore, it is more important than ever to scrutinize each feature to ensure the appropriate identification results in such scenarios. Since natural and manufactured diamonds are structurally identical, we often need to rely on advanced gemological and spectroscopic data, particularly for such low-nitrogen diamonds, to correctly identify their origin.

Manisha Bhoir and Shoko Odake

Yellow Zoning in Pink Diamonds

Recently GIA's Carlsbad laboratory received a few unusual natural, nitrogen-rich type IaA pink diamonds for color origin and identification service. The pink color of these diamonds is caused by the 550 nm visible absorption band, with the color concentrated within parallel narrow bands known as pink graining (S. Eaton-Magaña et al., "Natural-color pink, purple, red and brown diamonds: Band of many colors," Winter 2018 *G&G*, pp. 352–377). In diffused light, they displayed faint yellow color zoning (fig-

Figure 4. DiamondView imaging of the pavilion facets for this HPHT-treated natural diamond shows graining and zoning that resemble those of a laboratory-grown CVD diamond with HPHT treatment. The inset shows the DiamondView image of an HPHT-treated CVD-grown diamond.

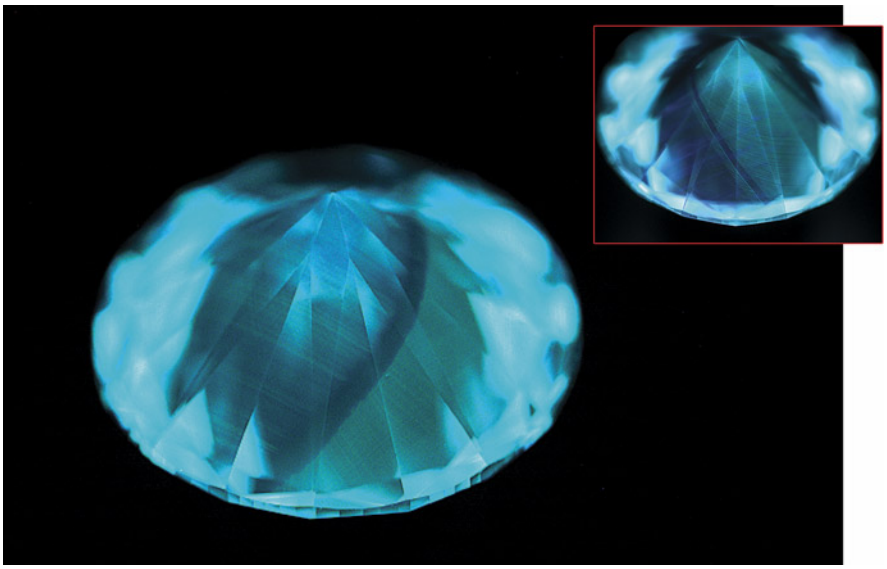

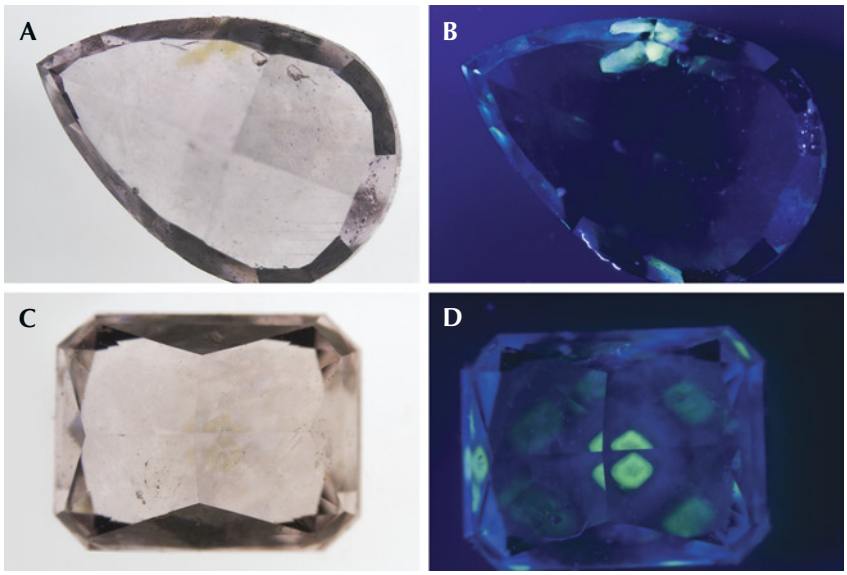

Figure 5. Fancy brownish pink pear and rectangular diamonds, each weighing 0.25 ct, shown in diffused light (A and C) and in long-wave UV light (B and D).

ure 5, A and C). Further inspection under long-wave UV revealed strong yellow fluorescence confined to areas with yellow color zoning (figure 5, B and D).

Photoluminescence (PL) spectra (excited by 514 nm laser) collected from the area with yellow zoning show a broad band centered at ~710 nm. This broad emission band and corresponding strong yellow fluorescence are typically observed in yellow or orange diamonds colored by the 480 nm visible absorption band (C.M. Breeding et al., "Naturally colored yellow and orange gem diamonds: The nitrogen factor," Summer 2020 *G&G*, pp. 194–219). These gemological and spectroscopic features suggest that separate color centers produce pink and yellow colors within these diamonds, though the 480 nm visible absorption band cannot be detected with ultraviolet/visible/near-infrared (UV-Vis-NIR) spectroscopy (possibly due to the fact that the yellow color zone is volumetrically small compared to the rest of the diamond, and that the UV-Vis-NIR absorption spectroscopy is a bulk analysis technique).

The mechanism of the formation of these unusual pink diamonds has not been determined and to the authors' knowledge, such diamonds showing localized regions colored by the 550 nm band and 480 nm band have not yet been documented. Since we know very little about the physics of the 480 and 550 nm visible absorption bands, their co-occurrence within single diamonds might help us to better understand the structures of defects that are related to these features. By paying careful attention to the details of color and fluorescence zoning, more of these unusual rare pink diamonds may be identified.

Shiva Sohrabi, Mei Yan Lai, and Sally Eaton-Magaña

GLASS Imitation of Cat's-Eye Chrysoberyl

The Hong Kong laboratory recently examined a ring mounted with an estimated 5.56 ct brownish yellow cat's-eye cabochon (figure 6). The client submitted the stone as cat's-eye chrysoberyl, which it resembled at first glance. Standard gemological testing yielded a spot refractive index of 1.57, well below chrysoberyl's range of 1.74–1.75. Under short-wave UV radiation, the stone displayed strong chalky fluorescence. Microscopic observation revealed long parallel tubes creating a cat's-eye when viewed from the top and a honeycomb structure when viewed from the side of the stone (figure 7). This confirmed the material was fiber-

Figure 6. A ring mounted with an estimated 5.56 ct brownish yellow cat's-eye cabochon resembling chrysoberyl.

Figure 7. The cabochon displayed the honeycomb structure frequently observed in fiber-optic glass. Field of view 2.00 mm.

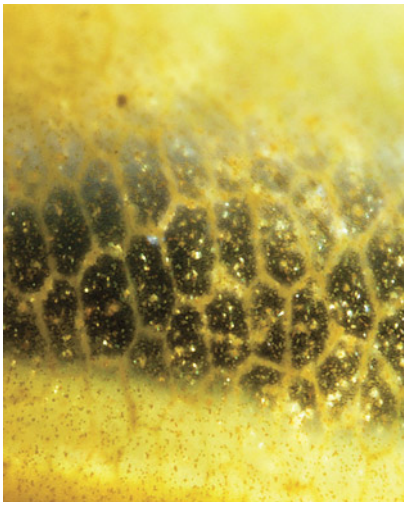

optic glass, made by fusing together very thinly spun glass fibers. Infrared spectroscopy showed two broad absorptions centered at 3500 and 2670 cm^{-1} associated with artificial glass, further validating our identification.

Artificial glass has been used as an imitation for different gems such as star sapphire (Fall 2021 Lab Notes, pp. 261–262), Paraíba tourmaline (Winter 2020 Lab Notes, pp. 518–520), nephrite and jadeite (Spring 2019 Lab Notes, pp. 93–94), and blue amber (Fall 2019 Gem News International, pp. 443–444). Its color and appearance can often lead to misidentification. Therefore, conducting basic gemological tests and observing the stone under a microscope is important, especially when the stone is set in jewelry.

Tsz Ying Fong

LABORATORY-GROWN DIAMOND

CVD Diamond Over 34 Carats

Chemical vapor deposition (CVD) growth technology has advanced significantly over the last two decades. In this study, we report on the largest CVD gem diamond GIA has encountered, recently tested in the Hong Kong laboratory. This emerald-cut diamond weighing 34.59 ct and measuring 24.94 × 13.95 × 9.39 mm (figure 8) was produced by Ethereal Green Diamond in India. It had G color and VS_2 clarity. Small black graphite inclusions were found. Some stood alone inside the body, while others formed clusters of clouds located between growth layers. Microscopic observation showed a weak oily or wavy graining when looking through the table facet, a feature sometimes seen in CVD gem diamonds. It tends to appear more prominently in CVD diamonds with high amounts of strain and a strong birefringence pattern when viewed through crossed polarizers (figure 9).

Infrared absorption spectroscopy revealed no absorption related to nitrogen, which is consistent with type IIa diamond. However, a weak absorption related to boron (an absorption peak at ~2800 cm^{-1}) was detected, corresponding to around 2 ppb of boron impurity. This trace amount of boron was very likely due to contamination during diamond growth. There are different opinions on whether this trace contamination should be considered in diamond type classification.

Photoluminescence (PL) spectroscopy was performed at liquid nitrogen temperature (–196°C) with several laser excitations (figure 10). In addition to strong emissions from NV^0 and NV^- centers at 575 nm and 637 nm, respectively, moderately strong doublet emissions from SiV^- at 736.6 and 736.9 nm were recorded. A weak emission at 946.4 nm, possibly from the SiV^0 defect, was also observed. Other important emission features included a strong emission from the H3 defect at 503.2 nm and a weak emission band with peaks at 566.0, 566.7, and 567.7 nm. The emission at 467.6 nm, which is common in as-grown CVD diamonds, was reduced by high-temperature treatment. These observations and spectroscopic features confirmed that this CVD diamond was annealed under high pressure and high temperature (HPHT) to improve its color appearance. In contrast, no post-growth color treatment was applied to the 16.41 ct CVD lab-grown diamond tested a year earlier in the New York laboratory (W. Wang et al., "New

Figure 8. This 34.59 ct CVD-grown diamond (24.94 × 13.95 × 9.39 mm), produced by Ethereal Green Diamond in India, is the largest GIA has tested.

Figure 9. A high amount of strain and a strong birefringence pattern were observed using crossed polarizers. Field of view 15.92 mm.

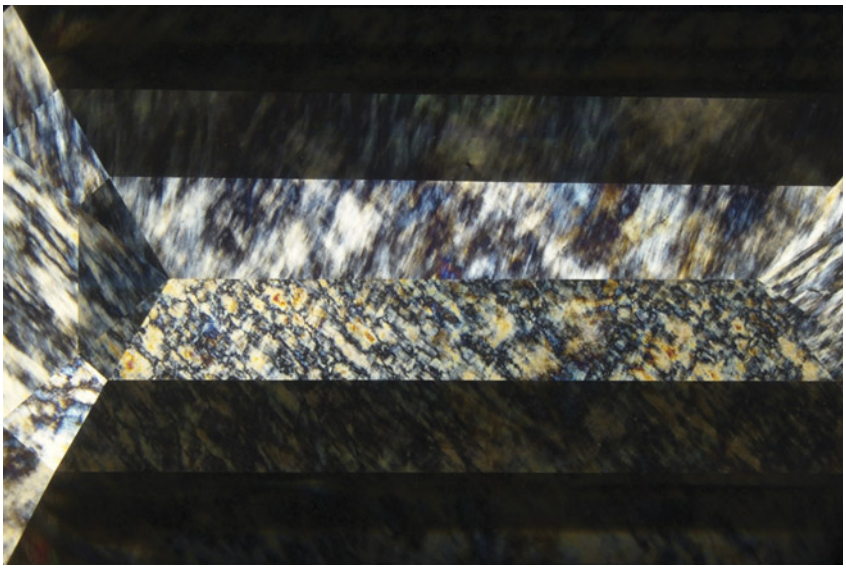

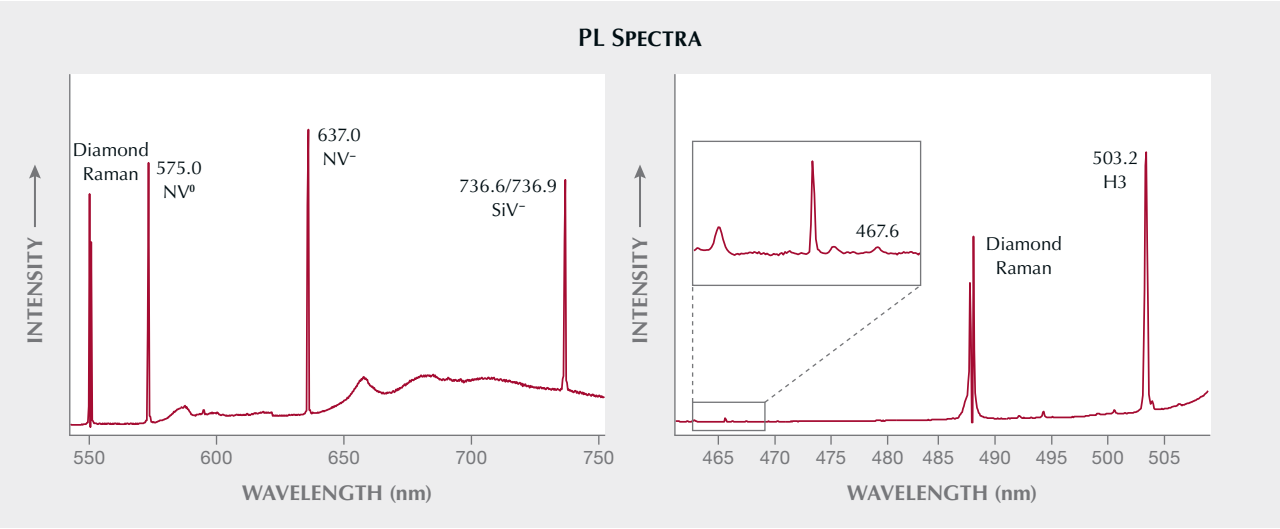

Figure 10. Left: The PL spectrum with 514 nm laser excitation under liquid nitrogen temperature showed features of treated CVD diamond. Right: The PL spectrum with 457 nm laser excitation under liquid nitrogen temperature recorded a strong H3 defect and a negligible 467.6 nm center.

record size for CVD laboratory-grown diamond," *GIA Research News*, January 27, 2022).

DiamondView fluorescence imaging showed green and blue colors with a banded pattern. Typical CVD growth striations were clearly visible (figure 11). Green fluorescence was from the H3 defect, produced during HPHT annealing. This banded structure revealed at least eight growth steps to achieve sufficient depth for this large diamond. Additionally, strong blue phosphorescence with similar banding was detected in the DiamondView.

This very large CVD diamond represents a milestone in CVD growth. Mined diamonds with similar size and quality are very rare. We will continue monitoring developments in gem diamond growth technology to ensure all diamonds are properly identified in GIA laboratories.

Ka Wing Tam and Terry "Ping Yu" Poon

CVD Diamonds with Invisible Markings

Laser inscription is a common practice that helps to easily identify a diamond. The inscriptions are so small as to be nearly impossible to read without magnification, but they can be easily read with a loupe or microscope to help match the diamond to a laboratory report. Laser inscription can be done on the girdle, on the center of the table, on a star facet, or under the table surface. Inscriptions under the table surface are very effective from a security standpoint, as they require significant weight loss to remove.

Recently, GIA labs in India tested two diamonds (1.93 and 0.60 ct) with interesting markings. No intentional markings were observed on these samples without magnification, nor could any be seen under a microscope. But when the diamonds were exposed to the deep ultraviolet light of the DiamondView, markings appeared (figure 12). Both samples were CVD laboratory-grown diamonds and

Figure 11. DiamondView imaging of the 34 ct CVD diamond revealed at least eight growth steps.

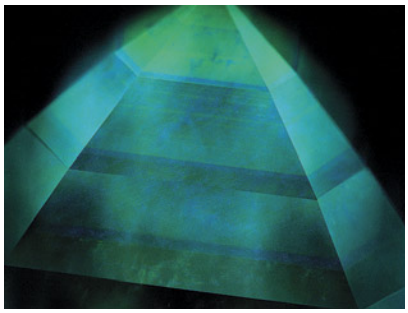

Figure 12. Left: The DiamondView image of the 1.93 ct CVD laboratory-grown diamond shows numbers on the table facet. Right: The 0.60 ct CVD laboratory-grown diamond shows a logo mark on the star facet.

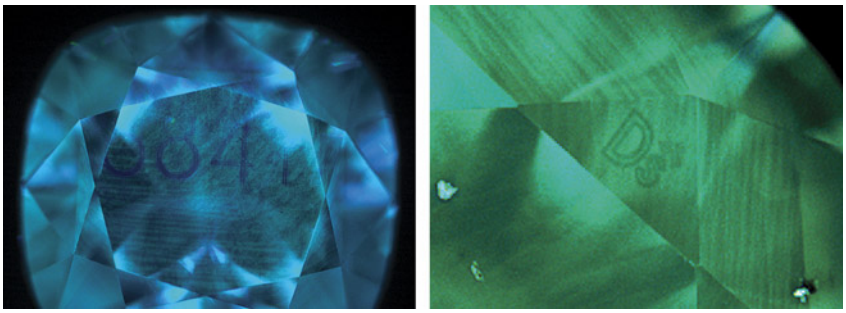

Figure 13. The Lord Hanumana pearl (left, 33.70 × 32.98 × 24.64 mm) and the Lord Ganesha pearl (right, 10.59 × 10.21 × 9.18 mm).

treated with high pressure and high temperature after growth. The invisible markings are thought to be caused by slightly different concentrations of defects, but we do not know how they were created.

The invisible markings in these two diamonds suggest the possible introduction of a new security measure in diamonds, similar to the anti-counterfeiting measure used with passports and banknotes upon exposure to a special light.

Shoko Odake and Priyanka Kadam

PEARLS

Two Pearls of Indian Cultural Significance

In India, pearls (also known as *moti* or *mukta*) and pearl-adorned jewelry have historically been coveted by the affluent and served as symbols of cultural importance for centuries. GIA's Mumbai laboratory has tested various jewelry items set with pearls that were not only artistic in their design but also of great symbolic and religious significance. Two recent submissions consisted of pearls fashioned into the likenesses of Indian deities (figure 13). The first was skillfully crafted to resemble Lord Hanumana, an Indian deity from the epic Ramayana bearing the likeness of a *vanara* (an ancient race of forest-dwellers). The ornament had a total weight of 24.91 g, and its surface was partially drilled in several positions. Yellow metal fittings set with green, white, yellow, and black enamel formed the head, eyes, body, and striped tail. A translucent red stone set on the pearl formed the tongue of the deity (figure 14, left). This baroque pearl was white and light gray in color with orient and measured approximately 33.70 × 32.98 × 24.64 mm. When viewed under 40× magnification, its surface showed typical nacreous structure with overlapping aragonite platelets, and minor surface openings were present on some areas. Most of the surface had good nacre condition, but a few small areas of the nacre were damaged or worn, and remnants of an adhesive glue were visible around some of the decorative enamel inserts.

Energy-dispersive X-ray fluorescence (EDXRF) spectrometry analysis of the pearl showed manganese levels below the detection level of the instrument and a higher strontium content of 1188 ppm. In addition, an inert reaction to X-ray fluorescence (XRF) confirmed saltwater origin. A moderate greenish yellow reaction was observed under long-wave ultraviolet radiation, and a weaker reaction of a similar color was noted under short-wave UV radiation. Such fluorescence reactions in nacreous saltwater pearls are often associated with pearls from the *Pinctada*-species mollusk. Real-time microradiography (RTX) imaging revealed the presence of a very large void that appeared to have been partially filled with a foreign material (figure 14, right). The clearest evidence of the void was observed within the ornament's head as a dark gray area beneath the nacre layer. The outline of this void was consistent with the external shape of the pearl, but the filling material par-

Figure 14. Left: External appearance of the Lord Hanumana pearl. Right: RTX image showing the internal structure. Also indicated are the gemstone tongue, the eyes, the tail, the void, and the filling.

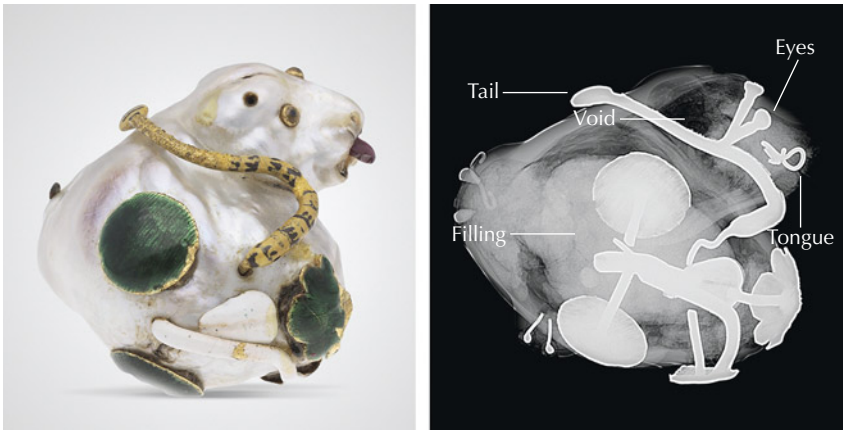

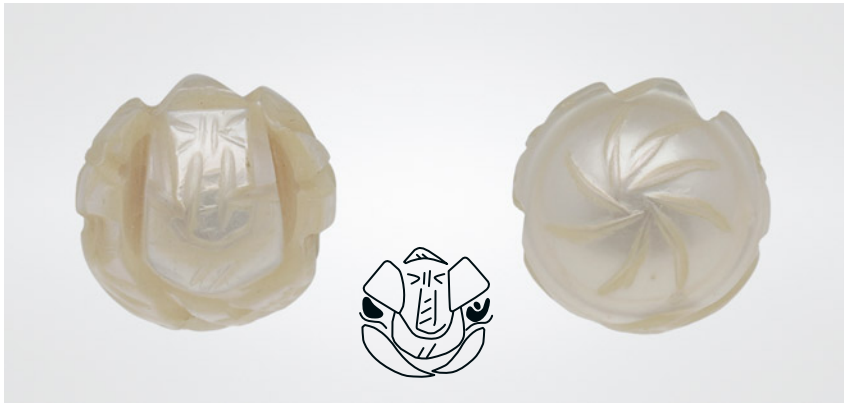

Figure 15. Front view of the Lord Ganesha pearl (left) with a line drawing of features (center) and back view (right).

tially masked the void in RTX and made it harder to see the complete structure clearly. (The radiopaque areas visible on the microradiographs represent the adornments decorating the pearl.) While large voids are more often associated with non-bead cultured pearls, the shape and form of this void resembled those associated with natural pearls. Hollow pearls are often filled (wholly or partially) with a variety of materials including wax, metal, resin, cement, and shell to increase the weight and inflate the perceived value (Winter 2022 Lab Notes, pp. 480–481). In the case of older pearls such as this one, filling can provide enough solid material within the pearl to support all the metal adornments, and it can also improve the durability of the item.

Also submitted was a pearl portraying Lord Ganesha (figure 13, right). The white undrilled, button-shaped pearl weighed 6.27 ct and measured 10.59 × 10.21 × 9.18 mm. Its surface was carefully carved to resemble the Indian deity, with the head of an elephant and the seated body of a man on the front and a swirling pattern on the back (figure 15). EDXRF analysis results showed a high manganese content of 598 ppm and relatively low strontium levels at 376 ppm. These readings were supported by a strong yellowish green fluorescence reaction when exposed to optical XRF (figure 16, left), indicating the pearl was from a freshwater environment. RTX imaging revealed the presence of a small twisted void, along with discoid-like features (figure 16, right) typically seen in non-bead cultured freshwater pearls (K. Scarratt et al., "Characteristics of nuclei in Chinese freshwater cultured pearls," Summer 2000 *G&G*, pp. 98–109).

Figure 16. X-ray fluorescence reaction (left) and an RTX image showing the Lord Ganesha pearl's internal structure (right). A small twisted void and discoid features can be seen in the center.

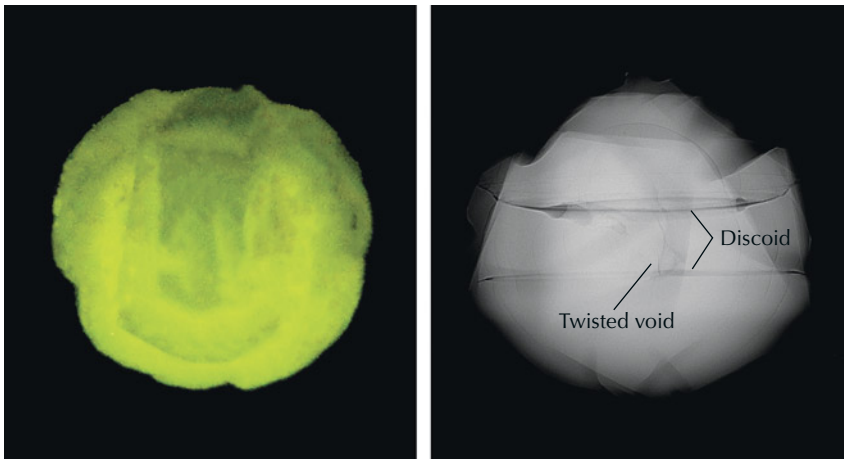

The transformation of pearls into valuable pieces of art is a specialized skill. Indian artists have mastered this ability and can transform pearls into symbolic pieces that have a special connection to ancient Indian scriptures. The laboratory staff at GIA in Mumbai continue to examine intriguing pearls of historical and cultural significance in India.

Nishka Vaz, Rajesh Patel, and Abeer Al-Alawi

A Fascinating Large South Sea Bead Cultured Pearl

A recent noteworthy submission to GIA's Mumbai laboratory contained a loose round, undrilled white pearl with strong orient, weighing 54.96 ct and measuring 19.90 × 19.53 mm (figure 17). Externally the pearl had a smooth, blemish-free surface and exhibited a homogeneous uniform color with a high luster. When viewed under 40× magnification, large and evenly spaced overlapping aragonite platelets were visible which helped account for the silky reflection on the surface. X-ray fluorescence (XRF) analysis gave a relatively inert reaction. Chemical analysis using energy-dispersive X-ray fluorescence spectrometry was performed on two surface areas. The data collected showed manganese levels on both areas below the detection level of the instrument and higher strontium levels of 1162 and 1163 ppm, confirming the pearl formed in a saltwater environment. A moderate greenish yellow reaction was observed under long-wave ultraviolet radiation, and a much weaker greenish yellow reaction was noted under short-wave UV.

Due to the pearl's large size, it was quite intriguing to see the growth

Figure 17. The large round bead cultured pearl weighing 54.96 ct and measuring 19.90 × 19.53 mm.

structure revealed from within. Real-time microradiography (RTX) imaging showed an extremely small bead nucleus together with distinct growth arcs flowing in an even pattern around the nucleus proving it to be a bead cultured (BC) pearl. The exceptional thickness of the nacre growth around the bead was particularly notable (figure 18) (L.M. Otter et al., "A look inside a remarkably large beaded South Sea cultured pearl," Spring 2014 *G&G*, pp. 58–62). The size of the bead and the nacre thickness were measured using an option available on the RTX instrument, resulting in a reading of 6.122 mm for the thickest part of the bead and a range of 5.987 to 6.283 mm, in four different directions, for the overlying nacre. These measurements indicated a composition of more than 96% nacre and less than 4% bead nucleus by volume.

The majority of beads used in the cultivation process of BC pearls are produced from freshwater mollusk shell (*Unionidae*) collected in the United States (A. Homkrajae et al., "Internal structures of known *Pinctada maxima* pearls: Cultured pearls from operated marine mollusks," Fall 2021 *G&G*, pp. 186–205). Due to the high levels of manganese present in freshwater mollusks, such BC pearls would emit a weak or moderate yellowish green fluorescence when subjected to XRF analysis. This reaction is normally based on the size of bead nuclei used in the cultivation process and the thickness of the surrounding nacre. Hence, the reaction observed via XRF for the pearl was relatively weak due to the thickness of its nacre overgrowth (figure 19) (S. Karampelas et al., "Chemical characteristics of freshwater and saltwater natural and cultured pearls from different bivalves," *Minerals*, Vol. 9, No. 6, 2019, article no. 357). Taking all these factors into consideration—external appearance, dimensions, size of the bead nucleus, nacre thickness measurements, and chemistry data—the pearl was classified as a BC pearl produced from the *Pinctada maxima* species.

Over the decades, South Sea BC pearls have played an important part in the global pearl trade. Larger pearls, some more than 20 mm, were also produced, but these are very rare even

Figure 18. RTX images revealing the pearl's internal structure. Left: Diameter of the bead in four directions. Right: The size of the nacre thickness measurements around the bead from its demarcation up to the outer nacre in four directions.

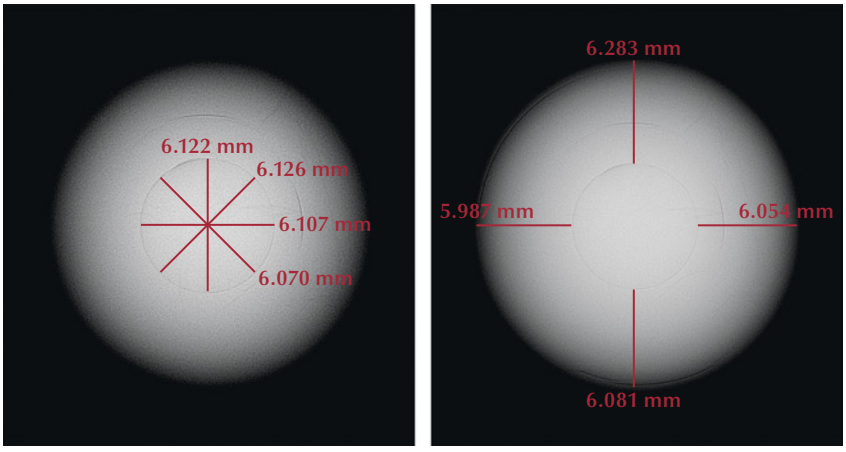

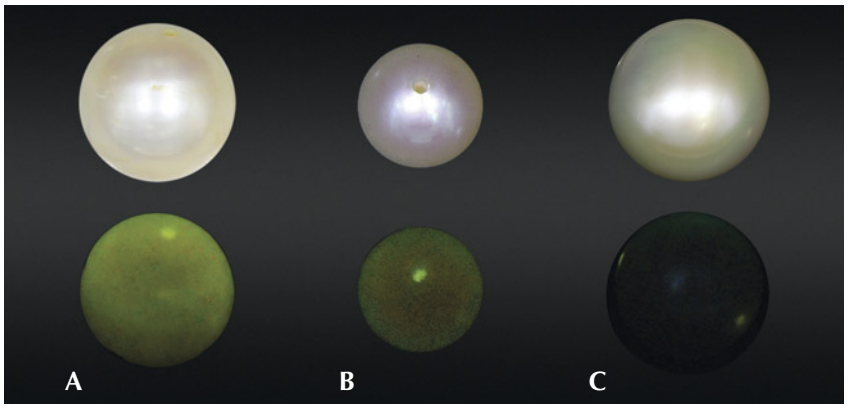

Figure 19. X-ray fluorescence reaction comparison for a freshwater non-bead cultured pearl (A), a saltwater bead cultured pearl with thin to medium nacre thickness (B), and the examined pearl with relatively thick nacre (C).

with today's modern farming methods. Their uniquely large size, silky luster, and greater nacre thickness compared with BC pearls from other mollusks make them more attractive and durable. This has allowed them to establish a prominent position in the cultured pearl value chain as the primary choice of consumers looking for large white to cream, or "golden" BC pearls. As a result, they have been used by renowned jewelry designers in their exclusive collections. GIA continues to test numerous South Sea cultured pearls, and this unique submission to the Mumbai laboratory was particularly notable for its size and fine quality.

Roxane Bhot Jain, Abeer Al-Alawi, and Chunhui Zhou

Fine Linear Structures in Non-Bead Cultured Pearls

Saltwater non-bead cultured (NBC) pearls are defined by the World Jewellery Confederation (CIBJO) as those without an internal bead nucleus that have "formed accidentally or intentionally by human intervention in marine pearl oysters." These are commonly referred to as "keshi" pearls in the trade. GIA's Mumbai laboratory has received many pearl submissions that revealed internal structures typical of NBC pearls such as large voids, elongated linear structures, and some with loose concentric "gaps." However, a recent submission of 23 loose pearls for pearl sorting service proved quite challenging to identify. Externally, all of them looked similar, with a white to light cream color and a medium to high luster. Some possessed a few surface blemishes, but on the whole they were quite clean and appeared cultured.

A majority of the pearls in the lot exhibited concave bases, while a few showed bases with concentric, graduating white to cream-colored rings, with distinct central white frosty patches which were part of the inner subsurface nacreous layers. Four pearls revealing different forms of linear structures were selected from this lot. All were white and button shaped, with sizes ranging from 3.24 × 2.55 mm to 10.33 × 6.84 mm (figure 20). Externally, all their surfaces exhibited typical nacreous overlapping aragonite platelets, with a fingerprint-like pattern when viewed under 40× magnification.

Energy-dispersive X-ray fluorescence spectrometry on the four pearls revealed low manganese levels ranging between 12.60 and 41.10 ppm and high strontium levels between 1767 and 2883 ppm. Additionally, optical X-ray fluorescence analysis yielded an inert reaction, thus confirming their saltwater origin. The pearls showed a moderate bluish green reaction when viewed under long-wave ultraviolet radiation and a weaker bluish green reaction under short-wave ultraviolet radiation. Raman analysis using 514 nm laser excitation showed a doublet at 702 and 705 cm^{-1} and peaks at 1085 and 1463 cm^{-1} indicative of aragonite.

Real-time microradiography (RTX) and X-ray computed microtomography (μ-CT) analysis revealed internal structures that were not straightforward and required more work to reach conclusive results. RTX imaging of pearl 1 showed a prominent, very fine central linear feature horizontal to the base (table 1, row 1). Analysis with μ-CT re-

Figure 20. Four non-bead cultured pearls (samples 1–4, left to right) weighing 0.22 to 4.84 ct.

TABLE 1. Surface appearance and internal structures of four non-bead cultured pearls.

Sample details	Macro image	RTX image	µ-CT image
Pearl 1 0.22 ct 3.24 × 2.55 mm		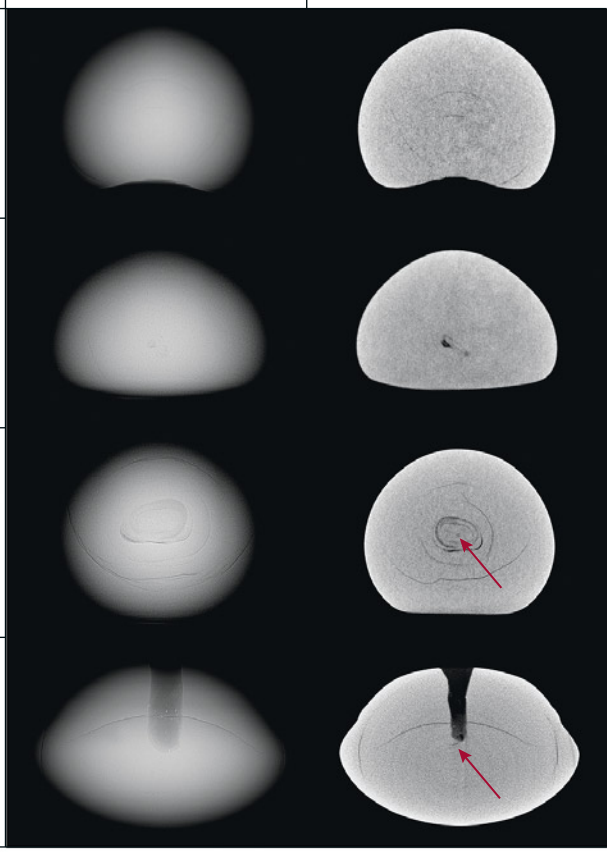	
Pearl 2 0.35 ct 4.10 × 2.81 mm			
Pearl 3[a] 0.81 ct 5.00 × 4.27 mm			
Pearl 4 4.84 ct 10.33 × 6.84 mm			

[a]*The red arrows indicate the identified linear features.*

vealed a more obvious linear feature showing that it was unaligned with the other growth arcs that generally followed the shape of the pearl. This structure was observed in most of the samples in the submitted lot. Externally, a small white frosty central spot was visible on the concave base surrounded by graduating circular rings.

RTX images of pearl 2 revealed a small circular light gray core associated with undefined gray arcs curving along the core in a distorted pattern (table 1, row 2). Moreover, only a couple of weak growth arcs were observed in the outer nacre layers. The structure was very similar to those observed in some natural pearls with small dense cores, making it inconclusive (A. Homkrajae et al., "Internal structures of known *Pinctada maxima* pearls: Cultured pearls from operated marine mollusks," Fall 2021 *G&G*, pp. 186–205). Further µ-CT analysis helped define the main feature, a short and fine linear structure accompanied by a minute void-like feature.

RTX images for pearl 3 revealed a medium-size button-shaped central organic-rich core, which was radiotranslucent and had a thin gray outline (table 1, row 3). This was surrounded by numerous fine growth arcs that followed the shape of the core. Although this organic-rich core looked quite natural from the RTX images, µ-CT images revealed a short linear feature in the center of the core, suggesting an NBC pearl.

The largest sample, pearl 4, had been partially drilled, and the drill hole was quite large (table 1, row 4). It was unlike the thinner and shorter drill holes often used for weight retention in natural pearls. While the choice of drill hole thickness is not decisive evidence on its own, it may be a useful indicator (Spring 1986 Lab Notes, pp. 51–52; Summer 1986 Lab Notes, p. 111). Externally, the pearl had a rounded base and a circled circumference with multiple deep indentations associated with the circled grooves. The RTX images showed minute metal remnants (visible as radiopaque white specks) within the drill hole and extensive curved growth arcs throughout the pearl, with additional arcs located on adjacent boundaries. The pearl showed minimal tight growth structure, and its external appearance aroused suspicion. Further examination via µ-CT analysis revealed a small linear feature that had been partially removed by the drilling.

Reaching a conclusion would be very challenging, if not impossible, using RTX analysis alone.

Given the volume of button-shaped pearls the Mumbai laboratory has been testing, it is quite evident that large quantities of such pearls are circulating in the market. These pearls mostly have smooth surfaces and high untreated luster. The linear features could not be identified in all the pearls using RTX alone due to a number of factors including size, appearance, radiotranslucency, and orientation. It is not difficult to remove minute linear structures by drilling, and such pearls could easily be passed off as natural due to the presence of fine growth features around the center. But with the availability of advanced technology, especially μ-CT imaging, remnants of the linear structure were evident in certain orientations. In some cases, with the proper alignment of the drill hole, such small linear structures may also be visible in the RTX images. This requires considerable skill and patience to align, starting from the thickest direction first with respect to the shape of the pearl and then repositioning the same pearl 90° in the profile view. Therefore, it may be risky to rely on RTX results alone (S. Karampelas et al., "X-ray computed microtomography applied to pearls: Methodology, advantages, and limitations," Summer 2010 *G&G*, pp. 122–127).

By analyzing these challenging internal structures using modern equipment, GIA and other laboratories aim to protect consumers by creating awareness of them and minimizing the chances of misidentification.

Gauri Sarvankar, Abeer Al-Alawi, Karan Rajguru, and Roxane Bhot Jain

Figure 21. An imitation emerald in the form of a chess knight measuring approximately 35.05 mm in height.

Figure 23. An assemblage of plastic and various minerals imitating rough emerald in matrix, measuring approximately 51.79 mm in height.

PLASTIC Imitations of Emerald

GIA's New York laboratory recently examined two imitations, each submitted for an emerald identification report, that might have been convincing to the untrained eye. One was a chess piece weighing 46.55 ct (figure 21). At a glance, the knight appeared to be carved emerald with remnants of metallic yellow "matrix" still intact. However, the low heft and relatively warm feel of the piece suggested otherwise. Microscopic examination revealed an aggregate structure composed of jagged blocks, clearly illustrated under long-wave ultraviolet light due to its marked whitish fluorescence, typical of plastic (figure 22). The presence of gas bubbles and bluish dye concentrations indicated that the material was in fact an assemblage. The lack of a polished surface prevented a refractive index reading. Infrared and Raman spectroscopy were used to identify the main component as plastic; no beryl was detected. The metallic yellow crystal fragments were identified as pyrite, consistent with matrix associated with natural emeralds, notably those from Colombia.

The second imitation emerald (figure 23) was in the form of an elongated hexagonal "rough" emerald crystal embedded in a "matrix" of white and metallic yellow crystals, with a total weight of 179.71 ct. It too appeared natural to the unaided eye, but microscopic examination quickly distinguished the specimen as an imitation.

Figure 22. A closer look at the knight's head (left, in daylight) reveals the material's aggregate structure when viewed under long-wave ultraviolet light (right).

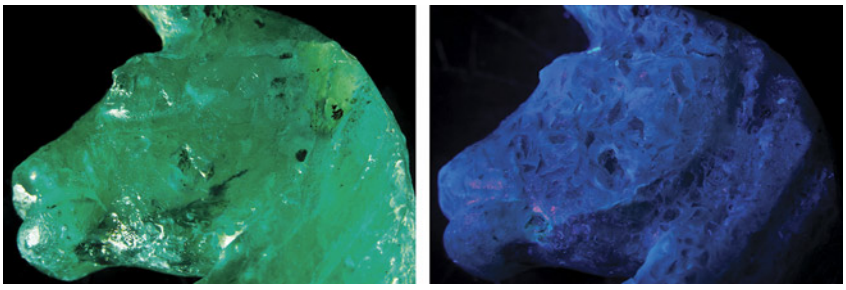

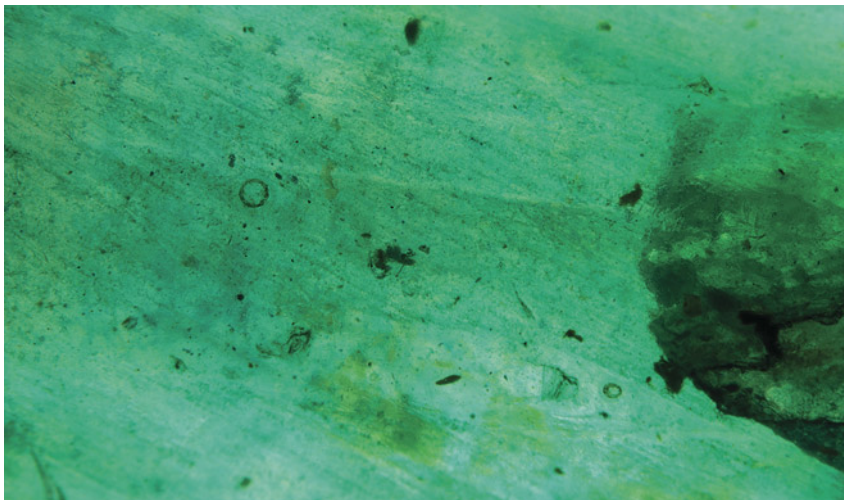

Figure 24. Gas bubbles and bluish green dye concentrations indicate that this "crystal" is in fact a manufactured product. Field of view 8.23 mm.

Figure 25. An exceptional pink zektzerite, cut as a square modified step cut, measuring 8.08 × 7.39 × 6.89 mm and weighing 2.95 ct.

The "emerald" portion of the rough contained large gas bubbles as well as bluish green dye concentrations (figure 24), an overall blotchy color appearance, and parallel surface striations. This material was identified as plastic using Raman and infrared spectroscopy. The surface striations were presumably created in the mold or carved to resemble the texture of a rough emerald crystal. Raman spectroscopy revealed that the smaller crystals mixed into the plastic were quartz and beryl. The white portion of the "matrix" was identified as calcite and the metallic crystals as pyrite, making this piece another convincing imitation of Colombian emerald.

The natural materials incorporated into these mostly plastic manufactured products might lead some astray upon first inspection. These two pieces demonstrate the need for a deeper inspection of all materials, regardless of how genuine they may seem on the surface.

Emily Jones and Abadie Ludlam

Pink ZEKTZERITE

Zektzerite, a member of the tuhualite group, is a very rare collectible mineral currently mined from only two sources: Okanogan County in the U.S. state of Washington (Spring 2011 Gem News International, p. 61), and the Darai-Pioz Valley in Tajikistan (L.A. Pautovet et al., "Zektzerite—occurrence in Tadzhikistan," *Mineralogicheskii Zhurnal*, Vol. 14, pp. 75–78). With the chemical formula $NaLiZrSi_6O_{15}$, these rare crystals are found in miarolitic cavities in riebeckite granite, along with many other rare minerals. The zektzerite crystals found in these locations are primarily between 4 mm and 15 mm and usually yield small faceted gems weighing less than 2 ct. This material is typically found with a low transparency and muted color saturations. Perfect cleavage in two directions and a brittle tendency make this fragile stone very difficult and risky to cut. Due to its low durability and overall dull appearance, collectors tend to leave zektzerite in its natural rough state.

An outstanding example of faceted gem-quality zektzerite (figure 25) was recently submitted to GIA's Carlsbad laboratory. The stone weighed 2.95 ct, measured 8.08 × 7.39 × 6.89 mm, and had a refractive index ranging between 1.578 and 1.584. A specific gravity of 2.81, along with Raman and infrared spectroscopic testing, all matched zektzerite, with no indication of dye or polymers. The outstanding pink color, relatively high clarity, and impressive size of this stone sets this specimen far above any other faceted zektzerite previously reported.

Jamie Price

PHOTO CREDITS
Towfiq Ahmed—1; Jessa Rizzo—2; Annie Haynes—3; Jemini Sawant—4, 12; Shiva Sohrabi—5; Johnny (Chak Wan) Leung—6, 8; Tsz Ying Fong—7; Ka Wing Tam—9, 11; Gaurav Bera—13, 14 (left), 15, 17, 19, 20; Kristin Reinheimer—21; Emily Jones—22; Michele Wong—23; Abadie Ludlam—24; Diego Sanchez—25

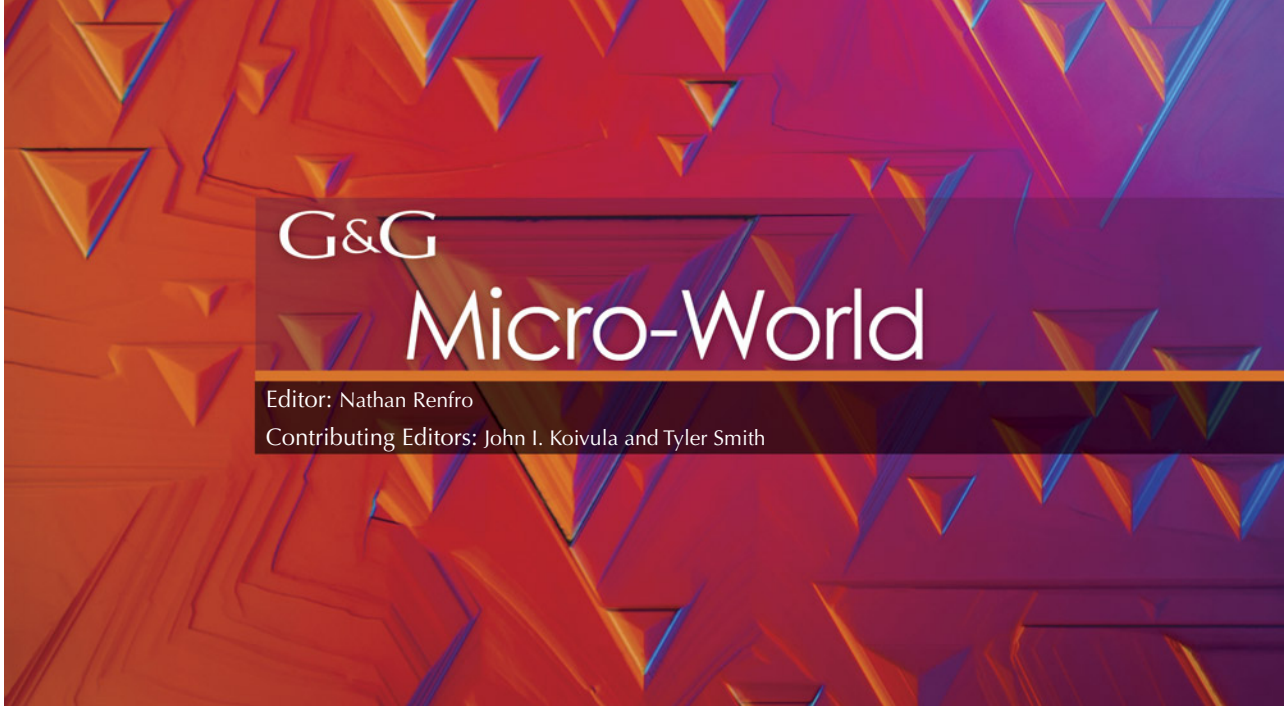

Internal World of Aquamarine from Xinjiang

The authors recently examined a batch of aquamarine samples from the Xinjiang autonomous territory of China. Microscopic observation revealed rich and colorful features.

The aquamarines contained yellow-brown to black-brown inclusions. Microscopic observation and further Raman analysis confirmed that these dot-like, flaky, and dendritic yellow-brown to black-brown inclusions were hematite. Interestingly, when observed with a microscope using LED white light illumination, the hematite inclusions appeared to extend from the center to the periphery, and the overall hexagonal shape resembled a rose floating on a calm sea (figure 1).

Colors generated by interference phenomena are very common in gemstones. A number of thin-film liquid inclusions were seen in the aquamarines, along with the spectral interference color phenomenon parallel to the *c*-axis (figure 2). Many disk-shaped inclusions (figure 3) were also found. Stress fractures were caused by solid inclusions in the middle to the surrounding areas, and tubular fractures extended in the direction perpendicular to the disk-shaped fractures. The disks were filled with thin films of

Figure 1. Hematite inclusions extend from the center of an aquamarine sample from Xinjiang, China. Photomicrograph by Yubing Chen; field of view 3.64 mm.

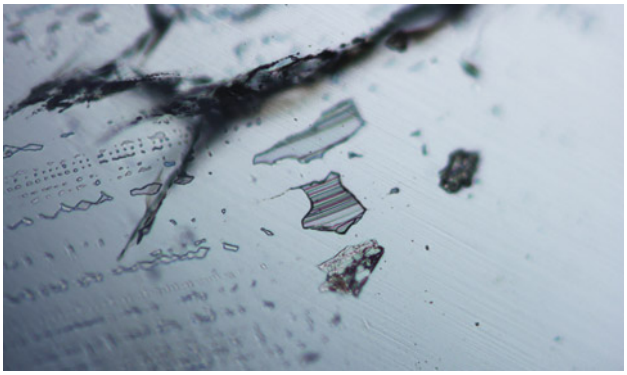

Figure 2. Thin-film liquid inclusions and visible internal tubes parallel to the c*-axis with spectral interference colors were observed in the aquamarine samples. Photomicrograph by Yubing Chen; field of view 0.70 mm.*

About the banner: Triangular etch features known as "trigons" are often seen on the surfaces of rough diamond crystals such as those shown here using differential interference contrast microscopy. Photomicrograph by Nathan Renfro; field of view 1.1 mm.

GEMS & GEMOLOGY, VOL. 59, NO. 2, pp. 222–231.

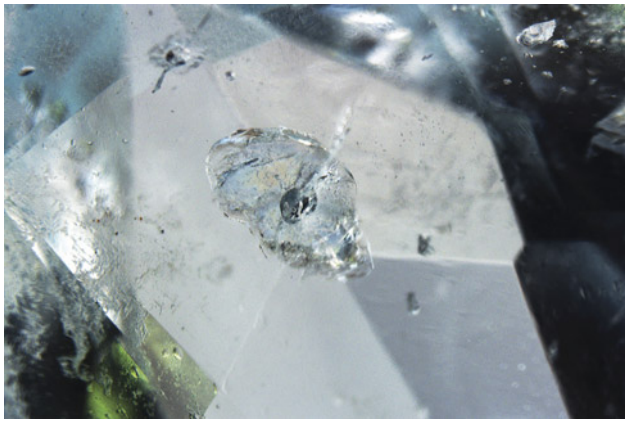

Figure 3. Disk-shaped fissures in the aquamarine were caused by solid inclusions in the middle with tubular fissures extending inward. Photomicrograph by Yubing Chen; field of view 1.50 mm.

liquid, and the interference phenomenon could be seen under the microscope using oblique fiber-optic illumination. The entire disk-shaped inclusion resembled a jellyfish floating in the sea.

Yubing Chen, Jun Shu, Yanling Wang, and Qishen Zhou
Gemmological Institute
China University of Geosciences, Wuhan

Clinochlore and Muscovite in Quartz from Colorado

Recently the author encountered a parcel of quartz with phantom layers consisting of beautiful bluish green and white spheres (figure 4). Raman analysis identified the green spheres as clinochlore (figure 5), $Mg_5Al(AlSi_3O_{10})(OH)_8$, a member of the chlorite group. Many of the white orbs appeared to be secondarily altered, presumably by fluids entering through fractures in the quartz host, though some showed no clear evidence of alteration. Raman analysis of one of the unaltered white spheres identified it as muscovite, $KAl_2(AlSi_3O_{10})(OH)_2$. Minute dark brown to black spheres were also present and visually consistent with hematite, but that could not be confirmed by Raman analysis.

This material is from Larimer County, Colorado, where it was collected in 2020 by Nico Jackson. So far, three pockets of material have been discovered, with a total production of about 10 kg. While chlorite-group minerals are relatively common inclusions in quartz, the soft texture and greenish blue color of these clinochlore spheres are less common in the author's experience. These green clinochlore spheres with contrasting white muscovite spheres are a striking addition to the possible minerals seen in the micro-world of quartz.

Nathan Renfro
GIA, Carlsbad

Figure 4. This quartz crystal cluster from Larimer County, Colorado, contains numerous bluish green and white spherical inclusions on phantom growth planes. Photo by Annie Haynes; courtesy of Nico Jackson.

An Iridescent "Insect Wing" in Diamond

Diamond is very resistant to scratching and is often referred to as the hardest mineral on Earth due to its compact crystal structure. However, diamond is not indestructible,

Figure 5. These bluish green spheres in the quartz crystal were identified as clinochlore, and the white spheres were identified as muscovite. Photomicrograph by Nathan Renfro; field of view 4.23 mm.

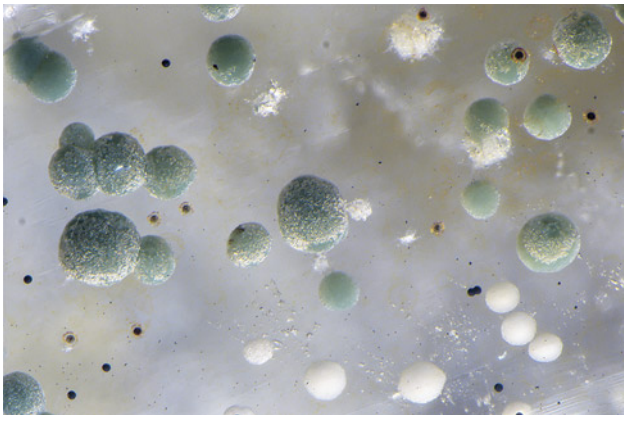

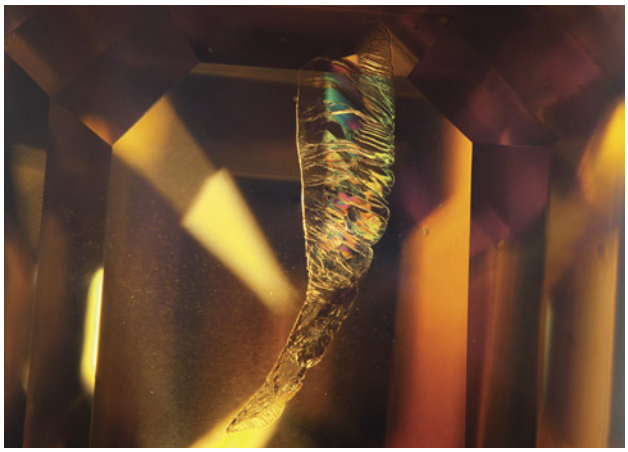

Figure 6. A subsurface feather in diamond resembling an insect wing, with visible iridescence caused by thin-film interference. Photomicrograph by Matthew Hardman; field of view 2.90 mm.

and it can be fractured or even broken apart during ascent from the mantle to the earth's surface through fast, violent kimberlite eruption. Collision with rocks in high-energy rivers also results in percussion marks on the surface of alluvial diamonds (e.g., J.W. Harris et al., "Morphology of monocrystalline diamond and its inclusions," *Reviews in Mineralogy and Geochemistry*, Vol. 88, No. 1, 2022, pp. 119–166). Surface cracks extending into the interior of a diamond are referred to as "feathers" in the gem trade, and these often have a negative effect on the clarity grade.

Fractures within diamond can cause fascinating optical phenomena on rare occasion. The authors recently examined a 0.39 ct Fancy Deep brownish yellowish orange type Ib/IaA diamond containing multiple feathers and graded as I_2 clarity. These natural features had not been filled with a clarity-enhancing material. The largest feather located on the table facet of the diamond resembled an iridescent insect wing (figure 6).

Iridescence is an optical phenomenon caused by interference of light, typically seen in gemstones with cleavage or repeating submicroscopic structures (e.g., X. Lin and P.J. Heaney, "Causes of iridescence in natural quartz," Spring 2017 *G&G*, pp. 68–81). In this diamond, the feather's iridescence was due to thin-film interference caused by a thin film of air with a thickness similar to the wavelength range of visible light. As diamond and air have very different refractive indices, there is a phase difference between the incident light reflected from the upper and lower boundaries of the thin film, resulting in constructive and destructive interference. When viewed using a broadband light source (light consisting of a wide range of wavelengths), constructive or destructive interference intensifies or attenuates certain wavelengths (colors), respectively, producing a rainbow-like interference pattern.

Mei Yan Lai and Matthew Hardman
GIA, Carlsbad

Patchy Yellow Trigon

Occasionally, diamonds show irregularity in their color related to heterogeneous distribution of atomic-level defects. "Yellow-skin" diamonds are evidence of this. Seen in figure 7 is the rough surface of a 0.98 ct diamond that shows a trigon with patchy yellow coloration. The yellow color is caused by isolated nitrogen that is confined to the outer surface of the rough stone, making it look like the rough diamond has a "yellow skin."

Yellow diamonds colored by isolated nitrogen are known to have uniform to patchy or irregular color zoning (more information on naturally colored yellow and orange diamonds can be found in C.M. Breeding et al., "Naturally colored yellow and orange gem diamonds: The nitrogen factor," Summer 2020 *G&G*, pp. 194–219). The color zoning (or lack of) correlates with the distribution of the nitrogen in the diamond's crystal lattice as it grows. It is theorized that the "yellow skin" is from a subsequent growth event, making it younger than the colorless diamond it surrounds.

Nicole Ahline
GIA, Carlsbad

Rainbow Mountain in Natural Diamond

At GIA, we occasionally see diamonds with inclusions that resemble natural objects. A breathtaking example was recently observed in a 1.71 ct, H-color, I_2-clarity natural diamond. The deep feather in figure 8 (top) shows an iridescence feature resembling Montaña Arcoíris (Rainbow Mountain) in the Andes Mountains of Peru (figure 8, bottom). Thirty years ago, a diamond with a similar feature (Summer 1993 Lab Notes, pp. 123–124) was described as having iridescence due to a thin-film separation caused by a "V"-shaped dislocation.

Figure 7. Trigons creating the impression of a thin and patchy "yellow skin" on a 0.98 ct rough diamond. Photomicrograph by Nicole Ahline; field of view 2.34 mm.

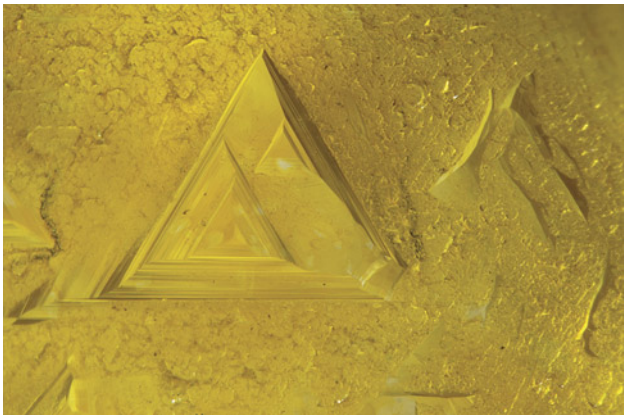

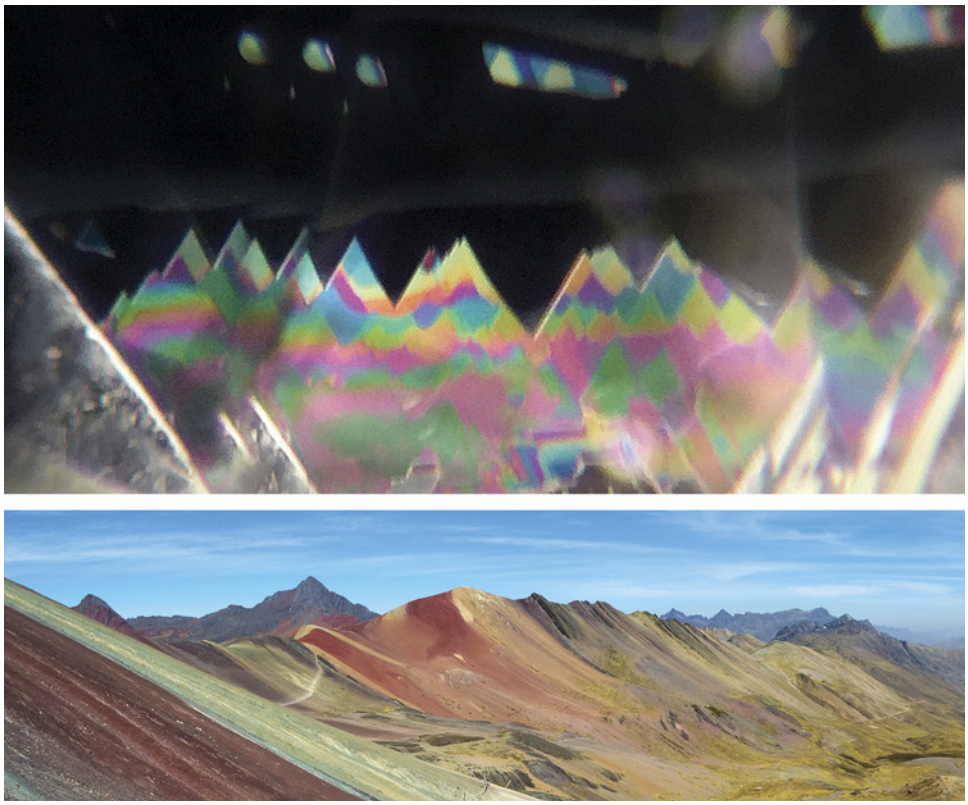

Figure 8. These iridescence features observed in a 1.71 ct natural diamond (top) were reminiscent of Rainbow Mountain in Peru (bottom). Photomicrograph by Tejas Jhaveri; field of view 2.90 mm. Bottom photo courtesy of Daniel Sánchez Ibarra (Wikimedia Commons).

As with the previously described diamond, the iridescence in this diamond is only visible at some orientations. This memorable effect showcases the beauty of the natural world within the diamond.

Tejas Jhaveri
GIA, Mumbai

Sally Eaton-Magaña
GIA, Carlsbad

Musical Diamond

Recently the author examined a 0.95 ct diamond with a special note. It only took one and a half beats to discover a dark crystal with a straight stress cleavage crack shaped like a dotted quarter note (figure 9).

Crystals, cleavages, and other inclusions are common occurrences that impact a diamond's clarity grade. This diamond received a clarity grade of SI_1, or slightly included with inclusions noticeable to a skilled grader at 10× magnification.

Michaela Damba
GIA, Carlsbad

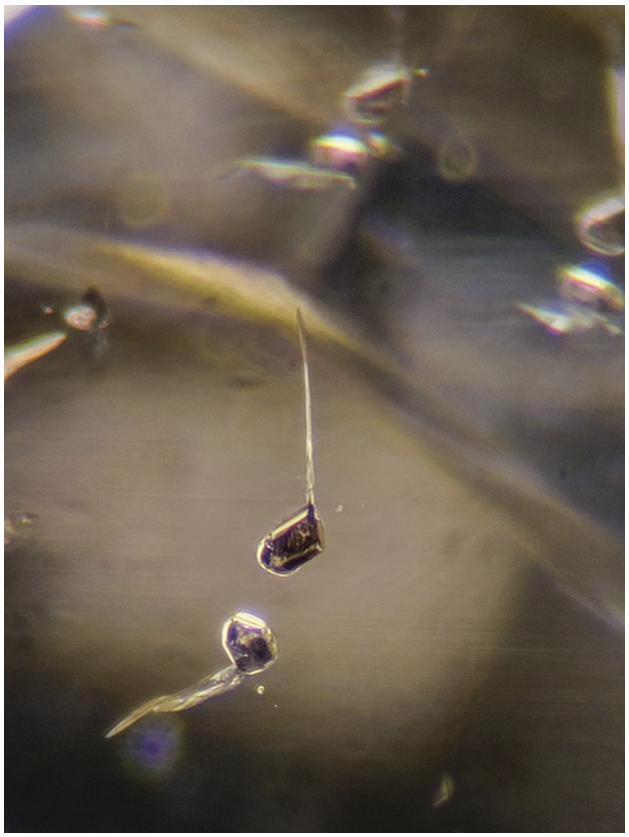

Figure 9. A crystal with a stress halo and a smaller adjacent crystal resembles a dotted quarter note. Several reflections of such crystals with stress fractures are visible. Photomicrograph by Michaela Damba; field of view 2.90 mm.

Figure 10. This "snail" inclusion was viewed through the upper half facet of a 4.00 ct near-colorless diamond. The purple-red "shell" was identified as pyrope garnet, while the green "body" was determined to be diopside. Photomicrograph by Christopher Vendrell; field of view 1.99 mm.

"Snail" in Diamond

While different types of inclusions often occur independently within diamond, it is quite rare to find more than one occurring simultaneously, let alone in contact with each other. In figure 10 we have a unique example of a purple-red pyrope garnet crystal and green diopside crystal suspended together, having been captured within this natural 4.00 ct near-colorless diamond during formation. Such inclusions can be utilized to verify what environment a diamond may have formed in. In this case, the diamond's genesis was likely in an ultramafic peridotite environment. The appearance of this unique inclusion series is playfully reminiscent of a snail.

Christopher Vendrell
GIA, New York

Guest in Garnet: Metal Sulfide?

Recently a faceted garnet containing a striking inclusion came across the author's desk. The solid inclusion was opaque with a metallic luster and had an uneven surface containing numerous sharp protrusions (figure 11). Al-

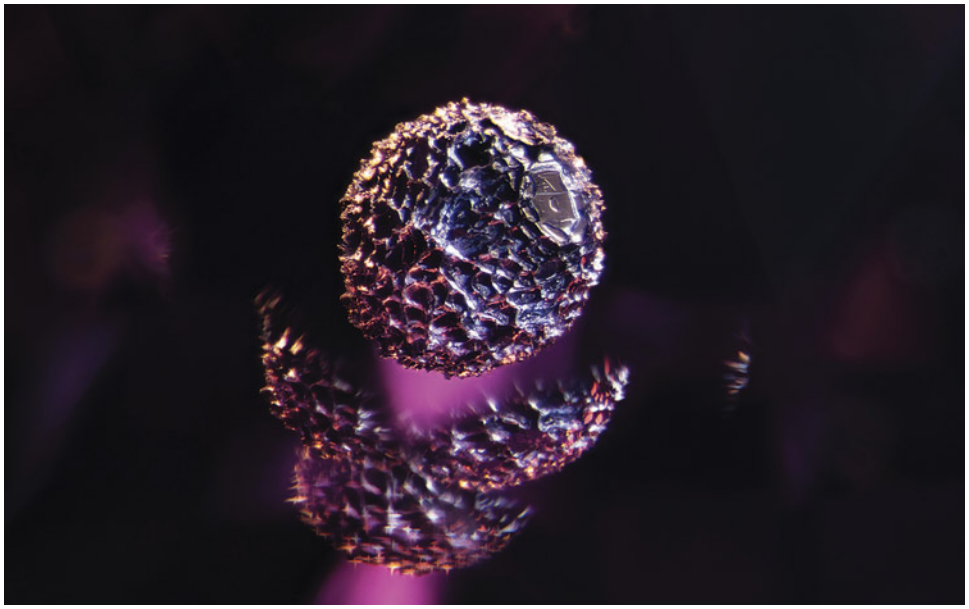

Figure 11. An opaque crystal, likely a metal sulfide, is suspended in a garnet. A combination of darkfield and oblique fiber-optic illumination makes it appear as though the crystal is hovering inside the stone. Portions of the inclusion are duplicated because of its split across several facet junctions, adding to the visual interest. Photomicrograph by E. Billie Hughes; field of view 4 mm.

though we were unable to definitively identify the inclusion, its opaque dark nature and crenulated texture were consistent with a metal sulfide crystal.

This inclusion scene inspired a variety of imaginative comparisons at our laboratory. Some thought it was reminiscent of the fire-breathing piranha plants from the Super Mario franchise, while others suggested it resembled a Ferrero Rocher chocolate. Regardless of what we might see in this piece, it is certain that we will continue to be fascinated by the delightful whimsy of Mother Nature's micro-world.

E. Billie Hughes
Lotus Gemology, Bangkok

Pink Sapphire with Graphite Inclusion

Graphite inclusions in corundum can occur as minute bodies inside negative crystals alongside trapped diaspore and carbon dioxide. They can also appear as separate large metallic-looking hexagonal plates or jumbled clusters of small flaky crystals. Graphite in sapphire commonly occurs in those from Sri Lanka or Batakundi, Pakistan (V. Pardieu et al., "Sapphires reportedly from Batakundi/Basil area," *GIA Research News*, May 12, 2009). The author recently found a surprisingly well-formed hexagonal graphite platelet with surface etchings in a pink sapphire from Sri Lanka (figure 12). Taking into account the luster and structure of the inclusion in this particular stone, it was identified as graphite under the microscope.

Graphite is a stable form of layered carbon occurring as a submetallic opaque mineral with a black to steel-gray color range. It typically forms in carbon-rich metamorphic rock or in pegmatite. Formation of this inclusion is dependent on the grade of metamorphism and temperature in the growth environment. It is rare to find such a clean example of a singular graphite inclusion demonstrating the crystal system it belongs to. This graphite inclusion in pink sapphire was a remarkably pristine example of this inclusion and host relationship.

Jeffrey Hernandez
GIA, Carlsbad

Night Sky in Yellow Sapphire

Fractures are usually not desired in gemstones, but in some cases they provide a great subject for photomicrography. When a 2.49 ct yellow sapphire from Ilakaka, Madagascar, was examined with a fiber-optic light, the scene in figure 13 was revealed. It is reminiscent of a long-exposure photograph of a star-filled sky with an extraterrestrial object floating in it. In reality, this is a globular iron stain in a large fracture, but the spotted iron staining evokes a faraway planet. The colorful curved lines are conchoidal patterns in the fracture. The combination of features makes the image seem as if viewed through a telescope rather than a microscope.

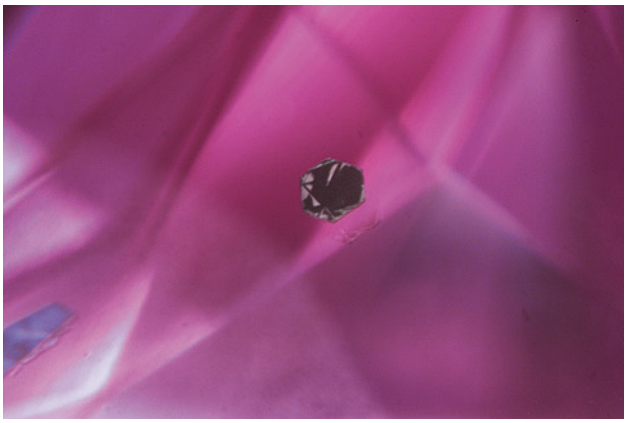

Figure 12. This pristine hexagonal platelet of graphite was seen in a pink sapphire from Sri Lanka. Photomicrograph by Jeffrey Hernandez; field of view 1.99 mm.

Illumination is very important for capturing the iridescence effect. Only if a strong fiber-optic light is used at the correct angle relative to the fracture will the colorful curved lines be highlighted.

Charuwan Khowpong
GIA, Bangkok

An "Eye" on a Tridacninae Pearl

The Tridacninae subfamily of giant saltwater clams consists of two genera: *Hippopus* and *Tridacna*. These bivalve

Figure 13. This scene of an iron stain and numerous curved lines showing rainbow colors in a fracture resembles a scene from the night sky viewed through a telescope rather than a microscope. Photomicrograph by Charuwan Khowpong; field of view 2.85 mm.

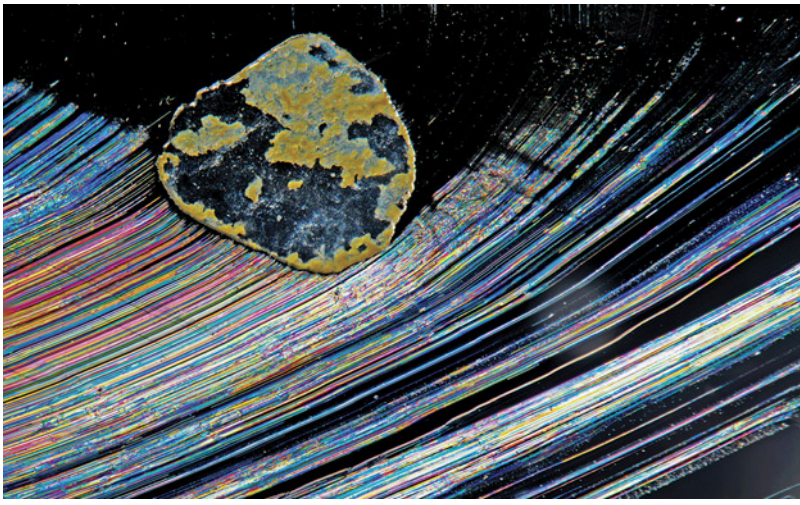

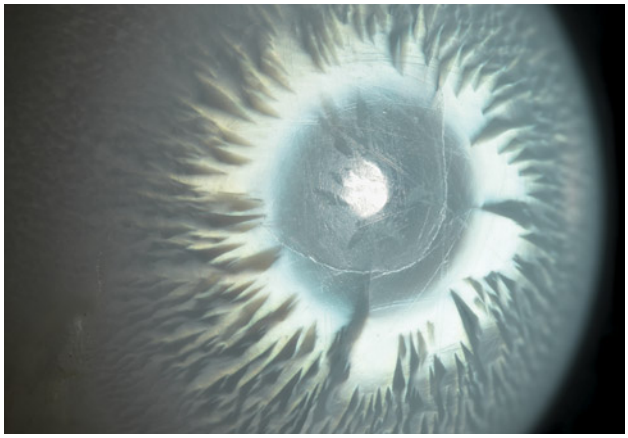

Figure 14. A 4.77 ct near-round white Tridacninae pearl exhibited an attractive sheen-like flame structure in a pattern resembling an eye when viewed in certain directions under a single white light source. Photomicrograph by Ravenya Atchalak; field of view 7.20 mm.

mollusks live only in the shallow waters of coral reefs in the tropical parts of the Indo-Pacific Ocean (E. Strack, *Pearls*, Rühle-Diebener-Verlag, Stuttgart, 2001, p. 60). They are known to produce white to cream non-nacreous pearls, with yellow or orange pearls less commonly found. Tridacninae pearls frequently exhibit a porcelain-like surface with a flame structure caused by stacked layers of aragonite lamellae in a crisscross fashion. The sheen-like effect occurs when those lamellae interact with light (H.A. Hänni, "Explaining the flame structure of non-nacreous pearls," *Australian Gemmologist*, Vol. 24, No. 4, 2010, pp. 85–88). Pearls with such characteristics are known as porcelaneous pearls.

A 4.77 ct near-round white Tridacninae pearl (figure 14) recently examined by the author displayed a well-arranged flame structure consisting of a wide base with spiky ends radiating outward from the apex of the pearl. Microscopic examination under fiber-optic light revealed a remarkable feature. A dramatic pseudo-chatoyancy occurred over the luminous flames, creating the appearance of an eye staring back at the observer. Pearls with prominent flame structures and high sheen often contain striking features.

Ravenya Atchalak
GIA, Bangkok

Ancient Script-Like Serpentine in Brown Peridot

Peridot is a green olivine often characterized by "lily pad" inclusions and high birefringence causing a doubling effect. Apart from its familiar green hue, peridot can also possess a brown color, though these gems receive little attention.

Recently, the author found a xenocryst of peridot from southeast Vietnam that appeared black in daylight and brown through a transmitted light source. Standard gemological testing of a cabochon (2.51 ct) and two faceted stones (2.35 and 4.65 ct) that were cut from this xenocryst indicated peridot, but the specific gravity and refractive index gave higher results than the values for green peridot. Finally, the Raman spectra confirmed the identification as peridot.

Microscopic examination did not reveal any typical "lily pad" inclusions. Instead, there were innumerable fascinating thread-like inclusions (figure 15). Some formed closed loops with round, oval, and distorted shapes measuring from a few nanometers to a millimeter. Others stretched or twisted together like tangled threads up to 2 mm long. The display was reminiscent of an ancient script.

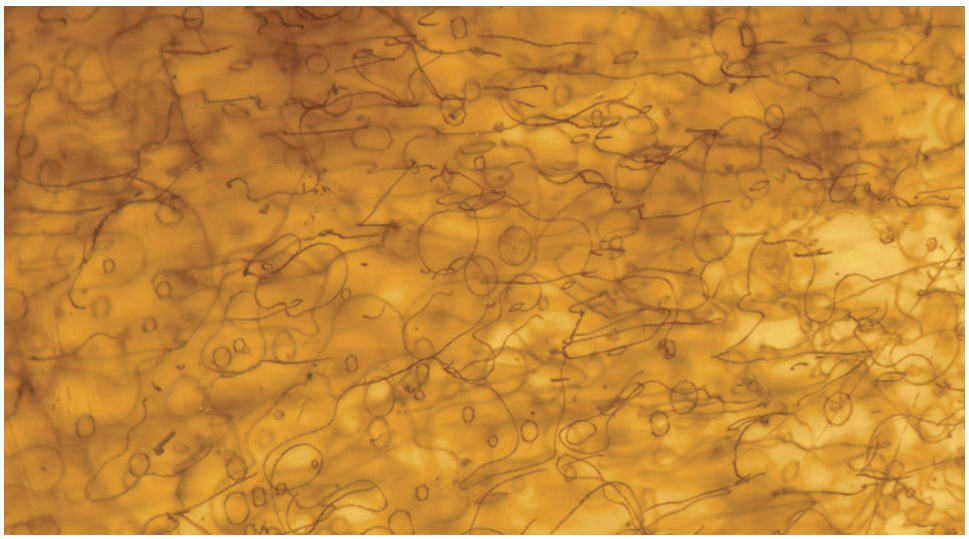

Figure 15. Thread-like inclusions of serpentine resembling an ancient text. Photomicrograph by Le Ngoc Nang; field of view 2.50 mm.

Figure 16. A 2.52 ct oval modified brilliant Paraíba tourmaline. Photo by Adriana Gudino.

Micro-Raman spectral analysis revealed these thread-like inclusions were serpentine.

Examination of this brown peridot revealed an unexpected inclusion scene quite different from the common inclusions found in green peridot.

Le Ngoc Nang
University of Science, Vietnam National University
Ho Chi Minh City
Liu Gemological Research and Application Center

Interesting Metallic Platelets in a Brazilian Paraíba Tourmaline

The authors recently examined the 2.52 ct saturated green oval modified brilliant shown in figure 16. The gemological properties, as well as trace element analysis using laser ablation–inductively coupled plasma–mass spectrometry, confirmed this gem was a Paraíba tourmaline from Brazil.

Microscopic observation revealed interesting metallic dark gray dendritic inclusions (figure 17). The metallic inclusions were similar in shape to previously documented native copper inclusions in Paraíba tourmaline (E.J. Gübelin and J.I. Koivula, *Photoatlas of Inclusions in Gemstones, Volume 1*, 2008, Opinio-Verlag Publishers, Basel, Switzerland, p. 167). Metallic inclusions with a dendritic pattern and similar brassy color in a Brazilian Paraíba tourmaline were previously identified as native copper (F. Brandstätter and G. Niedermayr, "Copper and tenorite inclusions in cuprian-elbaite tourmaline from Paraíba, Brazil," Fall 1994 *G&G*, p. 181). Because the inclusions in figure 17 are different in color from those previously documented, they are probably not copper. However, Raman analysis was unsuccessful in identifying them. Based on their morphology and color, the authors speculate they could be ilmenite, which has been observed as skeletal inclusions of a similar color in gems such as emerald. These are the first examples of dark gray skeletal metallic inclusions the authors have encountered in a Paraíba tourmaline.

Shiva Sohrabi and Amy Cooper
GIA, Carlsbad

Triplite Inclusions in Quartz from Yaogangxian, China

Quartz is host to a wide variety of inclusions. Recently, the authors examined a 30.80 ct transparent faceted quartz with several pinkish orange crystal inclusions, from the town of Yaogangxian in Hunan Province, China (figure 18). This quartz was cut from a rough stone collected by a local miner. In this quartz, the pinkish orange inclusions were unique and attractive.

Figure 17. Left: The skeletal formation that usually indicates very rapid growth of the mineral. Right: Skeletal formations showing a cross-hatch pattern. Photomicrographs by Shiva Sohrabi; fields of view 1.26 mm (left) and 2.95 mm (right).

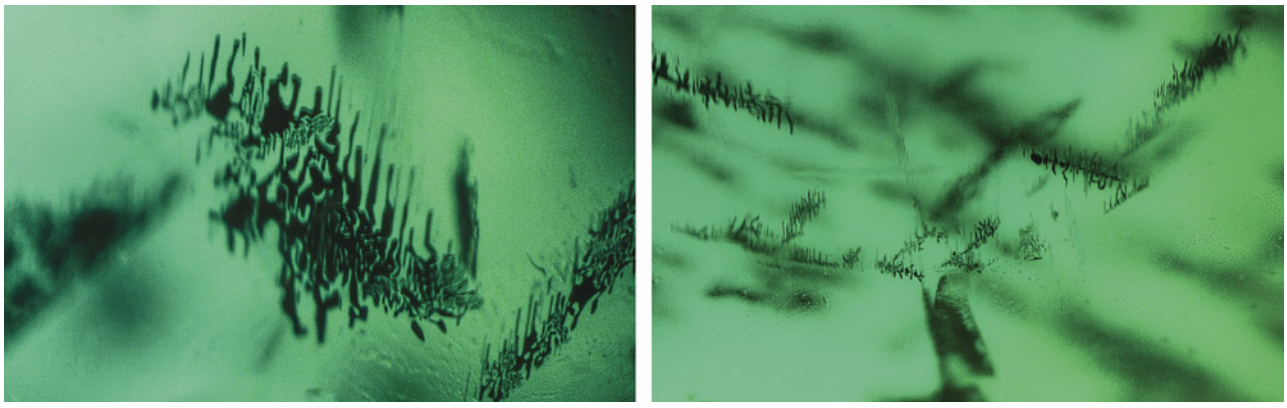

Figure 18. A 30.80 ct faceted quartz containing pinkish orange inclusions. Photo by Hongtao Shen; courtesy of Jinrui Dong.

Figure 19. Magnification of pinkish orange triplite in a transparent quartz from Yaogangxian in Hunan Province, China. Photomicrograph by Hongtao Shen; field of view 11.15 mm.

After grinding, one of these inclusions was exposed to the surface (figure 19). Raman spectroscopy and energy-dispersive X-ray fluorescence were used to identify the inclusion as triplite.

Triplite, $(Mn^{2+},Fe^{2+})_2PO_4(F,OH)$, is a rare phosphate mineral that can be found as either a gem material or an inclusion. Most triplites are produced in pegmatite, as with quartz. Triplite inclusions have been reported in topaz (Summer 2016 *G&G* Micro-World, p. 205) and beryl (Spring 2020 *G&G* Micro-World, p. 145). To the best of our knowledge, this is the first discovery of triplite as an inclusion in quartz.

Qian Zhang and Xingtong Li
Gemmological Institute
China University of Geosciences, Wuhan

Hongtao Shen
State Key Laboratory of Geological Processes and Mineral Resources
China University of Geosciences, Wuhan

Quarterly Crystal: Geocronite in Fluorite

A tight crystal cluster of bright apple-green fluorite and opaque silvery gray geocronite, $Pb_{14}(Sb,As)_6S_{23}$, was recently examined for this edition of Quarterly Crystal. The specimen shown in figure 20 measured 29.60 × 23.84 × 18.35 mm, and the fluorite portion played host to several small, well-formed monoclinic crystals, all situated near the surface. The crystals appeared to be geocronite, a very rare sulfide containing lead, antimony, and arsenic.

The specimen was obtained from Luciana Barbosa of Barbosa Minerals (Asheville, North Carolina). It came from a recent discovery at the Milpo mine in the Atacocha mining district of Pasco Province, Peru. The Milpo mine is known to produce fluorite crystals with inclusions of various sulfides. Since the fluorite and geocronite are intimately intergrown, the opaque silvery gray bodycolor of the inclusions in the fluorite, together with their monoclinic appearance shown in figure 21, strongly suggested geocronite.

The next logical step was laser Raman microspectrometry. Using this technique, we conclusively identified the inclusions as geocronite, thereby confirming our suspicions. It should be noted that, to the authors' knowledge, this is the first time geocronite has been identified as an inclusion in any mineral.

John I. Koivula and Nathan Renfro
GIA, Carlsbad

Figure 21. A combination of optical microscopy and Raman analysis identified the opaque silvery gray monoclinic inclusions as the very rare sulfide geocronite. Photomicrograph by Nathan Renfro; field of view 2.39 mm.

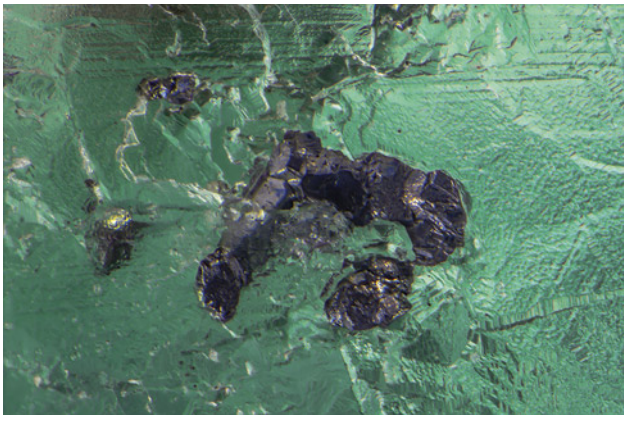

Figure 20. This 29.60 × 23.84 × 18.35 mm cluster of well-formed isometric fluorite and monoclinic geocronite crystals was recently discovered at the Milpo mine in Peru. Photo by Annie Haynes.

Gems Formed in Metamorphic Rocks

Over the eons, the interminable shifting of Earth's landmasses has dramatically altered the appearance of our planet's surface. The existence of ancient supercontinents such as Gondwana and Rodinia has fascinated the public since the concept of "plate tectonics" became widely accepted in the geological community in the 1960s. However, the gradual shifting of tectonic plates is of more than just "cosmetic" importance. The entire evolution of the Earth system is intricately related to tectonic activity, from the development of life on Earth to the creation of gemstone deposits. A previous installment of this column focused on gemstones produced through magmatic processes, which are associated with and controlled by tectonic processes. These tectonic forces also produce gemstone deposits by another process called *metamorphism*. In this process, gems form in the solid state in very specific situations when certain rocks experience an increase in pressure and temperature during tectonic events, with preexisting minerals no longer being stable and being replaced by new ones. This edition of Colored Stones Unearthed will focus on metamorphic gemstones.

Introduction to Metamorphism

The term *metamorphism* derives from the Greek *meta* meaning "change" and *morphos* meaning "form." The process of metamorphism describes changes in the mineralogical and/or structural form of rocks in the earth's crust. Generally, this happens with increased temperature and/or pressure in the earth. Metamorphism is part of the so-called rock cycle involving igneous, sedimentary, and metamorphic rocks (figure 1). Any of these rock types can be transformed into one of the others by processes of melting and solidification (igneous), erosion and deposition (sedimentary), or increased pressure and temperature (metamorphic).

One of the more obvious ways in which metamorphism can be observed is in the physical appearance of a rock. At low pressure and temperature, rocks exposed to stress undergo brittle deformation, meaning they will break or fracture. However, at high pressure and temperature, exposure to directional stress in the earth can cause rocks to behave more plastically, even folding up into themselves, such as the limestone and chert layers in figure 2.

Another possible change during metamorphism is the alteration of a rock's mineralogical composition. All minerals have specific sets of conditions at which they are stable. These conditions can include pressure, temperature, and chemical composition of the rocks in which they exist, as well as the presence or absence of coexisting fluids of various compositions. The naturally occurring mineral *ice* serves as a great example. At the earth's surface, at sufficiently low temperatures, liquid water will freeze and form ice. As the temperature rises above 0ºC, this ice will melt and form liquid water again. We can also alter the stability of ice by introducing other chemical components. As anyone living in a colder climate knows, adding salt to ice can lower its freezing temperature, making it easier for fresh snow or ice to melt, thereby minimizing slipping hazards.

The same concept applies to every other mineral, and it is usually expressed through the use of phase diagrams. These phase diagrams plot the stability fields of certain

Editors' note: Questions or topics of interest should be directed to Aaron Palke (apalke@gia.edu) or James Shigley (jshigley@gia.edu).

Gems & Gemology, Vol. 59, No. 2, pp. 232–241.

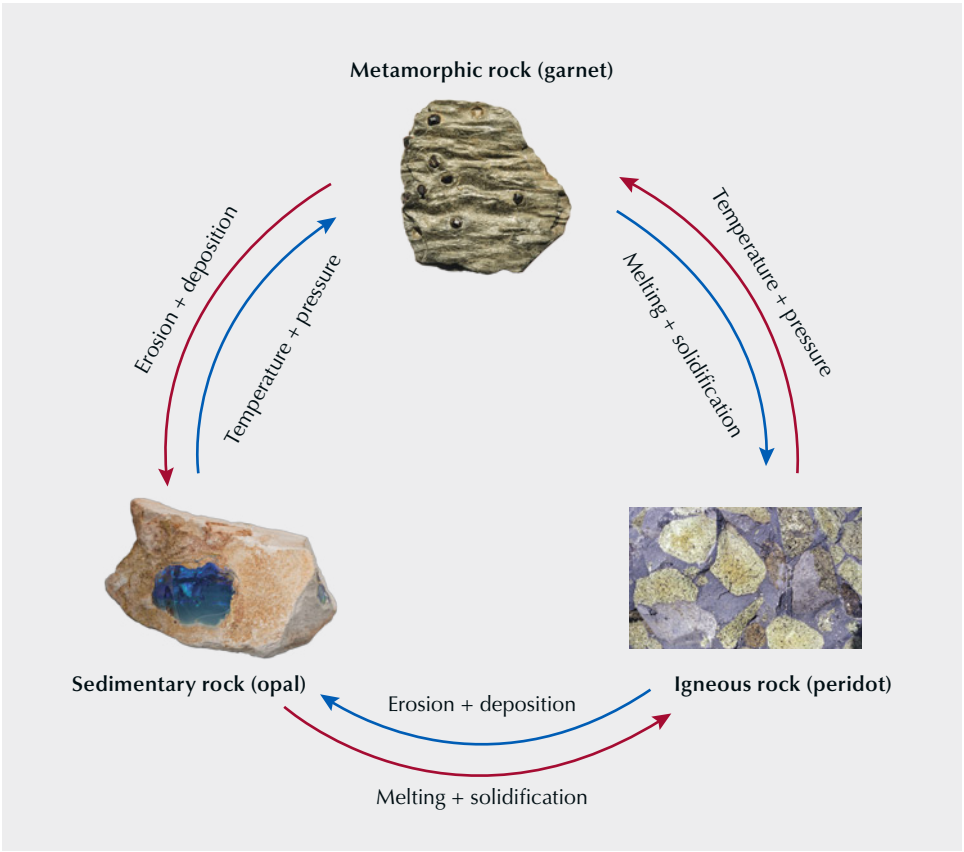

Figure 1. The concept of the rock cycle demonstrates the interplay between sedimentary, metamorphic, and igneous rocks. Photos by Robert Weldon (courtesy of Cody Opal), Orasa Weldon, and John I. Koivula, respectively.

minerals or mineral systems at various geological conditions. The most common phase diagram uses the variables pressure (P) and temperature (T). The phase Al_2SiO_5, which forms the gem minerals kyanite, sillimanite, and andalusite (figure 3), illustrates this concept. At conditions of very high pressure but lower temperature, the stable form

Figure 2. Layers of limestone and chert plastically deformed and folded at high pressure and temperature during metamorphism. Photo by Dieter Mueller (dino1948)/licensed under CC BY SA 4.0.

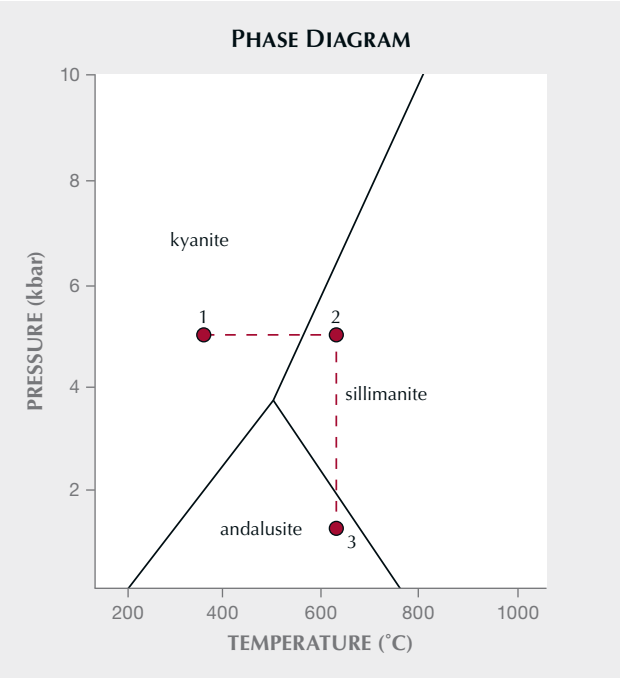

Figure 3. Phase diagram for kyanite, sillimanite, and andalusite, all having the chemical composition of Al_2SiO_5. Also shown are mineral transformations with changing temperature or pressure as discussed in the text.

of this phase is the mineral kyanite (figure 4). If a rock containing kyanite were heated up within the earth without changing the pressure, at a certain point it would cross over the boundary into the stability field of sillimanite (figure 5) and all the kyanite would be transformed in the solid state to this new phase (points 1 to 2 in figure 3). Similarly, if pressure were to decrease at this point without any drop

Figure 5. Sillimanite ranging from 7.85 to 9.91 ct. Photo by Robert Weldon; courtesy of Ivey Gemstones.

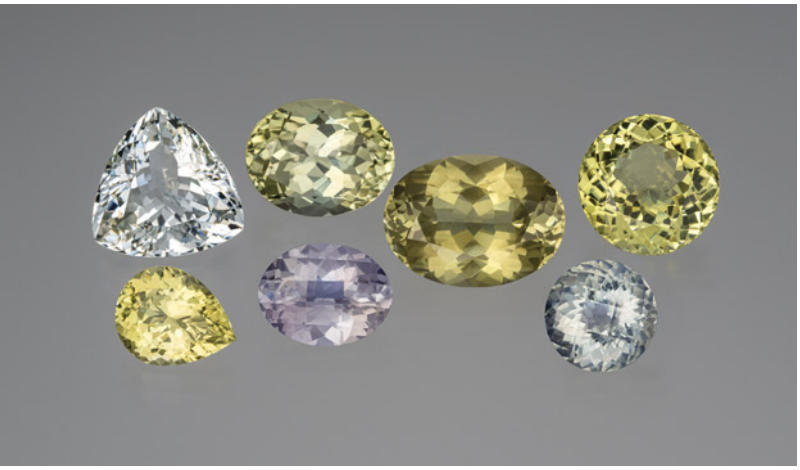

Figure 4. A 4.44 ct gem-quality kyanite from Kenya. Photo by Robert Weldon; courtesy of the Dr. Edward J. Gübelin Collection.

in temperature, the sillimanite would transform to andalusite (figure 6) if the temperature were low enough as it crossed over to the new stability field (points 2 to 3 in figure 3). This diagram has helped metamorphic petrologists get a better sense of the metamorphic conditions experienced when one of these three mineral phases is encountered in a rock.

Of course, the earth is much more complicated than this simple Al_2SiO_5 system. In nature, rocks are made up of multiple components, and the minerals making up the rocks often are not pure phases but solid solutions between different end-member compositions. Therefore, the mineral assemblages observed depend not only on conditions of pressure and temperature but also on the composition of the original rock being metamorphosed (the protolith).

Figure 6. Gem-quality andalusite weighing 23.75 ct (top left), 14.41 ct (top right), and 17.56 ct (bottom). Photo by Robert Weldon; courtesy of the Dr. Edward J. Gübelin Collection (top) and Pala International (bottom).

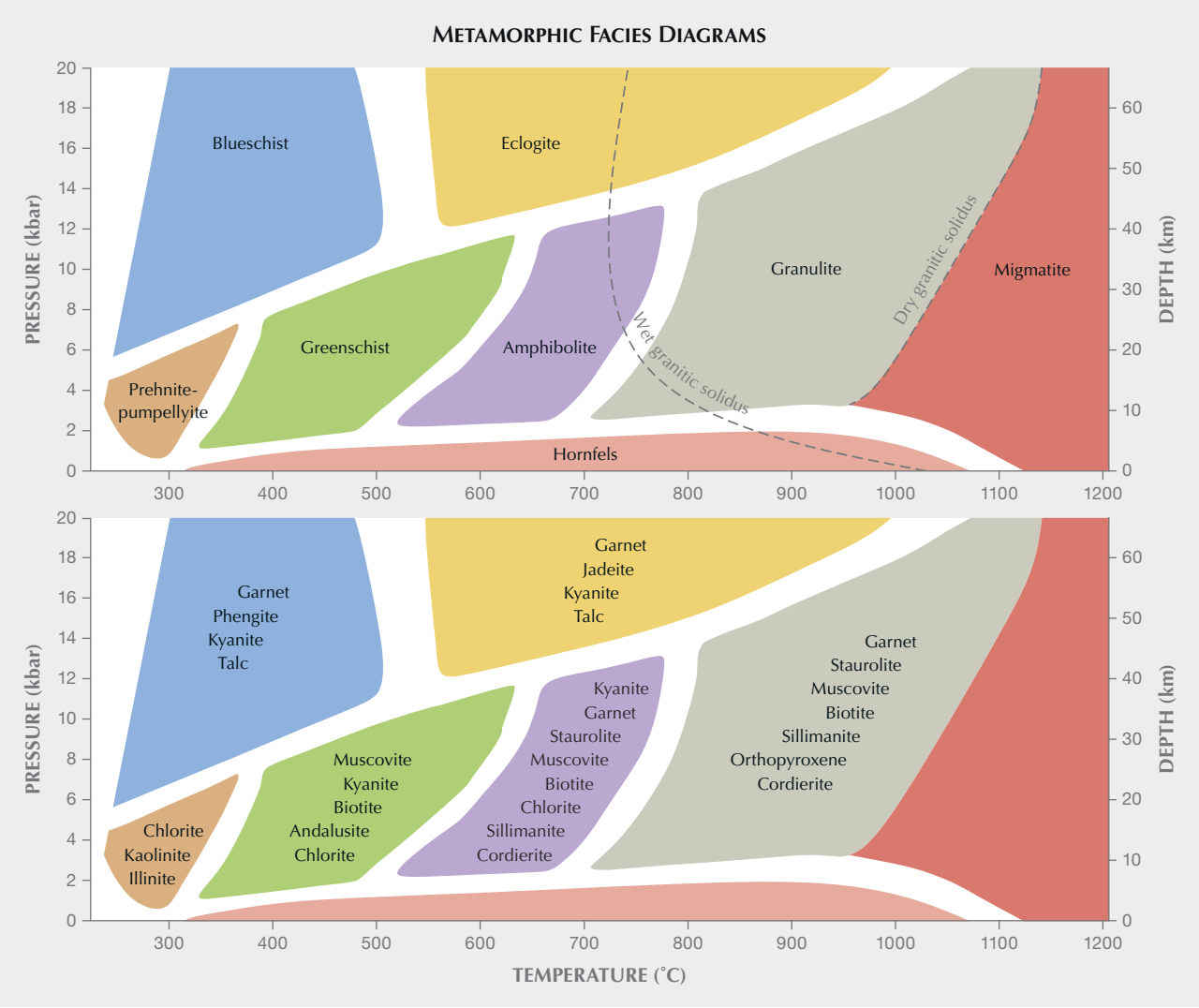

Figure 7. Top: Metamorphic facies diagram showing general range of P-T *conditions for different facies defined by their mineralogical assemblages and textural characteristics. Bottom: The same diagram, with typical mineralogical assemblages delineating the different facies for a metapelitic rock (a metamorphosed sedimentary rock such as a mudstone). Modified from Planet Earth Lab (planetearth.utsc.utoronto.ca/VirtualMic/charts/index.html).*

Metamorphic petrologists use the concept of *metamorphic facies* to describe general ranges of metamorphic conditions at varying pressures and temperatures. Metamorphic facies are general ranges of pressure and temperature that produce a specific mineralogical assemblage that helps to identify those conditions at which a metamorphic rock formed. Figure 7 shows a diagram of these metamorphic facies from relatively low-grade prehnite-pumpellyite facies to high-grade granulite or eclogite conditions. Also shown on the top diagram are dashed lines roughly indicating the boundary at which dry or hydrated granite will start to melt. While partially melted low-grade migmatites may still be considered essentially the product of metamorphism, this represents the somewhat fuzzy boundary between metamorphism and igneous processes. The different metamorphic facies are generally distinguished by broad changes in mineral assemblages with changing metamorphic conditions. The expected mineral assemblages for each facies for a metamorphosed pelitic rock (known as a mudstone) are also shown in figure 7.

Types of Metamorphism

There are multiple geological paths a rock can take toward metamorphism. The most straightforward is *contact metamorphism*, in which rocks are heated up due to nearby intrusion of a body of magma. Any changes to a rock's mineralogical assemblage are due simply to an increase in temperature. It is assumed that there is essentially no exchange of chemical components between a protolith and the intruding magma or associated fluid. It is, then, an isochemical form of metamorphism.

The more important form of metamorphism for gemstone formation is *regional metamorphism*. In this case, rocks are buried deep within the earth and experience increased temperature and pressure as they become progressively buried. The most common scenario for this is during orogenic, or mountain-building, events when landmasses collide due to the shifting of Earth's tectonic plates. The two most significant geological events leading to gemstone formation were the East African orogeny involving the collision of East and West Gondwana roughly 750–450 million years ago (Ma) and the Himalayan orogeny involving the collision of the Indian subcontinent with Asia starting about 60 Ma and continuing today. Gems from the East African orogeny are found across the eastern seaboard of the African continent as well as Sri Lanka, while gems from the Himalayan orogeny are located throughout Southeast and Central Asia in countries such as Vietnam, Myanmar, Pakistan, India, Afghanistan, and Tajikistan.

While scientists are fond of compartmentalizing nature into discrete classifications, these rock classifications typically have fuzzy boundaries and are not always clear-cut. For instance, classic metamorphism is considered to occur in the solid state without the melting of a rock or exchange of chemical components between different formations via fluids. However, this criterion is probably not strictly met, and most metamorphic reactions happen in the presence of some sort of fluid phase that may fundamentally alter the chemical composition of a metamorphic rock. Thus, the final form of metamorphism considered here is *hydrothermal metamorphism* in which changes in pressure and/or temperature are accompanied by changes in the chemical composition of the protolith by infiltration of hydrothermal fluids. This may also be described as "metasomatism" to emphasize the importance of both metamorphic and hydrothermal influences. For our discussion, this includes limestones or basalts that can be transformed into skarns or serpentinite, respectively, which in many cases may host gemstone deposits such as demantoid garnets.

Metamorphic Gemstones

Many of the world's most important colored stone deposits are the product of metamorphism. Several of these deposits resulted from ancient to modern orogenic events when massive continental collisions buried rocks in the earth's crust, fundamentally altering their mineralogical composition and in some cases producing fine gemstones. Sometimes hydrothermal fluids were an essential part of the process of gemstone formation in these metamorphic events. The following sections will provide a glimpse into the geological conditions of formation for some important metamorphic gemstones.

Jade. The term *jade* refers to two distinct gem materials that are characterized as extremely tough, essentially monomineralic fine-grained stones prized for their use in jewelry or ornamental carvings. The first type includes jade composed dominantly of the pyroxene mineral jadeite ($NaAlSi_2O_6$) but can also include the related minerals omphacite [$(Ca,Na)(Mg,Fe^{2+},Al)Si_2O_6$] or kosmochlor ($NaCrSi_2O_6$). This material is often referred to as *fei cui*. The second type is jade composed of amphibole minerals and is referred to as nephrite jade.

Figure 8. Rough jade boulder displaying a complex pattern not typically seen in finished gems. Photo by Wim Vertriest.

Fei cui jade is produced in subduction zone settings where convergent tectonic plate margins cause oceanic crust to be subducted deep within the earth. The subduction of relatively cold oceanic crust into the upper mantle creates a high-pressure, relatively low-temperature environment that is ideal for crystallizing jadeite. These conditions would be referred to as the blueschist up to eclogite metamorphic facies as seen in figure 7. *Fei cui* is essentially a rock and, as such, can record events in its geological history (figure 8). It occurs as veins or pods in bodies of serpentinized peridotites. These serpentinite bodies are the product of alteration of mafic or ultramafic igneous rocks by infiltrating fluids from the subducted oceanic crust in these geological settings. The same fluids responsible for serpentinization also likely played a role in the formation of jadeite. There is evidence that these jadeite bodies formed very deep within the earth, perhaps up to 80 km in depth, and were then exhumed or exposed later at the earth's surface.

Nephrite jade is dominantly composed of amphibole minerals usually varying between the tremolite [$Ca_2Mg_5Si_8O_{22}(OH)_2$] to ferro-actinolite [$Ca_2Fe_5Si_8O_{22}(OH)_2$] end members. Nephrite jade is the product of hydrothermal metamorphism (or metasomatism) in which either (1) silica-rich fluids infiltrate dolomite-rich rocks, or (2) calcium-rich fluids from silicic rocks interact with serpentinites (Harlow et al., 2014). Metamorphic petrologists often de-

Figure 9. A primary ruby deposit in Mogok, Myanmar, where rubies are mined directly out of the metamorphic marble created during the Himalayan orogeny. Photo by Wim Vertriest.

scribe the reactions implied above using reaction equations such as the following for the dolomite-related nephrite:

$$5\ Ca(Mg,Fe)(CO_3)_2 + 8SiO_{2aq} + H_2O \rightarrow Ca_2(Mg,Fe)_5Si_8O_{22}(OH)_2 + 3CaCO_3 + 7CO_{2aq}$$

or more simply

5(dolomite) + 8(aqueous silica) + water → tremolite + 3(calcite) + 7(aqueous carbon dioxide)

These equations can help clarify the likely reactions that took place during metamorphic events and roughly track the metamorphic conditions required to facilitate these reactions.

Ruby/Sapphire. Ruby and sapphire, gem varieties of the mineral corundum (Al_2O_3), can be broadly divided into metamorphic and magmatic varieties. The most significant deposits of metamorphic gem corundum were formed during two distinct geological events: the Pan African orogeny from 750 to 450 Ma and the Himalayan orogeny from 60 Ma to present. Sapphire from Sri Lanka, Madagascar, and Tanzania and ruby from Mozambique and Madagascar formed in the Pan African orogeny, while the Himalayan orogeny formed sapphire in Kashmir and Myanmar and ruby in Myanmar, Vietnam, Afghanistan, and Tajikistan. Metamorphic gem corundum forms in metamorphosed mafic or ultramafic rocks, marbles, gneisses, and metapelite complexes brought up to amphibolite or granulite facies conditions, generally at temperatures between 500° and 800°C (Giuliani and Groat, 2019). The rubies formed in the Himalayan orogeny at 620°–670°C at 2.6–3.3 kbar in marbles composed mostly of calcite (figures 9 and 10) within lenses of associated minerals including phlogopite, muscovite, scapolite, margarite, spinel, titanite, pyrite, and/or graphite (Garnier

Figure 10. A 97.3 ct rough ruby crystal on calcite (marble) from Myanmar. Photo by Robert Weldon; courtesy of Pala International.

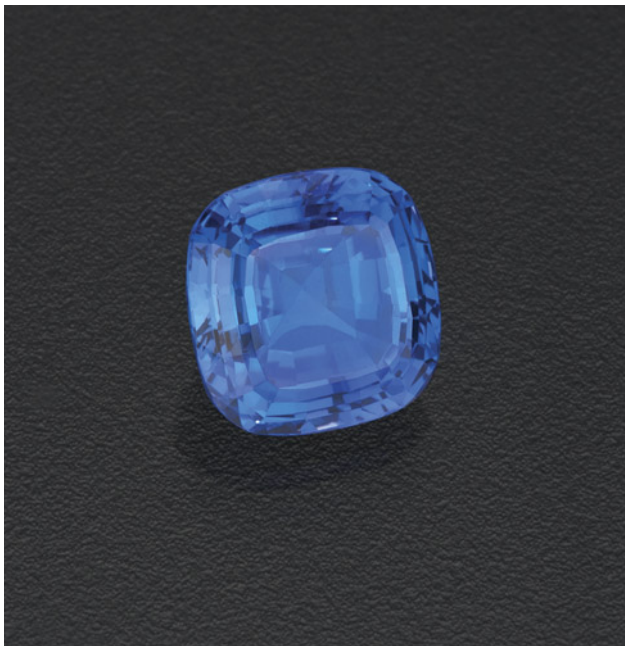

Figure 11. An 8.85 ct tanzanite. Photo by Orasa Weldon; courtesy of the Dr. Edward J. Gübelin Collection.

et al., 2008). Giuliani et al. (2015, 2018) also suggested the involvement of evaporate lenses within the original limestone protolith as a means of facilitating chemical exchange during metamorphism to form the rubies. In their model, it was suggested that molten evaporates may have infiltrated the carbonate layers, bringing along chemical components from clay layers and depositing corundum in veins and layers within the marble. Metamorphic sapphire deposits, such as those in Sri Lanka, Madagascar, Kashmir, and India/Pakistan, appear to require the involvement of metasomatic fluids infiltrating aluminum-rich protolith rocks during metamorphism to produce gem corundum (Atkinson and Kothavala, 1983; Silva and Siriwardena, 1988; Rakotondrazafy et al., 2008; Dharmaratne et al., 2012).

Tanzanite and Tsavorite. Tanzanite is the blue to violet variety of the mineral zoisite [$Ca_2Al_3(SiO_4)(Si_2O_7)O(OH)$] (figure 11), while tsavorite is the green gem variety of the garnet mineral grossular ($Ca_3Al_2Si_3O_{12}$) (figure 12). Both were created in similar geological settings during the Pan African orogeny. The host rocks are a package of quartzite, graphitic gneiss and schist, calc-silicate rocks, and marble with lenses of meta-evaporites. The gems formed within nodules or lenses within these rocks. Tanzanite likely formed at around 420°C and 2–4 kbar of pressure (Giuliani et al., 2014), while metamorphic conditions in the formations containing tsavorite likely reached around 600°–750°C and 6–9.1 kbar (Malisa, 1987; Muhongo et al., 1999; Olivier, 2006). The original protoliths were sedimentary formations derived from continental weathering and later metamorphism during continental collision. Some studies have indicated the likely role of evaporate lenses through open hydrothermal circulation within these sedimentary packages for formation of these gemstones (Olivier, 2006) as suggested for the following reaction for grossular (tsavorite) formation (Giuliani et al., 2014):

$$3CaSO_4 + 2Al^{3+} + 3SiO_2 + 6H_2O \rightarrow Ca_3Al_2Si_3O_{12} + 6O_2 + 3H_2S + 6H^+$$

where $CaSO_4$ is the mineral anhydrite and would have been sourced from evaporate lenses to create grossular garnet.

Figure 12. Nodule of tsavorite garnet from Tsavo, Kenya, within the metasedimentary host rock along with gemmy crystals obtained from similar formations. Photo by Vincent Pardieu/GIA.

Figure 13. Garnet schist from Alaska, 7.27 × 8.00 in. Photo by Orasa Weldon.

Garnet. As shown in figure 7, garnets (especially pyrope-almandine-spessartine type garnets [$(Mg,Fe,Mn)_3Al_2Si_3O_{12}$] tend to form only at conditions of increased pressure and temperature in metamorphic events. In fact, geology students learning metamorphic petrology will use the appearance of garnet in the field as a general indicator of the metamorphic grade of the host rock. Many of the red-colored pyrope-almandine-spessartine (pyralspite) garnets in the gem trade were derived from metamorphic rocks such as garnet schists (figure 13). Many more pyralspite garnets, including many color-change garnets (figure 14), are found in the Mozambique Orogenic Belt in East Africa and Sri Lanka. Their formation is assumed to be metamorphic in origin given the geological context, but they are generally found in secondary alluvial deposits. Therefore, their precise conditions of formation are typically not well understood because their original host rock is unknown and may have been completely removed by weathering.

Most of these pyralspite garnets fit more squarely into the classical definition of solid-state metamorphism. But other gem garnets, such as demantoid, require more complicated metamorphic conditions involving not only in-

Figure 14. A 5.44 ct pastel color-change pyrope garnet from Tanzania, faceted by Jason Doubrava. Photo by Robert Weldon; courtesy of Meg Berry.

Figure 15. A 10.02 ct Russian demantoid garnet. Photo by Robert Weldon; courtesy of Pala International.

creases in pressure and temperature but also the circulation of fluids to facilitate their formation. Demantoid is the green gem variety of the mineral andradite ($Ca_3Fe_2Si_3O_{12}$). These calcium-rich garnets form in two distinct geological environments. The first type of demantoid is found in serpentinized ultramafic rocks as in the classic deposit in the Russian Ural Mountains but also in Iran and Pakistan (Karampelas et al., 2007; Adamo et al., 2009). Here, demantoid forms in veins of serpentine mineralization cutting through peridotites and ultramafic rocks, facilitated by the circulation of hydrothermal fluids through these rocks. The second type is found in Madagascar and Namibia, and is related to skarn deposits in which the nearby intrusion of magma causes fluids to circulate through metasedimentary rocks rich in limestone or calc-silicate rocks (Pezzotta et al., 2011). Hand specimens of demantoid from both locales demonstrate the difference in geology through mineral associations: serpentinite-hosted demantoid occurs in a matrix of serpentine minerals (figures 15 and 16), while the skarn-hosted demantoid occurs in rocks dominantly composed of skarn minerals like diopside and wollastonite (figures 17 and 18).

Summary

Many of the world's premier gemstone deposits were derived from conditions of extreme stress, pressure, and temperature deep in the earth's crust. These gemstones often bear signs of these metamorphic processes in their inclusions, which can mirror their geological conditions of formation. The study of these gemstones can offer insight into

Figure 16. Nodules of demantoid garnet in a 28.87 g serpentinite rock. Photo by Aaron Palke.

Figure 17. An 11.63 ct demantoid garnet from Namibia. Photo by Robert Weldon; courtesy of Green Dragon Mine Company, Namibia.

Figure 18. Skarn-hosted demantoid from Madagascar is hosted in rocks composed of typical skarn minerals such as diopside and wollastonite, among others. This specimen measures 15 × 7 × 5 cm. Photo by Orasa Weldon; courtesy of the GIA Collection.

the earth's history and the evolution of tectonic activity that led to their formation. The next installment of Colored Stones Unearthed will focus on the influence of sedimentary processes in the development of gemstone deposits.

REFERENCES

Adamo I., Bocchio R., Diella V., Pavese A., Vignola P., Prosperi L., Palanza V. (2009) Demantoid from Val Malenco, Italy: Review and update. *G&G*, Vol. 45, No. 4, pp. 280–287, http://dx.doi.org/10.5741/GEMS.45.4.280

Atkinson D., Kothavala R.Z. (1983) Kashmir sapphire. *G&G*, Vol. 19, No. 2, pp. 64–76, http://dx.doi.org/10.5741/GEMS.19.2.64

Dharmaratne P.G., Premasiri H.M.R., Dillimuni D. (2012) Sapphires from Thammannawa, Kataragama area, Sri Lanka. *G&G*, Vol. 48, No. 2, pp. 98–107, http://dx.doi.org/10.5741/GEMS.48.2.98

Garnier V., Giuliani G., Ohnenstetter D., Fallick A.E., Dubessy J., Banks D., Vinh H.-Q., Lhomme T., Maluski H., Pêcher A., Bakhsh K.A., Long P.V., Trinh P.T., Schwarz D. (2008) Marble-hosted ruby deposits from Central and Southeast Asia: Towards a new genetic model. *Ore Geology Reviews*, Vol. 34, No. 1-2, pp. 169–191, http://dx.doi.org/10.1016/j.oregeorev.2008.03.003

Giuliani G., Ohnenstetter D., Fallick A.E., Groat L.A., Fagan A.J. (2014) Tsavorite and tanzanite deposits. In L.A. Groat, Ed., *Geology of Gem Deposits*, 2nd ed., Mineralogical Association of Canada, Short Course Series 44, pp. 29–112.

Giuliani G., Dubessy J., Banks D.A., Lhomme T., Ohnenstetter D. (2015) Fluid inclusions in ruby from Asian marble deposits: Genetic implications. *European Journal of Mineralogy*, Vol. 27, No. 3, pp. 393–404, http://dx.doi.org/10.1127/ejm/2015/0027-2442

Giuliani G., Dubessy J., Ohnenstetter D., Banks D., Branquet Y., Feneyrol J., Fallick A.E., Martelat J.-E. (2018) The role of evaporites in the formation of gems during metamorphism of carbonate platforms: A review. *Mineralium Deposita*, Vol. 53, No. 1, pp. 1–20, http://dx.doi.org/10.1007/s00126-017-0738-4

Giuliani G., Groat L.A. (2019) Geology of corundum and emerald gem deposits: A review. *G&G*, Vol. 55, No. 4, pp. 464–489, http://dx.doi.org/10.5741/GEMS.55.4.464

Harlow G.E., Sorensen S.S., Sisson V.B., Shi G. (2014) The geology of jade deposits. In L.A. Groat, Ed., *Geology of Gem Deposits*, 2nd ed., Mineralogical Association of Canada, Short Course Series 44, pp. 305–374.

Karampelas S., Gaillou E., Fritsch E., Douman M. (2007) Les grenats andradites-démantoïdes d'Iran: Zonage de couleur et inclusions. *Revue de Gemmologie A.F.G.*, No. 160, pp. 14–20.

Malisa E. (1987) Geology of the tanzanite gemstone deposits in the Lelatema area, NE Tanzania. In *Annales Academiae Scientiarum Fennicae. Series A3. Geologica-Geographica*, Vol. 146, 159 pp.

Muhongo S., Tuisku P., Mtoni Y. (1999) Pan-African pressure-temperature evolution of the Merelani area in the Mozambique Belt in northeast Tanzania. *Journal of African Earth Sciences*, Vol. 29, No. 2, pp. 353–365, http://dx.doi.org/10.1016/S0899-5362(99)00102-5

Olivier B. (2006) The geology and petrology of the Merelani tanzanite deposit, NE Tanzania. Doctoral dissertation, University of Stellenbosch.

Pezzotta F., Adamo I., Diella V. (2011) Demantoid and topazolite from Antetezambato, northern Madagascar: Review and new data. *G&G*, Vol. 47, No. 1, pp. 2–14, http://dx.doi.org/10.5741/GEMS.47.1.2

Rakotondrazafy A.F.M., Giuliani G., Ohnenstetter D., Fallick A.E., Rakotosamizanany S., Andriamamonjy A., Ralantoarison T., Razanatseheno M., Offant Y., Garnier V., Maluski H., Dunaigre C., Schwarz D., Ratrimo V. (2008) Gem corundum deposits of Madagascar: A review. *Ore Geology Reviews*, Vol. 34, No. 1-2, pp. 134–154, http://dx.doi.org/10.1016/j.oregeorev.2007.05.001

Silva K.K.M.W., Siriwardena C.H.E.R. (1988) Geology and the origin of the corundum-bearing skarn at Bakamuna, Sri Lanka. *Mineralium Deposita*, Vol. 23, No. 3, pp. 186–190, http://dx.doi.org/10.1007/BF00204299

GEM NEWS INTERNATIONAL

Contributing Editors
Gagan Choudhary, *IIGJ-Research & Laboratories Centre, Jaipur, India* (gagan.choudhary@iigjrlc.org)
Christopher M. Breeding, *GIA, Carlsbad* (christopher.breeding@gia.edu)
Guanghai Shi, *School of Gemmology, China University of Geosciences, Beijing* (shigh@cugb.edu.cn)

COLORED STONES AND ORGANIC MATERIALS

Unique Colombian emerald and matrix suite. The author recently examined a unique suite of cabochon stones consisting of emeralds with brown matrix weighing 112.25 carats total (figure 1). This spectacular set is reportedly from the Muzo mine in Colombia. Similar material with matrix has been found in Chivor, but never of comparable quality. The miners decided to cut a matching set of cabochons that could be made into a necklace and a pair of earrings. In 2021, Misael Angel Rodriguez of Colombia brought this unique set to the Tucson gem shows, where it received considerable attention. It was later purchased by Desmond Chan and Davey Thomas of Gem Arts International and submitted to the AGTA Spectrum Awards, receiving honorable mention in 2022. To this day, the author has yet to encounter such a remarkable set of matching emerald with matrix cabochons.

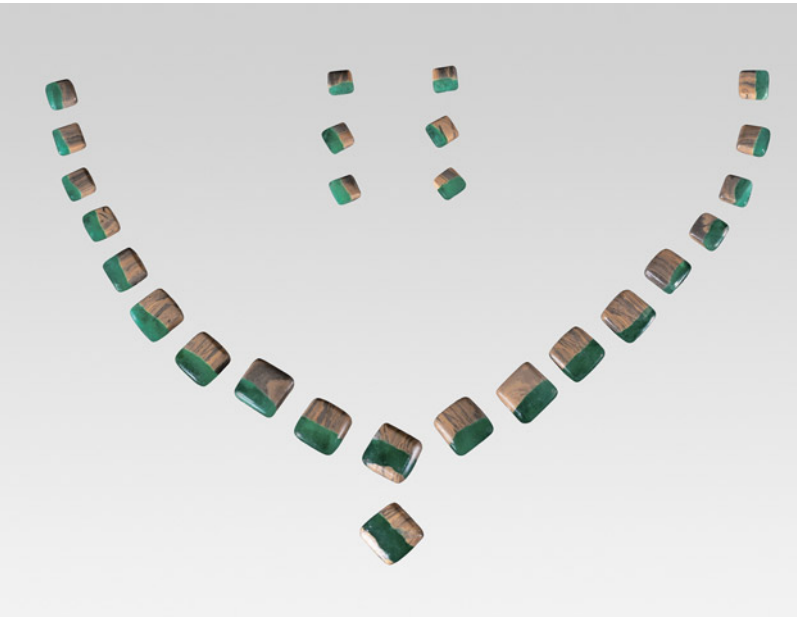

Figure 1. Emerald and matrix suite, 112.25 carats total. Photo by Jessa Rizzo.

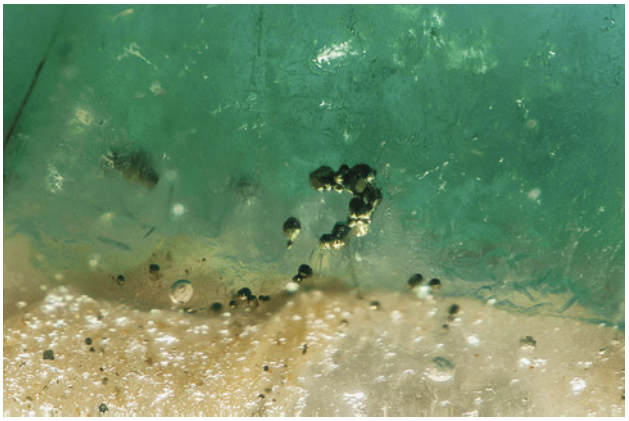

Figure 2. Cluster of pyrite crystals in emerald and matrix. Photomicrograph by Jessa Rizzo; field of view 1.99 mm.

Under the microscope, the matrix has a coarse, sand-like texture. Raman spectroscopy identified the matrix as primarily consisting of an aggregate of feldspar grains displaying a banded pattern. Under magnification, the green gem area showed jagged multiphase inclusions along with euhedral pyrite crystal inclusions (figure 2). Laser ablation–inductively coupled plasma–mass spectrometry and inclusion ob-

Editors' note: Interested contributors should send information and illustrations to Stuart Overlin at soverlin@gia.edu.

Gems & Gemology, Vol. 59, No. 2, pp. 242–260.

Figure 3. The white and cream non-nacreous pearl weighing 0.29 ct and measuring 3.75 × 3.55 mm. Photo by Gaurav Bera.

servation were consistent with a Colombian origin. It is remarkable to see such a well-matched suite of unusual emeralds with matrix in the gem trade.

Jessa Rizzo
GIA, Carlsbad

Calcite present in a pearl from *Pinctada maculata*. *Pinctada maculata* pearls, also known in the trade as "pipi pearls," form in shells considered to be the smallest of all the *Pinctada* species. The shell size ranges from 2 to 6 cm and produces pearls ranging from 1 to 4 mm. However, some rare examples may reach up to 9 mm (Spring 2014 GNI, pp. 89–90). Most pearls from this mollusk exhibit a yellow to "golden" color range, yet some are white to cream, orange, and gray. Round to near-round pearls are quite typical of the species, but other shapes may be found, as with all pearls (N. Nilpetploy et al., "The gemological characteristics of pipi pearls reportedly from *Pinctada maculata*," Winter 2018 *G&G*, pp. 418–427). They are distributed throughout French Polynesia and the Cook Islands and found in shallow waters and depths up to 20 meters. GIA's Mumbai laboratory had the opportunity to examine a quantity of these pearls, which were reportedly sourced from known divers who fished them from wild *P. maculata* mollusks off the Cook Islands. The parcel contained 306 natural pearls of various sizes and shapes, with measurements ranging from 2.87 × 2.69 × 2.55 mm to 8.34 × 3.25 mm.

Real-time microradiography (RTX) showed a variety of internal structures expected for natural pearls. Externally, most samples showed the typical nacreous overlapping aragonite platelets (platy structure) and surfaces that ranged from clean to moderately blemished. However, one near-oval, bicolor white and cream pearl, weighing 0.29 ct and measuring 3.75 × 3.55 mm (figure 3), revealed a very interesting surface structure under 40× magnification. The top part of the pearl exhibited a mosaic, or network of columnar calcite structures in a cellular form (hexagonal and clustered), creating an uneven surface. This was similar to the appearance of non-nacreous pen pearls (N. Sturman et al., "Observations on pearls reportedly from the Pinnidae family (pen pearls)," Fall 2014 *G&G*, pp. 202–215). The bottom part had a combination of both: areas of nacreous overlapping aragonite platelets (the circular ring-like area around the base) and areas of columnar calcite structure (figure 4). The surface was unique among those observed in the lot, as it exhibited both polymorph forms of calcium carbonate (aragonite and calcite). To confirm the non-nacreous cellular areas observed, Raman analysis using a 514 nm laser excitation was carried out on three spots of the pearl's surface (spots 1 and 2 with cellular structure and spot 3 with platy structure). Spots 1 and 2 showed peaks at 280 and 712 cm^{-1}, respectively, indicative of calcite. Spot 3 showed a doublet at 701 and 704 cm^{-1} and a peak at 1085 cm^{-1}, both characteristic features of aragonite (figure 5).

RTX imaging revealed an organic-rich fine acicular feature with no central core, associated with some concentric growth arcs (figure 6, left). X-ray computed microtomography (μ-CT) showed a large central fine acicular feature with a small core showing its calcitic nature, surrounded with thick, dense organic-rich concentric growth arcs (figure 6, right). The internal structure of the pearl matched with the expected columnar structure observed on the surface, as noted in previous research reports.

Energy-dispersive X-ray fluorescence spectrometry revealed a low manganese level of 16 ppm and a higher strontium level of 1286 ppm. Optical X-ray fluorescence was

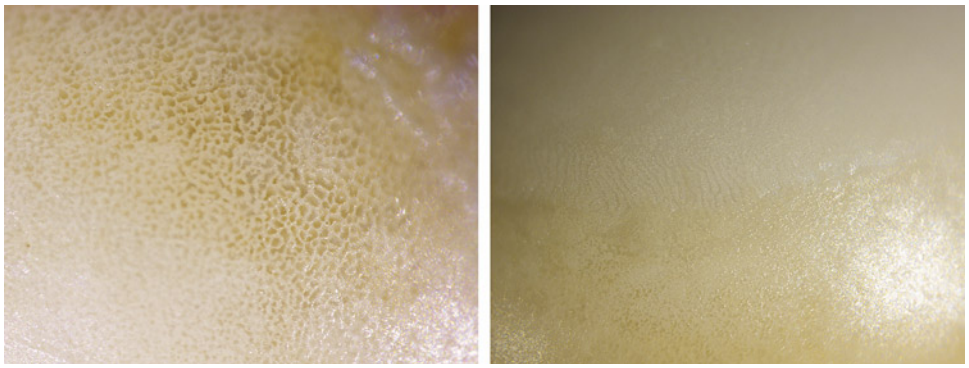

Figure 4. Left: Cellular calcite structure; field of view 0.5 mm. Right: Aragonite platy surface structure; field of view 0.8 mm. Photomicrographs by Pfokreni Nipuni.

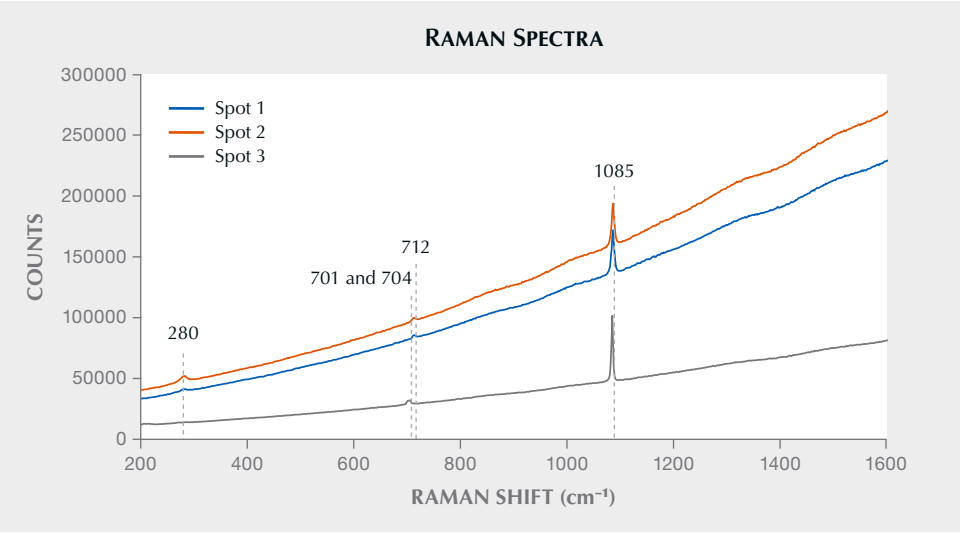

Figure 5. The Raman spectra showed peaks at 280 and 712 cm^{-1} indicative of calcite (spots 1 and 2) and typical aragonite features at 701, 704, and 1085 cm^{-1} (spot 3).

inert, and both results are characteristic of the saltwater environment in which the pearl formed. The pearl showed a moderate bluish green reaction under long-wave UV radiation and a much weaker bluish green reaction under short-wave UV. It was also examined by the ultra-short UV wavelength (230 nm) of the DiamondView, which revealed a clear bluish reaction with fine cellular hexagonal columnar features typically indicative of calcite.

Spectroscopic examination confirmed the presence of both calcite and aragonite. The top and bottom portions of this *P. maculata* pearl exhibited a combination of calcite and aragonite surface features aligned parallel to each other. Such external features are not typically observed in pearls from this mollusk, based on the extensive samples GIA has examined globally, which makes this pearl rare and interesting despite its lack of visual appeal.

Anukul J. Belanke, Roxane Bhot Jain, and Nishka Vaz
GIA, Mumbai

Abeer Al-Alawi
GIA, Global

An unusual metallic core in a natural *Pinctada radiata* pearl from Kuwait. The pearl (oyster) beds, or *heirat* in Arabic, around the State of Kuwait in the Persian (Arabian) Gulf have been known throughout history for producing some of the finest natural pearls. GIA's Bangkok laboratory recently examined a quantity of these pearls obtained from a Kuwaiti pearl diver. The trusted diver said they were fished from wild *Pinctada radiata* mollusks at depths of 6 to 15 meters from one of the main pearl beds in the waters of Kuwait. The parcel consisted of various shapes and colors ranging from white to light yellow, with a few colored pearls as well.

The samples showed a variety of internal structures, but one round cream-colored pearl in particular, weighing 0.23 ct and measuring 3.20 × 3.12 mm (figure 7), revealed an interesting structure using real-time microradiography (RTX) and X-ray computed microtomography (μ-CT) analyses. When viewed under 40× magnification, the pearl's smooth and high-luster surface exhibited typical nacreous overlapping aragonite platelets.

RTX imaging revealed a very unusual small ovalish radiopaque white core located in the pearl's center. The

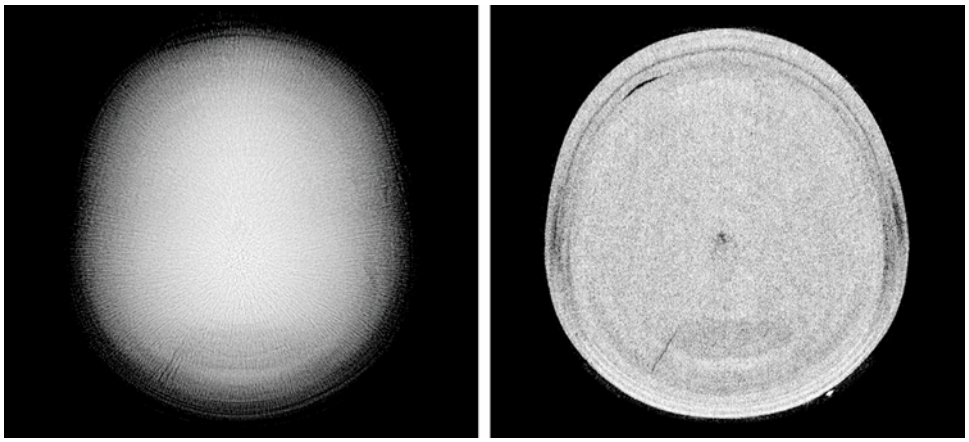

Figure 6. Left: RTX image revealing the calcitic nature of the pearl. Right: μ-CT scans showed a small core with a large acicular structure covering the entire area.

Figure 7. The cream-colored pearl weighing 0.23 ct and measuring 3.20 × 3.12 mm, shown against the anterior of a Pinctada radiata *mollusk. Photo by Nuttapol Kitdee.*

radiopaque core stood out in contrast to the rest of the pearl's structure (figure 8), indicating that the feature was composed of a material containing elements with higher atomic numbers on the periodic table. The appearance of the core was typical of that seen for metals when examined by X-rays, such as the metal post within the drill hole of the pearl in figure 9. The core measured approximately 0.19 × 0.15 × 0.13 mm and was surrounded by fine concentric rings with a small area of associated radiolucent organic-rich material. The small organic-rich area extending toward the outer growth layers appeared darker gray in the RTX and µ-CT images. Although the metallic core created doubts about the pearl's origin, the associated concentric ring structure surrounding it was more indicative of natural origin. The µ-CT scan images were also rendered using specialized software ("New 3-D software expands GIA's pearl identification capabilities," *GIA Research News*, May 13, 2016) to create a three-dimensional image that made it easier to visualize the form of the central metal core (figure 10; see video of the 3D model at www.gia.edu/gems-gemology/summer-2023-gemnews-metallic-core-pinctada-radiata).

Energy-dispersive X-ray fluorescence spectrometry revealed no manganese and a strontium level of 1400 ppm, which is characteristic of a saltwater environment. Raman analysis using 514 nm laser excitation was also carried out on the pearl's surface and showed a doublet at 702 and 705 cm^{-1} as well as a peak at 1085 cm^{-1} indicative of aragonite. Weak polyenic pigment peaks associated with the pearl's cream coloration were also observed at around 1135 and

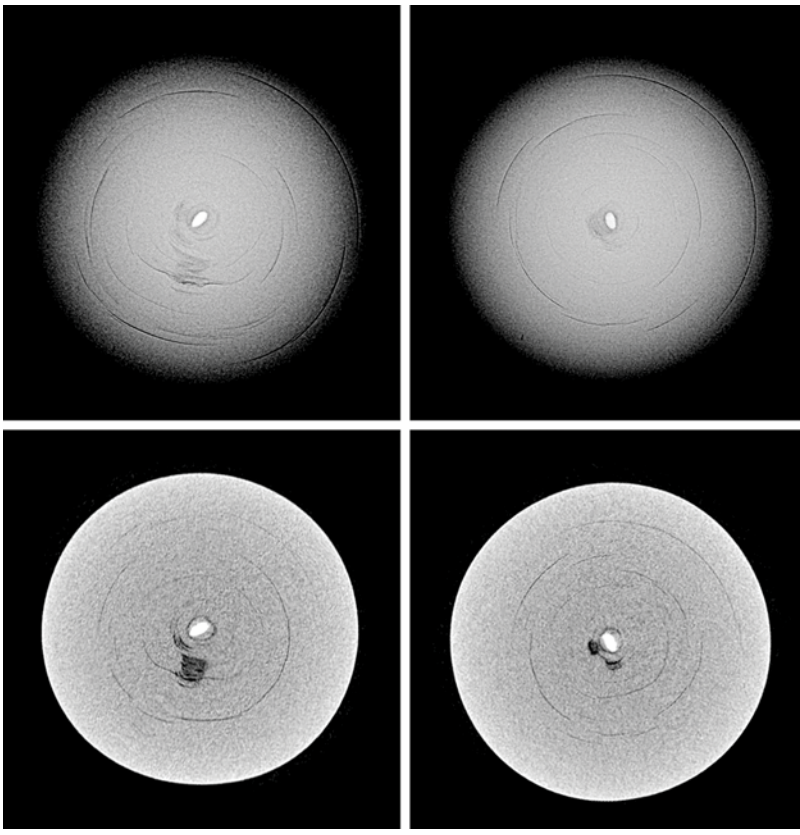

Figure 8. Top: RTX images revealing the entire volume of the pearl's internal structure in two different directions. Bottom: Slightly enlarged µ-CT scans showing the radiopacity of the core more clearly. The darker areas are organic-rich.

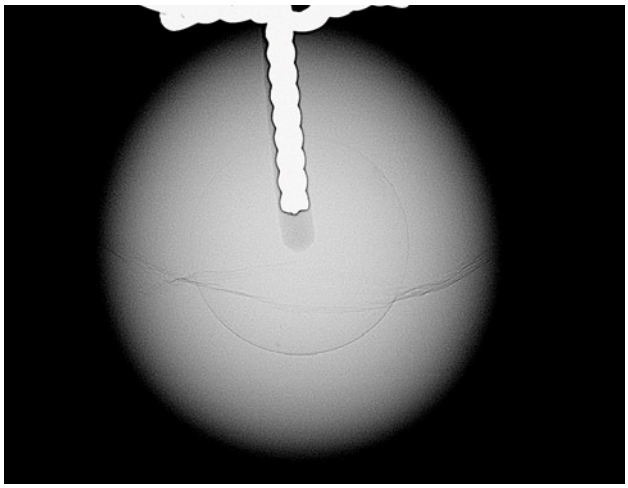

Figure 9. RTX image of a bead cultured pearl reference sample with a metal post in the drill hole. The metal appears radiopaque and matches the appearance of the core feature in the pearl examined in the present study.

1530 cm^{-1}. Ultraviolet/visible reflectance spectra showed features at around 410, 435, and 460 nm and an additional band at 495 nm, in keeping with observations previously recorded for *Pinctada radiata* pearls (A. Al-Alawi et al., "Saltwater cultured pearls from *Pinctada radiata* in Abu Dhabi (United Arab Emirates)," *Journal of Gemmology*, Vol. 37, No. 2, 2020, pp. 164–179).

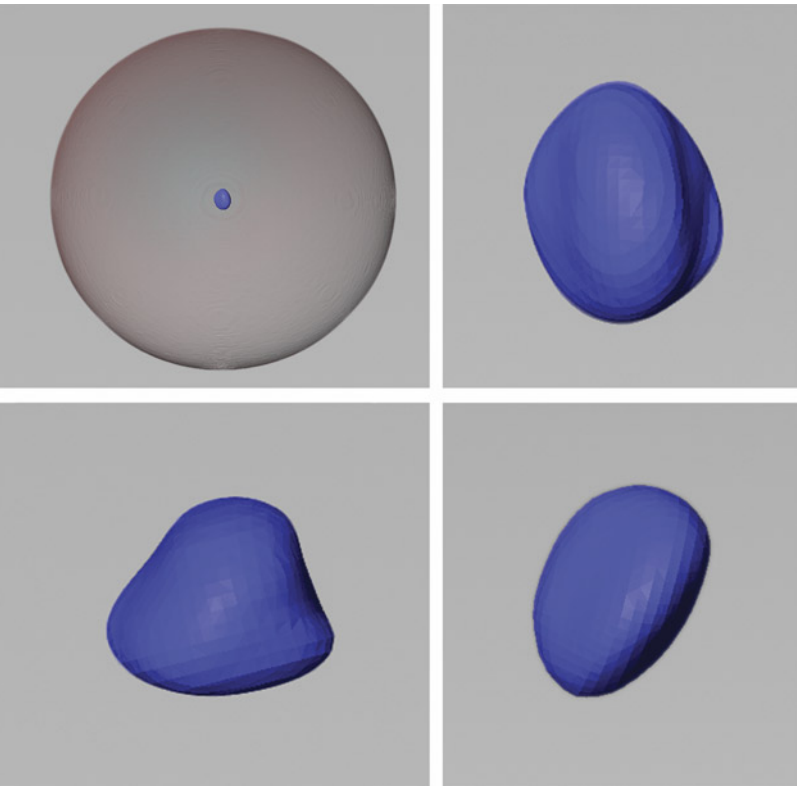

Figure 10. The 3D models generated using µ-CT scans show the blue area as the metallic core, while the surrounding area represents the pearl's growth structure.

Although GIA was not permitted to cut the pearl in half or grind the surface down to reach the metal, we believe the feature may be a metal oxide similar to one previously documented (M.S. Krzemnicki, "Pearl with a strange metal core," *SSEF Facette*, No. 24, 2018, p. 27). How this apparent metal found its way inside the mollusk is still a mystery. Since the diver found the pearl with other natural pearls that GIA also examined and confirmed, and it came from an area that lacks any pearl farms, it seems unlikely that a human inserted the metal core as a bead nucleus. It is possible that the core resulted from the pollution the region witnessed after the Gulf War in 1992, and a foreign metallic particle found its way into a mollusk. Residue from the shipping industry is another possibility, with potential pollution from the heavy volume of oil tankers and other vessels in the area. Hence, water contamination may be a convincing explanation for the unusual structure observed in this unique and fascinating natural Kuwaiti pearl.

Ravenya Atchalak and Kwanreun Lawanwong
GIA, Bangkok

Emiko Yazawa
GIA, New York

Abeer Al-Alawi

Saltwater clamshell beads (*Tridacna* species) used in freshwater cultured pearls. GIA's Bangkok laboratory recently studied 23 intriguing freshwater bead cultured pearls purchased from a vendor in Hong Kong. They displayed an elongated baroque shape with a surface protuberance at one end, and they weighed approximately 20 ct apiece and ranged from 16.73 × 12.58 × 12.49 mm to 18.98 × 13.53 × 13.43 mm (figure 11). Their shape and appearance are similar to saltwater bead cultured pearls known in the market as "Tokki pearls" (A. Homkrajae et al., "Internal structures of known *Pinctada maxima* pearls: Cultured pearls from operated marine mollusks," Fall 2021 *G&G*, pp. 186–205).

Real-time microradiography (RTX) revealed the distinct round demarcation of a bead nucleus with additional void and/or linear features in all the samples, as expected from their external appearance (figure 12, left). However, the beads were more radiopaque and appeared lighter gray in RTX imaging than the traditional freshwater shell bead nuclei widely used in both saltwater and freshwater bead cultured pearl production (P. Southgate and J. Lucas, *The Pearl Oyster*, 2008, p. 286; "Freshwater pearling in Tennessee," *GIA Research News*, October 7, 2016; N. Sturman et al., "Vietnam: Shell nuclei, pearl hatcheries, and pearl farming," Fall 2020 *G&G*, pp. 402–415). Numerous long, thick parasite tubes were visible within the beads,

Figure 11. A strand of baroque-shaped freshwater bead cultured pearls shown with two Tridacna*-species mollusk shells from GIA's shell reference collection. Each sample weighs approximately 20 ct, ranging from 16.73 × 12.58 × 12.49 mm to 18.98 × 13.53 × 13.43 mm. Photo by Nuttapol Kitdee.*

something not often seen in traditional beads (figure 12, right). Optical X-ray fluorescence imaging was used to verify the pearls' freshwater origin. They exhibited weak to moderate yellowish green fluorescence, confirming a freshwater origin. However, the reaction was much weaker than many freshwater bead cultured pearls of the same size and nacre thickness previously examined. These unusual characteristics observed in RTX and X-ray fluorescence imaging led us to cut two pearls in half to investigate the bead nuclei.

The cross sections revealed bead nuclei approximately 12 mm in diameter. The beads appeared chalky white and opaque, unlike traditional beads that are commonly white to cream-colored and semitranslucent. Moreover, the beads exhibited a porcelain-like texture and a subtle flame pattern. We ground the surface of two additional samples to better understand the material. Banded structures of shell formation with subtle flame structures in between were present (figure 13).

Energy-dispersive X-ray fluorescence was used to analyze the elemental concentration of the outer nacre layer and the bead nuclei. The nacre layer showed a high level of manganese and low strontium content, confirming the pearls formed in a freshwater environment. Conversely,

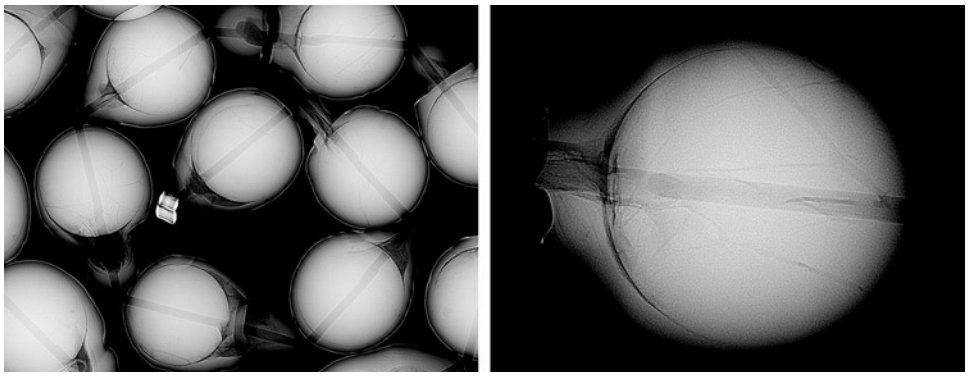

Figure 12. RTX imaging revealed shell bead nuclei approximately 12 mm in diameter entirely covered by the pearl's approximately 1 mm thick nacre (left), with numerous parasite channels in the beads (right).

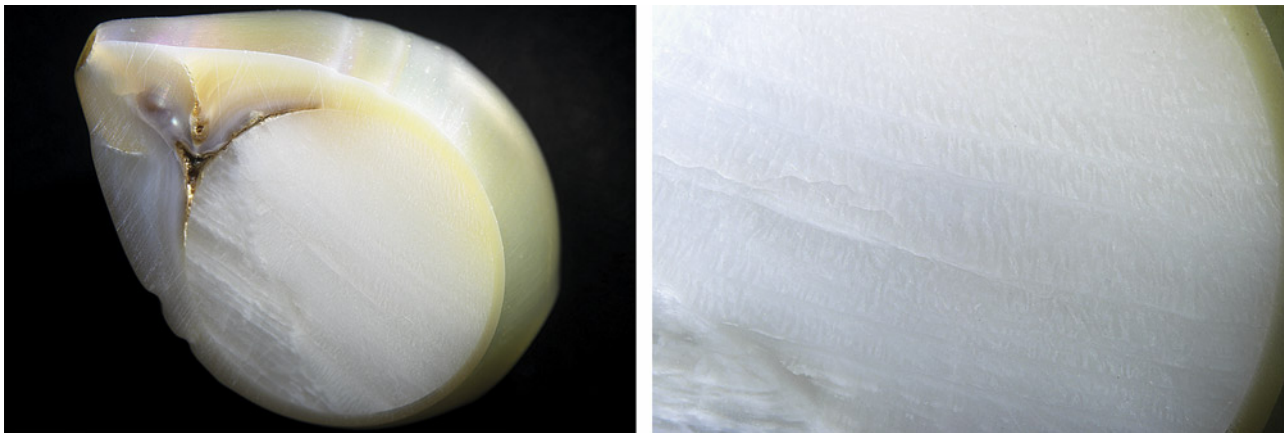

Figure 13. Left: A cross section with the Tridacna *fashioned shell bead nucleus inside showing fine subtle flames in between banded structures. Right: Magnified view of the clamshell bead's flame structure. Photomicrographs by Kwanreun Lawanwong; fields of view 19.20 mm (left) and 7.20 mm (right).*

the bead nuclei showed high strontium (around 1000 ppm) and no manganese was detected, which are typical results for pearls from a saltwater environment. X-ray fluorescence imaging of the cross section displayed a strong yellowish green reaction on the freshwater nacre due to high manganese content, while the saltwater bead nuclei were inert (figure 14). A Raman spectrometer with 514 nm argon-ion laser excitation was employed to analyze the bead nuclei composition, and double peaks at 701 and 705 cm^{-1} and a single peak at 1085 cm^{-1} of aragonite were recorded. Aragonite is a common component of shell and pearl.

The large size, white color, porcelain surface appearance, banded structure with flames, saltwater formation environment, and aragonite composition of the bead nuclei suggested they were created from the clamshell of *Tridacna*-species mollusks. Fashioned shells from *Tridacna* species have been applied particularly in pearl imitations (see Summer 2014 Lab Notes, pp. 153–154; Spring 2015 Lab Notes, pp. 62–63) but are not commonly used in culturing because they are easily broken during the drilling process. More importantly, shells from *Tridacna* species should be avoided for jewelry items or decoration since they are protected by the Convention on International Trade in Endangered Species of Wild Fauna and Flora (CITES), the international agreement that protects endangered species.

Kwanreun Lawanwong

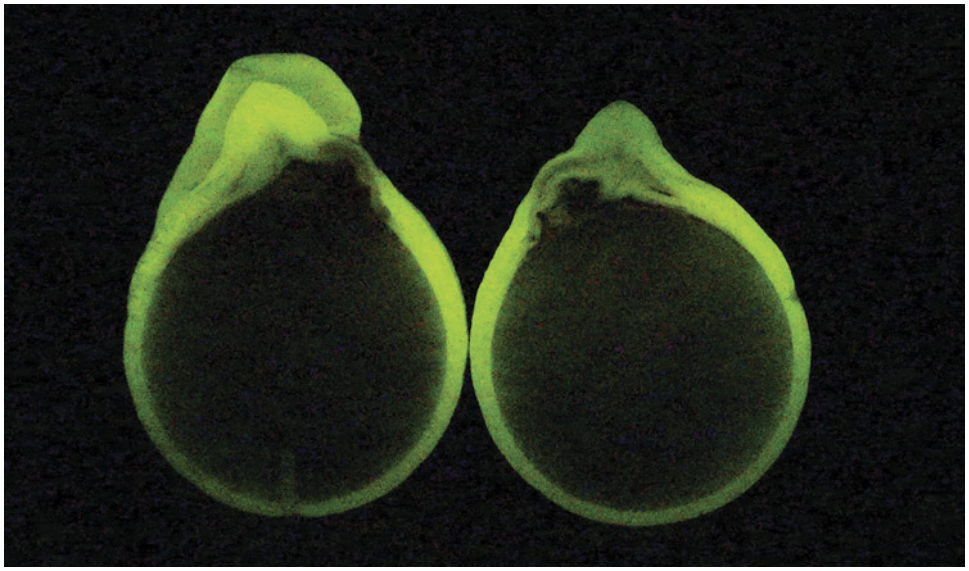

Figure 14. An X-ray illuminated cross section produced a strong yellowish green fluorescence reaction on the freshwater pearl's outermost surface nacre layer, while the inner rounded saltwater clamshell beads showed an inert reaction.

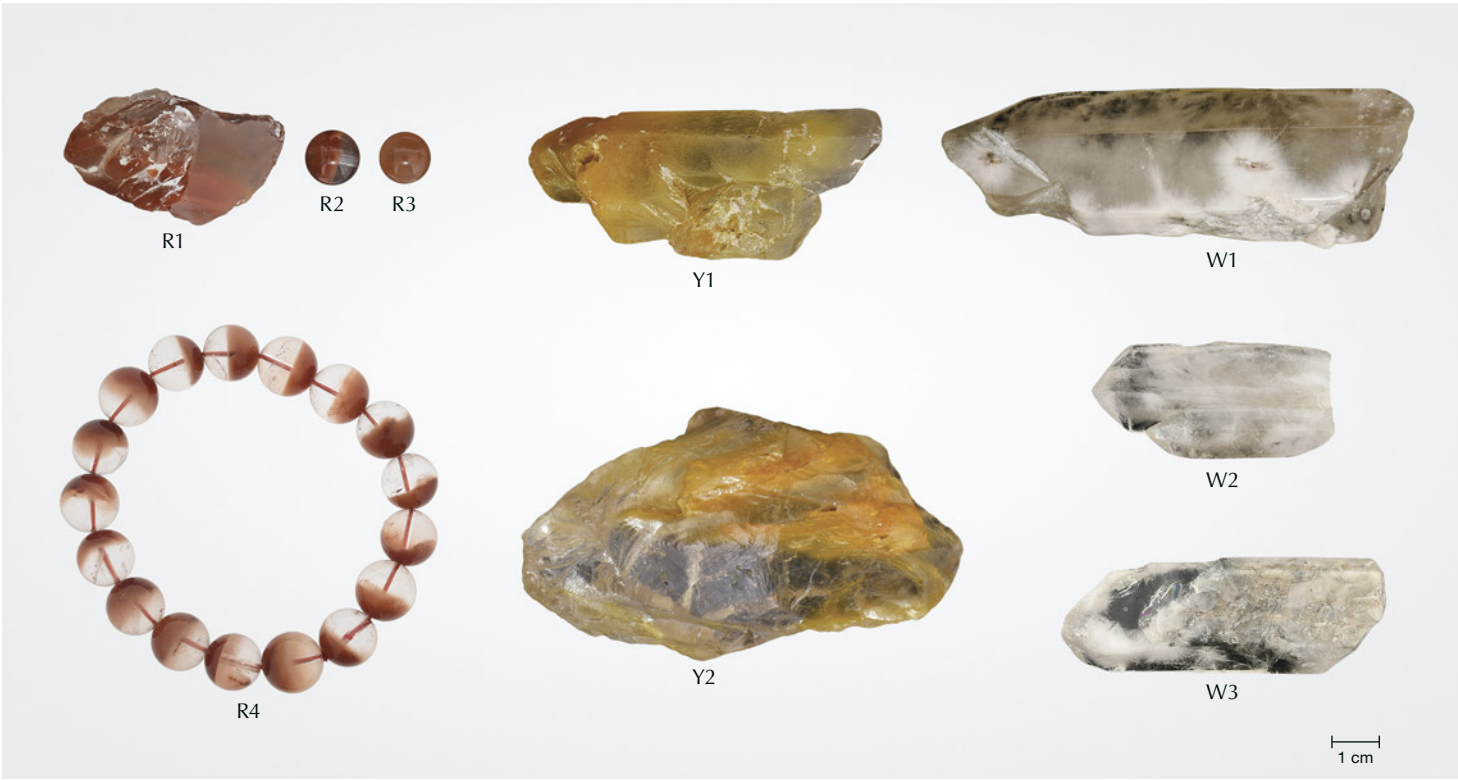

Figure 15. "Rabbit hair" quartz samples with different colors. Photos by Shuqian Rui.

Special hair-like inclusions in quartz. "Rabbit hair" quartz is a commercial variety of quartz with special inclusions. These inclusions resemble rabbit fur and are shorter and thinner than the typical rutile, tourmaline, or other acicular inclusions found in sagenitic quartz. To explore their internal features, nine rabbit hair quartz samples were classified according to the color of their inclusions (figure 15): red (R1–R4), yellow (Y1 and Y2), and white (W1–W3). The white rabbit hair quartz is rarer than the other colors.

Microscopic observation shows slight variation between the different colors of these hair-like inclusions. In the red rabbit hair quartz, massive curved red fibers are distributed evenly. They are mostly brownish red and less than 1 mm in length (figure 16A). The bright yellow needle-like inclusions are distributed regularly but with some localized disorder. Some of the disordered parts form divergent bundles (figure 16B). The white inclusions seem to be hollow tubes, measuring approximately 1–2 mm (figure 16C).

Figure 16. A: Fibrous inclusions in red rabbit hair quartz (sample R1). B: Needle-like inclusions in yellow rabbit hair quartz (sample Y2). C: The tubular inclusions in white rabbit hair quartz (sample W1). Photomicrographs by Shuqian Rui; fields of view 0.71 mm (A), 0.91 mm (B), and 1.26 mm (C).

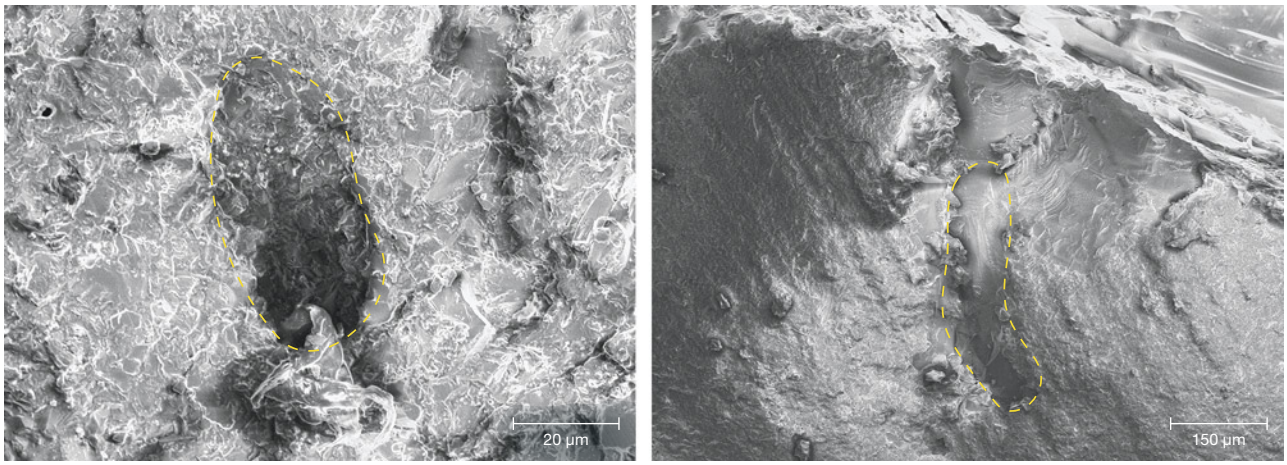

Figure 17. The secondary electron images of the oblique section of the hollow tubes, outlined in yellow (sample W1). Images by Jinyu Zheng.

Raman analysis identified the inclusions in samples W1, R1, and Y2. The hollow tubes in sample W1 with peaks at 208, 266, 355, 405, 465, 810, and 1083 cm^{-1} are the characteristic peaks of quartz. The fibrous red inclusions in sample R1 with peaks at 246, 295, 412, 612, and 1319 cm^{-1} are hematite. The yellow inclusions in sample Y2 with peaks at 305, 394, and 694 cm^{-1} are goethite.

The freshly exposed surface of sample W1 was observed by scanning electron microscope (SEM). Figure 17 shows the secondary electron images; the pits are oblique sections of exposed hollow tubular inclusions (left), and the morphology of parallel sections of hollow tubes can be observed as grooves (right). In the pits, SEM with energy-dispersive spectrometry indicated that the main composition was SiO_2, and no other impurity minerals filled into the hollow.

Fibrous hematite inclusions present in this study are rare in quartz, and their formation is likely related to the growth conditions (I. Sunagawa, *Crystals: Growth, Morphology and Perfection*, Cambridge University Press, Cambridge, 2005, p. 61). White hollow tubular inclusions might be the corroded product of hydrothermal fluids or weathering. In these processes, mineral inclusions were etched away, leaving the hollow tube with its original shape (Winter 2007 GNI, p. 370–373). However, the origin of yellow rabbit hair quartz still needs further research.

Qian Zhang, Shuqian Rui, and Xingtong Li
Gemmological Institute
China University of Geosciences, Wuhan

Jinyu Zheng
School of Earth Sciences
China University of Geosciences, Wuhan

TREATMENTS

Characteristics of treated rubies from Greenland. Rubies and pink sapphire from Greenland are a new addition to the trade. The deposits have been known for decades, but only in the last three years have the finished gems become available in the market. The vast majority of the material is mined by the company Greenland Ruby and disclosed as treated. The habits of the rough corundum crystals are tabular, barrel, or rounded in shape. Their color ranges from dark red to very light pink, with a varying purplish or grayish cast.

Since the stones are mined from a primary deposit, they are often attached to other minerals. Most are mechanically removed at the mine site during the highly automated sorting process. At Greenland Ruby's treatment facility, some stones might be further manually trimmed or clipped to remove more of the matrix. Next, the rubies and pink sapphires are intensely cleaned with strong acids. These dissolve most minerals but do not affect the corundum. Lime is used to neutralize the acid, sometimes leaving a thin white coating on the rough stones.

After cleaning, the stones are heated with flux in crucibles and heated in electric furnaces for multiple hours at high temperatures (>1500°C). This method improves the clarity by healing thin fractures. Excess flux covers the rough stones in a thin glassy layer. After cooling, this product is polished as cabochons or beads. Higher-clarity pieces are faceted. The small amount of corundum produced by artisanal miners is treated in a similar fashion, but their exact procedures are not known.

Inclusion scenes of untreated stones are described in C.P. Smith et al. ("Ruby and pink sapphire from Aappaluttoq, Greenland," *Journal of Gemmology*, Vol. 35, No. 4, 2016, pp. 294–306) and K. Thirangoon ("Ruby and pink sapphire from Aappaluttoq, Greenland: Status of ongoing research," *GIA Research News*, March 23, 2009). These studies highlight the unique and exotic suite of crystal inclusions, including sapphirine and cordierite. We were able to complement these earlier works by studying some of the high-grade material recently produced by Greenland Ruby that has been treated. This is a very intense treatment pro-

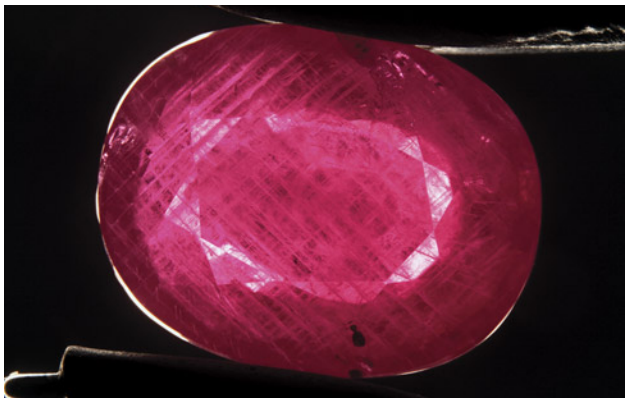

Figure 18. Greenland's rubies are characterized by abundant twinning planes. The twinning planes are not altered by the treatment at a larger scale, but features associated with the twinning can be significantly affected by heating. Photo by S. Wongchacree; field of view 14.40 mm.

cedure that significantly alters the inclusion scenes of Greenland's rubies and pink sapphires.

The most obvious internal features are linked to the omnipresent twinning in corundum from Greenland (figure 18). The twinning planes themselves are not altered by the treatment. The so-called Rose channels, which are hollow tubes at the intersection of twin planes, do show changes. Small fractures, often healed, develop around the linear features, while the tubes themselves usually take on a more spotted appearance when viewed at higher magnification (figure 19A).

Most crystal inclusions show strong alteration, as expected for high-temperature treatment. This makes the unique inclusion scene of Greenland ruby and sapphire unrecognizable. Many of these inclusions transform into "snowballs" with a white frosty opaque nature, often accompanied by discoid fractures that can show signs of healing (figures 19, B and C). In rare cases, crystal inclusions such as zircon remain unaltered.

Less common in Greenland rubies are particles and platelets. Since they require a correct alignment of the observer, platelet, and light source to be detected, they are often overlooked. The particles are a mix of elongated and irregularly shaped platelets. Some could be described as short, stubby needles resembling arrowheads (figure 20, left). They can also appear in dense clouds of finer particles with a roughly hexagonal outline (figure 20, right). These look very similar to the features observed in East African rubies from Mozambique and Madagascar, where they are very common. These seem to be only subtly affected by the treatment. In rare cases, the platelets take a roughly hexagonal form with concentric brightness zoning, resembling a fried egg "sunny-side up." These may be reminiscent of inclusions typically associated with Thai rubies, although Thai rubies almost never show the presence of other particles. We suspect that the unique appearance of these platelets is due to the intense heat they have been subjected to.

Apart from the twinning features, the most obvious features in the treated stones are flux-healed fractures. These are caused entirely by the treatment and are diagnostic of flux healing. As such, they are completely unrelated to a specific origin. Remnants of the flux trapped in the healing fracture can appear as small irregular droplets or connecting worm-like tubes (figure 21, A and B). These might bear some resemblance to natural fingerprints, but they usually have a coarser appearance with more translucent whitish patterns. When the healing is incomplete, the flux can be present in the fractures as a glassy substance showing swirling patterns and trapped gas bubbles (figure 21C).

The treatment has no impact on the corundum's trace element chemistry. The composition of the studied suite is in line with the data reported in Smith et al. (2016). The only values that show some deviation are the titanium concentrations, which are lower in the samples analyzed in this study (12–102 ppmw vs. 81–1227 ppmw in Smith et al.). This might be explained by the higher quality of the samples and thus the absence of cloudy, rutile-rich zones

Figure 19. A: The Rose channels take on a more spotted appearance and can have multiple partially healed fractures around them; field of view 1.44 mm. B: This crystal was completely destroyed; all that remains is a cottony "snowball" inclusion; field of view 1.80 mm. C: All of the inclusions in this cluster developed partially healed fractures around them; field of view 3.60 mm. Photomicrographs by S. Wongchacree (A) and C. Khowpong (B and C).

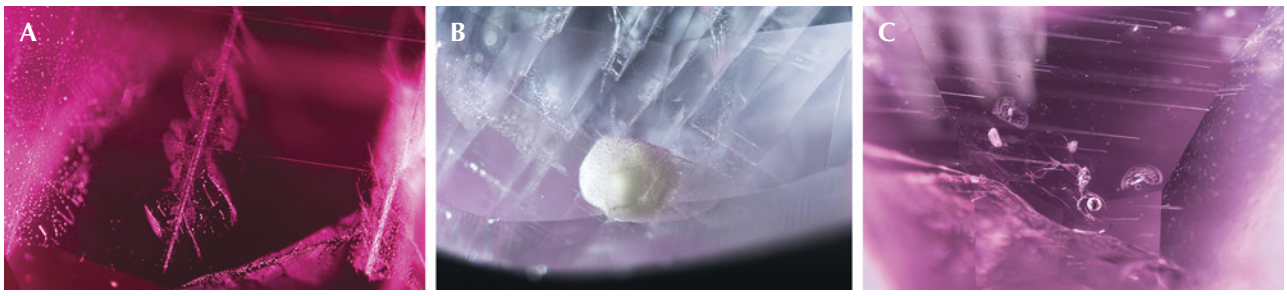

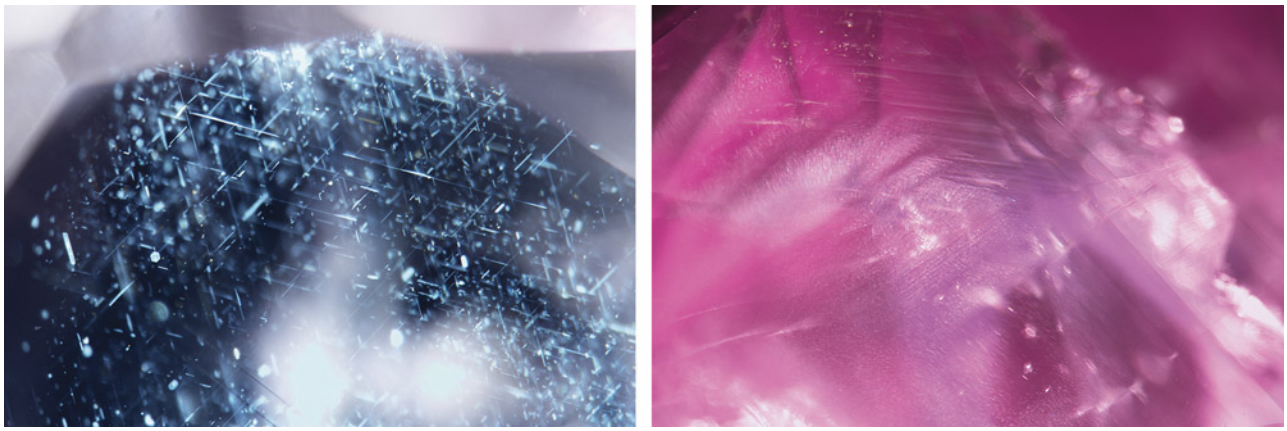

Figure 20. Left: The particles often appear as a mix of short needles, arrowheads, and more irregular shapes. Illuminating them requires the right orientation of the eye, particles, and light source. Right: Dense clouds of finer particles are occasionally found in Greenland rubies. Photomicrographs by C. Khowpong; fields of view 2.40 mm (left) and 2.88 mm (right).

that have higher titanium concentrations. As mentioned in earlier studies, the trace element composition of these stones can overlap with rubies that form in amphibolites, which are commonly encountered in East Africa (mostly Mozambique and Madagascar).

Heat treatment with added flux clearly has a significant impact on the overall appearance and can be easily detected by the multitude of healed fractures. The treatment does alter some important internal features that can complicate origin determination.

Martin Viala
Greenland Ruby, Bangkok
Wim Vertriest, Charuwan Khowpong, and Suwasan Wongchacree
GIA, Bangkok

A new treatment: Creating phantom structure in opal. Phantom structure in opal is a rare and interesting feature found only in Ethiopian opals (www.opalauctions.com/learn/opal-information/phantom-ghost-of-the-opal). The phantom consists of a large spherical inclusion, white and opaque, that is enclosed by transparent, yellow, or colorless host opal—whimsical names include "ghost," "egg," and "mother and daughter" opal. The exotic combination of precious opal surrounded by transparent opal renders this material more attractive and valuable. So far, there has been little research on its characteristics and formation.

At the end of 2021, while performing experiments on natural opal to test changes in transparency and the play-of-color effect with various solutions, the authors accidentally discovered how the phantom formed artificially in natural opal when immersing the stones in a mixture of water, oil, acetone, and other solutions (figure 22). As our curiosity continued to grow, we devised a treatment method to create a phantom in opal by adjusting the amount of solutions, time, and temperature. The phantom opal obtained by the treatment is visually similar to natu-

Figure 21. A: This healed fracture has irregular droplets of flux that were trapped during healing. They stand out due to their high relief and more translucent appearance; field of view 2.88 mm. B: Connecting networks of trapped flux in a healed fracture; field of view 2.80 mm. C: Not all fractures were able to heal to the same degree. Swirling droplets of trapped flux and air reveal that a large portion of this fracture is actually filled with solidified flux rather than healed corundum; field of view 1.20 mm. Photomicrographs by C. Khowpong (A and B) and S. Wongchacree (C).

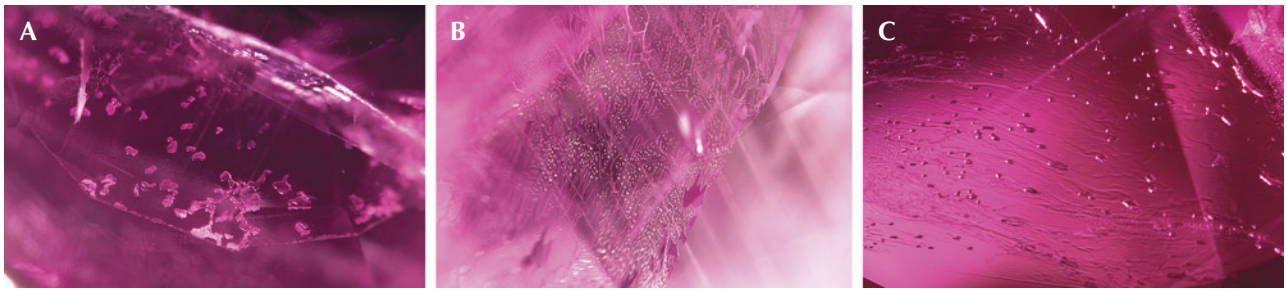

Figure 22. An 11.68 ct treated phantom opal in which the phantom structure appeared during experiments with various solutions. The sample is shown under daylight through the dome (left) and under halogen lighting through the bottom (right). Photos by Le Ngoc Nang.

ral phantom opal (figure 23). The treatment is simple, but it creates a spectacular and bizarre structure that improves the stone's appeal and value.

To reproduce the treatment process, we randomly selected an opal sample purchased from a jewelry store in Ho Chi Minh City (the seller did not know the gem's origin). The oval cabochon weighing 19.0 ct was white in bodycolor and semitranslucent, with weak play-of-color (dull orange, yellow, green, and blue). The gem was tested before and after treatment using standard gemological methods and Fourier-transform infrared (FTIR) spectroscopy with a spectral range from 650 to 4000 cm^{-1} at Liu Gemological Research and Application Center. The refractive index was 1.45 (spot method), and the hydrostatic specific gravity was 1.72–1.85. The stone was inert to long- and short-wave ultraviolet radiation. Examination with a gemological microscope revealed many black inclusions that might be black magnetite. FTIR spectroscopy displayed major absorption bands at 779, 999, and 1638 cm^{-1}. The gemological properties and FTIR analysis indicated natural opal.

After the gemological examination, the opal was soaked in a mixture of 90% vegetable oil and 5% ethanol, and the mixture was boiled at 80°C. Treatment time depended on the sample size and the expected size of the phantom. With longer heating time, more of the "phantom" was converted into transparent opal, resulting in a smaller center and larger surrounding transparent area. In this case, the author decided to treat the gem for 36 hours, and the finished artificial phantom was half the size of the host opal (figure 24). The shape of the phantom was similar to that of the host gemstone. Notably, the play-of-color area shrank after treatment. It went from covering the entire opal to just a thin layer at the outline of the phantom. Interestingly, the dull quality of the play-of-color did improve somewhat.

The characteristics of an opal sample before and after treatment are shown in table 1. Three distinct features can be used to identify the artificial phantom. The first is the morphological similarity between the host opal and its phantom. Second, the treated phantom opal strongly luminesces under long- and short-wave UV radiation as a result of the oil, while the natural opal is usually inert to weak green. Third, the FTIR spectra after treatment exhibit two additional significant peaks at 2853 and 2922 cm^{-1}, attributed to the symmetric and asymmetric stretching vibration of the aliphatic CH_2 group present in oil (N. Vlachos et al., "Applications of Fourier transform-infrared spectroscopy to edible oils," *Analytica Chimica Acta*, Vol. 573–574, 2006, pp. 459–465). The third feature is also the most noticeable evidence that the sample has been treated with oil.

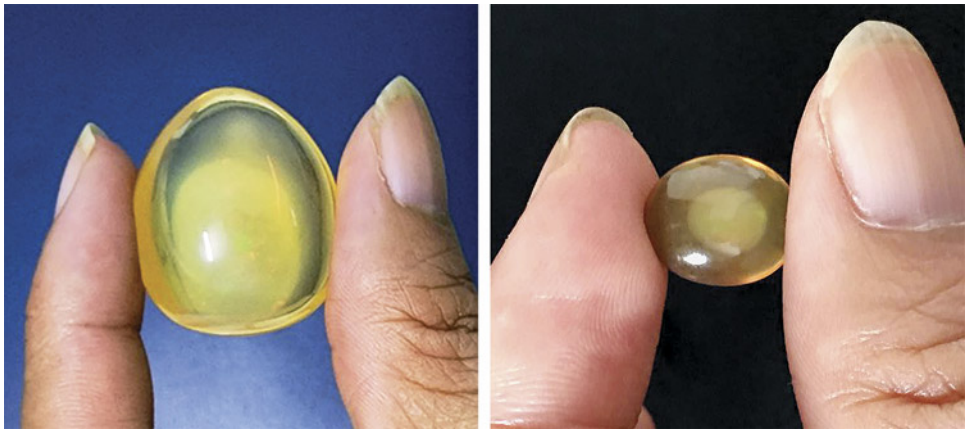

Figure 23. There is no significant visual difference between an untreated Ethiopian natural phantom opal (left, 35 ct) and a treated phantom opal (right, 6 ct). Photos by Le Ngoc Nang.

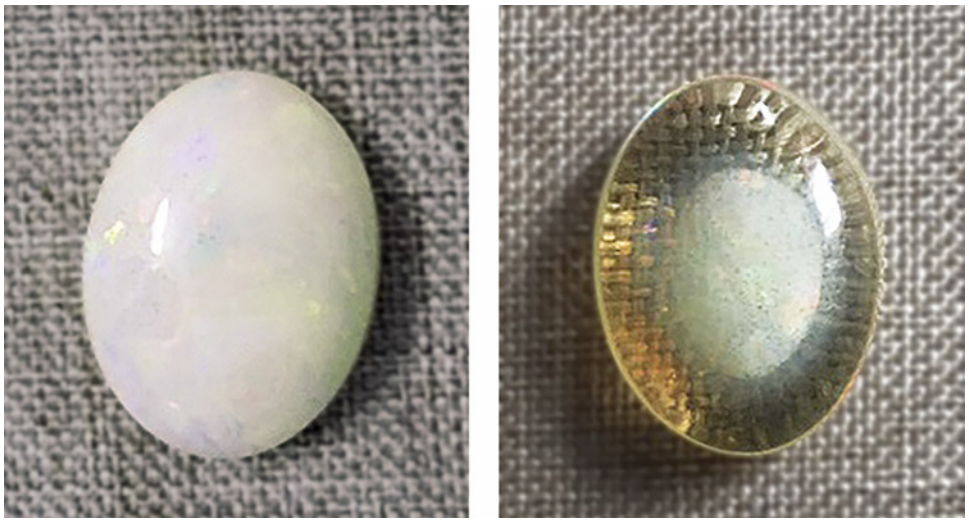

Figure 24. Left: The opal before treatment is semitranslucent white and shows a weak play-of-color. Right: After 36 hours of treatment, the opal becomes transparent light yellow, containing a white phantom. Photos by Le Ngoc Nang.

The treated sample was stored at room temperature under fluorescent lighting for three months to test the treatment's stability. The phantom remained intact, leading the authors to conclude that the treatment stabilization is permanent under normal conditions. The apparent stability of the transparent opal may be explained by the impregnated oil in the stone, which evaporates slowly. To avoid damaging the treatment, however, careful handling is still advised when wearing a stone treated in this way.

In gem trading, treated products must be disclosed. Treated phantom opal may appear commercially in the future, so it is important to disclose our treatment process used to create a phantom structure by impregnating opal with oil and heat, as well as the means to identify the treatment. More importantly, this report is intended to avoid confusion between natural and treated phantom opal.

Le Ngoc Nang and Pham Minh Tien
University of Science, Vietnam National University
Ho Chi Minh City
Liu Gemological Research and Application Center

TABLE 1. Gemological properties of a phantom opal before and after treatment.

Property	Before treatment	After treatment
Weight	9.31 ct	10.06 ct
Bodycolor	White	Yellow
Play-of-color	Weak green-blue-yellow-orange	Medium green-blue-yellow-orange[a]
Shape	Oval	Oval
RI	1.45	1.45
SG	1.72	1.85
Fluorescence	Inert	LW: Strong blue SW: Medium blue
Transparency[b]	Semitranslucent	Transparent
FTIR peaks	782, 1007, and 1645 cm^{-1}	782, 1007, 1645, **2853**, and **2924** cm^{-1}

[a]*The play-of-color on the outline of the phantom*
[b]*The transparency of the host opal*

AUCTION REPORT

Spring 2023 auction highlights. Following a lackluster start to the auction season in Hong Kong, all eyes were on the estate of late Austrian billionaire Heidi Horten in May, presented by Christie's in Geneva. Leading up to the three-part auction, the collection made headlines due to the controversial source of Horten's wealth. (Horten's late husband reportedly made his fortune buying businesses from Jews forced to sell well below value in Nazi Germany.) Despite the controversy, the sale became the most lucrative jewelry auction in history, garnering $202.2 million and surpassing the 2011 auction of Elizabeth Taylor's estate, which totaled $116 million. In accordance with her wishes, proceeds from Horten's estate were donated to a foundation for medical research, child welfare, and access to the arts, while Christie's pledged to donate part of its commission to Holocaust-related charities.

Also in Geneva, Sotheby's rebounded from a disappointing fall 2022 auction season for colored diamonds (Winter 2022 GNI, pp. 524–526) with the sale of the Bulgari Laguna Blu (figure 25). Cut by Bulgari in the 1970s for a private col-

Figure 25. The Bulgari Laguna Blu, an 11.16 ct Fancy Vivid blue diamond, was featured for the first time at auction in Geneva. Courtesy of Sotheby's.

Figure 27. The Estrela de Fura, a 55.22 ct ruby from Mozambique, became the largest and highest-priced ruby ever sold at auction. Courtesy of Sotheby's.

lector, the 11.16 ct Fancy Vivid blue diamond made its auction debut, selling just above its estimate at $25.2 million after only four minutes of bidding. As the highest-priced gem Bulgari has ever sold, the VS_1, type IIb diamond also holds GIA's highest color grade for a blue diamond.

Figure 26. The 126.76 ct Internally Flawless Light of Peace diamond sold for $13.6 million. Courtesy of Christie's.

The season ended on a high note in June with the New York auctions. Leading Christie's Magnificent Jewels sale, the 126.76 ct Internally Flawless Light of Peace diamond (figure 26) was offered without a reserve. Selling within its presale estimate, the GIA-graded type IIa diamond garnered $13.6 million. The largest stone cut from a 435 ct rough unearthed in West Africa, the Light of Peace was once owned by the Zale family, who used the diamond to fund peace-supporting missions. To continue this legacy of goodwill, a portion of the proceeds from the auction will be donated to the United Nations High Commissioner for Refugees.

At Sotheby's Magnificent Jewels auction, two gems smashed multiple records. The Estrela de Fura (figure 27), a 55.22 ct "pigeon's blood" ruby, became both the largest and most expensive ruby ever to sell at auction, raking in $34.8 million. The gem was cut from a 101 ct rough mined in Mozambique in July 2022, which made headlines as the largest gem-quality ruby ever discovered. Remarkable not only for its unprecedented size, the Estrela de Fura's florescence, clarity, and vivid red hue rival that of Burmese rubies. A portion of the proceeds from the sale will help establish the Fura Training Academy in Mozambique, encouraging access for locals to education and technical training in areas such as mining, engineering, carpentry, and agriculture.

Also selling for $34.8 million, the Eternal Pink (figure 28), a 10.57 ct Internally Flawless Fancy Vivid purplish pink diamond, fell just short of its estimate but still surpassed the previous record for a diamond of this color grade. The GIA-graded diamond, which was cut from a 23.78 ct rough from Botswana, set a new record price per

Figure 28. The 10.57 ct Eternal Pink diamond set a new record per-carat price at $3.3 million. Courtesy of Sotheby's.

carat at $3.3 million. Sales of the Eternal Pink and the Estrela de Fura helped Sotheby's break two more records, becoming the first auction to sell two items for more than $30 million each and achieving the highest total ever for a jewelry auction at Sotheby's New York. The overall sale brought in $95.9 million, topping the house's previous record of $65.1 million from April 2015.

Erica Zaidman
GIA, Carlsbad

Figure 29. Susan Jacques accepts the Robert M. Shipley Award at the American Gem Society's 2023 Conclave in Louisville, Kentucky. Courtesy of AGS.

ANNOUNCEMENTS

Susan Jacques receives Robert M. Shipley Award. Susan Jacques, GIA's president and CEO, has received the American Gem Society's Robert M. Shipley Award, honoring her steadfast commitment to the jewelry industry. Named for the founder of GIA and AGS, the prestigious award was presented to Jacques at the AGS Conclave in Louisville, Kentucky, on May 2, 2023 (figure 29).

Jacques previously served as president and CEO of Borsheims in Omaha, Nebraska, one of the nation's largest independent jewelry stores, where she reported directly to Warren Buffett. She served on GIA's Board of Governors beginning in 1996 and held the chair position from 2008 to 2013 before her appointment as president and CEO in 2014. Jacques holds a Graduate Gemologist diploma from GIA and is a fellow of the Gemmological Association of Great Britain. She is the sixth recipient from GIA to win the award.

GIA Alumni Collective. The GIA Alumni Collective offers an exciting new networking platform for GIA graduates. The online community at collective.gia.edu allows a diverse group of users to access both live and self-paced continuing education seminars, join virtual chapters, connect with global alumni, and more. The site also puts GIA alums in the spotlight (figure 30), celebrating those who uphold the highest standards of GIA's consumer protection mission.

Deeta Thakural earned her Graduate Gemologist diploma at GIA's Mumbai campus. As a fourth-generation jeweler, Thakural was drawn to design. Her award-winning collections blend organic shapes and rich hues that reflect the natural world.

Mélanie Matthes studied at GIA's Carlsbad campus, receiving Graduate Gemologist, Pearls Graduate, and Applied Jewelry Professional diplomas. Her education, fascination with gemology, and love of history led to her career with a well-known auction house, handling some of the world's most extraordinary jewelry pieces.

Learning from GIA guided each member of the Hodge family down a different path. Aldis, a self-taught watchmaker and business owner, and his sister Briana, a visual specialist and photographer, encouraged their mother, Yolette, to explore her childhood fascination with diamonds and earn a Diamonds Graduate diploma.

Visit https://collective.gia.edu/meet-the-collective.html to read stories from these alumni and more.

***Gemmes*.** Swiss-based Gemmologie & Francophonie has launched a French-language digital publication, *Gemmes* (figure 31). Released twice a year, the magazine covers a range of gem and jewelry topics and is open to submissions. Each article has an English-language abstract and figure captions. The debut issue can be downloaded at gemmologie-francophonie.com/index.php/la-revue-gemmes. The second

Figure 30. Deeta Thakural, Mélanie Matthes, Yolette and Briana Hodge, and Aldis Hodge are some of GIA's featured graduates on the Alumni Collective website.

issue, available in September, will examine lab gemology, art history, ethics, and more.

CONFERENCE REPORTS

2023 Sinkankas Symposium. The Nineteenth Annual Sinkankas Symposium was held at GIA in Carlsbad, California, on April 22. Cohosted by GIA and the Geo-Literary Society, the event's theme was "San Diego County Gems and Minerals." Pink tourmaline, kunzite, spessartine garnet, and aquamarine were the focus of 11 presentations (figure 32).

Emcee **Robert Weldon** (GIA, Carlsbad) welcomed the capacity crowd to the first in-person Sinkankas Symposium since 2019. **Dr. Raquel Alonso-Perez** (Mineralogical and Geological Museum, Harvard University) recounted the history of the Pala Chief mine starting in the nineteenth century. **Bill Larson** and son **Will Larson** (Pala International, Fallbrook, California) examined the tourmalines of the Pala Gem Mining District and the Himalaya mine, respectively. **Brendan Laurs** (*Journal of Gemmology*) overviewed the geology of San Diego County pegmatites. **Nathan Renfro** (GIA,

Figure 31. The new French-language digital publication Gemmes, *published by Gemmologie & Francophonie.*

Figure 32. Brendan Laurs, Meg Berry, and Aaron Celestian at the Sinkankas Symposium. Photos by Judy Colbert.

Carlsbad) showed fascinating inclusion features of various gem minerals from the county. **Dr. Skip Simmons** (Maine Mineral and Gem Museum, Bethel, Maine) detailed the tourmaline mineral group's compositional variation, crystal structure, and classification.

Cal Graeber (Fallbrook, California) shared insights based on more than 50 years of experience mining and collecting San Diego County minerals. Lapidary artist **Meg Berry** (Megagem, Fallbrook, California) shared her decades of experience cutting locally mined tourmalines and showed several of her award-winning creations. By video, **Paula Crevoshay** (Albuquerque, New Mexico) looked back on her love affair with the gems of Southern California, which have often been incorporated into her acclaimed jewelry designs. **Dr. Aaron Celestian** (Natural History Museum of Los Angeles County) spoke on the use of gems to illuminate art and science. Using the museum's special exhibit of Crevoshay jewelry as an example, he explained its integration with social media and traditional print media to communicate scientific content. **Dr. George Rossman** (California Institute of Technology, Pasadena) joined **Dr. Aaron Palke** (GIA, Carlsbad) in examining the range of colors and color-causing elements in San Diego County gem minerals.

The next Sinkankas Symposium, scheduled for May 2024 in Carlsbad, will be on Burmese gems from Mogok.

Sustainability conference at JCK. GIA participated in two panels on sustainability during the June 2023 JCK Las Vegas show. President and CEO Susan Jacques started the first panel by sharing with the audience the United Nations Brundtland Commission's definition of sustainability: "Meeting the needs of the present without compromising the ability of future generations to meet their own needs." A discussion covering GIA's sustainability initiatives followed, highlighting the goal of building an inclusive and resilient future for people and the planet. These initiatives focus on social inclusion, environmental protection, and economic growth—all interconnected and crucial for the well-being of individuals and societies.

Sustainability has risen to the forefront of the gem and jewelry industry in the past ten years. A 2022 joint study by the Boston Consulting Group (BCG) and Comité Colbert estimated that 65% of consumers consider brands' sustainability commitment when purchasing luxury products, and McKinsey & Company projected that sustainability-influenced fine jewelry sales will go from 5–10% in 2019 to 20–30% in 2025.

GIA uses scientific and research-based expertise to advance its crucial consumer-protection mission by driving transparency and bringing clarity to sustainability in the gem and jewelry value chain. In June 2023, GIA released its first sustainability report, developed in reference to the Global Reporting Initiative (GRI) framework and to the institute's first sustainability strategy.

Looking ahead, GIA has outlined a sustainability strategy for the next two years. GIA's 2025 sustainability strategy outlines the organization's ambition for change, aiming to champion transparency by building resilience in the gem and jewelry sector through pioneering research and innovation, ultimately instilling greater confidence in GIA. The institute will drive change from the inside out by building an inclusive culture and reducing its climate impact. Drawing on a science-led approach, GIA plans to improve traceability through digital tools. Collectively, the institute will accelerate circularity, spearhead sustainability-related gemology research, and continue to raise awareness through responsible education programs. By working together to champion transparency and build all-important trust, GIA intends to spark real, sector-wide sustainable change.

The second panel gathered sustainability experts from across the industry: **Sara Yood** (Jewelers Vigilance Committee), **Iris Van der Veken** (Watch and Jewelry Initiative 2030), **Josephine Silla-Afuwape** (SCS Global Services), and consultant **Christina Miller**. The session began with various definitions of sustainability, followed by a discussion of how the industry collaborated on the Federal Trade Commission's Green Guides. Panelists analyzed rising sustainability regulations in Europe and the U.S. and changing consumer behaviors. The presentation ended with key initiatives needed to start a sustainability journey.

Johanna Levy
GIA, New York

RESPECTED.
RENOWNED.
READY FOR YOU.

Online Courses from the Experts

Start learning from anywhere with self-paced online courses created by the leader in gemological research and education. Designed for working professionals, GIA® courses on diamonds, colored stones, pearls, and jewelry deliver knowledge you need to advance your career.

CHOOSE YOUR SAMPLE LESSON

Fire Obsidian's Beguiling Spectrum

Robert Weldon and Nathan Renfro | GIA, Carlsbad

Tom Dodge (figure 1) has come to be associated with the natural glass known as "fire obsidian." Since 2014 he has championed its vibrant beauty. He has also mined for it, for weeks at a time, at a private property owned by Emory Coons in the desolate Glass Buttes region of central Oregon in the United States (figure 2). This volcanic terrain is easier to mine in late spring and summer.

Dodge has spent years learning how to best fashion the material, first forming and then delicately polishing the glass at his lapidary workshop in Phoenix, Arizona. Although it is challenging to visualize where the colors may lie in the rough, he has developed an affinity for locating iridescence in the raw material (figure 3). Interviewed at his lapidary studio in Phoenix in 2022, Dodge noted that even among his carefully selected chunks of glass, there are countless samples that simply do not show the effect, even after lapidary work. Others contain reflective layers that are not flat—when fashioned, they appear to billow and ripple like a windblown flag.

Due to these nuances, which change from sample to sample, he takes time to carefully trim, fashion, and polish the pieces. He uses diamond abrasive cabochon-cutting equipment and optical-grade cerium oxide polishing powder to reveal vivid spectrums of undulating color and depth. While the exterior shapes he produces are large oval cabochons or tablets, the patterns and colors experienced in any piece, with proper lighting and orientation, are never replicated.

Figure 2. The Glass Buttes region of the U.S. state of Oregon.

Figure 1. Tom Dodge was interviewed in February 2022 by GIA at his lapidary studio in Phoenix. Photo by Pedro Padua.

Fire Obsidian

"Obsidian, a natural volcanic glass, is not particularly rare," Dodge said, demonstrating how to shine a light on samples of his most vibrant cabochons. "The material is widespread across the world. Most of it comes from the Western United States, but [it can be found] anywhere there are volcanic terrains. In North America, Mexico, and South America, there is an abundance."

Fire obsidian, so named for its vivid spectrum of colors, is rare and so far has been found in only one site within the Glass Buttes region of central Oregon. A rhyolitic dome field, Glass Buttes has vast quantities of obsidian in various patterns and varieties. But only a tiny percentage of it is suitable for fire obsidian.

Dodge differentiates fire obsidian from so-called rainbow (or sheen) obsidian, which exhibits broad, mostly even bands of pastel colors. Much of that material comes from the Mexican state of

Figure 3. Dodge describes taking a chip off of the rough. This provides a "window" into the stone so he can spot flow bands in the glass. The flow bands give rise to the phenomenal colors, and provide guidance in his lapidary work. Photo by Pedro Padua.

Jalisco and from northern California (C. Ma et al., "Micro-analytical study of the optical properties of rainbow and sheen obsidian," *Canadian Mineralogist,* Vol. 39, 2001, pp. 57–71). Obsidian typically appears black or brown and is generally translucent in smaller pieces. Impurities in the glass such as magnetite (an iron oxide) or manganese give the material its natural bodycolor.

Beyond the bodycolor, though, it is the sudden flashes of vivid iridescent colors that give fire obsidian its distinctive appeal.

"This is caused by a thin-film interference, when one type of the obsidian is in contact with another type of obsidian, such as an iron-rich obsidian. This contact zone interacts with light as light reflects from the surface, enters the material, and is in part bent due to the optical characteristics of glass—its angle of refraction," said Dodge. "This phenomenon resembles the color effect you see in soap bubbles, oil on water, or windshield wiper fluid in contact with the windshield... So when those two reflected portions of light come back to your eye, you'll see red, you'll see green. And if you move the stone or change the angle of the light, some areas of that stone will reveal or change the perceived colors. There must be two overlying layers that have a different refractive index, which produces this remarkable iridescence."

Dodge also noted that the flow bands of obsidian that exhibit color are very thin—between 300 and 700 nm (C. Ma et al., "The origin of color in 'fire' obsidian," *Canadian Mineralogist*, Vol. 45, 2007, pp. 551–557)—which means that stones must not be polished to such an extent that the color spectrum is removed. When cut properly, often paralleling the flow structure in the glass, the optical effect is both sudden and stunning. Additionally, the flow structures give rise to unusual patterns that can resemble blades of grass, sections of ribbon, branches, or sharp blades.

"They are just intrinsically beautiful. The more you look at them, the more they have to offer—the more you will see. I still spend time with some stones that I cut five years ago, and I see things that I didn't see before."

Gemology of Fire Obsidian

The gemological properties of fire obsidian from Glass Buttes, Oregon, are quite consistent with those of nonphenomenal obsidian. The refractive index measured on one sample was 1.469, with a hydrostatic specific gravity of 2.36. The material was inert to both long- and short-wave UV. Microscopic examination of the material revealed distinct, paper-thin dark layers as the source of the vibrant iridescence. These layers are composed primarily of nano-size crystals of magnetite, which result in thin-film interference colors (C. Ma et al., 2007).

When illuminated properly with diffuse reflected light, a history of the once molten glass is revealed in the vibrant patterns showing flow structures that have obviously been stretched, sheared, and compressed in ways that only a molten material can be. These structures are preserved in the solidified glass, an amorphous material, and revealed only through human intervention with a keen eye and some basic lapidary equipment.

The photo gallery on the following pages shows images of fire obsidian fashioned by Dodge. Because of the directionality and highly reflective character of glass, fire obsidian is often photographed immersed in liquid to reduce surface light reflections. The photomicrography reveals numerous flow structures and vibrant patterns of thin-film interference resulting from layers of nano-size magnetite particles.

The photos are by Robert Weldon, and the accompanying photomicrographs are by Nathan Renfro. All specimens are from the collection of Tom Dodge.

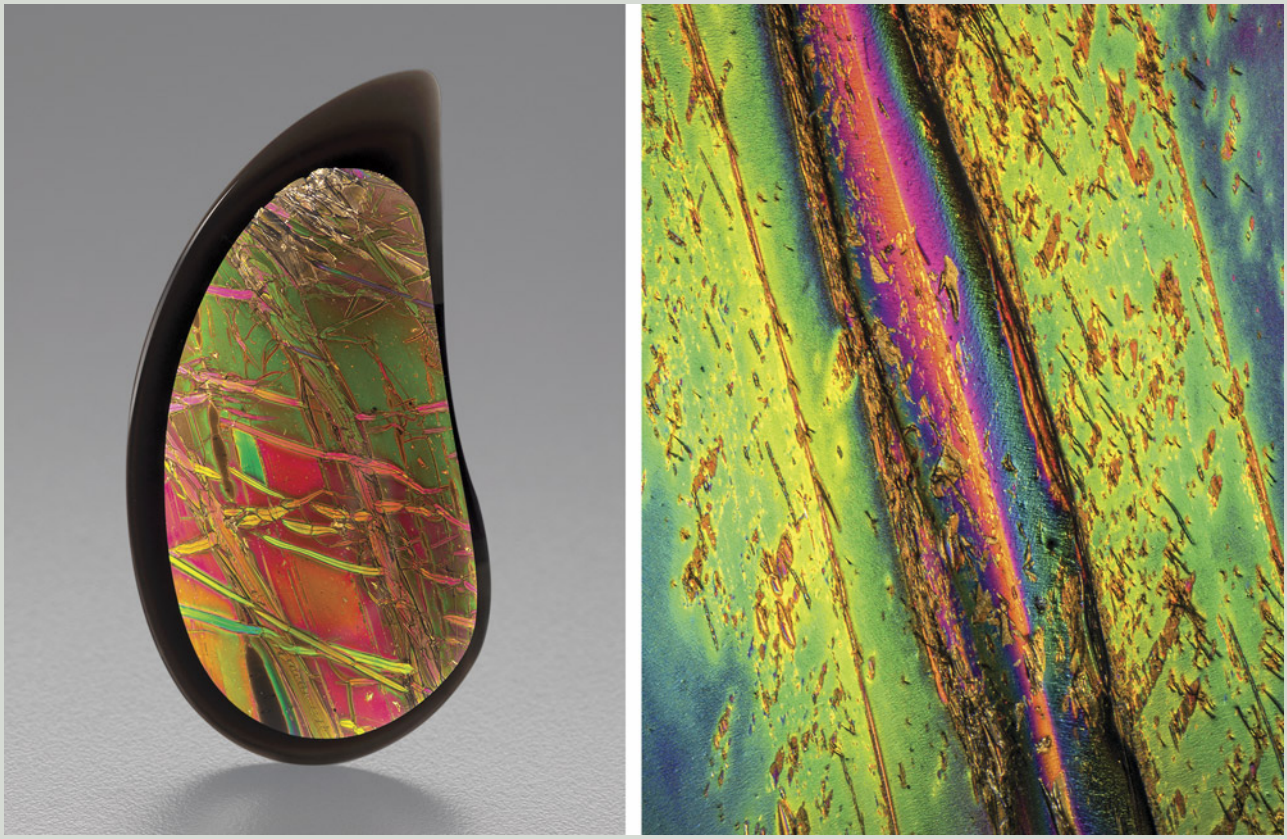

Left: 75.58 ct, 47.5 × 38.9 mm. Right: field of view 8.95 mm.

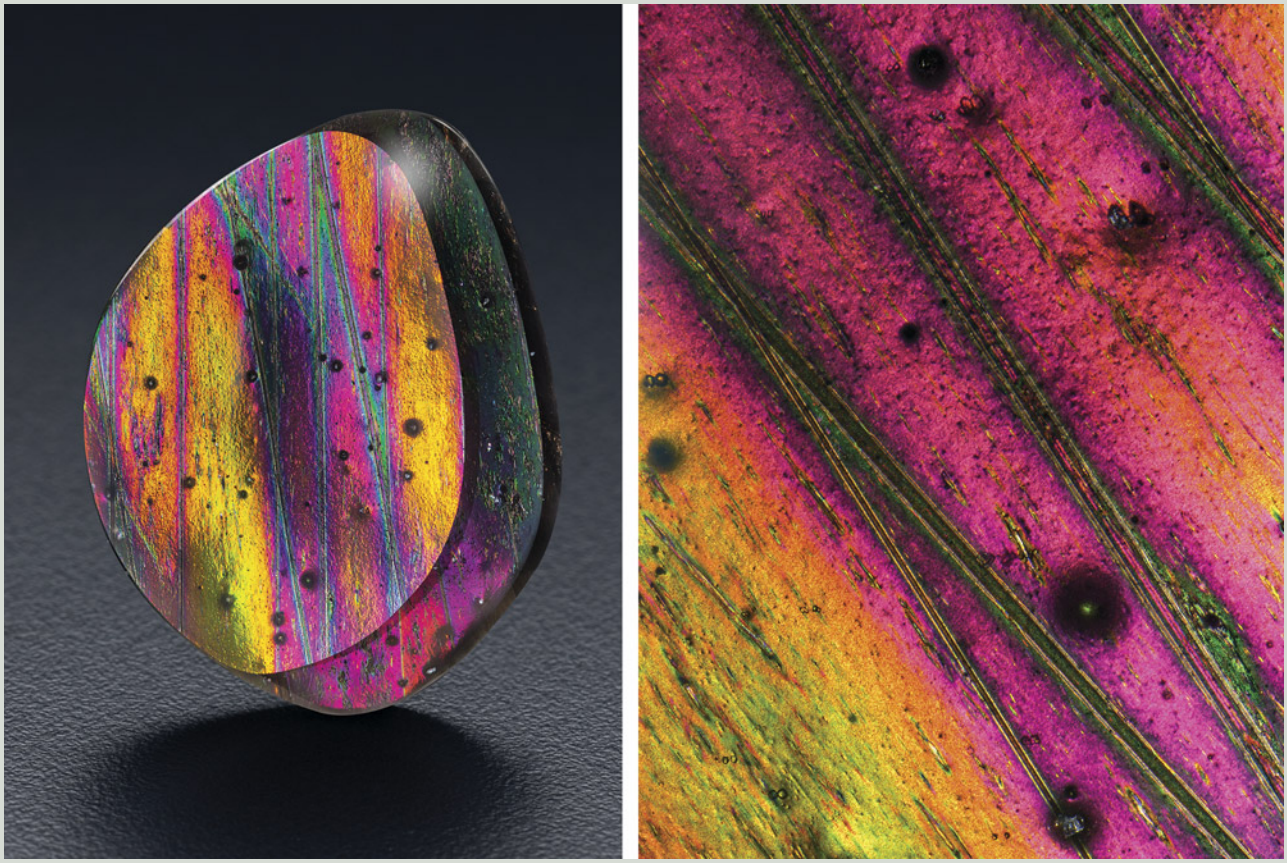

Left: 39.98 ct, 33.3 × 26.7 mm. Right: field of view 8.54 mm.

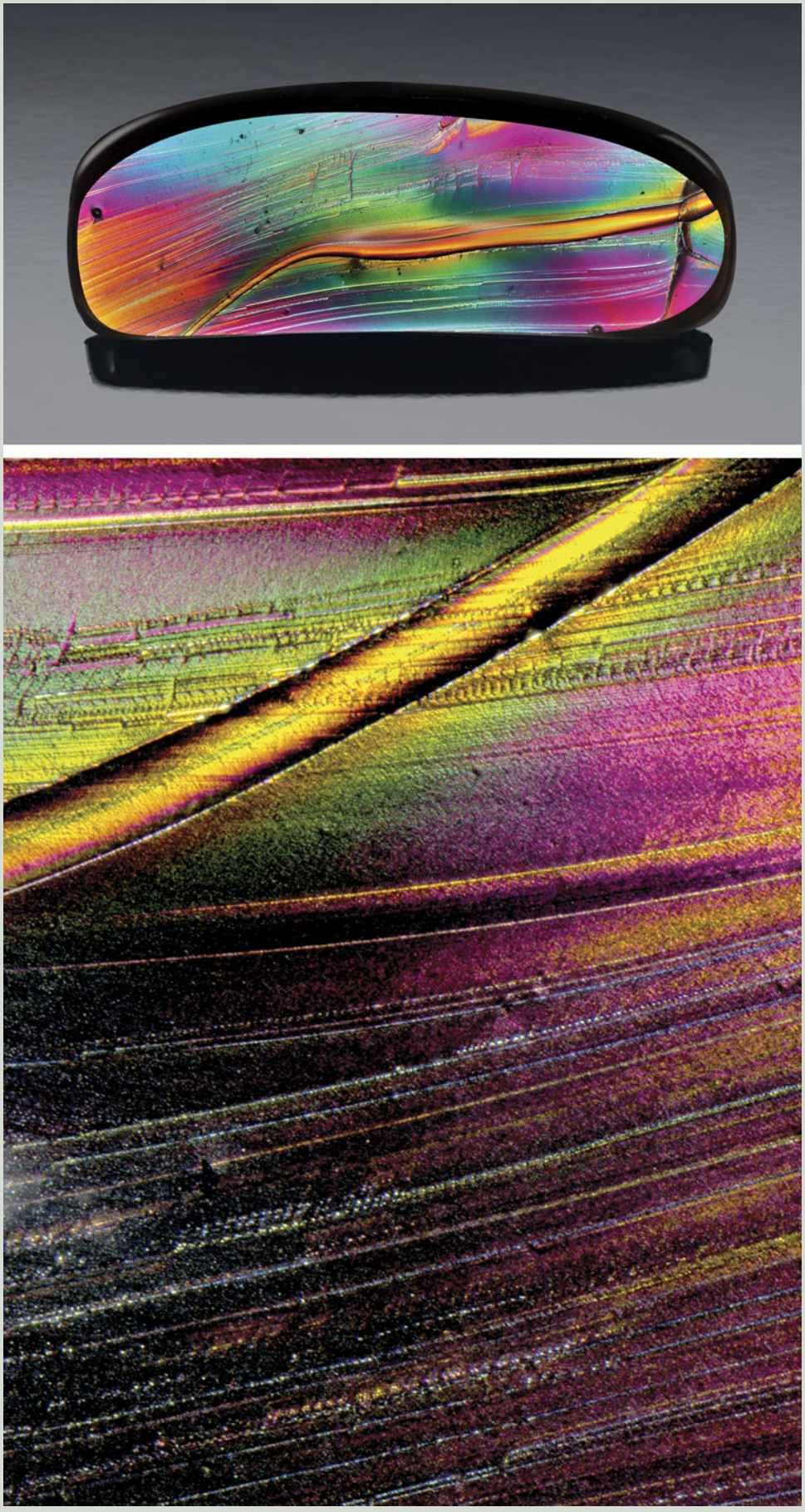

Top: 54.32 ct, 50 × 19 mm.
Bottom: field of view 6.27 mm.

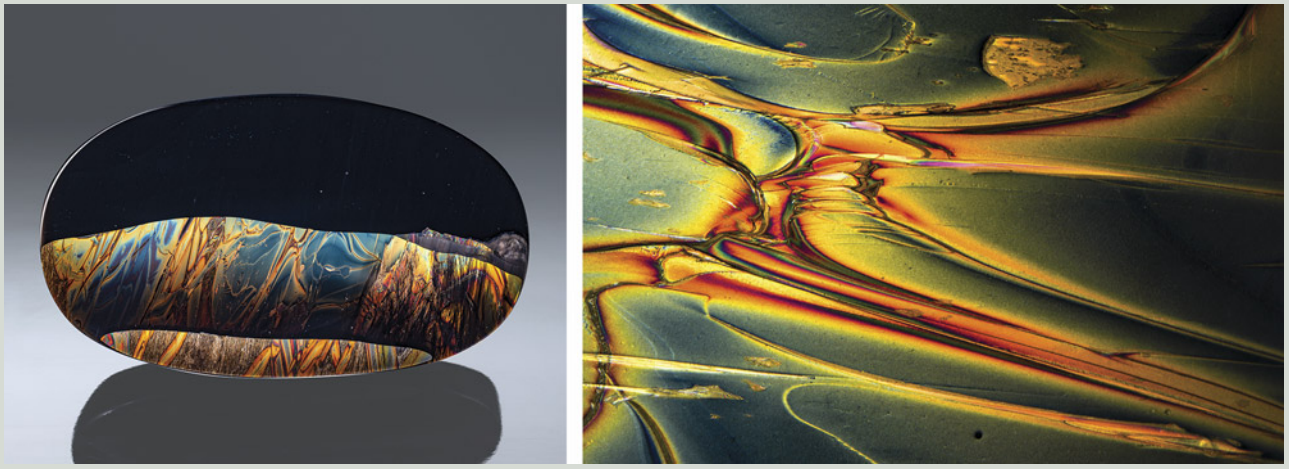

Left: 894.00 ct, 113 × 66 mm. Right: field of view 13.43 mm.

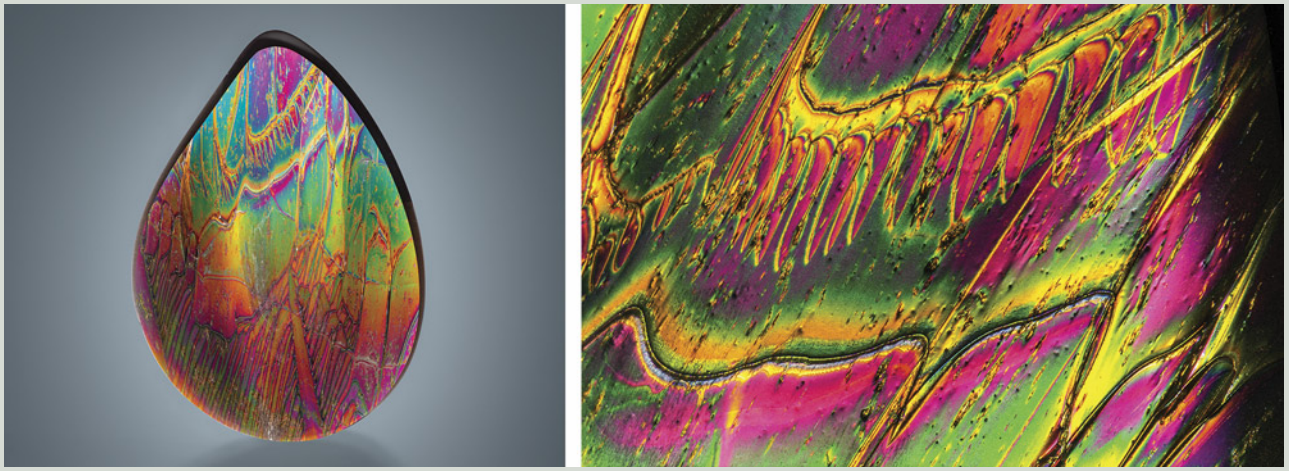

Left: 38.44 ct, 39.4 × 27.2 mm. Right: field of view 12.74 mm.

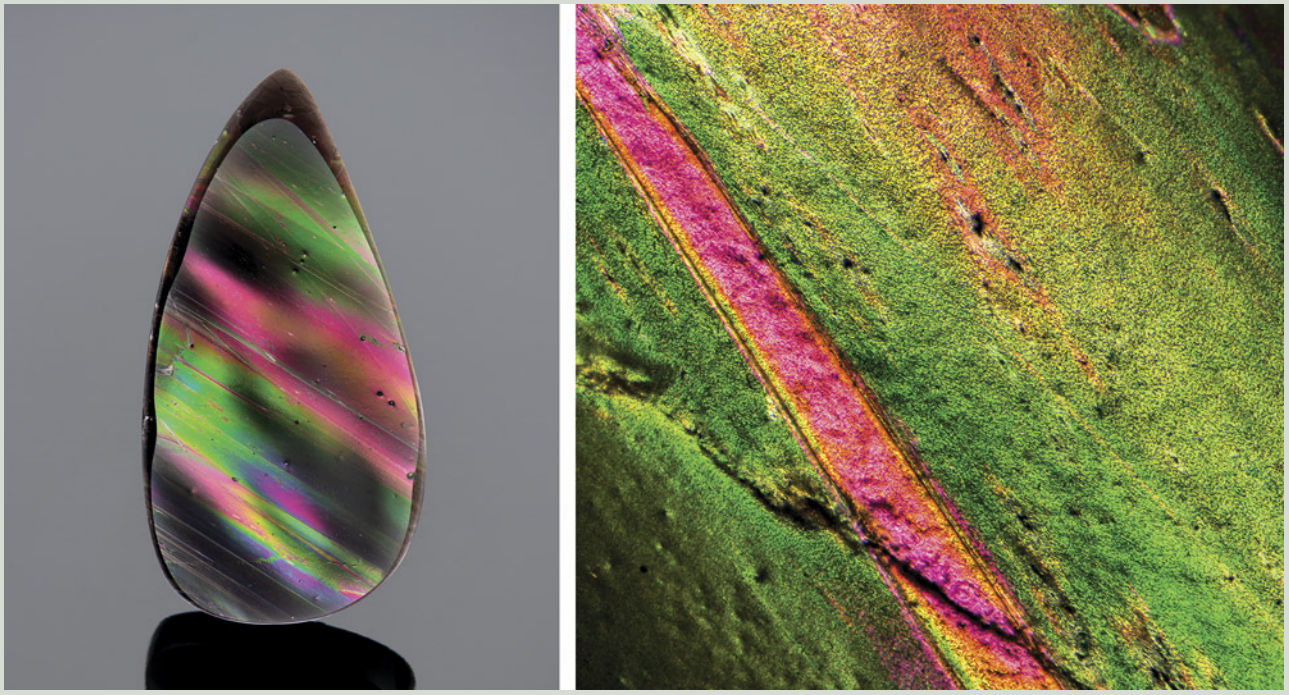

Left: 87.87 ct, 56 × 30 × 7 mm. Right: field of view 3.13 mm.

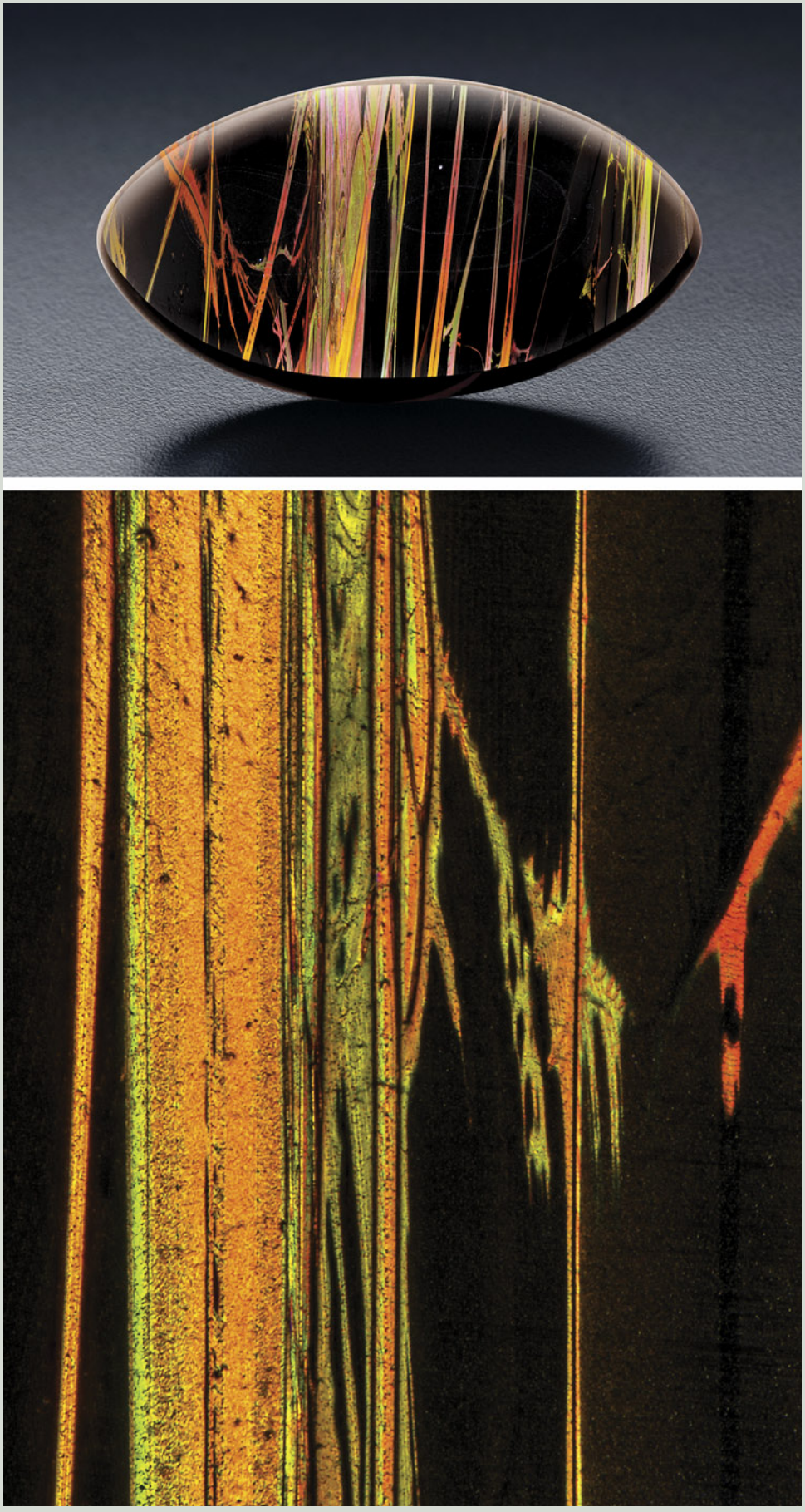

Top: 96.36 ct, 58.2 × 33.3 mm.
Bottom: field of view 4.36 mm.

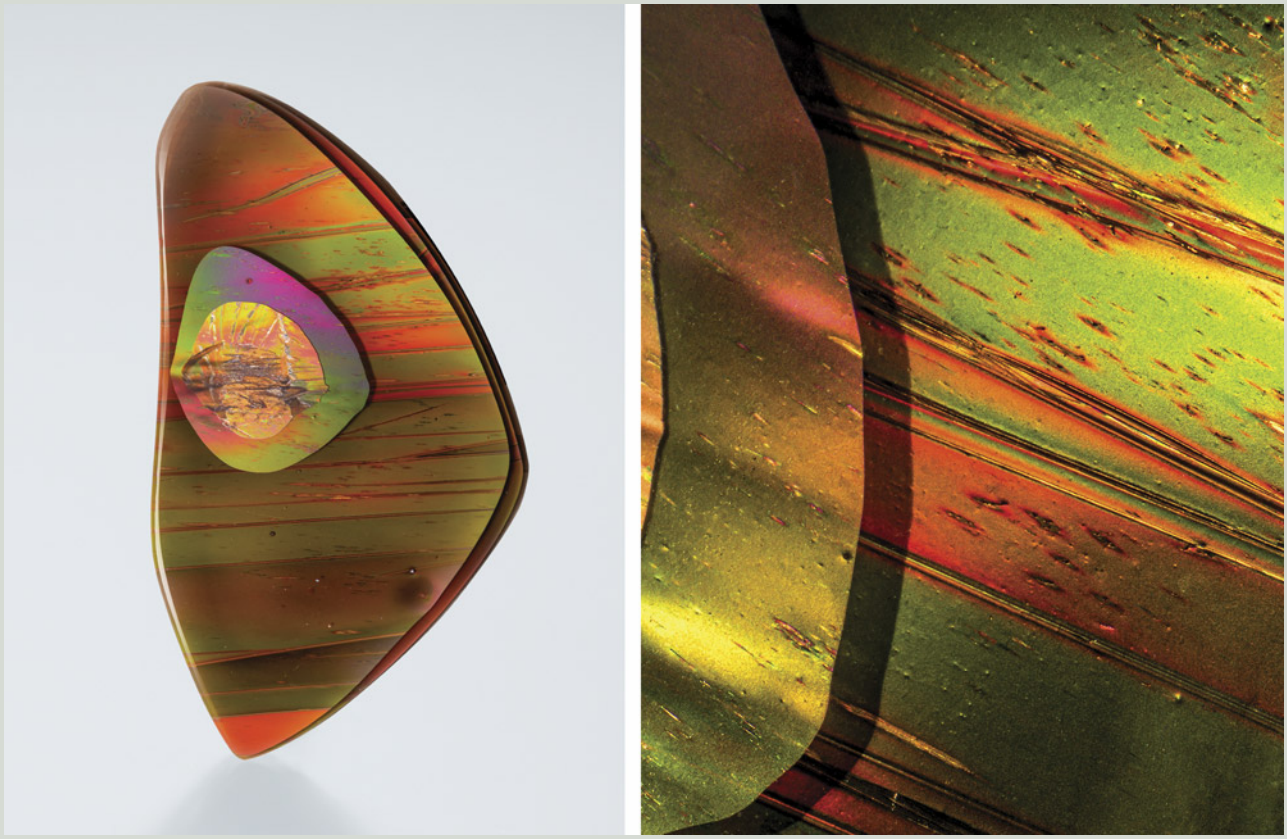

Left: 126.35 ct, 65.8 × 37.3 mm. Right: field of view 11.06 mm.

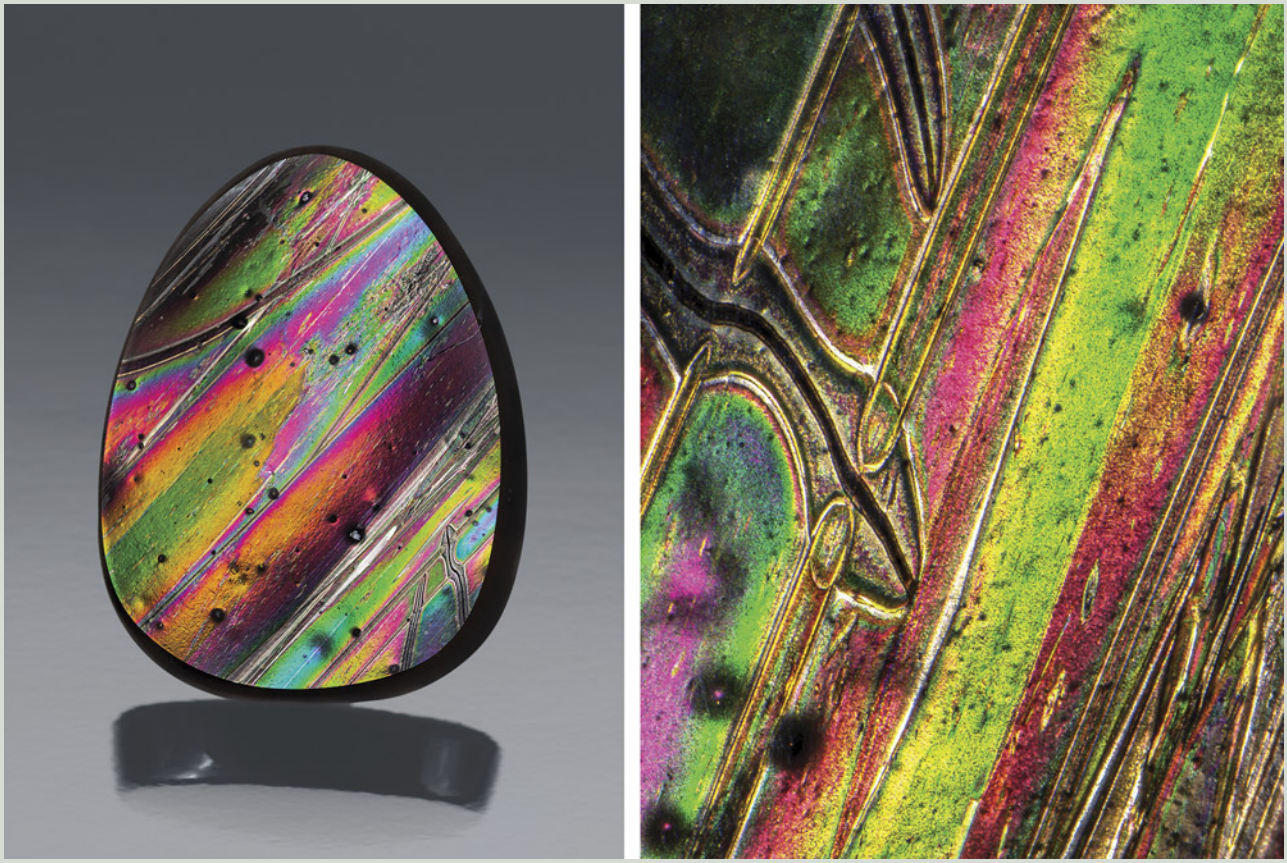

Left: 36.12 ct, 31.8 × 22.8 mm. Right: field of view 4.57 mm.